NANYANG
TECHNOLOGICAL
UNIVERSITY
SINGAPORE

SYNTHESISATION, CHARACTERISATION AND WATER ADSORPTION ON NOVEL FUNCTIONAL METAL ORGANIC FRAMEWORKS FOR HEAT TRANSFORMATION PROCESS

HAN BO

SCHOOL OF MECHANICAL AND AEROSPACE ENGINEERING

2020

SYNTHESISATION, CHARACTERISATION AND WATER ADSORPTION ON NOVEL
FUNCTIONAL METAL ORGANIC FRAMEWORKS FOR HEAT TRANSFORMATION PROCESS
HAN BO 2020

SYNTHESISATION, CHARACTERISATION AND WATER ADSORPTION ON NOVEL FUNCTIONAL METAL ORGANIC FRAMEWORKS FOR HEAT TRANSFORMATION PROCESS

HAN BO

SCHOOL OF MECHANICAL AND AEROSPACE ENGINEERING

A thesis submitted to Nanyang Technological University
in partial fulfilment of the requirements for the degree of
Doctor of Philosophy

July 2020

Statement of Originality

I hereby certify that the work embodied in this thesis is the result of original research, is free of plagiarised materials, and has not been submitted for a higher degree to any other University or Institution.

韓博

30 June 2020
. . . .
Date

. . . .
Han Bo

Supervisor Declaration Statement

I have reviewed the content and presentation style of this thesis and declare it is free of plagiarism and of sufficient grammatical clarity to be examined. To the best of my knowledge, the research and writing are those of the candidate except as acknowledged in the Author Attribution Statement. I confirm that the investigations were conducted in accord with the ethics policies and integrity standards of Nanyang Technological University and that the research data are presented honestly and without prejudice.

Anutosh Chakraborty

24 July 2020
. . . .
Date

. . . .
Assoc. Professor Anutosh Chakraborty

Authorship Attribution Statement

This thesis contains material from four (4) papers published in the following peer-reviewed journals and two (2) conference papers in which where I am listed as an author.

Chapters 3, 4 and 5 were published in the following articles and conference papers:

1. Han, B. and A. Chakraborty, Water adsorption studies on synthesised alkali-ions doped Al-fumarate MOFs and Al-fumarate+ zeolite composites for higher water uptakes and faster kinetics. *Microporous and Mesoporous Materials* **288**, 109590 (2019). DOI: 10.1016/j.micromeso.2019.109590.

The contributions of the co-authors are as follows:

- Associate Professor Chakraborty proposed the initial project direction and edited the manuscript drafts.
- I wrote the GCMC simulation code based on the molecular-interaction mechanism for water adsorption on Al-Fum based MOFs.
- I performed the GCMC simulations on water adsorption and analysed the collected data.
- The original and modified Al-Fum MOFs were synthesised by me in Fuel Cell Lab.
- I conducted the XRD, SEM and TGA characterisation on Al-Fum based MOFs samples in Materials Lab.
- The N_2 and water adsorption experiments were completed by me in Energy Systems Laboratory.
- Associate Professor Chakraborty guided me on the analysis of the water adsorption isotherms and kinetics results.

2. Han, B. and A. Chakraborty, Advanced cooling heat pump and desalination employing functional UiO-66 (Zr) metal-organic frameworks. *Energy Conversion and Management* **213**, 112825 (2020). DOI: 10.1016/j.enconman.2020.112825.

The contributions of the co-authors are as follows:

- The initial direction was provided by Assoc Prof Chakraborty.
- I prepared the manuscripts and Assoc Prof Chakraborty revised the drafts.
- I synthesised the parent and functionalised UiO-66 (Zr) MOFs in Fuel Cell Lab.
- The XRD, SEM and TGA characterisations on UiO-66 (Zr) based samples were performed by me in Materials Lab.
- The N_2 and water adsorption investigations were conducted by me in Energy Systems laboratory.
- I performed the modelling of the water adsorption in UiO-66 (Zr) based adsorbent structure.
- I wrote the simulation code for an integral AHT (adsorption cooling, heat pump and desalination) system based on the Thermodynamic Framework in MATLAB.
- I performed the simulation on the performance of the AHT system and analysed the simulated results.

3. Han, B. and A. Chakraborty, Adsorption characteristics of methyl-functional ligand MOF-801 and water systems: Adsorption chiller modelling and performances. *Applied Thermal Engineering* **175**, 115393 (2020). DOI: 10.1016/j.applthermaleng.2020.115393.

The contributions of the co-authors are as follows:

- The initial direction was proposed by me.
- Associate Professor Chakraborty provided his advice on the direction of this work.
- I prepared the drafts and Assoc Prof Chakraborty edited the manuscripts.
- The original and methyl functionalised MOF-801 (Zr) samples were synthesised by me in Fuel Cell Lab.
- I performed the N_2 and water adsorption experiments in the Energy Systems Laboratory.
- I conducted the XRD, SEM and TGA characterisation of the samples in Materials Lab.
- The theoretical fittings on the isotherms and kinetics data, the simulation regarding to the MOF-801 (Zr) based adsorption cooling systems and the analysis of the collected results were completed by me.

4. Teo, H.W.B., A. Chakraborty, and Han, B., Water adsorption on CHA and AFI types zeolites: Modelling and investigation of adsorption chiller under static and dynamic conditions. *Applied Thermal Engineering*, **127**, 35-45 (2017). DOI: 10.1016/j.applthermaleng.2017.08.014.

The contributions of the co-authors are as follows:

- The initial project direction was proposed by Assoc Prof Chakraborty.
- Dr Teo prepared the manuscript drafts and Assoc Prof Chakraborty revised the manuscript.
- I assisted in the modelling of water adsorption in AFI and CHA type zeolite adsorbent structure.
- I conducted part of the AFI/CHA type zeolite + water adsorption experiments in the Energy Systems Laboratory.

- Dr Teo performed the theoretical adsorption analysis and conducted the simulation for adsorption cooling application in MATLAB.

5. **Han, B.** and A. Chakraborty., Methyl-Functionalised Fumarate-based MOFs for Heat Transmission Applications: Fabrication, Characterisation and Water Adsorption Performances, 5th International Conference of Polygeneration (ICP 2019); May 15-17, 2019; Kyushu University, Fukuoka, Japan.

The contributions of the co-authors are as follows:

- I proposed the initial project direction.
- I prepared the manuscript draft and Assoc Prof Chakraborty revised the manuscript.
- I synthesised the original and methyl-functionalised fumarate-based MOFs in Fuel Cell Lab.
- I conducted all the XRD, SEM, TGA and N_2 adsorption characterisation of the fabricated MOF materials.
- I performed the theoretical adsorption analysis and adsorption cooling simulation via MATLAB.

6. **Han, B.** and A. Chakraborty., Water Adsorption on Parent and Alkali-ions Doped Aluminium Fumarate MOFs and Al-Fumarate-Zeolite Composites Employing Grand Canonical Monte Carlo (GCMC), 5th International Conference of Polygeneration (ICP 2019); May 15-17, 2019; Kyushu University, Fukuoka, Japan.

The contributions of the co-authors are as follows:

- The initial project direction was proposed by Assoc Prof Chakraborty.

- I wrote the GCMC simulation code and conducted the GCMC simulations on original and modified Al-Fum based MOFs + water adsorption system.
- The synthesisation and characterisation of the Al-Fum based MOFs are completed by me.
- I conducted the water adsorption experiments for all the Al-Fum based MOFs.
- Assoc Prof Chakraborty instructed me on the analysis of water adsorption data and the comparison study between GCMC simulation and experimental result.
- I prepared the draft and Assoc Prof Chakraborty edited the manuscript.

韓博

30 June 2020

. . . .

Date   Han Bo

ACKNOWLEDGEMENTS

I am sincerely grateful to my supervisor, Associate Professor Anutosh Chakraborty for presenting me this golden opportunity. Professor Chakraborty has always provided academic knowledge and inspiration to my study, and he also offered considerable support and encouragement to my personal life. His integral guidance is the foremost factor for the accomplishment of this thesis.

I would also like to thank Dr. Teo How Wei Benjamin, Dr. Sibnath Kayal and Dr. Fan Wu for sharing their specific knowledge. They have offered continuous assistance in theoretical discussion and experimental investigation for this research work.

Next, I am grateful to Mr. Lee Keng Yuan Roger, Mr. Yeo Boon Chuan Edward, Mr. Ang Koon Teck Lawrence and Mr. Koh Tian Guan from Energy Systems Laboratory, Mr. Leong Kwok Phui, Ms. Yeong Peng Neo Sandy and Ms Yong Mei Yoke from Materials Laboratory, Mr. Chan Ming Jiu Nick from Fuel Cell Laboratory, Ms. Chia Hwee Lang from Aerospace Structures Laboratory, all the Final Year Project students (Mr. Koh Wei Jin, Mr. Lee Wei Jiat, Mr. Loh Hong Wah Marcus, Mr. Tan Jun Hao Jarrell, Mr. Leong Zheng Kang, Mr. Tan He Jiang, Mr. Ng Mai Sheng, Mr. Lek Khiang Boon Gabriel, Mr. Saravanan S/O Munusamy, Ms. Chan Jing Ting and Ms. Tan Jing Wen Caselyn) and exchange students (Mr. Tahmid Hasan Rupam and Mr. Sumeet Merzara) for their contribution to the research.

I would also extend my appreciate to the University for offering me the NTU Research Scholarship. I would thank for the financial support from Ministry of Education (MOE), Singapore (grant no. RG 98/17-2017).

Lastly, I wish to express my deepest gratitude to my parents (Mr. Han Dong and Mrs. Zhang Hua), my parents-in-law (Mr. Liu Yong and Mrs. Luo Ying), my wife (Mrs. Liu Yanling) for their unconditional support and love throughout the process of pursuing the Ph.D. studies. Specially, I would dedicate this thesis to my new-born daughter, Ms. Han Zhiyun, for being an invaluable source of happiness.

Table of Contents

ABSTRACT

Referring to the present situation of the global climate condition, the reduction of the energy consumption is always of great importance in combatting the grave situation of enhanced global warming potential (GWP). Adsorption-assisted heat transformation (AHT) systems such as chillers, heat pumps and desalination can predominantly help us to reduce the global warming. Therefore, the adsorption devices should be improved with the use of highly efficient adsorbents. The main drawback of AHT system is its large thermal compressor size, which depends on the quality of the porous adsorbents, ranging from surface characteristic to uptake-offtake difference (Δq) per adsorption cycle. Therefore, novel adsorbents with desirable adsorption performances need to be designed and synthesised. Due to some striking properties such as high microporosity with structure diversity, promising isotherms and kinetics characteristics and outstanding thermal stability, metal organic frameworks (MOFs) have been identified as the potential adsorbent in recent years.

This thesis aspires to develop the thermodynamic frameworks of AHT from entropy flow and generation points of view employing the experimentally confirmed isotherms and kinetics of novel functionalised metal-organic-frameworks (MOFs). The MOFs are synthesised by hydrothermal techniques with alkali ions doping, conventional zeolite mixing and functional group implanting methods. Prior to fabrication of the proposed MOFs, a Grand Canonical Monte Carlo (GCMC) simulation is performed to predict the water adsorption performances on various structural-configuration of MOFs in terms of shorter hydrophobic length and uptake-offtake difference. It is found that the addition of alkali ions or zeolite-MOFs composites increases the hydrophilicity in Henry's regions, which thereby shows "S-shaped" isotherms. Secondly, the hydrophilicity of the parent UiO-66 (Zr) MOFs in Henry's region are enhanced by the

functionalisation of -NH_2, -N or -OH. Furthermore, it is also observed from GCMC results that the implantation of -CH_3 additives on MOF-801 (Zr) shows longer hydrophobic length as compared to that of the parent MOF-801 (Zr), which delivers higher uptake-offtake difference (Δq) with fast kinetics per adsorption desorption cycle. The GCMC results show here the benchmark for the synthesisation and post modification of MOFs and composite adsorbents.

The MOFs such as Al-Fum, UiO-66(Zr), MOF-801 (Zr) and AL-Fum/zeolite composites are at first synthesised and later the MOFs are post synthesised with various alkali dopants and the additives (-NH_2, -N, -OH and -CH_3). After synthesisation, the parent and modified adsorbents are characterised by X-Ray diffraction (XRD), scanning electron microscopy (SEM), thermogravimetric analysis (TGA) and N_2 adsorption approaches. The water adsorption isotherms and kinetics are studied by a thermo-gravimetric analyser. It is found that 5% Li-Al-Fum, 30% AFI-Al-Fum and 30% CHA-Al-Fum adsorbents provide faster water-adsorption kinetics and higher uptake-offtake difference (Δq) as compared with the original MOFs. Secondly, it is also found that the amino (-NH_2) and hydroxyl (-OH) functionalised UiO-66 (Zr) MOFs improve water transfer from 0.05 kg/kg to 0.32 kg/kg. On the other hand, N-UiO-66 (Zr) shows the faster uptake/offtake rates as compared with the parent UiO-66 (Zr) MOFs. Furthermore, the methyl (-CH_3) functional group also improves Δq with two-times faster adsorption kinetics as compared to the parent MOF-801 (Zr) adsorbent.

Employing experimentally confirmed isotherms, kinetics and data related to bed dimensions and overall heat transfer coefficient, the energy and entropy balances for each component of heat transformation system (for cooling, heat pumping and desalination) are developed to calculate the system-performance and overall entropy generation from transient to cyclic steady state. The present results show that the smaller entropy generation ($\dot{S}_{gen}$) of an AHT system is obtained under lower regeneration temperature and shorter half cycle time, which leads to the reduction of system irreversibility and the improvement of efficiency. By analysing temperature-entropy maps for each component of the adsorption heat transformation process, the functionalised $(CH_3)_2$-MOF-801 (Zr) is shown to be a the promising adsorbent for adsorption cooling purpose whereas N-UiO-66 (Zr) is found suitable for adsorption desalination application. The temperature-entropy maps could be used to analyse $\dot{S}_{gen}$, which could be used as a tool to enhance the performances of the AHT system. These contributions provide a benchmark for new MOFs design, fabrication and the optimisation of adsorption assisted cooling/heat pump and desalination system.

The simulation results show that as compared with the original Al-Fum, the modified Li doped Al-Fum achieves 42.3% higher COP and 70% higher SCP. By functionalisation on the parent UiO-66 (Zr) MOF, the SCP (specific cooling capacity) improves from 0.36 kW/kg to 0.84 kW/kg, the SHP (specific heating power) enhances from 0.9 kW/kg to 1.48 kW/kg and the SDWP (specific daily water production) increases from 24 m^3 to 40 m^3 of desalinated water per tonne of functionalised UiO-66 (Zr) adsorbent per day. Furthermore, the methyl functionalised MOF-801 (Zr) provides relatively higher SCP, SHP and SDWP as compared with the parent MOF-801 (Zr). By analysing temperature-entropy generation diagrams with respect to the best AHT-performance-parameters, it is found that $(CH_3)_2$-MOF-801 (Zr) is the best candidate for adsorption cooling application and N-UiO-66 (Zr) is the most promising adsorbent for adsorption desalination applications.

LIST OF PUBLICATIONS ARISING FROM THIS THESIS

The author is grateful to his supervisor, Associate Professor Anutosh Chakraborty, to be the co-author of all the following publications.

JOURNAL ARTICLES

1. **Han, B.** and A. Chakraborty, Advanced cooling heat pump and desalination employing functional UiO-66 (Zr) metal-organic frameworks. *Energy Conversion and Management* **213**, 112825 (2020). DOI: 10.1016/j.enconman.2020.112825.
2. **Han, B.** and A. Chakraborty, Adsorption characteristics of methyl-functional ligand MOF-801 and water systems: Adsorption chiller modelling and performances. *Applied Thermal Engineering* **175**, 115393 (2020). DOI: 10.1016/j.applthermaleng.2020.115393.
3. **Han, B.** and A. Chakraborty, Water adsorption studies on synthesised alkali-ions doped Al-fumarate MOFs and Al-fumarate+ zeolite composites for higher water uptakes and faster kinetics. *Microporous and Mesoporous Materials* **288**, 109590 (2019). DOI: 10.1016/j.micromeso.2019.109590.
4. Teo, H.W.B., A. Chakraborty, and Han, B., Water adsorption on CHA and AFI types zeolites: Modelling and investigation of adsorption chiller under static and dynamic conditions. *Applied Thermal Engineering*, **127**, 35-45 (2017). DOI: 10.1016/j.applthermaleng.2017.08.014.

CONFERENCE PAPERS

1. **Han, B.** and A. Chakraborty., Methyl-Functionalised Fumarate-based MOFs for Heat Transmission Applications: Fabrication, Characterisation and Water Adsorption

Performances, 5th International Conference of Polygeneration (ICP 2019); May 15-17, 2019; Kyushu University, Fukuoka, Japan.

2. **Han, B.** and A. Chakraborty., Water Adsorption on Parent and Alkali-ions Doped Aluminium Fumarate MOFs and Al-Fumarate-Zeolite Composites Employing Grand Canonical Monte Carlo (GCMC), 5th International Conference of Polygeneration (ICP 2019); May 15-17, 2019; Kyushu University, Fukuoka, Japan. (Best Paper Award in the entire conference)

List of Figures

List of Tables

Nomenclature

Abbreviations

Acronyms	Meaning
AC	-Adsorption Cooling
AD	-Adsorption desalination
AHP	-Adsorption Heat Pump
BET	-Brunauer-Emmett-Teller Theory
C-C	-Clausius-Clapeyron relation
COP	-Coefficient of Performance for Adsorption Cooling
COP_h	-Coefficient of Performance for Adsorption Heat Pump
GCMC	-Grand Canonical Monte Carlo
IUPAC	-Interactional Union of Pure and Applied Chemistry
MD	-Molecular Dynamics
MOF	-Metal Organic Framework
SCP	-Specific Cooling Power
SHP	-Specific Heating Power
SDWP	-Specific Daily Water Production
SEM	-Scanning Electron Microscopy
TGA	-Thermo-gravimetric Analyser
XRD	-X-ray Diffraction

Greek Letters

Symbol	Meaning	Unit
α	-pre-exponential coefficient	[-]

β_0	-sticking coefficient	[-]
$\in$	-dielectric constant	[-]
σ	-collision diameter	Å
ε	-potential well depth	J
ϕ	-adsorbate-adsorbent interaction potential	kJ
ρ	-density of gas	$\mathrm{kg/m^3}$
θ	-surface coverage	[-]
θ_t	-real time surface coverage	[-]
θ_{ini}	-initial adsorption fraction	[-]
λ	-thermal conductivity	$\mathrm{W/(m \cdot K)}$
τ	-cycle time	s
μ	chemical potential	kJ
ψ	-flag for defining switching and operation modes	[-]

Latin Symbols

Symbol	**Meaning**	**Unit**
A	area	$\mathrm{m^2}$
C	energy-conversion constant	[-]
c_p	specific heat capacity	$\mathrm{kJ/(kg \cdot K)}$
d	distance of MOFs two layers	Å
E_a	BET activation energy	$\mathrm{kJ/mol}$
h	enthalpy / heat transfer coefficient	$\mathrm{kJ/kg}$ / $\mathrm{W/(m^2 \cdot K)}$
h_{fg}	latent hear of vapourization	$\mathrm{kJ/mol}$
k_{ads}	adsorption rate	$\mathrm{1/s}$
k_{des}	desorption rate	$\mathrm{1/s}$
K_H	Henry's law constant	$\mathrm{mol/(m^3 \cdot Pa)}$

L	adsorbent structure diagonal length	Å
m	Mass/heterogeneity coefficient	$\mathrm{kg}/-$
dm/dt	Mass flow rate of heat transfer fluid	$\mathrm{kg/s}$
P	pressure	kPa
P_s	saturated pressure	kPa
P_a	ambient pressure	kPa
q	amount of water vapour uptake	$\mathrm{g/g}$
q^0	limiting uptake	$\mathrm{g/g}$
Q	heat input/output	kW
Q_{st}	isosteric heat of adsorption	$\mathrm{kJ/kg}$
q_{st}^0	isosteric heat of adsorption at zero surface coverage	$\mathrm{kJ/kg}$
r_0	radius of adsorption bed	m
r_c	cutoff distance	Å
r_p	average pore size	Å
r	radial direction	m
R	gas constant	$\mathrm{kJ/(mol\cdot K)}$
S_{BET}	BET surface area	$\mathrm{m^2/kg}$
ΔS	entropy of adsorption	$\mathrm{kJ/(mol\cdot K)}$
T	temperature	K
t	time	s
$t_{half\ cycle}$	half cycle time	s
u	velocity	$\mathrm{m/s}$
U	overall heat transfer coefficient	$\mathrm{W/(m^2\cdot K)}$
v	specific volume	$\mathrm{m^3/kg}$
V	volume	$\mathrm{m^3}$
v_{pore}	pore volume	$\mathrm{cm^3/g}$
z	axial direction	m

Subscripts/Superscripts

Symbol	**Meaning**
a	adsorbed phase
ads	adsorption
bed	adsorption bed
cc	cooling capacity
chill	chilled water
cond	condenser
cool,in	cooling fluid at inlet
cw	cooling water
cw,in	cooling water inlet
des	desorption
eff	effective
evap	evaporator
f	fluids
f-m	fluid to metal (heat transfer)
fin	fin
fin-b	fin to bed (heat transfer)
g	gaseous phase
heating	heat transfer fluids
hot,in	heating fluid at inlet
in	inlet/input
i	heating/cooling water
l	liquid phase
m	metal
m-b	metal to bed (heat transfer)
m-M	metal to MOFs (heat transfer)
mt	metal tube
MOF	MOF adsorbents
ref	refrigerant (water vapour)

s	surface/saturated
tube	heat exchanger tube
w-bed	water to bed heat transfer

Chapter 1. Introduction

This chapter illustrates the details of the context in which the proposed work has been thought and developed along with the problem statement, motivation, and the main objective. The thesis outline and the contents of each chapter are also provided.

1.1 Background

The major needs of mankind are the production of electricity, heating, cooling, and desalting water. Due to rapid technological advancement and population growth, the global energy consumptions were increased significantly from 371×10^5 to 850×10^5 TW h in the last century [1]. Conti et al. [1] reported that the net electricity generation was 25.8 trillion kWh in 2020, which is 19.4% higher than that in 2012 and 15% of the global electrical energy being consumed for cooling applications. The higher energy consumption (18.6%) for the daily cooling generation in Singapore was reported by Chua et al. [2]. Furthermore, Chen et al. [3] projected the electricity consumptions for household heating and cooling loads as 224 billion kWh per year in some cities of east Asia. Generally, such needs are conventionally supplied by the burning of fossil fuels at power stations for electricity generation whilst the thermal and cooling needs are met in-situ by installation of energy efficient boilers and chillers [4]. All processes in the generation of the mentioned major needs involve irreversible resource exhaustion and environmental pollution. For example, serious atmosphere degradation such as global climate change, smog and acid rain are due to the excessive emission of greenhouse gas and other pollutants [4]. Based on the report stated by Conti et al. [1], the world energy-related CO_2 emissions was 35.6 billion metric tons in 2020 and it will rise up to 43.2 billion metric tons in 2040 under the current CO_2 emission growth rate. In addition, the abuse and improper disposal of refrigerants also leads to increased global warming [5]. On the other hand, 70% of the earth surface is covered by water and only 2.5% fresh and drinkable water are available. Kim et al. [6] reported that there is a growing demand for potable water with an increase rate of 2% annually to an estimate of 6,900 billion m^3 (Bnm^3) by the year 2030. Therefore, the desalination technology for converting seawater to fresh water is essential. However, the production and supply of clean, potable water consume energy from various energy sources, such as fossil fuel, natural gas, and coal and result global warming. The implementation of adsorption cycle for desalination is environmentally friendly and requires renewable energy such as solar to operate [7]. Therefore, for the sustainable development purpose, researches on innovative heat transformation systems to produce cooling [8], heating [9] and desalting water [10] become much more popular.

The adsorption-assisted heat transformation (AHT) system is energy-efficient and environmentally friendly. The AHT has no noise or vibration with low maintenance cost and long system life. In addition, the adsorption heat can be regeneratively re-cycled during the operation. Water is adopted as the refrigerant (adsorbate) due to its high latent heat of evaporation. On the other hand, silica gel and zeolites are used as adsorbents. Furthermore, a good numbers of research activities on the performances of AHT for cooling [11], heat pump [12] and desalination [10] are investigated, both experimentally and theoretically. Recently, silica gel and zeolites assisted AHT systems are gradually matured and broadened into commercial applications. The first adsorption chiller appeared in the market was designed by Nishiyodo Kuchouki, Co.Ltd in 1986, Japan [13]. The first adsorption chiller was driven by the heat source temperature of 85 ^{o}C and produced a rated cooling capacity of 51 to 1000 kW. The SorTech in Germany commercialised silica gel-water based compact adsorption chiller with the dimension of 0.795 m × 1.10 m × 1.19 m [14, 15]. Furthermore, the AHT systems (for cooling and heat pumps) are commercially promoted by the collaboration of SJTU and Jiangsu Shuangliang Air

Conditioner Equipment Company, and some representative products are summarised as: (i) silica gel-water adsorption chiller with the cooling power and the COP of 15 kW and 0.55, respectively [16, 17]; (ii) compact-scale adsorption air conditioner, with the dimensions of 300 mm × 500 mm × 950 mm and the cooling capacity of 1 kW [18] and (iii) $CaCl_2$/expanded graphite-ammonia assisted adsorption refrigerator with the cooling power and the COP of 11.4 kW and 0.27, respectively [19]. These commercially available AHT systems are bulky in nature and require more adsorbents to meet the cooling/heating loads.

In an AHT, the cooling and heat pumping effects are produced by the amalgamation of (1) evaporation assisted adsorption and (2) desorption triggered condensation [20] as shown schematically in Figure 1.1. The AHT consists of two or multi switchable adsorption beds. For a two-bed AHT system, one bed (Bed-2 in Figure 1.1) adsorbs the evaporated working fluid (occurs due to cooling load, Q_{evap} in the evaporator), and the other bed (Bed-1 in Figure 1.1) desorbs the water vapour from the porous materials. A multi-bed AHT system is operated under the same principle and a four-bed AHT is explained here for example [21]. The two beds are first cooled jointly for adsorption purpose and the other two beds are heated collectively for desorption purpose. In the next half cycle, the direction of the cooling/heating fluid switches, first two beds are heated and the other two beds are cooled sequentially. The heat generated during adsorption process (Q_{ads}) is released by the flowing of cooling water to the adsorption bed. For desorption process, the hot water releasing the desorption heat (Q_{des}) is supplied to the bed and later, the desorbed water vapour is condensed in the condenser. During desorption, both the temperature and pressure are increased. Finally, the liquid condensate flows back to the evaporator through a capillary tube to reduce the pressure in the evaporator. During condensation, the heat of condensation (Q_{cond}) is released through the cooling water of heat sink. The adsorption and desorption beds are switched in the next cycle, and these processes are repeated for the production of cooling and heating energies continuously. In an AHT cycle, the combined effects of enthalpies of adsorption and condensation of working fluid are used for heat-pumping purposes. The enthalpy of evaporation is used as the required cooling effect. In addition, the condensed water vapour could also be stored in the product water tank for desalination purpose. The schematic of AHT system is shown in Figure 1.1. Hence the TES (thermal energy storage) amalgamating the heat and mass recovery between the adsorption and desorption beds improves the heat pumping capacity and the distilled water production i.e. the overall efficiencies or the COP.

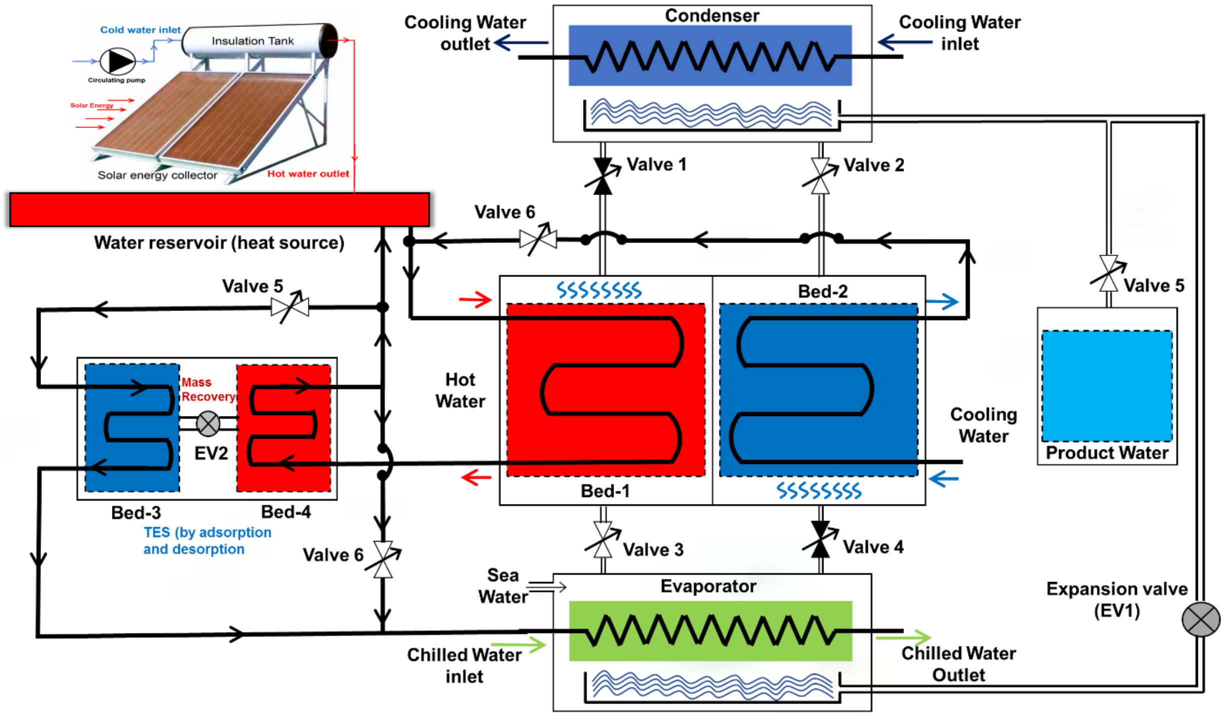

Figure 1.1: The schematic diagram of an adsorption assisted heat-transformation-system for hybrid cooling/heat pump/desalination operating mode [20].

1.2 Motivation

The thermal performances of the AHT are usually predicted from the shapes of the adsorption isotherms and kinetics graphs, which depend on the adsorbent porosity, pore-structure and adsorbent-adsorbate interaction [22]. Researches on conventional adsorbents such as zeolite and silica gel with water adsorption have a long tradition [11]. However, there are some disadvantages, for example, zeolites are highly hydrophilic and relatively higher temperature is required to desorb the water vapour from the adsorbent surface, resulting in high operational cost [23]. Silica gel is generally less hydrophilic as compared to zeolite structure and gives lower water adsorption capacity at the relative pressures of 0.1 – 0.3 [24]. Hence, both silica gel and zeolite fail to achieve higher water transfer (Δq) per adsorption-desorption cycle. The use of silica gel/zeolite leads to bulky thermal compressor size with poor AHT performances. Myat et al. [25] has shown that the "S-shaped" isotherm provides higher Δq as compared with type I isotherms under AHT working conditions, and requires lower regeneration temperature (< 60 °C) to drive the AHT. Theoretically, the Carnot COP (coefficient of performance) of an adsorption chiller is calculated by COP_{Carnot} = $[(\bar{T}_{ads} - \bar{T}_{des})/\bar{T}_{des}] \times [\bar{T}_{evap}/\bar{T}_{ads} - \bar{T}_{evap}]$ [26], which is about 0.8. However, all the published works show that the practical COP of adsorption chiller usually ranges from 0.2 to 0.5. Besides the low sorption quantity (Δq) of the solid sorption technology, another main reason is its low heat transfer performance. One approach to overcome this drawback is the development of high quality heat exchanger, such as employing plate finned heat exchangers [27] and feasibility coating with adsorbents [28]. In addition, another method is the system optimisation based on entropy study [29]. However, to our knowledge, there has been less previous evidence for the connection between adsorbent-adsorbate interaction, entropy generation and AHT performance. The interaction between the water vapour and the adsorbent is governed by adsorbent's porosity, hydrothermal stability, water adsorption capacity, recyclability and hydrophilicity/hydrophobicity [30]. Besides silica gel and zeolites, metal-organic frameworks (MOFs) are attracting more attentions in recent years for the design and development of adsorption bed [31]. MOFs are metal-containing nodes with organic ligands. As for water adsorption applications, MOFs exhibit superiorities over conventional materials for their versatile pore structure, fast synthesis kinetics, controllable pore size, multifunctional micro-porosities and highly hydro-thermodynamic stability. For example, Cr-terephthalate-based MOF namely MIL-101 (Cr) exhibits extremely high pore volume (up to 2.0 cm^3/g) and ultrahigh BET surface area (up to 4100 m^2/g) [32]. These ample mesopores make MIL-101 (Cr) show a high water limiting uptake of 1.0 g/g, which is over twice as compared with the conventional silica gel or zeolite (limiting uptake normally smaller than 0.35 g/g) [32]. Besides the high water capacity, the coordinatively unsaturated sites (CUSs) inside of the MIL-101 (Cr) could be further modified by dehydration process and the created unsaturated chromium spot could be decorated by the ionic liquids, which will eventually deliver the benefit for water adsorption [33]. In addition, An et al. [34] reported that the hydrophilicity of the water adsorption on parent MIL-125 (Ti) could be enhanced by the amino-functionalisation and hydrochloric acid-protonation process, and the limiting uptake is increased from 0.41 g/g to 0.49 g/g. However, these structural modification approaches mentioned above are not applicable to the conventional adsorbents. Furthermore, Butova et al. [35] proposed that by adding certain amount of acetic acid/formic acid, the MOF-801 (Zr) could be fabricated within in 2 hours, which is much faster as compared with the preparation (exploitation, polishment and purification) of the conventional materials. Qualified adsorbents such as MOF-801 (Zr) [36], MIL-160 [37], MIL-68 [38], CAU-10 [39] and Al-fumarate [40] etc. deliver high Δq with fast kinetics per adsorption-desorption cycle.

Currently, numbers of MOFs such as Ni-MOF-74 [41] and HKUST-1 [42] are synthesised and tested widely for various applications.

The foremost problem with the parent MOFs is their defective hydrophobicity/hydrophilicity behaviours at low pressure region. Normally, a three-step uptake should be found in a typical "S-shaped" water adsorption isotherm, which is shown in Figure 1.2. The type I isotherm is also shown here for comparison purpose. It is noted here that the type I or type V water adsorption isotherms shown in Figure 1.2 is for demonstration only, it is not related to any adsorbent + water adsorption system. Firstly, rarely no water vapour is adsorbed onto the MOFs structure at low pressure region and the water uptake is extremely low (nearly zero). Secondly, as the pressure is increased to a certain point, an intense rise of water uptake is observed with a steep slope (approximately vertical). Finally, as the adsorption continues, some more water vapour is adsorbed onto the MOFs and the isotherm becomes smooth. For water adsorption with "S-shaped" isotherm, the hydrophobic length is evaluated in terms of the relative pressure, which is measured from the beginning of adsorption ($P/P_s = 0$) to the point where a rapid increase of water uptake is observed.

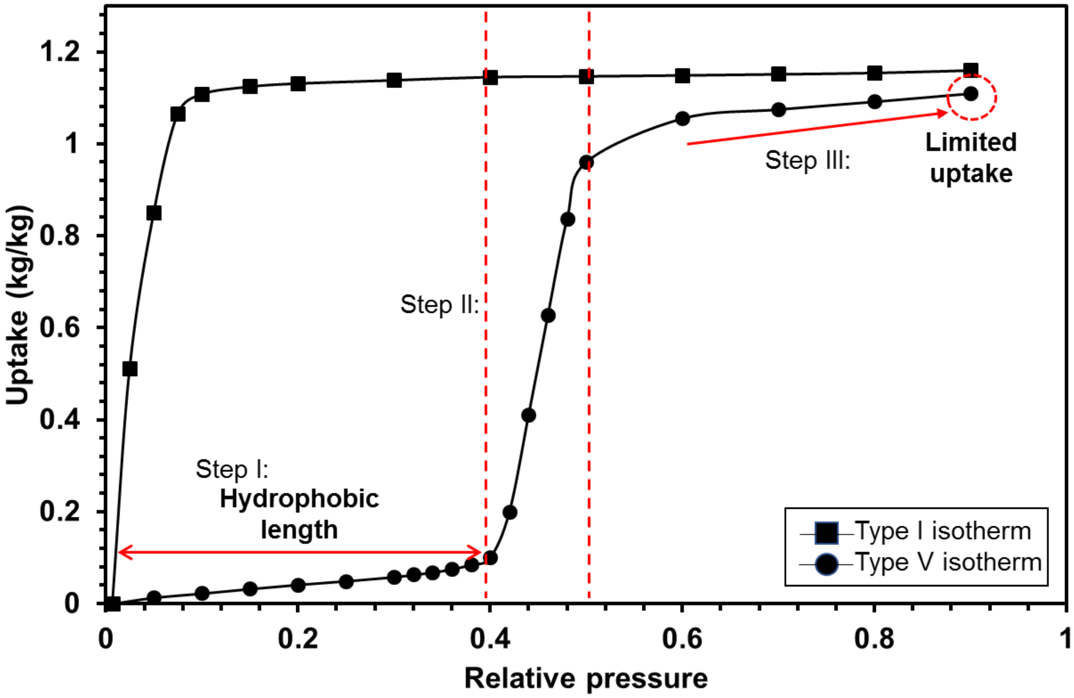

Figure 1.2: Schematic diagram of Type I and Type V water adsorption isotherm.

For example, for Al-Fum [30], a relative long hydrophobic length is found ($P/P_s \approx 0.23$) and it leads to a low uptake-offtake difference (Δq) per adsorption chiller operation cycle, which results unfavourable impact on practical AHT applications. Even longer hydrophobic lengths are found for UiO-66 (Zr) ($P/P_s \approx 0.33$) [20]. Different from the MOFs discussed above, the key problem with MOF-801 (Zr) [43] is that its hydrophobic length is too short. Although MOF-801 (Zr) results a type V or "S-shaped" isotherm with water adsorption, the isotherm shape behaviours more like type I due to its extremely short hydrophobic length, therefore, it requires high regeneration temperature up to 85 or 90 ℃ for the AHT applications. Besides the hydrophobicity/hydrophilicity performance issue at low pressure region, some other problems also exist. For example, the adsorption kinetics for original Al-Fum [30] and UiO-66 (Zr) [20] is too slow and a long cycle time is required for the AHT operation. These constraints prevent the parent MOFs from being developed in the adsorption assisted heat transmission applications.

It should be noted here that the porosity of MOFs influences the adsorption behaviours strongly. For example, MOFs with extensively large BET surface area and higher pore volume such as MIL-101 (Cr) could achieve a very high water uptake capacity (up to 1.0 g/g), however, it results a pretty long step pressure or hydrophobic length (up to $P_s/P \approx 0.4$) [32], which leads to a poor performance outcome in cooling/heat pump application. Therefore, direct or post modification by the addition of alkali metal cations (Li^+, Na^+, K^+) dopants into the parent Cr-based MOFs, reconstructs the microstructure of the parent MOFs so that more water vapour can be adsorbed and desorbed under the operating conditions of AHT cycle [32]. Another method involves the replacement of the original solvent molecules with polar ligands featuring chemical functionalities. For example, Bae et al. [44] achieved promising improvement of N_2/CO_2 selectivity by introducing the highly polar ligands to the original MOFs structure. In addition, by implanting ethylenediamine (ED) and ethylene glycols (EG), the unsaturated metal sites of MIL-101 (Cr) is activated and enhanced water selectivity is achieved in the low pressure region [45]. Other modification approaches such as ligand functionalisation [46], hydrothermal post-synthesis treatment [47], colloidal crystallisation [48] or acid immersion [49] are used for adsorbent micro-structure reconstruction (pore size enlargement, micropore generation and so on) purposes.

Besides experiments, simulation methods such as Grand Canonical Monte Carlo (GCMC) [50], Molecular Dynamics (MD) [51] and Density Functional Theory (DFT) [52] are applied to study various adsorbates-adsorbents adsorptions. Generally, the GCMC simulation method is used as a predictive tool to analyse the adsorption performance for water on various novel adsorbents at certain pressure region. Approaches such as molecular dynamics and static molecular simulation are usually applied to investigate the adsorbate-adsorbent interaction and link it with the pore structure of adsorbent. As compared with experiment, it is inexpensive, time-saving and immune from the experimental errors by applying reasonable idealisations and assumptions in the analysis.

The performances of the AHT system can be predicted from the shapes of adsorption isotherms and kinetics graphs, which are usually fitted with isotherms [53] and kinetics models [40]. Combining the theoretical models and thermodynamic frameworks of adsorbent-adsorbate system, the AHT performances are predicted and simulated. The AHT-modelling is based on the working principles for each component of the system including the heat source, heat sink and cooling with chilled water source loops. The thermodynamic modelling of AHT system can be further improved by temperature-entropy analysis.

1.3 Research Objectives

The overall aims of this thesis are to develop novel functional adsorbents and study their behaviours with water under the operating conditions of AHT applications employing temperature entropy analysis. The objectives are listed as follows:

- Fundamental understanding of MOFs synthesisation, functionalisation for water and MOFs based AHT system.
- Fundamental understanding of the interactions between water molecules and MOFs from entropic and energetic perspectives.
- Experimental investigation for water uptakes under static and dynamic conditions and the thermodynamic modelling of AHT system.
- Fundamental understanding and development of temperature-entropy analysis for novel functional adsorbent based AHT systems.

1.4 Research Scope

These objectives are accomplished via the following research scope and activities:

- GCMC Simulation

GCMC (Grand Canonical Monte Carlo) method is used to study MOFs adsorption behaviours in the molecular scale. It allows the MOF adsorbent and gas adsorbate molecules to interact in an imaginary gas reservoir for specific temperature and chemical potential.

- Thermodynamic property analysis

The energetic behaviours (entropy and isosteric heat of adsorption) between various adsorbate-adsorbent pairs are investigated based on the classical thermodynamics knowledge.

- MOF synthesis

Various MOFs are synthesised via hydrothermal reaction method. The original MOFs are modified with the additions of functional groups, alkali ion dopants or mixing with conventional adsorbents.

- MOF characterisation

The original and modified MOFs' porosities, thermal properties are characterised by X-ray diffraction (XRD), scanning electron microscopy (SEM), N_2 adsorption and thermo-gravimetric analysis (TGA) analysis.

- Water adsorption experiments

The water adsorption uptakes and kinetics on various original and modified MOFs within wide a range of temperature and pressure are measured by the gravimetric methods.

- Modelling and simulation of AHT system

Evaluation of the AHT performance employing various MOFs + water in terms of the coefficient of performance for cooling (COP), specific cooling power (SCP), coefficient of performance for heat pump (COP_h), specific heating power (SHP) and SDWP (specific daily water production) employing experimentally confirmed adsorption isotherms and kinetics data.

- Temperature-entropy analysis

The entropy generation for each component of AHT are evaluated as a function of time. The temperature-entropy maps for each component of AHT for cooling, heat pump and desalination are shown for the first time.

1.5 Thesis Overview

This thesis comprises the structure of scientific works to present the novelty of the proposed research activities with the methodologies and a comprehensive description and discussion of the results findings.

Chapter 1 provides a rationale for the background, motivation, objective, and scope of the proposed research activities with the related research questions and possible solutions.

Chapter 2 reviews the literature concerning the adsorption phenomenon, isotherm and kinetics mechanism, the theory of isosteric heat of adsorption, the principle of adsorption assisted heat transformation system, the Grand Canonical Monte Carlo (GCMC) technique and detailed discussion on various original and modified MOFs such as functional groups, porosities and topologies. The literature review also highlights the research gaps in MOFs development for AHT applications.

Chapter 3 describes the modelling and simulation for calculating water interactions on various MOFs and composite adsorbents. Hence, the GCMC (Grand Canonical Monte Carlo) methodology is applied to predict the isotherms of water adsorption. Based on the GCMC results, the MOFs and composite adsorbents are synthesised.

Chapter 4 describes the synthesis of various functional MOFs. This chapter also presents (i) the surface characterisation of the synthesised MOFs and (ii) the measurement of water adsorption on these MOFs in terms of isotherms and kinetics. This chapter ends with the detailed discussion for (i) the surface characteristics of MOFs structures, (ii) the isotherms and kinetics of MOFs + water systems and (iii) the isosteric heat of adsorption of MOFs + water systems.

Chapter 5 illustrates the thermodynamic modelling of adsorption assisted heat transformation systems with heat and mass recovery analysis. Hence, the thermodynamic frameworks are formulated for each component of AHT system employing the first and the second laws of Thermodynamics. The entropy generation of the overall AHT cycle is presented in temperature-entropy maps. The performances are also presented in this chapter.

Chapter 6 shows the major findings and the novelty of the thesis. The chapter provides a summary of the results achieved and their possible impacts, as well as the limitations and further improvements that can be developed in the future.

Chapter 2. Literature Review

This chapter provides a general and broad literature review on isotherms, kinetics and isosteric heats of adsorption and various adsorbents for heat transformation applications. Once the state of the art is defined, a clear research gap can be identified for proceeding the main steps of the current research activities based on the areas of opportunities identified.

2.1 Introduction

Adsorption arises when a liquid or gas adheres onto a solid surface, and is characterised by the increase in the concentration of the liquid or gas in the region of the interface. Desorption is the reverse of adsorption. The solid substance on which adsorption takes place is defined as the adsorbent, the fluid (liquid or gas) material in the adsorbed phase is known as the adsorbate. Based on the types of the interaction between the molecules in the fluid phase and the solid, adsorption is classified into two categories namely physisorption and chemisorption [54]. The main differences between the physisorption and chemisorption are summarised as: (i) the types of the adsorption force. Physisorption interactions are related to the condensation of vapours and the deviations from ideal gas behaviour, while the chemisorption forces are related to the formation of chemical bonds; (ii) the degree of specificity. Chemisorption is usually with a relatively high degree of specificity as compared with that of the physisorption; (iii) the number of the molecule-surface interaction layers. Chemisorption is confined to a monolayer, whereas physisorption occurs as a multilayer (especially at high relative pressures); (iv) reversibility. The physi-sorbed molecules can be recovered to its fluid phase by desorption without any identity change, which is not applicable to the chemi-sorption molecules; (v) energy level. Physisorption is an exothermic process with a relatively low energy level (comparable to the energy of condensation of the adsorbate). However, Chemisorption usually generates relatively high energy level (same magnitude order as compared to the chemical reaction). It is noted here that the physisorption is the current research focus in this work. The mechanism of physisorption is shown schematically in Figure 2.1 [55].

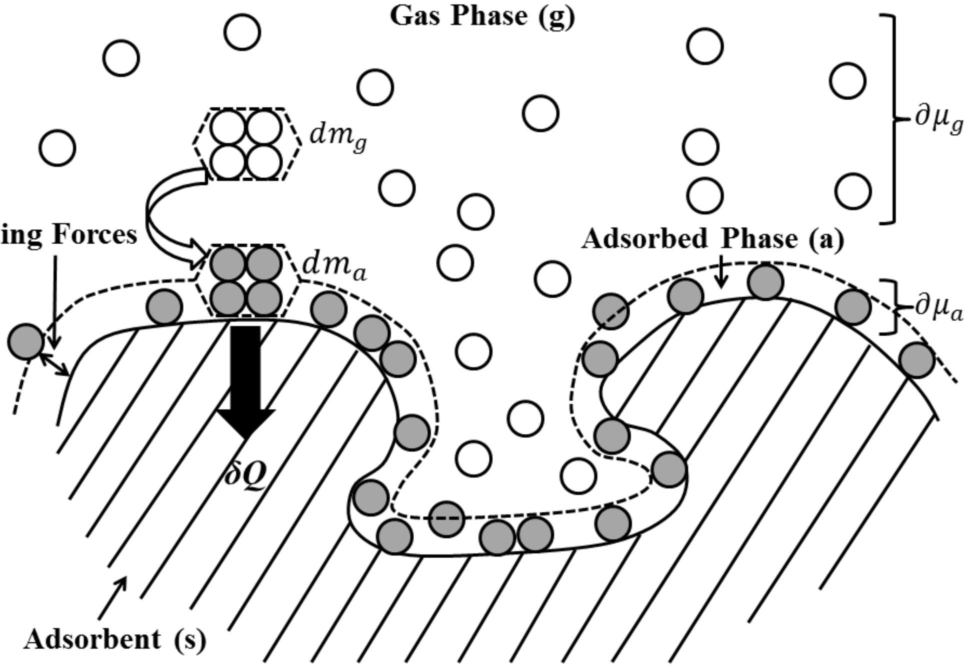

Figure 2.1: Schematic diagram of adsorption mechanism [55].

Adsorption is governed by the interaction between adsorbent and adsorbate as a function of pressure and temperature. Research on physisorption has a long history and this field has met with great success in many applications such as heterogeneous catalysis, drug delivery, liquid purification, gas separation and energy storage. According to the official organisation such as International Union of Pure and Applied Chemistry (IUPAC) [56-58], the general terminology and definitions of adsorption are summarised in Table 2.1.

Table 2.1: Definitions and terminology of adsorption.

Term	Definition
Adsorption	Adhesion of particles (atoms, ions or molecules) to a porous surface

Adsorbent	Solid substance on which adsorption occurs
Adsorbate	Fluid or refrigerant that interacts with adsorbent
Physisorption	Adsorption with no chemical bonds
Chemisorption	Adsorption with chemical bonds
Porous solid	Solid with void pores which are deeper than wide
Open pore	Void pore which communicates with the surface
Surface area	Extent of the surface determined during the whole adsorption process
Specific surface area	Total surface area per unit mass of porous solid
Pore size	Distance between two opposing slit walls or the diameter of cylindrical pore, also known as the pore width
Pore volume	Volume of the pore assessed by Ar or N_2 adsorption method
Porosity	Ratio of overall pore volume to apparent particle volume

Solids with distinct porosities are preferred as the suitable adsorbent for various gas storage, separation and heat transformation applications. The pore size distributes from micropore (internal pore width < 2 nm) to mesopore (2 nm < internal pore width < 50 nm) and a competent adsorbent should have small pore sizes with big pore volume, which results in larger surface area and higher adsorbate capability. However, the adsorbate capacity in terms of hydrophilic or hydrophobic behaviours depends on adsorbent-adsorbate interaction factor. The widely used adsorbents (such as silica gel, zeolite and various types of activated carbons) are usually synthesised and prepared in the form of powder, pellet, rod or monolith.

Nitrogen or argon adsorption has become the most practical technique for measuring the pore size distribution and surface area of adsorbents [59]. On the other hand, the adsorption of water vapour on solid porous adsorbents is important for industrial applications, such as cooling [60], heat pump [61], desalination [6], dehumidification [62], thermal energy storage [63] and water purification [64].

2.2 Adsorption Isotherms

Adsorption isotherms are measured at a constant temperature to study the relationships between the amount of the adsorbate uptakes (q_e) and the pressure (P). Theoretically, an adsorption process for the specific temperature and pressure is considered to reach the equilibrium state if the adsorbate concentration in the adsorbed phase is in a dynamic balance with that in the bulk phase, hence, the rates of both adsorption and desorption are equal. According to IUPAC [65], the adsorption isotherms are categorised into six types as shown schematically in Figure 2.2. The shape of the adsorption isotherms mainly depends on the adsorbent-adsorbate interaction and the types of adsorbent structure. Type I isotherm represents the adsorption on microporous adsorbents with hydrophilic behaviours whilst the type II describes the adsorption on macroporous or non-porous adsorbents. Weak adsorbent-adsorbate interactions are usually found for type III isotherm while type IV isotherm works with the mesoporous adsorbents. Type V isotherm ("S-shaped" isotherm) is related to monolayer and multilayer adsorptions where the hysteresis is found. Water adsorption on adsorbents with type V isotherm provides favourable benefits for the design of adsorption chiller/heat pump due to higher uptake-offtake difference (Δq) per adsorption-desorption cycle. In addition, type VI isotherm with a hybrid stepwise adsorption behaviour is found for the adsorbent which is non-porous or macroporous. The study of adsorption isotherms plays a crucial role in adsorbent design, modelling analysis and practical optimisation of the adsorption systems.

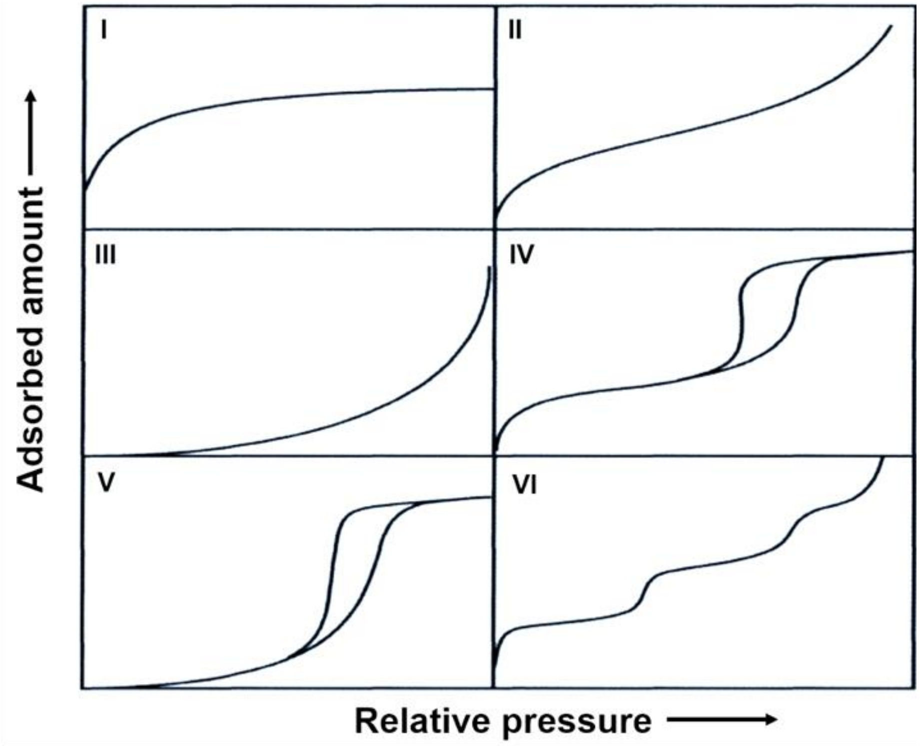

Figure 2.2: Types of adsorption isotherms by IUPAC classification [56]. Type I: adsorption on microporous adsorbents with hydrophilic behaviours; Type II: adsorption on macroporous or non-porous adsorbents; Type III: weak adsorbent-adsorbate interaction; Type IV: adsorption on mesoporous adsorbents; Type V: monolayer and multilayer adsorption; Type VI: hybrid stepwise adsorption on non-porous or macroporous adsorbents.

Based on experimentally confirmed uptake versus pressure/concentration data as a function of temperature, various adsorption isotherm models are correlated and formulated and summarised in Table 2.2 [66]. By introducing different isotherm parameters with physical meanings, each isotherm model could feature certain characteristics of adsorption mechanism. For example, Henry’s equation [67] is applicable for the adsorption in low pressure region where pressure $P \rightarrow 0$ with finite uptake. The Langmuir isotherm model [68] is restricted for the monolayer adsorption where the adsorbed layer equivalent to single-molecule-thickness is assumed for the localised site. Dubinin-Radushkevich isotherm model [69] is postulated to describe the mechanism of subcritical vapours adsorbed onto micropore adsorbents employing the micropore filling theory. However, it is not approaching the Henry's law at low-pressure region. In addition, an empirical model namely Freundlich equation [70] could be applied for multilayer adsorption cases such as geosmin-water adsorption on activated carbons [71]. One key problem with the Freundlich equation is that it fails to predict the isotherm at Henry's region due to the lack of the fundamental thermodynamic basis. The Tempkin isotherm model [72] assumes that the isosteric heat of adsorption decreases linearly with the adsorbed-phase concentration increase. The Toth isotherm model [73] is developed from the Langmuir equation to provide a better isotherm fittings for the heterogeneous adsorption systems. The Brunauer-Emmett-Teller (BET) isotherm model [74] is widely used in describing the multilayer physisorption process where the theoretical isotherm uptake capacity q_s (g/g) and the BET constant C_{BET} (L/g) are involved. One primary application for the BET theory is to measure the pore size distribution and pore volume of the novel porous materials. Similarly, the MacMillan-Teller (MET) equation [75] exhibits a more comprehensive modelling as compared with BET theory where the effects of the surface tension is considered. Furthermore, Sips [76] and Redlich-Peterson [77] isotherm models are hybrid isotherms formulating both the Langmuir and Freundlich isotherm features. Other adsorption isotherm models such as Hill, Flory-Huggins, Khan and Koble-Corrigan isotherm models are also used broadly in adsorption fields [78-81].

Table 2.2: Examples of adsorption isotherm models.

One parameter adsorption isotherm model		
Type	Isotherm	Remarks
Henry [67]	$q_e = bP$	Applicable at low pressure region (Henry's region)
Two parameters adsorption isotherm models		
Type	Isotherm	Remarks
Langmuir [68]	$q_e = \frac{Q_0 bP}{1 + bP}$	Homogeneous and localised adsorption is assumed. Adsorbate-adsorbate interaction is not considered.

Dubinin-Radushkevich [69]	$q_e = (q_s)\exp(-k_{ad}\varepsilon^2)$	Not available to Henry region.
Freundlich [70]	$q_e = K_F P^{\frac{1}{n}}$	The earliest reversible adsorption isotherm. Motion of adsorbates is not considered. Not applicable to low (Henry's region) and high (saturation state) end concentration boundaries.
Tempkin [72]	$q_e = \frac{RT}{b_T} \ln A_T P$	Reverse linearly relationship between the concentration of the adsorbed phase and the isosteric heat of adsorption is assumed.
Three parameters adsorption isotherm models		
Type	Isotherm	Remarks
Toth [73]	$q_e = \frac{K_T P}{(a_T + P)^{1/t}}$	Successfully fits heterogeneous adsorption systems for a wide relative pressure ranges (0< P/P$_s$ < 1).
BET [74]	$q_e = \frac{q_s C_{BET} P}{(P_s - P)[1 + (C_{BET} - 1)(P/P_s)]}$	Applicable to multilayer physisorption process.
Sips [76]	$q_e = \frac{K_s P \beta_s}{1 + a_s P \beta_s}$	It is a combination of Langmuir (high pressure region) and Freundlich (low pressure region) isotherms.
MET [75]	$q_e = q_s(\frac{k}{\ln(P_s/P)})^{1/3}$	The effect of adsorption surface tension is considered.
Redlich-Peterson [77]	$q_e = \frac{K_R P}{1 + a_R P_g}$	Hybrid isotherms of Langmuir and Freundlich models.

Adsorbents with water delivering "S-shaped" (type V) isotherms are suitable for adsorption chiller/heat pump and desalination applications. However, most of the classical adsorption isotherm models fail to describe the "S-shaped" isotherm and the hydrophobic length. To overcome these limitations, Sun and Chakraborty [82] proposed a new adsorption isotherm model from the concept of Fermi-Dirac distribution function, which takes into account both the surface-energy and surface-structural heterogeneity factors from Henry's region to the saturated pressure. The Sun-Chakraborty isotherm model is expressed as $\theta = \frac{K\left(\frac{P}{P_S}\right)^m}{1+(K-1)\left(\frac{P}{P_S}\right)^m}$, where $\theta = q/q^0$ is the surface coverage that represents the percentage of adsorption sites occupied by water vapour. Hence, q indicates the water vapour uptake as a function of pressure and temperature and q^0 refers to the limited water vapour uptake. K resembles the adsorption equilibrium constant with the expression of $K = \alpha\exp\,[m(Q_{st}^{*} - h_{fg)}/RT]$, where α defines the pre-exponential coefficient, m is the heterogeneous coefficient. Q_{st}^{*} represents the isosteric heat at zero coverage and h_{fg} is the enthalpy of evaporation. The combined item $(Q_{st}^{*} - h_{fg})$ defines the adsorption characteristics energy and it can be estimated from the experimental data. In addition, R denotes the gas constant, T is the adsorption temperature in kelvins. The Sun-Chakraborty isotherm equation is capable to fit the various types of experimentally measured adsorption isotherms data. It should be noted that, Sun-Chakraborty isotherm equation gives precise fitting results for “S-shaped” water adsorption on many MOFs such as CAU-10, MOF-801 (Zr), MIL-101 (Cr), Al-Fum and UiO-66 (Zr).

2.3 Adsorption Kinetics

Adsorption kinetics refers to the diffusion of adsorbate in the adsorbent pores as a function of time at constant temperature and pressure. Adsorption and desorption kinetics are important for the design and performance evaluation of an adsorption bed or thermal compressor (the thermal compressor of the AHT system is particularly referred to the adsorption-beds, where isobaric adsorption or desorption process occurs as a result of the temperature and pressure swing). By studying the residence time of water vapour on various adsorbents, crucial parameters such as the operation cycle time and the size of the adsorption bed are designed and developed for adsorption assisted heat transformation applications. Overall, the physisorption based kinetics is related to the adsorbate diffusion where three sequential steps are involved [83]: (1) film or external diffusion (adsorbates diffuse across the liquid film adjacent to the external pore of adsorbent); (2) intra-particle diffusion or internal diffusion (adsorbates permeate deeply into the inner pores of adsorbent) and (3) mass action (adsorbates adsorb and desorb dynamically inside the active sites). Normally, mass action process is faster as compared with another two processes and can be neglected [84]. The adsorption diffusion models are primarily formulated to describe the external and/or internal diffusion process. For the explanation of adsorption kinetics, varieties of adsorption diffusion models are proposed in terms of first- or second-order reversible models [85], pseudo first- or second-order models [86] and first or second-order irreversible models [87]. Some typical adsorption kinetics models are furnished in Table 2.3.

Table 2.3: Examples of adsorption kinetics models.

Type	Equation	Remarks
Pseudo first-order equation [88]	$\frac{d\theta}{dt} = k_1(\theta_e - \theta)$	Example: methylene blue adsorption on mesoporous carbons [89].
Pseudo second-order equation [90]	$\frac{d\theta}{dt} = k_2(\theta_e - \theta)^2$	Example: Dye-contained wastewater adsorption on MCM-22 zeolite [91].
Second-order equation [92]	$\frac{1}{C} = k_3 + \frac{1}{C_0}$	Example: water adsorption on HZSM-5 zeolite [93].
Elovich's equation [94]	$\frac{d\theta}{dt} = ae^{-\alpha\theta}$	Example: Organic compounds adsorption on platinum electrodes [95].
Ritchie's equation [96]	$\frac{d\theta}{dt} = \alpha(1 - \theta)^n$	Example: cadmium-ions-contained solution adsorption on bone char [97].

In the Table 2.3, θ and θ_e are the amount of adsorbate at time t and equilibrium conditions. C and C_0 are the concentration of the adsorbate at equilibrium and initial states. k_1, k_2, k_3, a and α are the parameters characterising the kinetics models.

As compared with various adsorption diffusion models, the Langmuir adsorption kinetics model is considered as one of the simplest. The kinetics expression is $\theta_t = \theta\left[1 - \exp\left(-\frac{t}{\gamma}\right)\right] + \exp(-\frac{t}{\gamma})\theta_{ini}$ with the boundary conditions $\theta_t = \theta_{ini}$ $(t = 0)$ and $\theta_t = \theta_\infty$ $(t \to \infty)$. Recently, a Langmuir-based kinetics framework was derived by Sun and Chakraborty [98] to model the water adsorption kinetics in which the surface structural heterogeneity factor of adsorbents is involved. According to the Langmuirian analogy, $K = k_{ads}/k_{des}$, where k_{ads} is the adsorption rate coefficient and k_{des} is the desorption rate coefficient. Under experimental equilibrium conditions, substituting $K = k_{ads}/k_{des}$ into the Sun-Chakraborty isotherm equation, the surface coverage becomes:

$$k_{ads}(1-\theta)\left(\frac{P}{P_s}\right)^m = k_{des}\theta\left[1-\left(\frac{P}{P_s}\right)^m\right] \tag{2.1}$$

where $k_{ads} = W\beta A_s$, A_s is the adsorbent BET specific surface area and it can be determined through nitrogen adsorption experiment. β is the sticking coefficient and it is given by $\beta = [\beta_0 \exp\left(E_a/RT\right)]$, where β_0 is the frequency factor or pre-exponential with unit value for monolayer; E_a is the activation energy. W defines the collisions of adsorbate molecules with the adsorbent surface per unit time and it is given by $W = MP/\sqrt{2\pi MRT}$, where M is the adsorbate molecular weight.

Since adsorption is a reversible process between adsorbents and adsorbate particles in the real case, under non-equilibrium conditions, the amount of surface coverage as a function of time θ_t can be obtained by derivation:

$$\frac{d\theta_t}{dt} = k_{ads}(1-\theta_t)\left(\frac{P}{P_s}\right)^m - k_{des}\theta_t\left[1-\left(\frac{P}{P_s}\right)^m\right] \tag{2.2}$$

By rearranging operation, Eq. (2.2) becomes:

$$\frac{d\theta_t}{dt} = k_{ads}\left(\frac{P}{P_s}\right)^m - \theta_t\left\{k_{ads}\left(\frac{P}{P_s}\right)^m + k_{des}\left[1-\left(\frac{P}{P_s}\right)^m\right]\right\} \tag{2.3}$$

Here the time constant (τ) is defined by $\frac{1}{\tau} = k_{ads}\left(\frac{P}{P_s}\right)^m + k_{des}\left[1-\left(\frac{P}{P_s}\right)^m\right]$, therefore Eq. (2.3) becomes

$$\frac{d\theta_t}{dt} = k_{ads}\left(\frac{P}{P_s}\right)^m - \theta_t\frac{1}{\tau} \tag{2.4}$$

The analytical solution of Eq. (2.4) becomes, $\theta_t = C'e^{\frac{-t}{\tau}} + (k_{ads}(P/P_s)^m)/(1/\tau)$=$C'e^{\frac{-t}{\tau}} + \theta$. At the very beginning of adsorption process (t=0), $\theta = \theta_{ini}$, then the constant C' is calculated as $\theta_{ini} - \theta$. After rearrangement operation, the adsorption kinetics equation becomes:

$$\theta_t = \theta - \theta e^{\frac{-t}{\tau}} + \theta_{ini}e^{\frac{-t}{\tau}}$$

$$\theta_t - \theta_{ini} = \theta - \theta e^{\frac{-t}{\tau}} + \theta_{ini}e^{\frac{-t}{\tau}} - \theta_{ini}$$

$$\theta_t - \theta_{ini} = \theta\left(1 - e^{\frac{-t}{\tau}}\right) - \theta_{ini}(1 - e^{\frac{-t}{\tau}})$$

$$\frac{\Delta\theta_t}{\Delta\theta} = \frac{\theta_t - \theta_{ini}}{\theta - \theta_{ini}} = 1 - e^{\frac{-t}{\tau}} \tag{2.5}$$

The kinetics model as shown in Eq. (2.5) works well for water adsorption of silica gel, zeolites, MOF-801 (Zr), Aluminium fumarate, CAU-10, MIL-101 (Cr) etc.

2.4 Isosteric Heat of Adsorption

Physisorption of gas or liquid on porous solid results a release of energy, which is associated with the adsorbate-adsorbent and adsorbate-adsorbate interactions. Thermodynamically, the negative change in the enthalpy of adsorption is known as the isosteric heat of adsorption (Q_{st}). At constant loading and temperature, Q_{st} defines the amount of heat release per unit adsorbate transferred from the bulk phase to the adsorbed phase. The isosteric heat of adsorption (Q_{st}) plays an important role in characterising the adsorbate loading kinetics and equilibria on the adsorbent, which ultimately govern the performance of various adsorption applications. For example, the information about the isosteric heat of adsorption at zero surface coverage (Q_{st}^{0}) could be used to predict the adsorbate uptake in the Henry's region and the design of adsorbent materials in the area of gas storage/separation/purification [99] and adsorption chiller/heat pump/desalination [100]. Experimentally, the isosteric heat of adsorption (Q_{st}) could be evaluated by three techniques: (1) direct acquirement via an adsorption calorimeter [101]; (2) measurement of adsorption isosteres [102] and (3) derivation from the adsorption isotherm results (differentiating the isotherms at constant uptake) [103]. To date, numbers of Q_{st} modellings have been proposed to investigate the energetic performance of adsorption and the most widely used model is the Clausius-Clayperon equation [104] as given by

$$\frac{d(\ln C_e)}{dT} = -\frac{Q_{st}}{RT^2} \tag{2.6}$$

where C_e refers to the equilibrium concentration (or vapour pressure) of the adsorbed adsorbate at constant loading; T is the adsorption temperature and R is the gas constant. Hence, the value of the isosteric heat of adsorption (Q_{st}) is calculated from the slope of the $\ln C_e$ versus *1/T* at different adsorbate uptakes. The usage of the Clausius-Clapeyron equation is based on the hypothesis that the adsorbate is considered as the ideal gas and the volume of the adsorbate in the adsorbed phase is negligible. It should be noted here that the ideal gas assumption is more suitable for the adsorption at low pressure region and it may cause distinct errors for high pressure region analysis. Other researchers also pointed out that the linear behaviours of the $\ln \mathrm{C_e}$ versus 1/T plot could only be obtained when the isosteric heat of adsorption does not change significantly with the temperature [105]. Several revision works have been performed to overcome these constraints. For example, Rahman et al. [106, 107] developed a Q_{st} model where the volume of the adsorbate in the adsorbed phase is addressed. Chakraborty et al. [55, 108] proposed an isosteric heat of adsorption model for both low and high pressure regions where the pressure gradient term for the gaseous phase is added into the original Clausius-Clapeyron equation. Moreover, the non-ideality of the adsorbate is involved in Askalany et al. [109] work. Theoretically, few thermodynamic frameworks are well established to study the relationship between the Q_{st} and the adsorbate orientation as well as the structure of adsorbent. However, the field of studying the isosteric heat of adsorption via the Grand Canonical Monte Carlo simulation is mature, where the Q_{st} could be expressed by adsorbate uptakes or the gas fugacity [50]. Some examples of the isosteric heat of adsorption (Q_{st}) study using various techniques is shown in Table 2.4.

Table 2.4: Examples of the isosteric heat of adsorption (Q_{st}) for various adsorbent + adsorbate pairs.

Adsorption systems	Method	Remarks
Hydrogen + IRMOF-16 [110]	Grand Canonical Monte Carlo (GCMC) simulation	• $\mathrm{H_2/H_2}$ interaction is neglected • The optimal Q_{st} for hydrogen storage on IRMOF-16 is around 20 kJ/mol
Water/methanol + graphitized carbon [111]	Grand Canonical Monte Carlo (GCMC) simulation	• The Q_{st} increases as adsorbate increases (liquid-like adsorbate clusters are observed) • The Q_{st} decreases rapidly when the functional groups' concentration is low
Water + natural zeolite [60]	Experimental measurement (Clausius-Clapeyron	• Q_{st} decreases with the increase of adsorption capacity

	equation)	• $(Q_{st})_{max} \approx 3800$ kJ/kg with a zeolite equilibrium adsorption capacity of 0.02 kg/kg
Carbon monoxide + Pt/Al_2O_3 catalyst [112]	Fourier transform infrared (FTIR) spectroscopy in the temperature range 298-740 K	• Q_{st} decreases with the increase of the coverage θ • $(Q_{st})_{max}$ = 140 kJ/mol at θ =0.9
Toxic metal ions + rice husk ash (RHA) [113]	Experimental measurement (Toth isotherm fitting)	• Q_{st} is quantitatively correlated with the amount of adsorbed metal ions • $(Q_{st})_{max} \approx 194$ kJ/mol

2.5 Conventionally Used Adsorbents for Heat Transformation

Research on conventional adsorbents has a long tradition. Cavenati et al. [114] presented that zeolite 13X with a pore volume 0.34 cm^3/g would be an efficient medium for carbon dioxide separation from exhaust gas. Yahya et al. [115] showed that reactive dyes could be removed from acidic solutions by activated carbon which the bulk density is 0.64 g/cm^3. In addition, silica gel with the pore volume ranging from 0.32 to 0.46 cm^3/g is found competent for waste-heat-driven water adsorption refrigeration and desalination [21]. Furthermore, L.Z Zhang [116] built one adsorption cooling system motivated by the automobile waste heat and obtained promising COP (coefficient of performance) with a value of 0.38. Here, representative examples of adsorption chillers employing various conventional adsorbent-water systems are summarised in Table 2.5. Here, the COP (coefficient of performance) of the adsorption chiller is defined as COP = Q_{evap}/Q_{des}, where the Q_{evap} represents the energy generated in the evaporation process and Q_{des} indicates the energy required for the desorption process. Although all the systems described in Table 2.5 could be driven by low grade heat source below 95 ℃, the defects of the conventional adsorbents lead to the poor performance of the system. It is proved that the "S-shaped" isotherm provides higher Δq as compared with type I isotherms under the working conditions of an adsorption chiller, and requires lower regeneration temperature (< 60 °C) to drive the AHT system [32]. Unfortunately, due to the relatively low structure varieties and restricted modification potentials, traditional adsorbents meet the choke point for further exploitation. With the development of the technology in chemistry and material science, novel adsorbents synthesis field really takes off in the late few years and it becomes more accessible to obtain directionally designed porous materials. Nowadays, novel material namely metal-organic frameworks (MOFs) has drawn much attention for its designable porosities and microstructure diversities [117].

Table 2.5: Detailed literature survey on the adsorption chiller performance employing various conventional adsorbent (zeolite / silica gel) + water systems.

Adsorbent + water pairs	System remarks	ADC performances
Silica gel [118]	Two sorption chambers Powered by low-grade heat Experimental study Cycle time 600 s to 900 s	Cooling power: 42.8 kW COP: 0.51 SCP: 125 W/kg (under 86/11/30 ℃ hot water inlet/chilled water outlet/cooling water inlet temperatures, cycle time 720s)
Silica gel [119]	Three-bed adsorption chiller heat source 60-85 ℃ Numerical optimisation Provides a new cycle time allocation for ADC	Hot water inlet: 65 ℃ optimal mass recover time 8-12 s optimal switching time 27-35 s COP:0.36
SWS-8L Silica [120]	Single-bed adsorption chiller Thermodynamic modelling Experimental investigation Heating temperatures 77-95 ℃	SCP: 190-389 W/kg VSCP: 104-212 W/dm^3 COP: 0.18-0.31 (for the cycle time 600 s)
Microporous Silica gel [121]	Double condensers system Driven by solar energy Finned-tube heat exchanger Performance optimisation	Better performance at higher hot water inlet and chiller water outlet temperature Cooling capacity: 17.9 kW COP: 0.63

Synthetic zeolite [122]	Pressure and heat recovery Low regeneration temperature up to 70 ℃ Fin-tube heat exchangers Cyclic steady state studies	COP: 0.1 – 0.6 (under different operation conditions)
FAM Z01 zeolite [29]	Low grade heat source 65-85 ℃ Chiller's thermodynamic and irreversibility analysis Specific entropy generation	COP: 0.44 at heat source of 65 ℃ Optimised adsorption/desorption cycle time: 200 s to 300 s
Zeolite 13X/$CaCl_2$ composite [8]	Porous characteristics of composite adsorbent Solar adsorption cooling system Adsorption kinetics Numerical analysis	COP is increased by 81% up to 0.76 SCP is increased by 34% up to 18.4 W/kg by introducing the Ca-ion-exchange composite as compared with pure zeolite

2.6 Metal-organic frameworks (MOFs)

Metal-organic-frameworks (MOFs) are a class of crystalline meso-microporous hybrid structures, composed of metals or metal clusters and organic building ligands [117]. Normally, divalent (Cu, Mg, etc.), trivalent (Al, Fe, Cr, etc.) or tetravalent (Zr, Ti, etc.) metals are chosen as the metallic component, and the organic ligand with multidentate chains are usually used to connect the metal clusters [123]. Research on metal-organic frameworks (MOFs) took off in the late decades as it became more accessible to various synthesis approaches such as conventional electric (CE) heating, electrochemistry (EC), ultrasonic (US), mechanochemistry (MC) and microwave (MW) heating methods [123]. MOFs with three-dimensional networks usually attains massive pore volumes, large surface areas, uniform pore sizes and stable pore structures. These highly porous materials have been widely adopted in the field of gas storage [124], liquid adsorption/purification [125], filtration [126] and catalysis [127]. Among these applications, water + MOFs based heat transmission systems for cooling, heat pump and desalination are met with much success and gradually broadened into commercial use. A detailed literature survey of MOFs-based cooling/heat pump/desalination applications are furnished in Table 2.6. In this thesis, series of metal-organic frameworks (MOFs) adsorbents are synthesised and investigated thoroughly for their performance regarding to the water adsorption via both simulation and experimental methods.

Table 2.6: Various MOFs + water pairs for adsorption assisted cooling, heat pump and desalination applications.

MOFs type	Water adsorption characteristic	Remark and performance	Application
MIL-101 (Cr) [128]	S-shaped isotherm Long hydrophobic length up to $P/P_s \rightarrow 0.45$ Super high limiting uptake $\approx 1.01\ \mathrm{g/g}$	Δq=0.939 g of water/g of sorbent at desorption temperature of 363 K and 5.6 kPa while adsorption temperature of 313 K. Lower SCP.	Not suitable for cooling or heat pump, but applicable for water dehumidification
Al-Fum [129]	S-shaped isotherm Narrow hysteresis Limiting uptake $\approx 0.45\ \mathrm{g/g}$ Good hydrothermal stability within 4500 water adsorption/desorption cycles	Thermal conductivity: 0.12 $\mathrm{W/(m \cdot K)}$ Heat capacity: 1.05 to 1.35 $\mathrm{J/(g \cdot K)}$ (in the temperature range between 323 K and 418 K)	Cooling/ Heat pump
CAU-10-H [130, 131]	BET surface area of 660 $\mathrm{m^2/g}$ Pore volume of 0.28 $\mathrm{cm^3/g}$ S-shaped isotherm Limiting uptake $\approx 0.25\ \mathrm{g/g}$ at 303 K	Numerical and experimental study Adsorption enthalpy: -49 kJ/mol	Heat pump/ thermal storage
UiO-66 [132]	S-shaped isotherm Hydrophobic length up to $P/P_s \rightarrow 0.20$ Limiting uptake $\approx 0.4\ \mathrm{g/g}$ Amine-functionalised UiO-66 limiting uptake: 0.38 $\mathrm{g/g}$ Stable cyclic performance	Average heat of water adsorption: 41.3 kJ/mol for UiO-66 and 89.5 kJ/mol for NH_2-UiO-66	Cooling/ Heat pump/ thermal energy storage
MIL-160 [130]	BET surface area of 1070 $\mathrm{m^2/g}$ Pore volume of 0.40 $\mathrm{cm^3/g}$ Type I resembled isotherm Limiting uptake $\approx 0.35\ \mathrm{g/g}$ at 303 K	Experimental analysis and GCMC simulation Adsorption enthalpy: -54 kJ/mol COP: 1.65	Heat pump

		(under the conditions of $T_{ev} = 288$ K, $T_{ads} =$ 318 K and $T_{des} = 370$ K)	
MOF-801 [133]	S-shaped isotherm Short hydrophobic length: $0.05 < P/P_s < 0.1$ Relative fast adsorption/desorption kinetics: $<$ 600 s for the temperature ranging from 293 K to 363 K	Δq=0.31 g COP: 0.67 SCP: 2 KW/kg(under the conditions of $T_{ads} = 303$ K and $T_{des} = 353$ to 358 K)	Cooling/ heat pump/ thermal storage
MIL-125 [132]	S-shaped isotherm Hydrophobic length up to $P/P_s \to 0.32$ Limiting uptake ≈ 0.33 g/g Amine-functionalised MIL-125 limiting uptake: 0.37 g/g and step rise of water loading in the $0.1 < P/P_s < 0.25$ region	Average heat of water adsorption: 56.0 kJ/mol for NH_2-MIL-125	Heat pump
fam-Al-Fum [23]	Water limiting uptake of 0.45 g/g with hydrophobic characteristics length of P/Ps = 0.2 and faster water adsorption kinetics	Water transfer per adsorption cooling cycle increases up to 12%	Cooling and heat pump
CPO-27(Ni), aluminium fumarate and MIL-101(Cr) MOF [24]	MIL-101(Cr) has the highest water uptake of 1.47 kg·kg^{-1}. The limiting uptake for COP-27(Ni) is 0.47 kg/kg and that for Al-Fum becomes 0.53 kg/kg.	Modelling of two-bed adsorption desalination system. CPO-27(Ni) is more suitable at low evaporation (5 °C) temperature. For Al-Fum, the specific daily water production is found to be 6.3 m^3·(ton·day)$^{-1}$.	Adsorption desalination

2.6.1 Current Research Activities in Parent MOFs

Al-Fumarate (Al-Fum) MOFs are chosen for desirable “S-shaped” isotherms with water adsorption plus the impressive hydrothermal stability [129]. Normally, Al-Fum with the monoclinic lozenge-shaped inner cell has a relatively large BET surface area (750-1200 m^2/g) and high pore volume (0.87-0.99 cm^3/g) [134]. By using Al-Fum as adsorbent, Youssef et al.

[135] simulated 3.4 m^3 water per tonne of Al-Fum MOFs and 20.0 Rton cooling energy per tonne of Al-Fum MOFs per day at 65 ℃ heating water temperature with the evaporator temperature of 10 ℃, which is almost three times higher as compared with zeolite and silica gel adsorbents. Karmakar et al. [134] used Al-Fum as the clean agent to extract fluoride from water and potable water was obtained at room temperature. Furthermore, Marta et al. [136] developed one continuous process to achieve large-scale Al-Fum production at a rate of 5.6 kg/h and space-time-yields of 97159 kg/m^3 per day. Besides experimental investigations, some inherent simulation works were performed to study the interaction between Al-Fum with various adsorbates in molecular aspects [137]. On the other hand, Zr-MOF-801 is selected for fast kinetics and moderate water adsorption limiting uptakes (0.3 g/g of adsorbent) [36]. For example, Kim et al. [36] captured water from air employing solar energy as the driven heat force and they achieved 2.8 liter of water uptake per kilogram of MOF-801 (Zr) per day from 20% relative humidity of moist air. Furukawa et al. [138] addressed the relationship between the MOF-801 (Zr) adsorbent-water molecules interaction with water adsorption sites by the powder neutron diffraction study. Furthermore, UiO-66 (Zr), a zirconium-based microporous material, should be considered as a qualified candidate for ADC applications for its high adsorption heat and good recyclability [132]. For example, Liu et al. [139] used UiO-66 polycrystalline membranes to desalinate water and the membranes exhibited impressive ion rejection, good permeability with high water stability. Felix et al. [132] obtained high heat of water adsorption up to 90 kJ/mol by using UiO-66 based MOFs as adsorbent. Technically, UiO-66 with fcu (face-centred cubic) topology possesses considerable BET surface area (around 1200 m^2/g) and pore volume (0.49 cm^3/g). In addition, water adsorption with UiO-66 (Zr) delivers the “S-shaped” isotherm, which also provides the possibility of low regeneration temperature in adsorption cooling application.

Collectively, MOFs presented in this thesis exhibit diversified metal cation types, different topologies (from face-centred cubic to inner-caged) and various water adsorption behaviours.

2.6.2 Modification on Parent MOFs

To revise the water adsorption behaviours of the parent MOFs and optimise the MOFs based AHT system performance, structural modification on the parent MOFs is necessary. A number of direct or post-synthesis modification methods are available to reconstruct MOFs pore topologies and metal-doping is one of them. For example, by doping alkali metal ions (Li^+, Na^+ and K^+), Teo et al. [32] enhanced the hydrophilicity of the parent MIL-101 (Cr) at low pressure region and faster adsorption kinetics are observed. Yang et al. [140] doped Ni (II) ions into the MOF-5 framework and adsorbents with larger Langmuir surface area, higher pore volume and enhanced hydro-stability are obtained. Additionally, Zhu et al. [141] proved that the porosity and hydrophobicity of the parent MOF STU-1 could be improved by doping various metal ions such as Fe^{2+}, Cd^{2+} or Cu^{2+}. Another popular MOFs modification method is functionalisation. By implanting organic ligands with hydrophilic/hydrophobic functional groups onto the parent MOFs, the pore-structures are re-constructed and the water adsorption behaviours on the functionalised MOFs are revised. For example, Jeremias et al. [132] showed that amino-functionalised MIL-125 exhibits much shorter hydrophobic length as compared with that of the original MIL-125 and it is very promising for heat storage and heat transformation applications. It is also found that a significant enhancement of water uptakes at low pressure region is obtained by introducing $-NH_2$ functional groups onto the original UiO-67. Furthermore, Ortiz et al. [142]proposed that the hydrophobicity/hydrophilicity traits of MOFs are determined by the geometry, porosity and structural flexibility of the MOFs, which could be tailored by functionalisation.

In this thesis, the original MOFs is mainly modified with three following approaches: (1) post-mixing with conventional zeolite-based (AFI/CHA type) adsorbents; (2) post-doping with hydrophilic alkali dopants (Li^+) and (3) direct-implanting with various of hydrophobic/hydrophilic functional groups. The functional group additives involving in this thesis are: Pyridine group (-N), with one methine group replaced by a nitrogen atom, has been proved to be a key factor to affect adsorption isotherm shape [143]. Hydroxyl group (-OH), a versatile polar functional group, has already been used to enhance the MOFs affinity with various adsorbates [47]. Amine group ($-NH_2$), another efficient functional group, plays an important role in MOFs' hydrophilic enhancement at low pressure region [144]. The nonpolar hydrophobic methyl functional group ($-CH_3$), for its impressive water capture stability [145].

2.7 Water Adsorption Simulation Techniques

Theoretically, molecular dynamics (MD) and the Grand Canonical Monte Carlo (GCMC) simulations are chosen for understanding adsorbent-adsorbate interactions in terms of pressure and temperature. Molecular dynamics shows the physical movements of water molecules inside the adsorbent pore structure. However, the MD requires numerous water molecules to simulate the adsorption environment, which makes it time consuming. Another limitation of the MD method is that for Lennard-Jones (LJ) potential, the potential divergence may occur when two atoms are approached. Therefore, instabilities are the result and the cumulative errors are generated during the integration process [146]. On the other hand, the GCMC models the adsorption environment for MOFs-water-pairs as a function of temperature and pressure [147]. As compared with MD or experimental methodology, GCMC provides high simulation accuracy and is cost-efficient and time saving. From the GCMC simulation, the water adsorption isotherm on different adsorbents are predicted.

Hence, the water adsorption is calculated by a thermodynamic force field consisting of the binding energy between water molecules and the MOFs - structure, where the Lennard-Jones (LJ), electrostatic and induction effects are considered. Employing this technique, the number of adsorbed water molecules are estimated.

The key point to model a well-defined adsorption simulation environment is to calculate the interatomic potentials for the adsorbent-adsorbate and the adsorbate-adsorbate pairs, respectively. For specific positions within the adsorption domain, the interatomic potentials reflect the interrelation of the attractive and repulsive effects between adsorbate molecules and MOFs structure. It provides essential information about the mechanics and energetic performances of adsorption. To date, various theoretical models and simulation techniques are proposed to investigate the interaction potentials of the adsorption systems. For example, Morse potential considered as the arguably most original interaction model was first introduced by Morse [148]. The Morse Potential model is applied to compute the interactions between mono-atom and a surface where the bond breaking effect is involved. One significant extension of Morse potential is the Morse/Long-rang potential (MLR model) proposed by Le Roy et al. [149]. By activating the long-rang behaviours inside the interaction system, MLR model predicts the spectroscopic versions of the diatomic or even polyatomic molecules [150, 151]. In addition, Lennard-Jones (LJ) potential [152] is widely adopted to calculate the binding energies between neutral atoms/molecules pairs such as water. The LJ potential is characterised by both energy (potential well depth) and length (collision diameter) scales where the short-range Pauli repulsion and long-rang dispersion effects are included. By replacing the repulsive portion with an exponential function and introducing an extra parameter, the original Lennard-Jones (LJ) potential is further simplified into the Buckingham potential [153], which investigates the phase of noble gases.

Other models and techniques such as Stockmayer potential [154], based on quantum chemistry [155] delivers more precise results. However, they need high computational cost. Moreover, the Coulomb electrostatic interactions [156] should be considered for the ionic system, and the higher order induction potentials [157, 158] are necessary if the interatomic potentials with high accuracy are required.

From the adsorption interatomic potentials, the mechanism of water adsorption could be analysed from a molecular perspective and the water adsorption isotherms at different pressures is predictable. For example, Carrasco et al. [159] investigated the water molecules at various metal interfaces and confirmed that the whole bilayer structure stability is determined by the quality instead of the quantity of hydrogen bonds. Bourg et al. [51] conducted MD simulations on silica nanopores adsorbed with water molecules for a wide pore diameter range (1-4 nm), where the bulk-liquid-like water is found at the centre of the larger pores (≥ 2 nm) while the interfacial water properties are independent of the silica surface curvature. Furthermore, by employing the Grand Canonical Monte Carlo (GCMC) simulation, Ghose et al. [160] proved that the hydrophilicity of the UiO-66 MOF could be enhanced by the defects of the missing ligands inside the framework. Ortiz et al. [142] also suggested that the water affinities of the zeolite imidazolate structures depend on many factors such as the geometry, topology and the ligand functionalisation of the adsorbent structures. Besides the research on water uptakes, Fan et al. [161] further developed the isosteric heats q_{st}^0 modelling where polar molecules such as water/methanol are selected and dipole induction potentials are involved. It is found that the maximum potential well depth for graphite and polar molecules are obtained between 2.9 to 4.0 Å and the orientations of the molecules affect the q_{st}^0 dramatically.

2.8 Adsorption Assisted Heat Transformation Research in Nanyang Technological University

In the recent decades, many remarkable works related to the adsorption assisted heat transformation (AHT) system are proposed by the researchers in Nanyang Technological University (NTU), Singapore. For example, Ali et al. [162] developed one CO_2-assisted vapour compression and adsorption hybrid system for cooling and desalination applications and 60% improvement in COP was obtained as compared with conventional CO_2 cooling system. Additionally, Kayal et al. [163] performed the adsorption characterisation of AQSOA-Z01/Z02 zeolites and water for adsorption chillers and the authors found that AQSOA-Z01 zeolite is suitable for cooling generation at relatively low regeneration temperature of 60 ^{o}C due to the "S-shaped" isotherms of AQSOA-Z01 + water systems. Besides the experimental investigation, several theoretical studies on AHT applications have also been reported by NTU researchers. For example, Leong et al. [162] reported the effects of operational parameters and system design on the performances of adsorption chiller where the effects of heat exchanging fluid velocity, heat transfer coefficients and bed dimensions were studied. Based on the experimental adsorption isotherm and kinetics, Ali et al. [164] developed one double stage cooling and desalination system for various adsorption pairs where internal heat recovery between the condenser and two evaporators were considered, and 26% more water and 45% more cooling capacity were observed as compared with conventional equivalent adsorption desalination and cooling systems. In addition, Liu et al. [165] proposed a new transient two-dimensional model with non-constant condensing pressure for zeolite + water adsorption cooling system and it is found that the cycled adsorbate and cycle duration are both increased as compared with the constant condensing pressure model. In one study, Chakraborty et al. [166] presented one thermodynamic formulation to calculate the energetic performance of an adsorption cooler as a function of pore widths and volumes of solid adsorbents. The simulated COP (coefficient of performance) was validated with experimental data and good agreement was found. Furthermore, Teng et al. [167] reviewed the present status of adsorption cooling cycle thoroughly, from experimental investigation to mathematical modelling, from intrinsic development (adsorbent and heat exchanger) to extrinsic development (operation mechanism and parametric investigation). Besides the investigation on the AHT system, researches related the adsorbents synthesis and modification have also been reported by NTU researchers. For example, Zhao et al. [168] fabricated one carbon-based microtubes by pyrolysis of plant tissues via facile synthesis method. These methods and results from the papers mentioned above provide valuable guidelines for the design and optimisation of AHT system.

2.9 Summary

The literature related to adsorption terminology, various adsorbents for cooling and heat pumps and MOFs are revisited. The adsorption mechanism together with adsorption isotherms, kinetics, isosteric heat of adsorption are shown in detail, which are applied to analyse the water adsorption performance in terms of uptake-offtake difference and rates. Additionally, the metal-organic frameworks (MOFs) involved in the current research activities for heat transformation applications are introduced. Research works related to the water adsorption simulation technique namely the Grand Canonical Monte Carlo (GCMC) is elaborated. Furthermore, the progression of research in adsorption assisted heat transformation (AHT) system that recently carried out in Nanyang Technological University (NTU) is summarised. The next chapter will discuss about the modelling of water adsorption with different MOFs adsorbents via GCMC.

Chapter 3. Metal Organic Frameworks – Water Adsorption Analysis

This chapter presents the studies of water adsorption on the parent and modified MOFs employing molecular dynamics (MD) and Grand Canonical Monte Carlo (GCMC) simulations. Based on simulation results (water uptakes versus relative pressure), the novel metal organic frameworks (MOFs) can be designed for higher water transfer with faster kinetics. This methodology is able to select the suitable MOFs for cooling, heat pump and desalination applications.

3.1 Molecular Structure Model

Water molecule models such as TIP3P, SPC/E [169] and TIP4P [170] are used to investigate the interaction for various water + adsorbent systems, and each model reflects certain characteristics of water. Normally, water molecules with TIP3P characteristics [171] and SPC traits [169] are preferred for GCMC simulation. For TIP3P water molecule model, the partial charges of hydrogen atoms and oxygen are 0.415 and -0.830 elementary charge respectively. The hydrogen-oxygen-hydrogen angle is $104.52°$ and length of oxygen - hydrogen bond is 0.9572 Å. Additionally, the corresponding values for SPC water molecule is 0.410, -0.820, $109.47°$ and 1.0 Å, respectively. It is noted that during the simulation process, the adsorbent surfaces are considered as chemically homogeneous, which is independent of adsorption site occupancy of adsorbate. In addition, the angles and the bonds between atoms are held rigid for all adsorbate molecules.

MOFs generally show diverse structures. For Al-Fum, the monoclinic lozenge-shaped unit cell is formed by linking the corner-sharing aluminium octahedral with fumarate [30]. The cell volume is $990.41\ \text{Å}^3$ and the crystallographic indices are $a = 9.33$ Å, $b = 14.21$ Å and $c = 12.09$ Å .

The inclination angle and the diagonal length of the Al-Fum unit cell are 122.55° and 12.79 Å, respectively. The distance d between two fumarate (Al) layers is 6.84 Å. Unlike Al-Fum, prototypical Zr-based MOF such as UiO-66 (UiO represents University of Oslo) with the formula $Zr_6O_4(OH)_4(BDC)_6$ exhibits fcu (face-centred cubic) topology [139]. The cell volume of UiO-66 (Zr) is 8929.65 $Å^3$ and the average aperture size is 6.0 Å. Additionally, another Zr-based MOFs such as MOF-801 also presents fcu topology where abundant metal cluster-bounded hydroxyl groups are observed surrounding the networks of the structure [172]. It is the smallest cubic unit cell among all the zirconium-based MOFs where the cell volume is 5672.90 $Å^3$. Furthermore, the conventional adsorbents namely AFI and CHA type zeolites are analysed here for comparison purpose. The multi-layers cylindrical channels are found for both cases. The AFI (e.g. AQSOA-Z01) type zeolite is ferro-alumino-phosphate (FAPO-5) based with the joint molecular structure of Al-P-O atoms and four channel layers radii of 5.64 Å, 7.24 Å, 8.39 Å and 9.69 Å. On the other hand, the CHA (e.g. AQSOA-Z02) type framework is silico-alumino-phosphate (SAPO-34) based zeolite with (i) four channel layers radii of 3.65 Ǻ, 5.9 Ǻ, 8.75 Ǻ, and 10.88 Ǻ, and (ii) the joint molecular structure of Si-O atoms [100]. The frameworks of all the MOFs and conventional zeolite adsorbents are shown schematically in Figure 3.1.

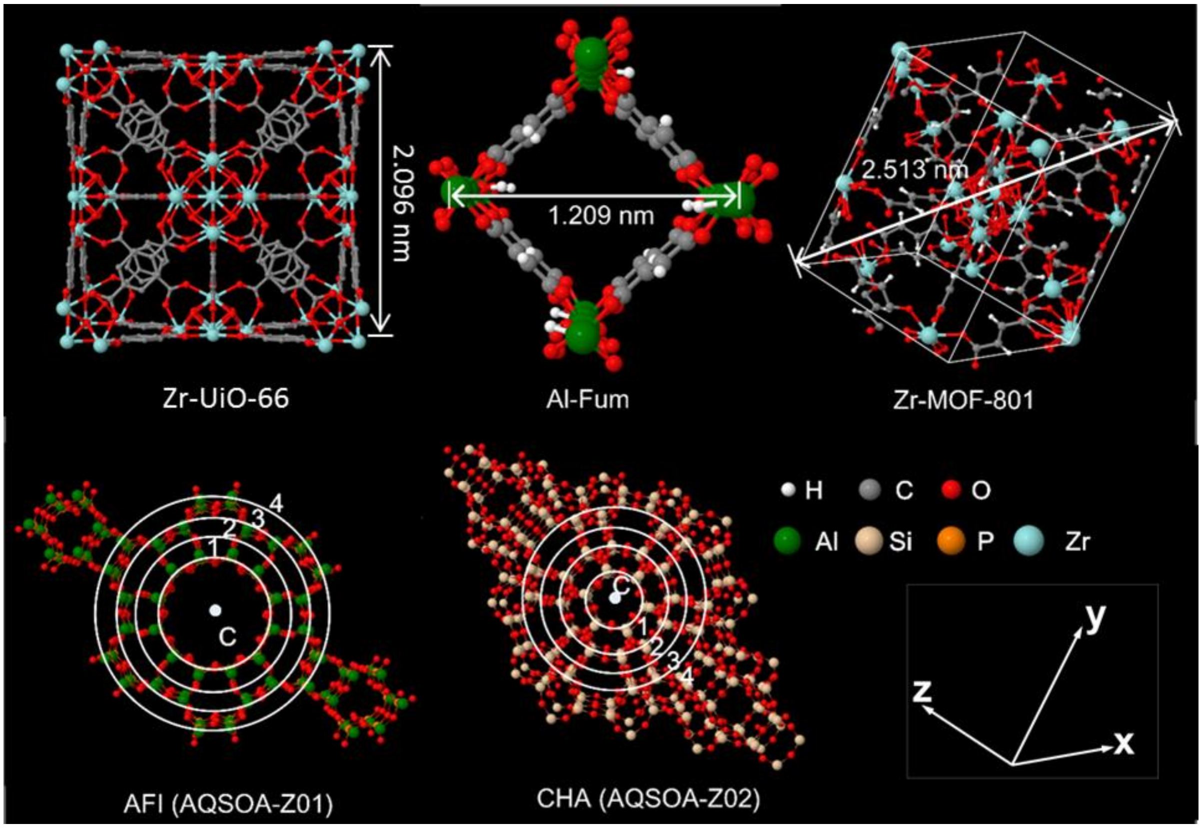

Figure 3.1: Schematic structures of UiO-66 (Zr) [139], Al-Fum [30], MOF-801 (Zr) [172] MOFs and zeolite-based functional adsorbents (types AQSOA-Z01 and AQSOA-Z02) [100].

The original MOFs are modified via mixing with conventional adsorbents, implanting the functional groups or doping with the alkali metal ions. During physi-mixing process of Al-Fum MOFs and AFI/CHA zeolites, the number of possible relative positions between the two structures are infinite. Therefore, the Al-Fum MOFs and AFI/CHA zeolite frameworks are mixed randomly where a reasonable pore structure is formed without any atoms overlap or bond creation. Functionalisation works are completed by replacing the original organic ligands with the functional group ones. For example, amino implanted UiO-66 (Zr) MOFs are structured with one additional amine group on the parent benzene ring, where the parent terephthalic acid is replaced by 2-amino-terephthalic acid. The overall electrostatic potentials of the atomic charges of functionalised MOFs are minimised and estimated by the density functional theory (DFT)

[173]. The DFT calculation is performed using the Becke-Lee-Yang-Parr (B-LYP) correlations plus the double-ξ numerical polarisation (DNP) basis set. With the estimated electrostatic potentials, the atomic charges of the modified MOFs are fitted with the Merz-Kollman (MK) scheme [174]. Figure 3.2 shows the post-modified UiO-66 (Zr) frameworks with various functional groups (-NH_2, -N and -OH). In addition, many works have proved that specific mixing rules should be followed for the alkali metal ions doped into MOFs. The relative position between the additives and the receptors depends both on MOFs structure and the type of the cations. For example, Lan et al. [175] suggested that the optimal distance between the doped Na^+ and oxygen atoms inside the COF-105 is 2.482 Å. Ghoufi et al. [176] also showed that ions should not be inserted more than 2.5 Å away from the MOFs frameworks. In order to build the theoretical Li-Al-Fum framework, certain amount (5% weight) ions pairs of LiCl are placed randomly where the Li^+ cations are located adjacent to the oxygen atoms of Al-Fum and the mean square displacement of Li^+ cations are remained closed to zero.

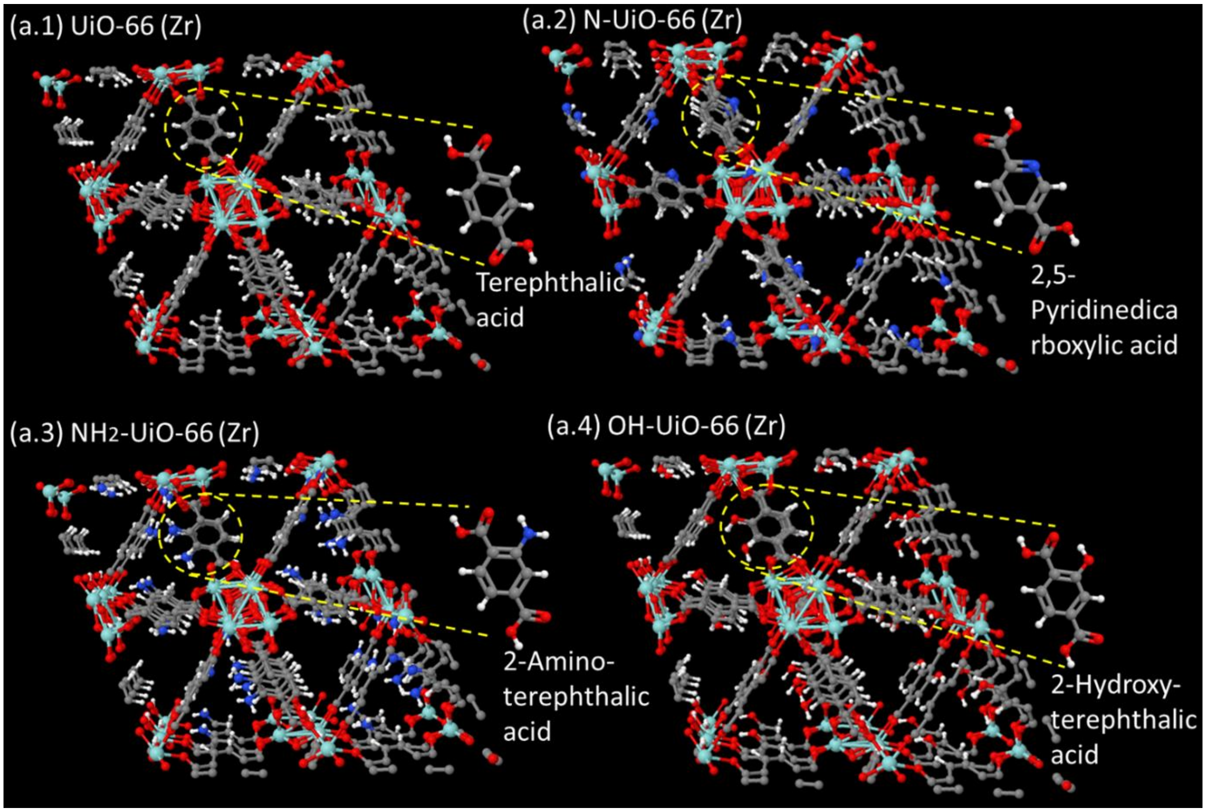

Figure 3.2: Molecular structure of the original and functionalised UiO-66 (Zr): (a.1) UiO-66 (Zr); (a.2) N-UiO-66 (Zr); (a.3) NH_2-UiO-66 (Zr) and (a.4) OH-UiO-66 (Zr). Here, the terephthalic acid with various functional groups are also shown for better understanding.

3.2 Simulation Methods

3.2.1 Interatomic Potential

Interatomic potentials are theoretical functions for investigating the interaction potential energy of a restrained geometry at specific positions with pre-defined force fields. It is the fundamental infrastructure of molecular mechanics. Some typical uses of interatomic potential are to predict (i) new molecule structure and physi/chemi-reaction process and (ii) minimise of the overall system energy. The interatomic potential of an arbitrary system for one molecule is denoted as a series of mathematical items which represent the superposition of multi-body interactions. Normally, a thorough potential energy consists of both bonded (valence) interactions and nonbonded interactions, where bond stretching and angular distortions are involved for bonded terms and van der Waals and electrostatic portions are summed up for nonbonded interactions. During the process of water adsorption on MOFs adsorbents, only nonbonded interactions exist between adsorbate-adsorbate and adsorbent-adsorbate frameworks. Although pairwise potential models such as Morse [177], Buckingham [153] and Born-Mayer-Huggins [178] are available and easy to handle, the universal force field (UFF) model is chosen due to the presence of molecular interactions during adsorption. As compared with other force fields, UFF describes the molecular system with high accuracy and impressive computational simplicity. The mathematical expression for UFF nonbonded interactions is expressed as

$$\phi_{ij} = 4\varepsilon_{ij}\left[\left(\frac{\sigma_{ij}}{r_{ij}}\right)^{12} - \left(\frac{\sigma_{ij}}{r_{ij}}\right)^{6}\right] + \sum_{a_i}\sum_{b_i}\frac{Cq_a q_b}{\in r_{ab}}\ (r < r_c) \tag{3.1}$$

Here, ϕ_{ij} is the overall interaction potentials (adsorbate-adsorbate and adsorbent-adsorbate). The first item on the right side of equation represents the 12-6 Lennard-Jones potentials (van der Waals forces), where ε indicates the potential well depth in kcal/mol and σ denotes the collision diameter or van der Waals bond length in Å, r defines the distance between two atoms. The Lorentz-Berthelot combining rules ($\varepsilon_{ij} = \sqrt{\varepsilon_i \varepsilon_j}$ and $\sigma_{ij} = \frac{1}{2}\left(\sigma_i + \sigma_j\right)$ [179] is applied to calculate the pairwise potential well depths and collision diameters. The r^{-12} item stands for the short-range repulsive part caused by the electron orbital overlapping; the r^{-6} item is the long-range attractive part mainly related to the dispersion force. The second item on the right side of the equation defines the Coulomb interactions, where long-rang electrostatic attractions are considered. Here, q is the point charge of one atom in molecules, $\in$ represents the dielectric constant, C is the energy-conversion constant and r_c denotes the cutoff distance (r_c = 9 to 13 Å, depending on the size of adsorbate molecule’s type and adsorbent structures).

The interaction potential calculation employing the proposed model for one water molecule and Al-Fum MOF is presented in Figure 3.3. For the selected Al-Fum supercell (6×6×10), each layer contains 144 aluminium atoms, 576 carbon atoms and 720 oxygen atoms. The geometrical model shown here is for demonstration purpose, more water molecules and bigger MOFs frameworks are involved for the Grand Canonical Monte Carlo (GCMC) simulations. The total interaction potentials (ϕ) of the whole system depends on the relative position of the water molecule to the atoms (aluminium/oxygen/carbon) inside the Al-Fum, which could be represented as a function of water-adsorbent atoms position vector $r\ (X, Y, Z)$. The atomic charges of metal and organic linkers constituents for the original MOFs are obtained via ab initio electrostatic potential fitting scheme [138, 180-182], other pairwise force field parameters such as the well depth potential and collision diameter for all the adsorbate + adsorbent systems are furnished in Table 3.1.

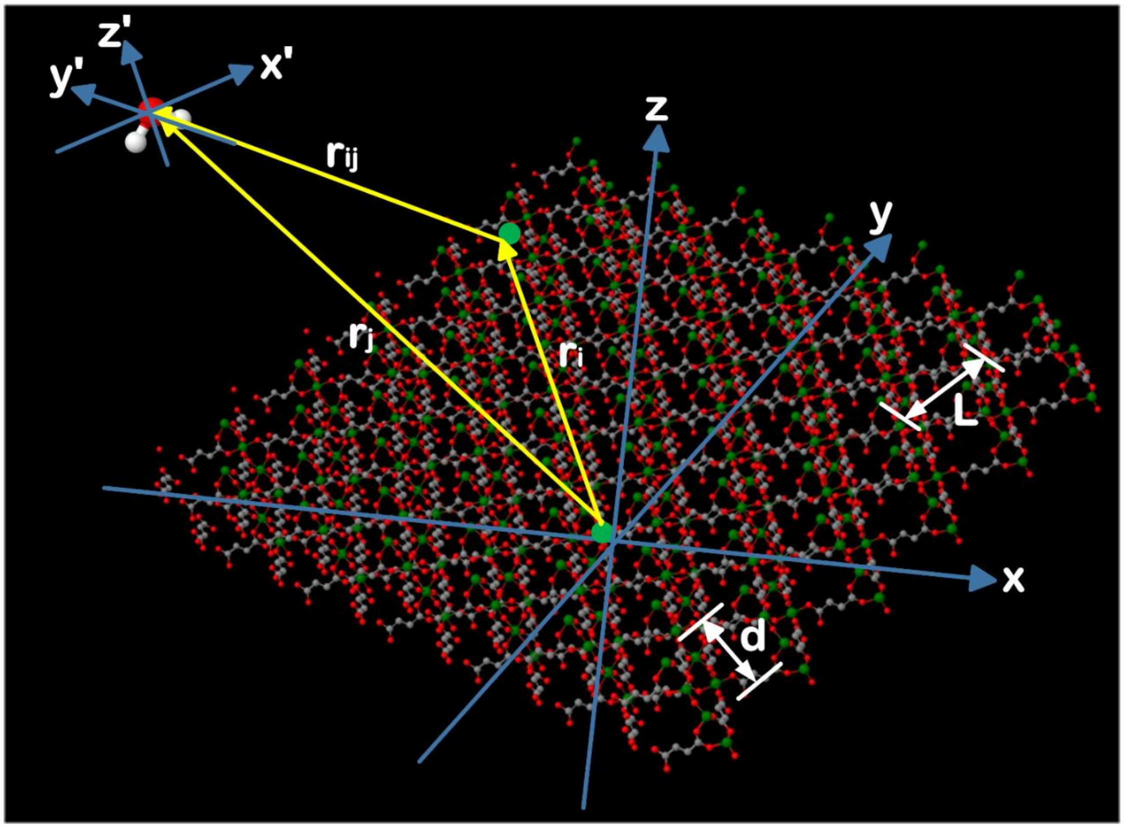

Figure 3.3: Molecular simulation model of Al-Fum structure and TIP3P water molecule. The distance between the two layers is *d* = 6.84 Å, and the diagonal length is *L* = 12.79Å. The position vector points from the ith atom of the adsorbent (Al/O/C) to the jth atom of the adsorbate molecule (O/H). Position vector in TIP3P water molecule coordinate system X' Y' Z' can be converted to Al-Fum coordinate system based on the translational vector and rotational matrix transformation rules. (Hydrogen atoms in the adsorbent's structure are omitted for clarity purpose)

Table 3.1: Pairwise Force-field-parameters for interactions in original and modified MOFs (Zr-UiO-66, Zr-MOF-801 and Al-Fum) with water molecule (H_2O). (H_i and O_i define the hydrogen and nitrogen atom of in water molecules. Other atom such as Zr_j, Al_j, C_j, O_j, N_j, Si_j, P_j and H_j represent the atoms in MOF and zeolite adsorbents) [152].

Atom type	Force field parameter	Zr_j	Al_j	C_j	O_j	N_j	Si_j	P_j	H_j
H_i	ϵ(kcal/mol)	0.055	0.149	0.068	0.051	0.055	0.133	0.116	0.044
	σ(Å)	3.005	3.693	3.369	3.193	3.273	3.591	3.517	2.886

O_i	ϵ(kcal/mol)	0.203	0.174	0.079	0.060	0.064	0.155	0.135	0.051
	σ(Å)	3.312	3.999	3.676	3.500	3.580	3.900	3.824	3.193

3.2.2 Water Adsorption Isotherm via GCMC

The GCMC method is applied to simulate water adsorption behaviours on MOFs at the molecular level. During the simulation process, a rectangular simulation cell is created by applying the periodic boundary conditions in both the x and y directions where the z direction is bounded by the diabatic and porous walls. For the overall simulation process, the temperature (T), chemical potential (μ) and volume (V) constant whist the total number of adsorbates and the fluid density fluctuate. Water molecules with TIP3P characteristics could be momentarily inserted or deleted between the imaginary reservoir and simulation cell where the energy biasing scheme is applied [183]. In addition, water molecules can move freely in the grand canonical ensemble where translations and rotations are proportioned at 50% probability each. The coordinates of the inserted water molecule are chosen at random position where the centre of mass is located and the orientation of the water molecule is also randomly chosen by rotating about this insertion point. Once the simulation process starts, two O-H bonds and the H-O-H angle are held rigid. Furthermore, the overall relative velocity of all atoms in the water molecules is maintained zero. The ideal-gas assumption is applicable due to the low bulk pressure of the reservoir. Therefore, the fugacity of the water vapour is assumed to be the same as its gas pressure. However, the size of the simulation systems could influence the results dramatically [184]. Additionally, the long-range electrostatic attractions calculated by Ewald summation methods [185] (a common method used to calculate the long-range electrostatic interactions in periodic systems where both the short-range contribution in real space and long-range contribution in reciprocal space are considered) is not applicable here due to the asymmetry of some of the MOFs, for example Al-fumarate. Hence, to minimise the impact of periodic boundary conditions and overcome these deficiencies, adequate supercells (for example, the surface dimensions are about 48.18 Å × 54.02 Å for Al-fumarate) are selected.

The simulation environment is considered to reach equilibrium conditions when the chemical potential of a water vapour in the adsorbed state is the same as the chemical potential of its bulk phase. Generally, it takes at least 20 million steps for the system to achieve equilibrium state and the data collection is conducted after another 20 million production runs proceeded. For each adsorption temperature and pressure, the number of water molecules is counted under the equilibrium state and the uptakes are deduced. The overall adsorption isotherms are obtained. The uptakes of water molecules at each condition is calculated by $q = (n \cdot M_w)/M_{MOF}$, where n is the total number of water adsorbed onto the framework, M_w represents the molecular weight of water and M_{MOF} indicates the overall molecular weight of MOFs adsorbents, which is related to the total number of metal and organic atoms inside it. The calculation procedure of the water adsorption isotherm on various original and modified MOFs at certain temperature from Henry's region to the saturation state via GCMC is shown schematically in Figure 3.4.

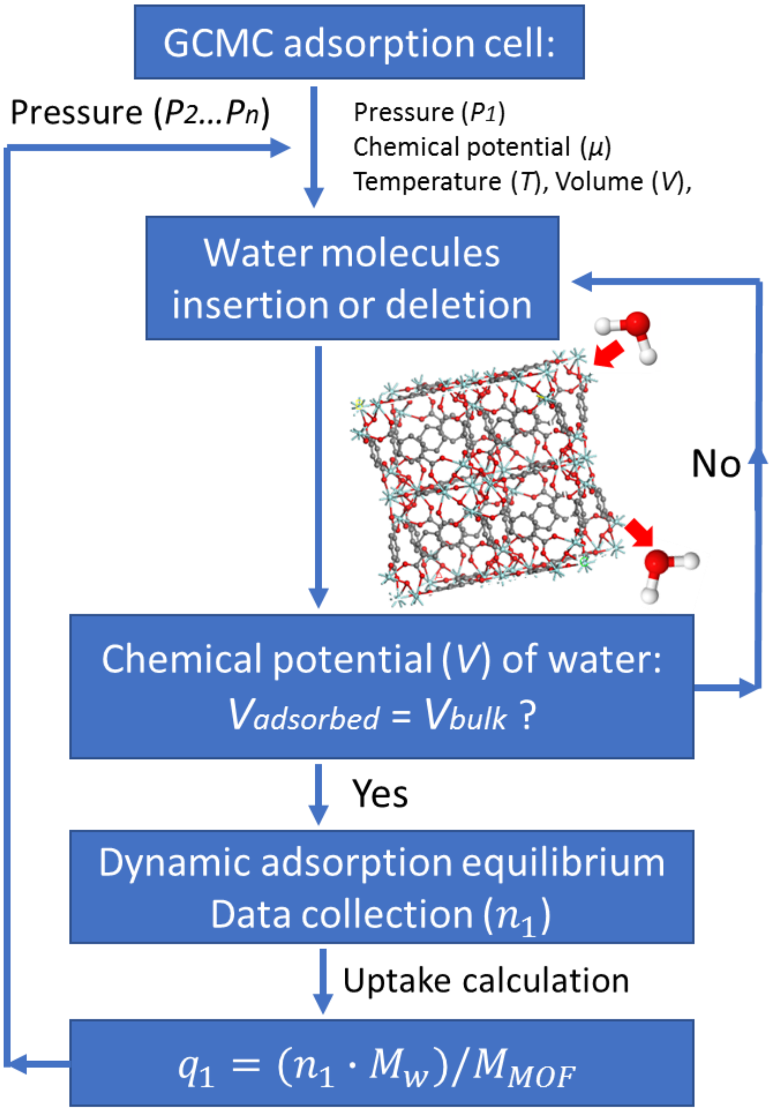

Figure 3.4: Flow chart of the water adsorption isotherm calculations for a wide pressure range (0 < *P/Ps* < 1.0) at certain temperature via GCMC.

3.3 Results and Discussion

3.3.1 UiO-66 (Zr) MOFs

Figure 3.5 shows the GCMC snapshots of the water adsorption on original and functionalised UiO-66 (Zr) for various relative pressures (*P/Ps* = 0.1/0.2/0.3), from which one can see how the water molecules are adsorbed onto the MOFs pore-structures. From Figure 3.4 (a.1) to (a.3), strong hydrophobic performances are observed for the original UiO-66 (Zr). At *P/Ps* = 0.1, only 5 water molecules are adsorbed onto the UiO-66 framework and this number increases to 22 when the relative pressure increases to 0.3, where there are still numerous empty pores. After introducing amine, hydroxy and nitrilo functional groups onto the UiO-66 (Zr) structure, enhanced hydrophilic behaviours are resulted for the modified materials and more water molecules are adsorbed even at low pressure region. For example, at *P/Ps* = 0.1, the number of the adsorbed water molecules is 7, 36 and 173 for NH_2-UiO-66 (Zr), OH-UiO-66 (Zr) and N-UiO-66, respectively. As the pressure increases, more water molecules are adsorbed onto the functionalised UiO-66 (Zr) pore-structures. During the GCMC simulation, water molecules are firstly adsorbed to the higher energy site. As the adsorption continues, more water molecules are adsorbed onto the sites of lower energy. It is also observed that water molecules tend to be adsorbed near $-NH_2$, -OH and -N group locations, for these hydrophilic functional groups attracts water molecules with strong affinities. Furthermore, at *P/Ps* =0.3, the number of the adsorbed water molecules on NH_2-UiO-66 (Zr), OH-UiO-66 (Zr) and N-UiO-66 (Zr) are 312, 211 and 264, respectively.

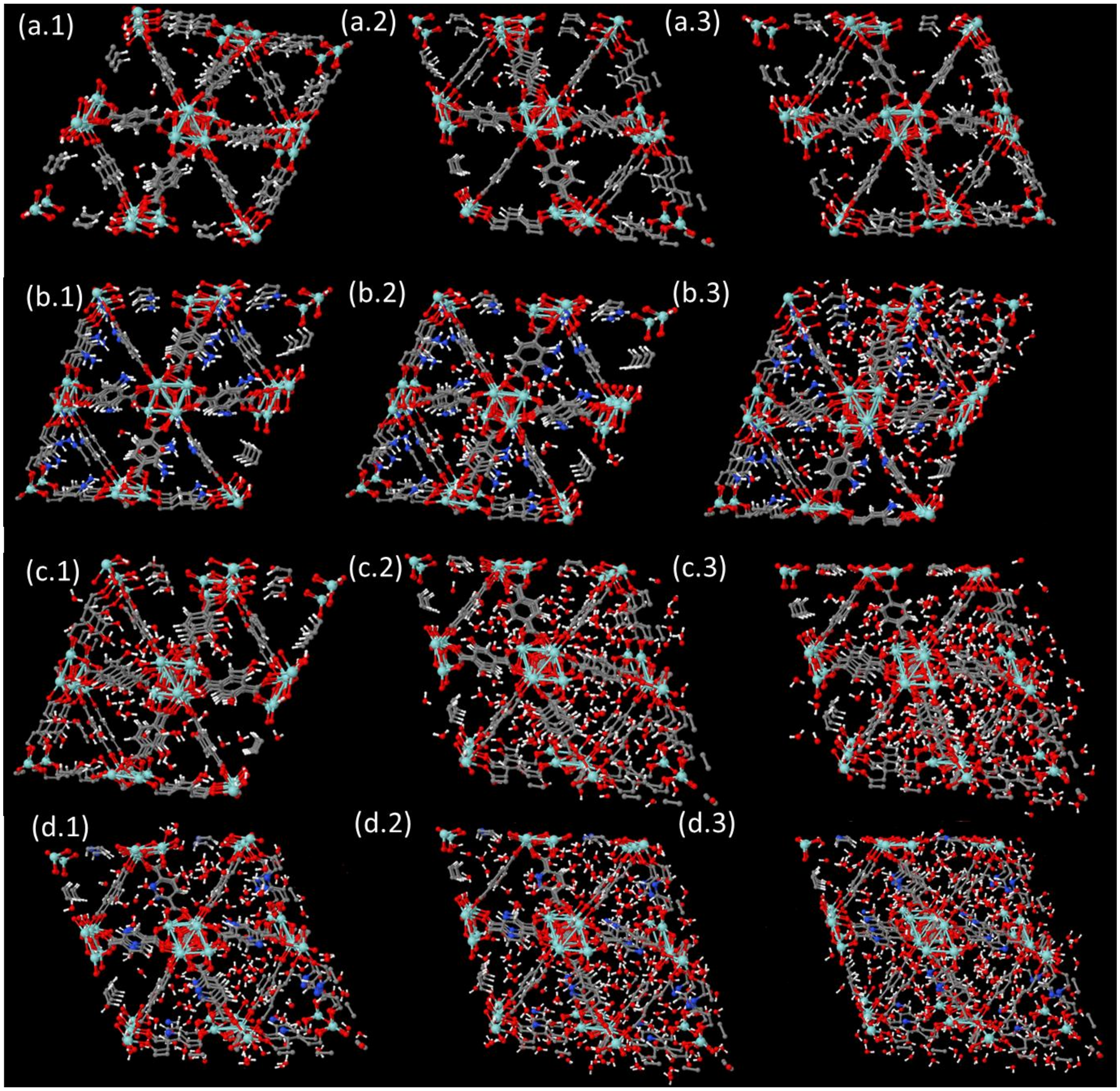

Figure 3.5: Snap shots for molecular structure of water adsorption at 30 °C: (i) UiO-66 (Zr) MOF: *P/Ps* = 0.1 (1.a), *P/Ps* = 0.2 (1.b), *P/Ps* = 0.3 (1.c); (ii) NH_2-UiO-66 (Zr) MOF: *P/Ps* = 0.1 (2.a), *P/Ps* = 0.2 (2.b), *P/Ps* = 0.3 (2.c); (iii) OH-UiO-66 (Zr) MOF: *P/Ps* = 0.1 (3.a), *P/Ps* = 0.2 (3.b), *P/Ps* = 0.3 (3.c); (iv) N-UiO-66 (Zr) MOF: *P/Ps* = 0.1 (4.a), *P/Ps* = 0.2 (4.b), *P/Ps* = 0.3 (4.c). (red: oxygen in water and UiO-66 based MOFs, white: hydrogen, grey: carbon, cyan: zirconium, blue: nitrogen in NH_2-UiO-66 (Zr) and N-UiO-66 (Zr) MOFs).

The GCMC simulated water + UiO-66 (Zr) based MOFs adsorption isotherms from Henry's region to the saturated state at 30 °C is shown in Figure 3.6. The red-dotted line represents the original UiO-66 (Zr) and the dark-solid lines stand for the functionalised UiO-66 (Zr) MOFs. The GCMC results show the enhanced hydrophilic performances for the functionalised materials as compared with the original UiO-66 (Zr) at low pressure region. For example, as compared with the original UiO-66 (Zr), NH_2-UiO-66 (Zr) also exhibits "S-shaped" isotherm with a much shorter hydrophobic length ($P/P_s \approx 0.2$). OH-UiO-66 (Zr) starts to adsorb water sharply at even low-pressure region ($P/P_s \approx 0.1$). Furthermore, N-UiO-66 (Zr) shows a type I water adsorption isotherm and could reach 80% of the limiting uptakes at $P/P_s = 0.2$. At $P/P_s = 0.2$, the GCMC simulated water uptakes for UiO-66 (Zr), NH_2-UiO-66 (Zr), OH-UiO-66 (Zr) and N-UiO-66 (Zr) MOFs are 0.01 g/g, 0.06 g/g, 0.175 g/g and 0.318 g/g, respectively. These results provide valuable references for the synthesisation of functional MOFs with organic linker modification and also experimental investigation. It should be noted here that the results obtained by GCMC method are very sensitive to the potential parameters and water molecule models [186]. For example, Ramachandran et al. [187] showed that using the same GCMC algorithm, the SPC/E water model results a shorter hydrophobic length as compared to the TIP4P model. Hence, all the simulations are carried under the same operating conditions of water adsorption on MOFs. The only variable is the framework of UiO-66 MOFs (original and functionalised).

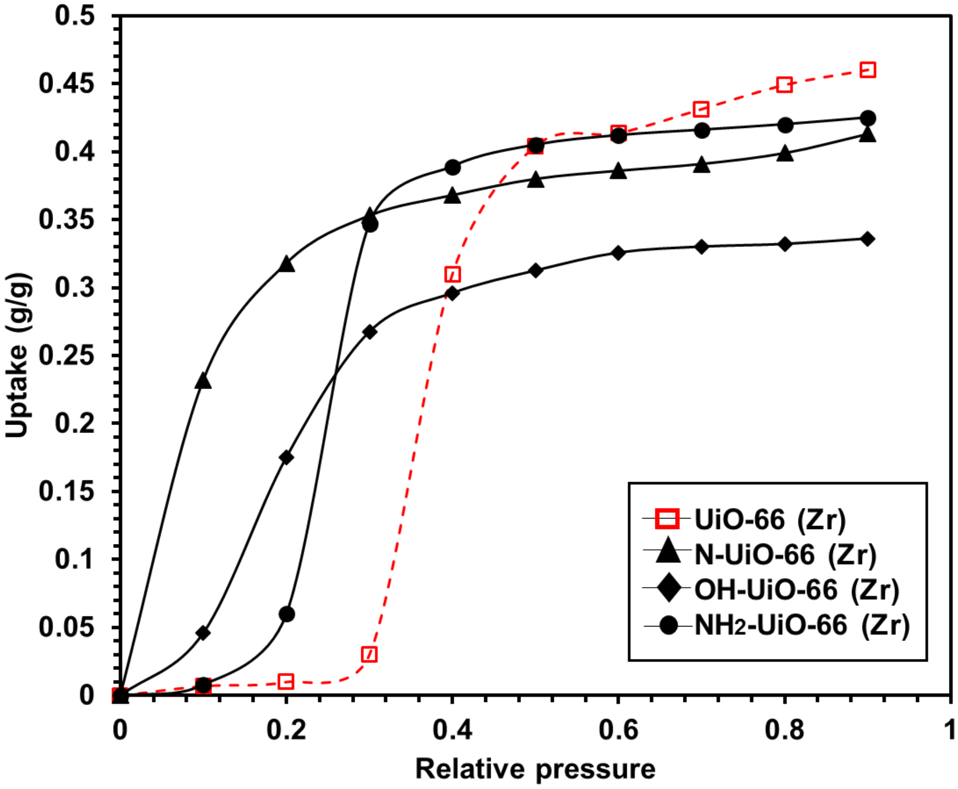

Figure 3.6: Simulated isotherms for water adsorption on UiO-66 (Zr) based MOFs (UiO-66 (Zr), NH_2-UiO-66 (Zr) MOF, OH-UiO-66 (Zr) MOF and N-UiO-66 (Zr) MOF) at 30 °C.

3.3.2 MOF-801 (Zr)

Figure 3.7 shows the GCMC snapshots for water adsorption on MOF-801 (Zr) and $(CH_3)_2$-MOF-801 (Zr) at 30 °C at different relative pressures of P/P_s. Here, low relative pressures of P/P_s = 0.05/0.08/0.1 are chosen to investigate the effects of the methyl-functional groups on water adsorption in the Henry's law region. For the original MOF-801 (Zr), strong hydrophilic behaviours are found and 18 water molecules are adsorbed even at extremely low pressure (P/P_s = 0.05). As the relative pressure increases to 0.1, 102 water molecules are adsorbed onto the MOF-801 pore-structures and water aggregations are observed. However, hydrophobic traits are obtained for $(CH_3)_2$-MOF-801 (Zr) where almost no water molecules are adsorbed at P/P_s = 0.05. As the relative pressure increases to 0.1, only 38 water molecules are found in $(CH_3)_2$-MOF-801

(Zr) frameworks, which is 37% of that in MOF-801 (Zr). Additionally, no water molecules are found near the methyl functional groups as hydrophobic -CH_3 repel water molecules from being adsorbed.

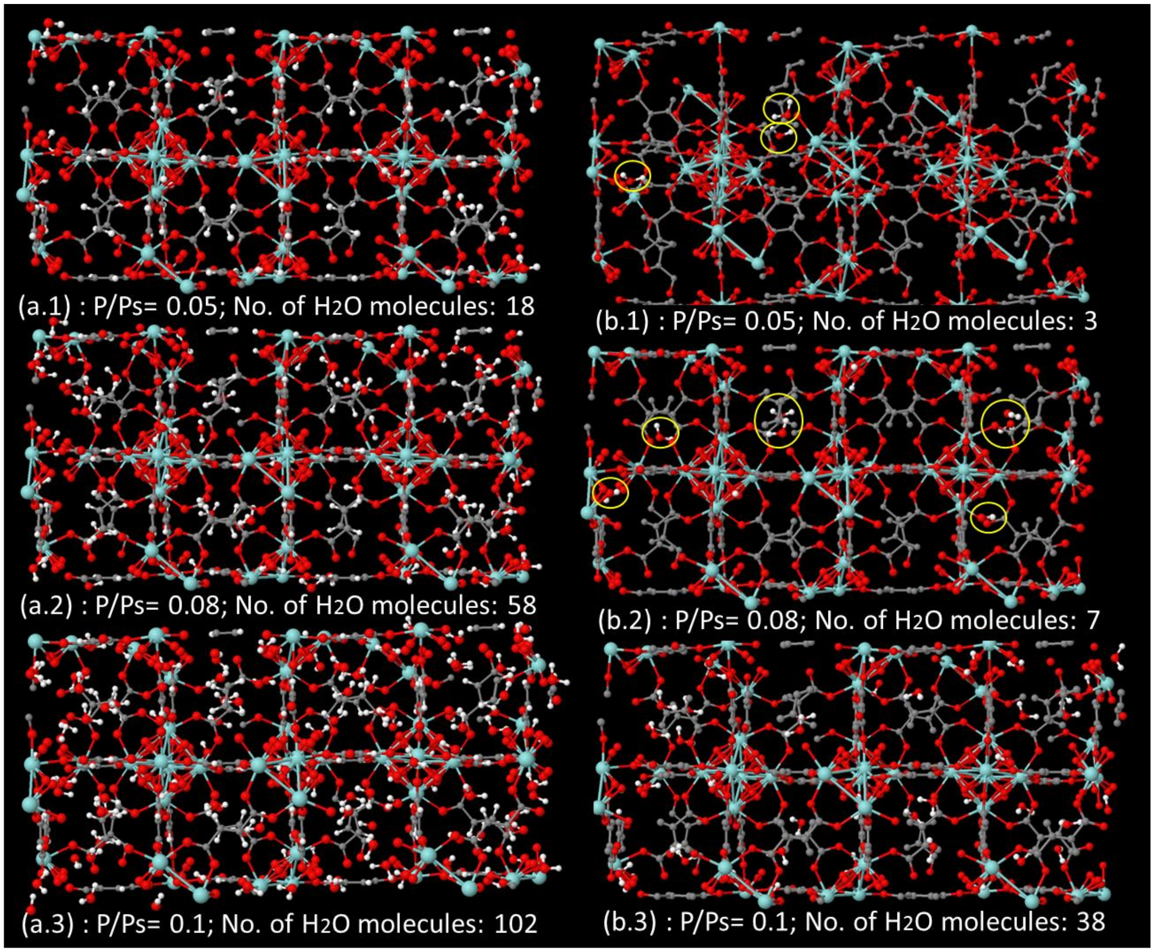

Figure 3.7: Snap shots for molecular structure of water adsorption at 30 °C: (i) MOF-801 (Zr): *P/Ps* = 0.05 (a.1), *P/Ps* = 0.08 (a.2), *P/Ps* = 0.1 (a.3); (ii) $(CH_3)_2$-MOF-801 (Zr) : *P/Ps* = 0.05 (b.1), *P/Ps* = 0.08 (b.2), *P/Ps* = 0.1 (b.3). (grey: carbon, cyan: zirconium, red: oxygen in water and MOF-801 based MOFs, white: hydrogen in water and MOF-801 based MOFs)

Based on the GCMC simulation results, the water adsorption isotherms on original and methyl-functionalised MOF-801 (Zr) are plotted and shown in Figure 3.8. Here, the red-dotted line and the dark-solid line indicate the parent MOF-801 and $(CH_3)_2$-MOF-801 (Zr), respectively. For the parent MOF-801 (Zr), super hydrophilic behaviour is found at Henry's region, which agrees well with the experimentally data [172]. After implanting methyl functional groups, a longer hydrophobic length is obtained for $(CH_3)_2$-MOF-801 (Zr), where almost no water is adsorbed up to $P/P_s \rightarrow 0.1$. For example, at $P/P_s = 0.08$, the water uptakes for parent MOF-801 and $(CH_3)_2$-MOF-801 are found 0.09 g/g and 0.009 g/g by GCMC simulation, which indicates that the water uptakes are reduced to one-tenth in Henry's region by the addition of $(CH_3)_2$ in original MOF-801 (Zr) adsorbent. Additionally, at $P/P_s = 0.1$, the GCMC simulation results show that water uptakes for the parent MOF-801 and $(CH_3)_2$-MOF-801 are 0.152 g/g and 0.051 g/g, respectively i.e. only one-third of the water uptakes are obtained for the methyl-functionalised MOFs. The weaken hydrophilic traits in MOF-801 (Zr) at low pressure region provides benefits for the heat transformation applications, with lower regeneration temperature of 55 °C.

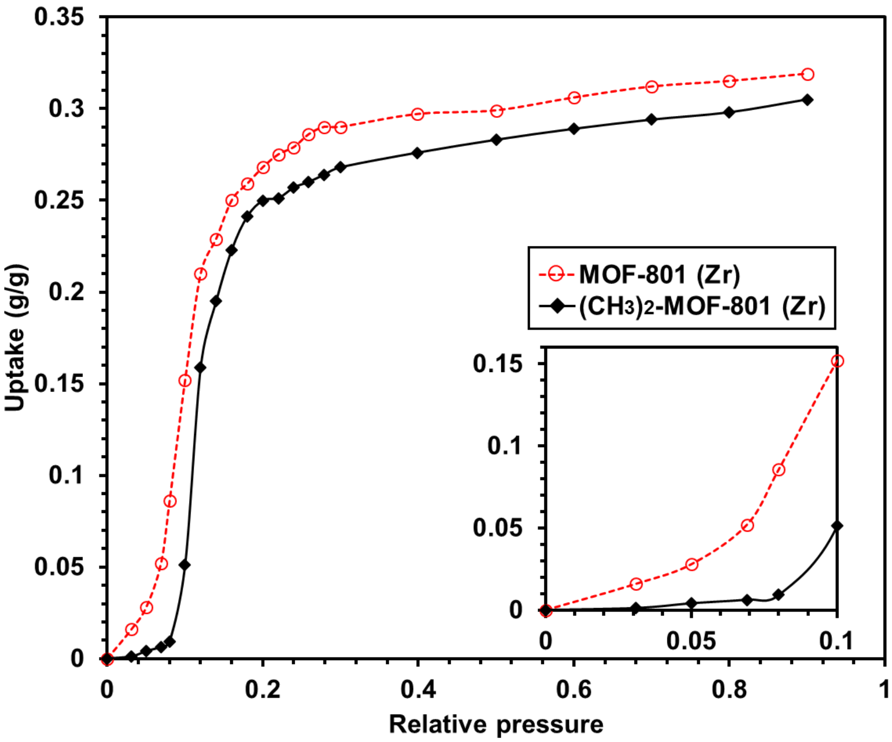

Figure 3.8: GCMC simulated isotherms for water adsorption on MOF-801 (Zr) based MOFs (MOF-801 (Zr) and $(CH_3)_2$-MOF-801 (Zr) at 30 °C. Here, the Henry's region ($0 < P/Ps < 0.1$) are enlarged for comprehensive understanding.

3.3.3 Al Fumarate MOFs

The simulation snapshots for water adsorption on parent Al-fumarate, Li doped Al-fumarate, AFI-type zeolite – Al-fumarate and CHA-type zeolite – Al-fumarate composites are presented in Figure 3.9. Different relative pressures ($0.05 < P/Ps < 0.3$) are chosen here for various adsorbents according to their diverse hydrophobic or hydrophilic performances in the low pressure region. Hence the snap shots of 30% AFI/CHA and Al-fumarate composite are shown from different angles better understand the random mixing structure. At lower pressure region, more water molecules are observed to be adsorbed in Li^+ doped MOFs and MOF-zeolite composite structures. Water molecules are observed near the Li^+ cations or zeolite frameworks. As the pressure increases, some small cluster of 2-3 water molecules are formed. At higher pressure, bigger clusters (4-5 molecules) are found as the cluster size depends on the water affinity to the framework.

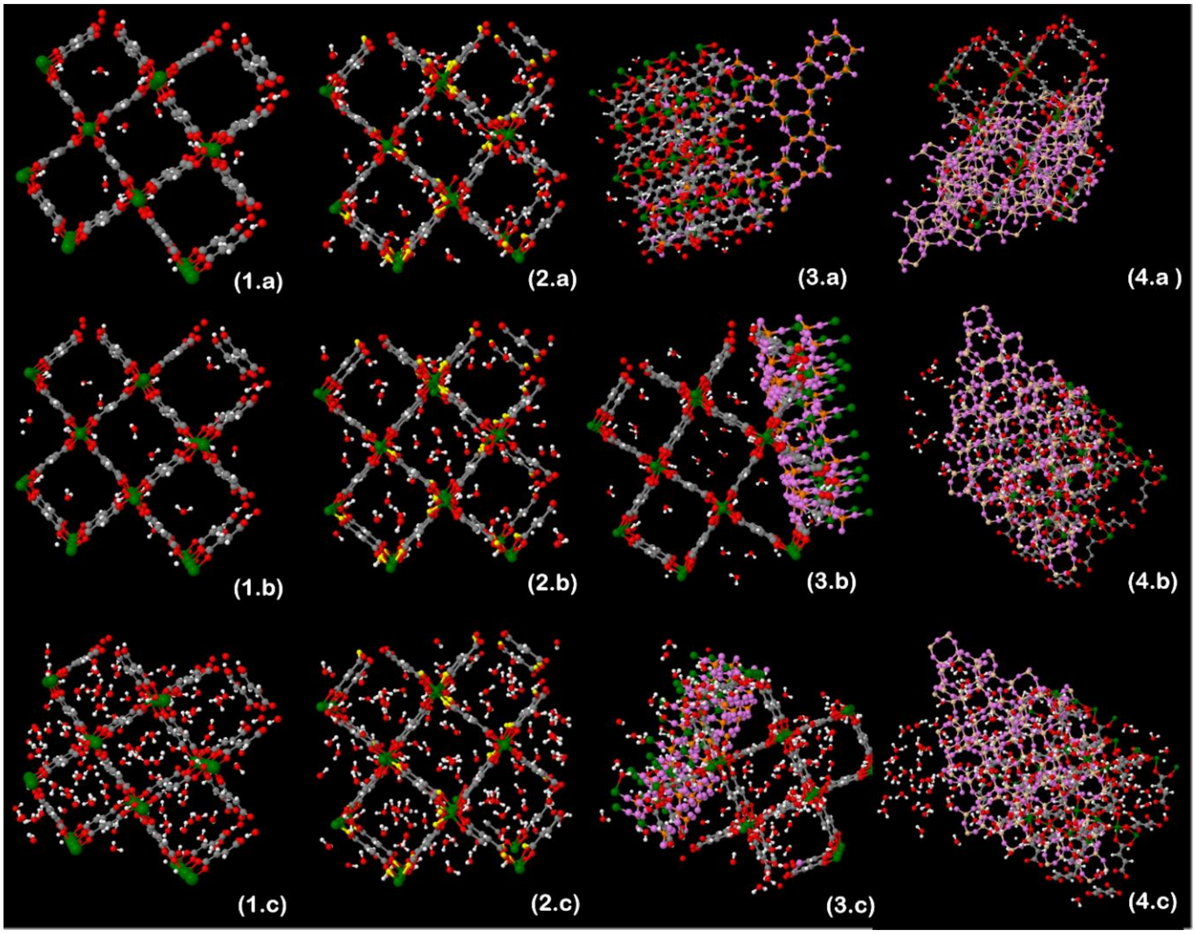

Figure 3.9: Snap shots for molecular structure of water adsorption at 30 °C: (i) Al-Fum MOF: *P/Ps* = 0.05 (1.a), *P/Ps* = 0.2 (1.b), *P/Ps* = 0.3 (1.c); (ii) 5%Li-Al-Fum MOF: *P/Ps* = 0.05 (2.a), *P/Ps* = 0.2 (2.b), *P/Ps* = 0.3 (2.c); (iii) 30%AFI-Al-Fum MOF: *P/Ps* = 0.05 (3.a), *P/Ps* = 0.1 (3.b), *P/Ps* = 0.25 (3.c); (iv) 30%CHA-Al-Fum: *P/Ps* = 0.05 (4.a), *P/Ps* = 0.1 (4.b), *P/Ps* = 0.25 (4.c). Hence 'Al-Fum' means 'Al-fumarate'. (red: oxygen in water and Al-Fum, white: hydrogen, grey: carbon, yellow: lithium, violet: oxygen in AFI or CHA zeolite, orange: phosphorus, cream-colour: silicon, green: aluminium)

Employing GCMC, the amount of water uptakes on Al-fumarate MOFs and MOF-CHA/AFI-type zeolite composites are calculated from the relative pressures of $P/P_s \rightarrow 0$ to $P/P_s \rightarrow 1$ at 30

^{o}C. The isotherm plots are shown in Figure 3.10, from which one can find that the water uptakes are very small up to the $P/P_s \rightarrow 0.1$ (smaller hydrophobic length), later a rise in water uptake is found as the pressure increases. Finally, the uptake curve reaches the limit under saturated conditions. Hence, all post-synthesised Al-fumarate and composite structures show the shorter hydrophobic length as compared with that of the parent Al-fumarate MOF. As can be observed from the simulation results that water vapour starts adsorbing into adsorbent pores at the relative pressure (P/Ps) of 0.1. Furthermore, the GCMC simulation shows the maximum water loading per unit cell is (i) 104 molecules for Al-fumarate, (ii) 122 molecules for 5%Li- Al-fumarate, (iii) 212 molecules for 30% AFI- Al-fumarate and (iv) 243 molecules for 30% CHA- Al-fumarate. It is observed from GCMC simulation that Li ions dopants and AFI/CHA zeolite and Al-Fum MOFs show promising results due to higher water uptakes at the relative pressure of 0.2 to 0.25. Hence, the higher uptake – offtake difference under chiller operating range is expected as compared with the parent Al-fumarate -water systems.

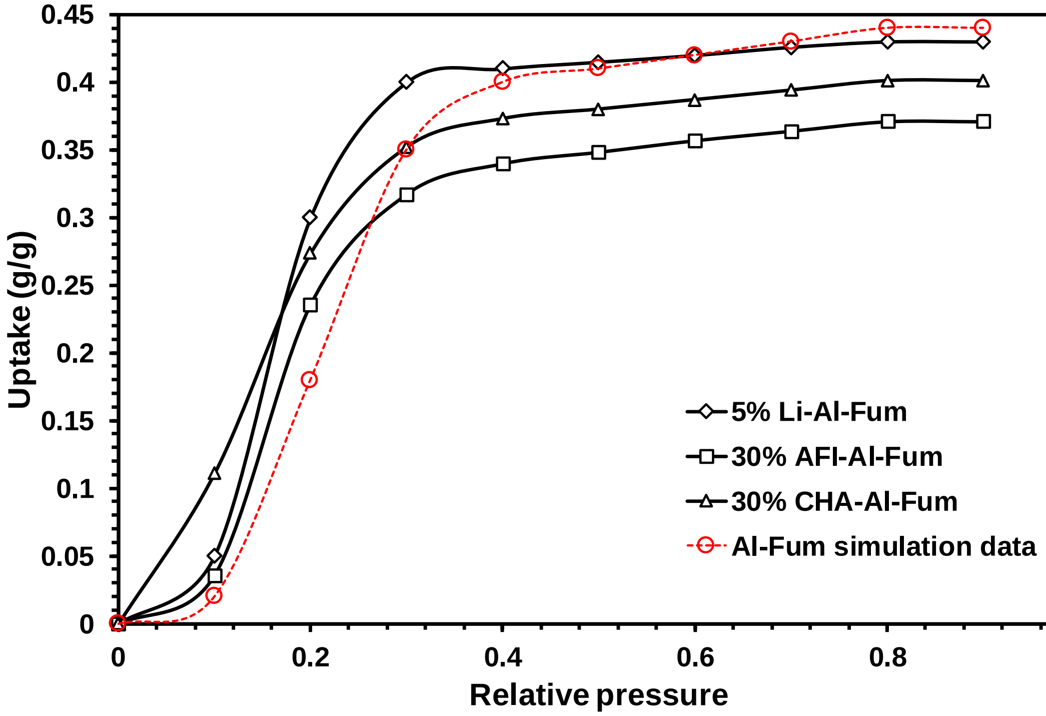

Figure 3.10: Simulated isotherms for water adsorption on aluminium based MOFs (Al-fumarate -MOF, 30%AFI- Al-fumarate MOF, 30%CHA- Al-fumarate MOF, 5%Li- Al-fumarate MOF) at 30 °C. Hence ‘Al-Fum’ means ‘Al-fumarate’.

3.4 Summary

In this chapter, the grand canonical Monte Carlo (GCMC) is described in detail. The water molecule models and the adsorbent (MOF and conventional material) frameworks are constructed. The interaction potentials between the water molecules and the adsorbents are elaborated. Furthermore, the water adsorption isotherms at various pressures are predicted. This new knowledge is employed here as a bench mark for MOFs-design, structure modification, water adsorption revision and AHT system evaluation. The experimental method is presented in the next chapter.

Chapter 4. Methodology, Experiments and Analysis

This chapter at first shows the synthesis and the characterisation of the parent and structural-modified MOFs/zeolite-MOFs composites. Subsequently water adsorption on these adsorbents are presented in terms of isotherms and kinetics. Based on the Clausius Clapeyron equation, the isosteric heat of adsorption is also evaluated.

4.1 MOFs Synthesis

4.1.1 Original MOFs Synthesis

4.1.1.1 MOFs Type UiO-66 (Zr)

The hydrothermal reaction method is applied to fabricate MOF UiO-66 (Zr) [188]. Firstly, 2.7 mol terephthalic acid ($\mathrm{C_8H_6O_4}$, 98%), 2.7 mol zirconyl chloride octahydrate ($\mathrm{ZrOCl_2 \cdot 8H_2O}$, 98%), 5 ml formic acid (HCOOH, $\geq$ 96%) and 106 ml N, N-dimethylformamide (DMF, 98%) are mixed in a beaker. The mixture is stirred uniformly at room temperature for 30 minutes. Secondly, the mixed liquor is transferred into the stainless autoclave, sealed tightly and heated for 24 h at 120 °C. Next, the mixture is separated via the filter paper. The purification process is conducted by rinsing the fabricated materials with DMF (three times) and ethanol (twice). Finally, the UiO-66 (Zr) sample is dried (80 °C overnight) and activated (150 °C and 5 h). The fabrication process of UiO-66 (Zr) is schematically shown in Figure 4.1.

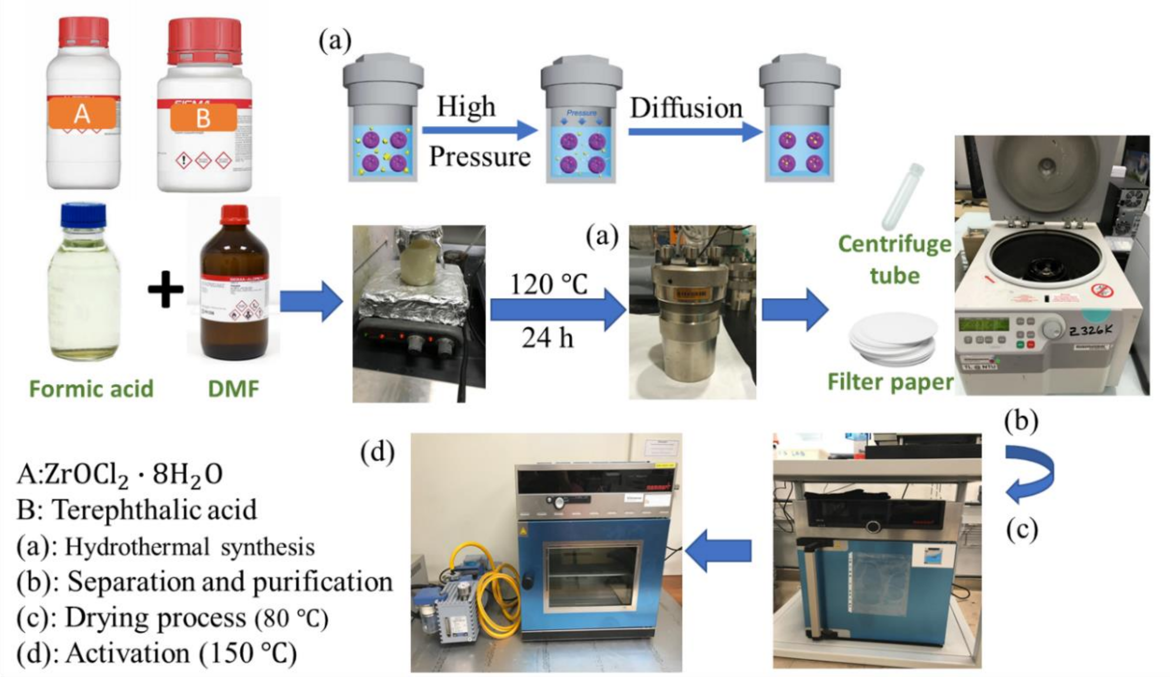

Figure 4.1: Synthesis process (hydrothermal reaction) of MOF UiO-66 (Zr).

4.1.1.2 MOF-801 (Zr)

Zr based MOF-801 is fabricated via hydrothermal reaction method [172]. 0.005 mol of zirconium oxide chloride octahydrate ($ZrOCl_2 \cdot 8H_2O$, 99%, Merck) and 0.005 mol of fumaric acid ($C_4H_4O_4$, 99%, Merck) are dissolved in the DMF-formic acid solution (volume ratio: v/v=20:7, 27 ml in total). The mixture is then transferred into the sealed autoclave for heating 130 ^{o}C for 24 h. After seperation, the white materials are washed three time with DMF and two times with ethanol. The humid fumarate-based MOFs are dried overnight at 80℃ and then placed in the vacuum oven at 150 ℃ for 5 h. The synthesis conditions and purification processes stay the same for $(CH_3)_2$-MOF-801 except replacing the organic linker with dimethyl fumarate.

4.1.1.3 Al Fumarate MOFs

The Al Fumarate (Al-Fum) is fabricated via reflux reaction method under ambient pressure [189]. Firstly, 0.01 mol aluminium chloride hexahydrate ($AlCl_3 \cdot 6H_2O$, 99%, Sigma-Aldrich) and 0.01 mol fumaric acid ($C_4H_4O_4$, 99%, Sigma-Aldrich) are added into the beaker, 50 ml of N, N-dimethylformamide (DMF, 99.8%, Sigma-Aldrich) is used here as reagent. The mixture is stirred at constant temperature of 130 ℃ for 96 h. Secondly, the mixture is separated by a centrifugal spinning machine with a speed of 10,000 rpm. Next, the condensed solid is washed twice with acetone then twice with methanol for purification purpose. After purification, the moist synthesised adsorbent is heated at 80 ℃ overnight for drying. Finally, the white powder is heated in the vacuum oven at 150 ℃ for 3 h. This activation process is aimed to further remove residual unreacted organic ligands, reagent, water vapour or any impurities. It is noted that the activation process is necessary for fully unlocking the potentials of MOFs. It is also important in minimizing the side reactions during the post-synthesis process. The whole synthesis procedure for Al-Fum is shown schematically in Figure 4.2.

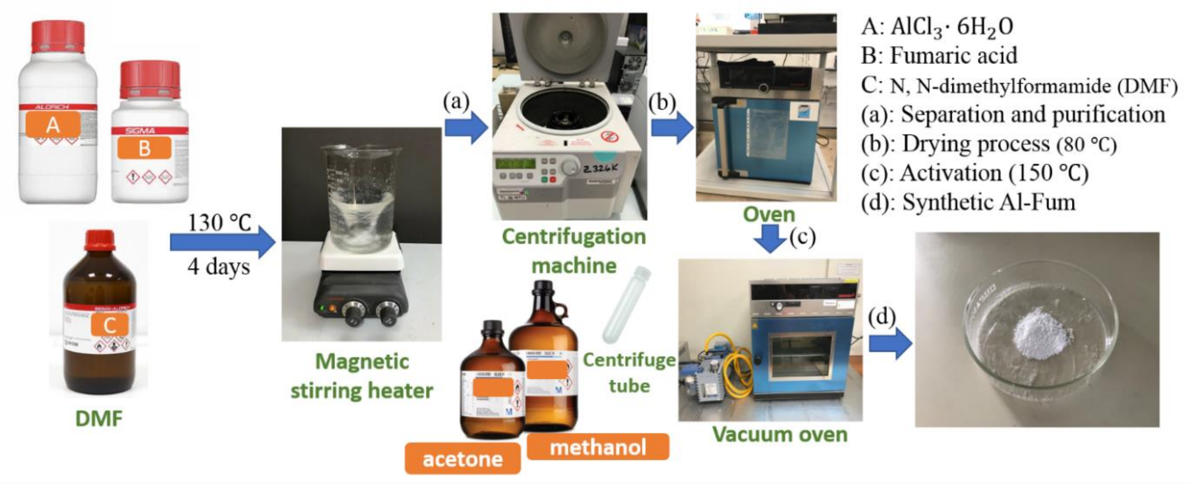

Figure 4.2: Synthesis process (reflux reaction) of MOF Al-Fum.

4.1.2 Post Synthesis

4.1.2.1 MOFs Functionalisation

The synthesis of UiO-66 (Zr) based MOFs is performed via two different methods (methods A and B). The standard UiO-66 synthesis [188] procedures are used as reference and certain modifications are conducted by different organic ligands [20].

Method A: Hydrothermal reaction method is conducted here. At first, 2.7 mmol of zirconyl chloride octahydrate ($\mathrm{ZrOCl_2 \cdot 8H_2O}$, 98%) and 2.7 mmol of terephthalate-based acid are added into the stainless autoclave. Secondly, 106 ml N, N-dimethylformamide (DMF, 98%) mixed with 5 ml formic acid ($\mathrm{HCOOH}, \geq$ 96%) are added into the mixture. After stirring 30 min at room temperature, the reactor is tightly sealed and heated at 120 °C for 24 h. Later, the mixture is separated via the filter paper. After separation, the fabricated materials are washed three times with DMF and twice with ethanol (10000 rpm, 10 min, each). Finally, the synthesised materials are dried at 80 °C.

Method B: UiO-66 based MOFs are synthesised at ambient pressure condition. At first, 2.2 mmol of zirconyl chloride octahydrate and 2.2 mmol of terephthalate-based acid are mixed in 30 ml of acidic solution (27 ml formic acid + 3 ml distilled water). The mixture is stirred under reflux for 3h and the temperature is maintained at 120 °C. The suspension is quenched under cold water at 25 °C and separated through the spinning machine. The purification process is completed by rinsing the fabricated materials with water and ethanol (8000 rpm, 20 min, twice each). Finally, the synthesised material is heated at 80 °C for drying purpose.

The terephthalate-based acid as shown in Figure 4.3 includes: terephthalic acid ($\mathrm{C_8H_6O_4}$, 98%) for parent UiO-66 (Zr); 2,5-Pyridinedicarboxylic acid ($\mathrm{C_7H_5NO_4}$, 98%) for N-UiO-66 (Zr); 2-

Hydroxyterephthalic acid ($C_8H_6O_5$, 97%) for OH-UiO-66 (Zr) and 2-Aminoterephthalic acid ($C_7H_7NO_4$, 99%) for NH_2-UiO-66 (Zr). Here, the original UiO-66 (Zr) and NH_2-UiO-66 (Zr) are fabricated via method A while OH-UiO-66 (Zr) and N-UiO-66 (Zr) are synthesised by method B.

Activation procedure is required for all synthesised materials. UiO-66 (Zr) based MOFs are placed in the vacuum oven and heated up to 155 °C (method A) or 110 °C (method B) for at least 5 h. The purification process aims to further remove any residual water vapour, reagent or unreacted acid.

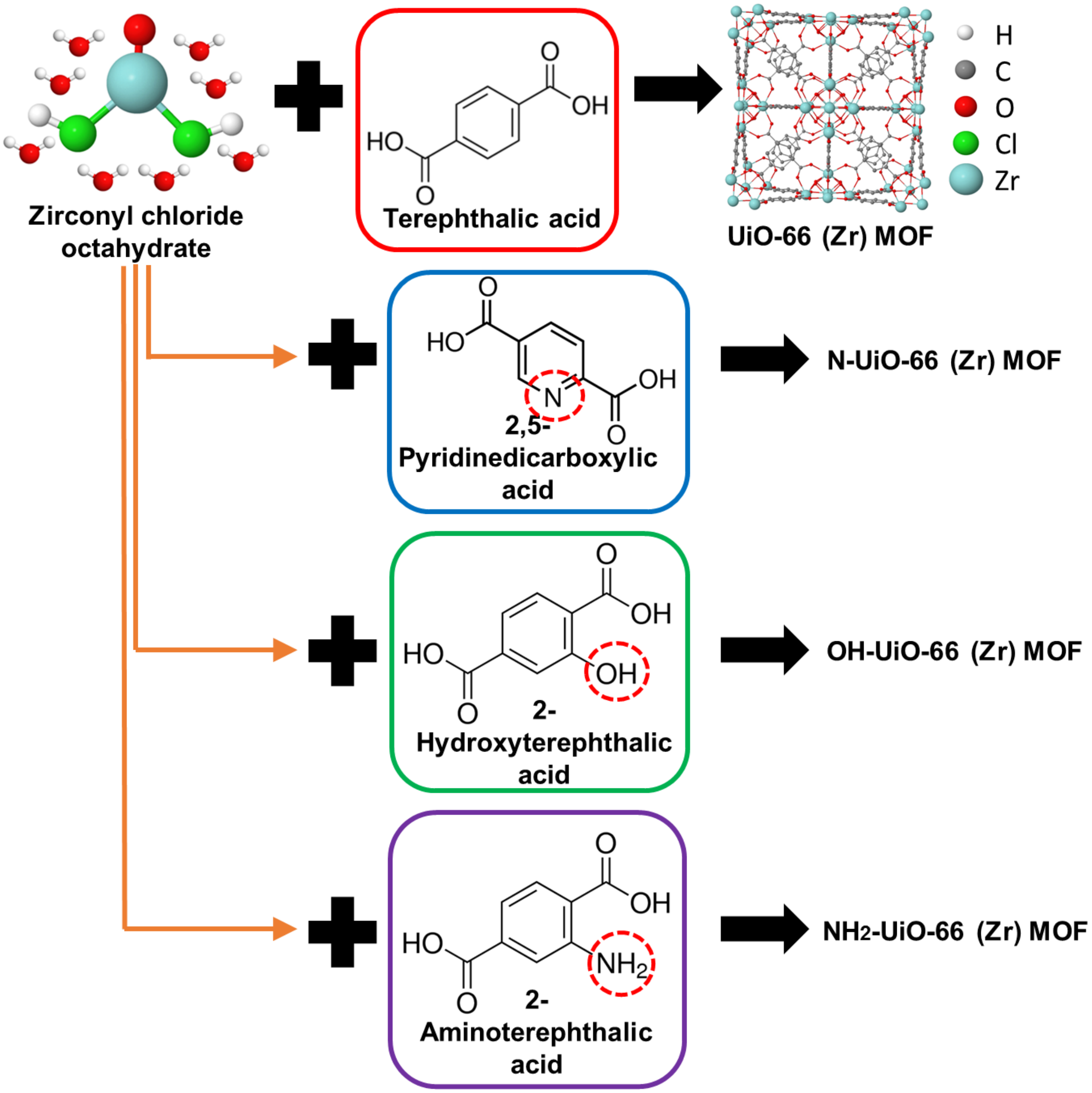

Figure 4.3: Schematic diagram of the synthesis process of the parent and methyl-functionalised UiO-66 (Zr) adsorbents.

The parent MOF-801 synthesis procedures are performed by the hydrothermal reaction method [172]. The synthesis conditions and purification processes remain the same for $(CH_3)_2$-MOF-801 except replacing the parent organic linker (Fumaric acid, $C_4H_4O_4$) with two-methyl-groups modified ligand (2,3-Dimethylfumaric acid, $C_6H_8O_4$). After synthetization, the product materials are dried overnight at 80 ℃, and then placed in a vacuum oven at 150 ℃ for 5 h. The activation process aims to remove residual water vapour, acid or any other unreacted reagent. The schematic synthesis process of the parent and methyl functionalised MOF-801 (Zr) are shown in Figure 4.4.

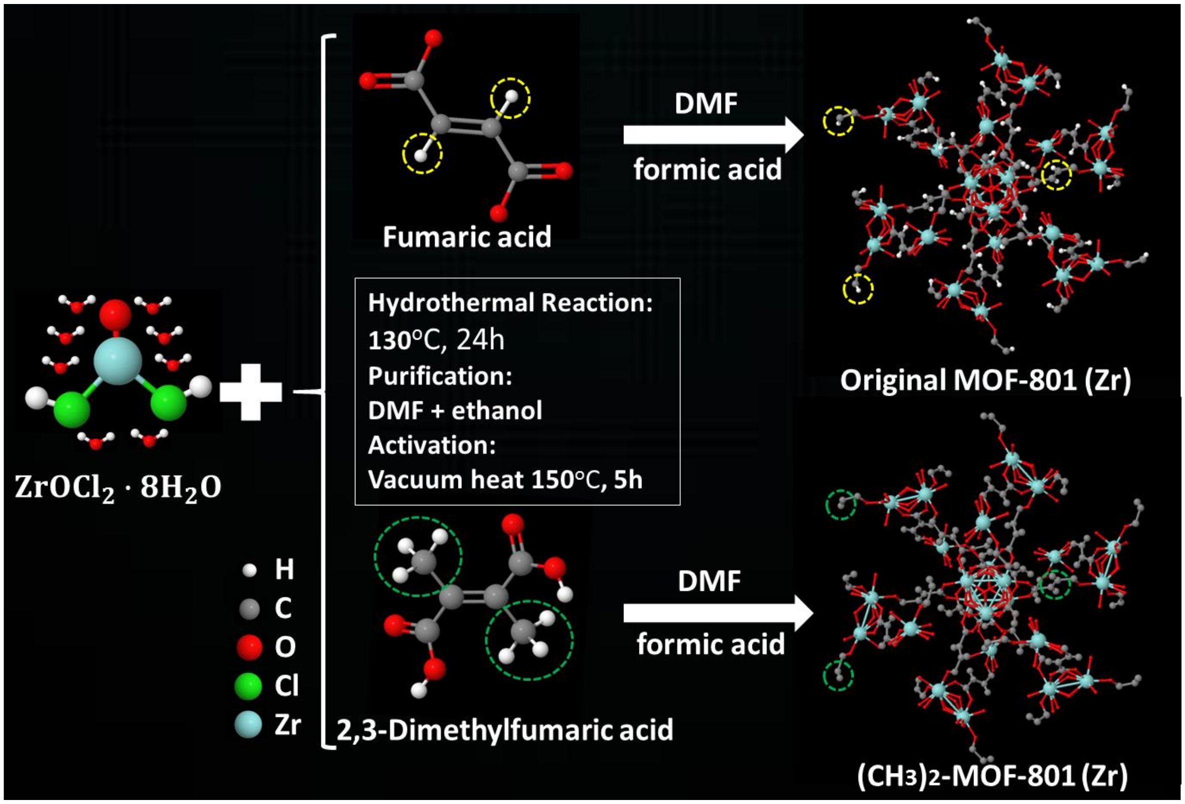

Figure 4.4: The schematic representation of the original and functionalised MOF-801 (Zr) MOFs.

4.1.2.2 MOFs Mixing or Doping

For the synthesisation of composite materials, the mixing process is conducted after the activation of original MOF Al-Fum [30]. Firstly, 2 g of synthesised Al-Fum is dissolved into 50 ml hexane (C_6H_{14}, 95%) or distilled water. Next, the suspension is stirred at 90 °C for 30 minutes and certain weight of zeolite-based adsorbent (type AFI or CHA) is added into the suspension. The mixture is stirred for one hour for complete physi-mix purposes. After stirring, the post-synthesised zeolite-Al-Fum adsorbent is extracted by the filter method and heated at 80

°C for drying. Hence, zeolite-based adsorbents with various weight concentration ratios (10%, 20%, 30%, 50%, 70%, 80%, 90%) are synthesised and tested.

The doping process is conducted after the activation [30]. 2 g of activated Al-Fum sample is added into 50 ml suspension of hexane. The suspension is stirred at 80 ℃ for 30 minutes. During the stirring process, alkali metal ions solution is poured into the suspension carefully. The alkali metal ions ($\mathrm{Li}^+, \mathrm{Na}^+, \mathrm{K}^+$) solutions contain of alkaline metal salt with 5% weight concentration and 1 ml of distilled water. After stirring, the suspension is separated and the post-synthesised doped Al-Fum is dried at 80 ℃.

4.2 Characterisation

X-Ray diffraction:

The X-ray diffraction (XRD) analysis is conducted to identify the crystallography of MOF adsorbents. The machine is fitted in 0.2 mm Cu Attenuator (detector protection of direct beam), operating at 40 kV and 40 mA, using parallel beam X-ray mirror, Cu radiation prefix. 1/6 or 1/4 degree divergence slit is recommended depends on peak max.

Scanning electron microscopy:

The microstructures, particle sizes and morphologies of the MOF materials are evaluated by the SEM (scanning electron microscopy) technique. Pre-platinum-coating work on MOF powders is performed to enhance the electrical conductivity of the sample. The investigation voltage range is 2-10 kV.

Thermogravimetric measurement:

Thermogravimetric analysis is used to measure the thermal stability of MOFs adsorbents. Before the TGA measurements, all the MOF adsorbents are dried at 80 ℃ in a vacuum oven and then exposed to the atmosphere for 24 h at ambient conditions to reach fully hydrated state. The porous sample is heated from the room temperature up to 600 ℃ with a ramp rate of 10 ℃ under a constant flow of air. The weight loss of the hydrated sample is recorded momentarily as a function of temperature. Technically, the MOF adsorbents is considered as thermally stable if no evident weight loss is observed at high temperature.

4.3 Adsorption Uptake Investigation

Generally, the amount of adsorbate uptakes under static and dynamic conditions are measured by the volumetric (manometric), the gravimetric and the dynamic flow adsorption methods. The volumetric method is used to calculate the amount of adsorptive uptakes under various pressures. The pressure changes are achieved by partial vacuum conditions within the confined-adsorbent-volume. Hence, the pressure transducers with high accuracy are required. The volumetric gas adsorption is a mature technique to characterise the porosities of adsorbent materials. Nitrogen is recommended to be the guest gas as compared with other gases such as argon, krypton or carbon dioxide for its distinct advantages. For example, nitrogen has the similar buoyancy to atmospheric air, and it is easily available. Due to its non-polar feature, the adsorption is not affected by the surface charge of the adsorbent. Furthermore, the gravimetric method is preferred for water adsorption, where the adsorption uptakes are monitored by varying the relative humidity or concentration of water vapour and measuring the mass change of the adsorbent.

4.3.1 Nitrogen Adsorption

The N_2 adsorption/desorption experiment are conducted by Autosorb instrument at 77 K to determine the average pore size, total pore volume, specific surface area and pore size distribution of the MOF adsorbents. The outgassing station, analysis station and the main instrument accessories of the N_2 adsorption apparatus are shown in Figure 4.5. To remove any undesirable adsorbed vapours and water, the sample is outgassed at 160 ℃ for 3 h before N_2 adsorption experiment. The N_2 isotherms data can be deduced to calculate adsorbent-surface area by using BET (Brunuer-Emmet-Teller) equation, and total pore volume is obtained under saturation conditions ($P/P_s = 1$), which is equivalent to the total liquid N_2 adsorbed in the MOF sample. The liquid volume is calculated by $V_{liq} = \frac{P_a V_{ads} V_m}{RT}$, where P_a is the ambient pressure, V_{ads} is the volume of N_2 adsorbed, V_m is the molar volume of liquid of N_2 with a value of $3.47 \times 10^{-5}\ \mathrm{m^3/mol}$, R defines the gas constant and T is the temperature. Moreover, the average pore size (r_p) is calculated by $r_p = \frac{2V_{liq}}{A_s}$, where A_s is the BET surface area of the adsorbent sample.

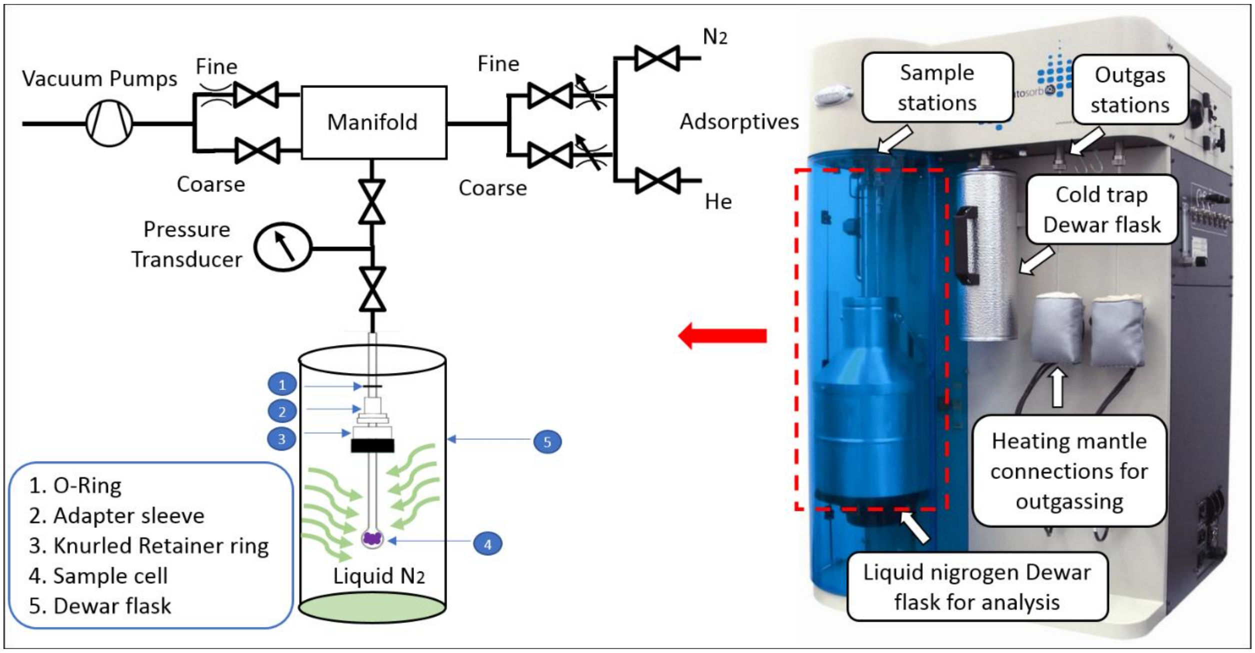

Figure 4.5: Main components and schematic diagram of N_2 adsorption machine.

4.3.2 Water Adsorption

The amount of water adsorbed/desorbed on MOFs samples at different pressures ($0 < P/P_s < 1$) and temperatures (from 25 °C to 70 °C) are measured by a thermogravimetric analyser (TGA) as shown schematically in Figure 4.6. The TGA machine is made up of six main components: microbalance, balance purge, humidifier, sample cell, pumps and temperature humidity probe. At the very beginning of the experiment, the purified and water-free MOFs sample is placed on the sample cell, which is held by the microbalance. The microbalance with a maximum load capacity of 5g (± 0.1 μg) is located at the top of the temperature-colltrolled chamber. The sample cell and the microbalance are connected by an extension wire which makes the TGA give a direct mesearment of adsorbate uptake during the adsorption and desorption processes. The mass gain or loss of MOFs sample are measured by the microbalance and the recorded data are then deduced to the adsorption isotherms. The water adsorption experiment is conducted under various relative humidity or relative pressure (P/P_s) under isothermal condition over time. The temperature sensor (class A RTD, accuracy ± 0.15 °C) is installed inside the TGA, and by controlling the furnace heating system, the isothermal condition is maintained. To maintain pressure same inside the TGA apparatus, the adsorption system is evacuated and purged by the vacuum pump at the beginning of experiment. Maintaining the temperature and regulate the relative pressure inside the chamber are considered as two key procedures for adsorption experiment. Before the experiment, the adsorbent materials are heated at 80 °C by a heater as installed hermetically around the reaction chamber.

The termperaure is regulated by the balance process employing the combination of radiant heater heat and the cooling air flows into the chamber. To prevent possible condensation effects, the temperature of adsorption chamber is maintained 15 °C higher than the experimental conditions of the gravimetric apparatus. The dry nitrogen (99.999% purity) is continuously supplied across the adsorption chamber to maintain the control of the microbalance buoyancy effect and to remove the residual moisture on the MOFs adsorbents. On the other hand, the relative humidity is controlled by regulating the flow of dry nitrogen into the chamber and is measured by the humidity probe. When the relative humidity is lower than the expected value, the flow of nitrogen flow additional water vapour (generated from the humidifier) is supplied to the adsorption chamber. On the other hand, dry nitrogen is injected to the adsorption chamber when the relative humidity of water vapour is higher than the desired value. Thus, the relative pressure is controlled experimentally in the adsorption chamber. During the adsorption process, the overall mass of the adsorbent sample is increased as water vapour adsorbs onto the adsorbent. The change of mass in the adsorbent-adsorbate system is detected and recorded by the build-in microbalance. The mass of the water vapour adsorbate is given by $m_{a,i} = M_s(P_i) - M_s(P_0)$, where $M_s(P_0)$ is the initial known mass of the MOF-sample, and $M_s(P_i)$ is the overall sample mass as a function of pressrue. In addition, the gravimetric water uptake is measured by $q_i = m_{a,i}/M_s$. During adsorption process, the mass changes are varied from the transient to steady state, and all uptake values are recorded by the build-in software, and they could be deduced to analyse the adsorption isotherms, kinetics and the isosteric heat of adsorption under dynamic and equilibrium conditions.

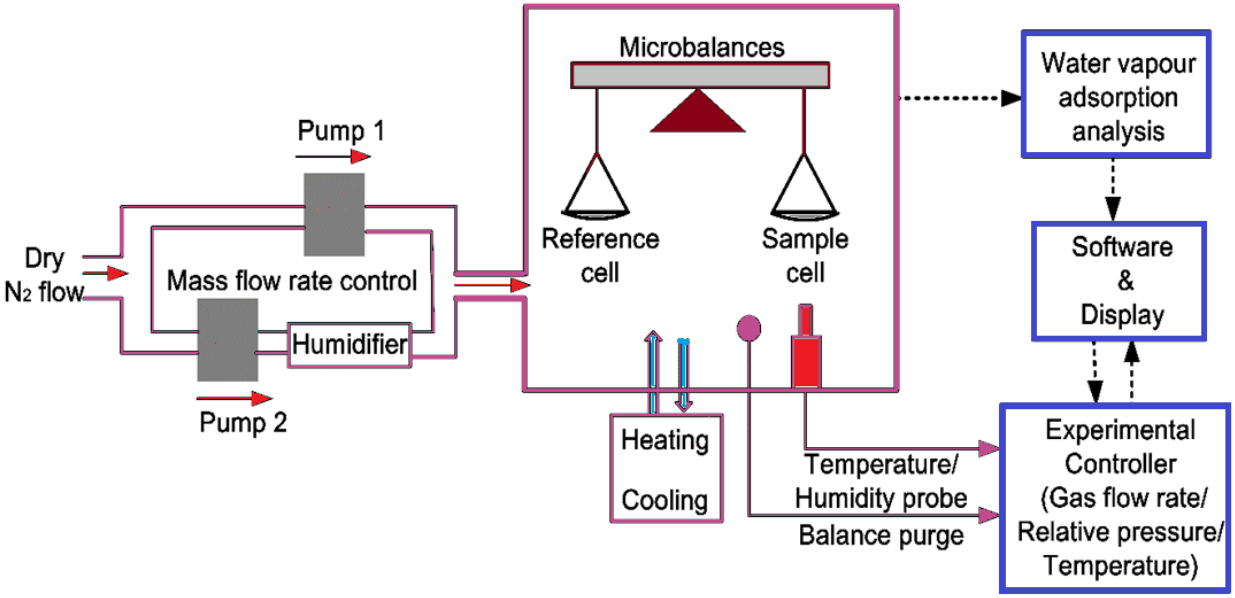

Figure 4.6: Schematic representation of the gravimetric apparatus for the measurement of water adsorption isotherms and kinetics.

4.4 Results and Discussion

4.4.1 Surface Characteristics

4.4.1.1 Functional UiO-66 (Zr) MOFs

Power X-ray diffraction (PXRD)

The PXRD (Power X-ray diffraction) graphs of the parent and functionalised UiO-66 MOFs are shown in Figure 4.7. The modified MOFs exhibit the similar XRD trends as compared with the original UiO-66 (Zr) which synchronises with the standard shape [132]. Therefore, the MOFs are fabricated properly and the structure integrity are not distorted by the addition of functional groups. The distinct reflection is found at around 7.5° for UiO-66. Minor peak divergences are observed for the modified materials, which may be caused by the functional group additives. A further finding is that comparing with other MOFs, N-UiO-66 MOF exhibits extra peaks at certain degrees, which proves that the synthesis approach affects the MOF crystallography weightily. Hence, all the UiO-66 based MOFs generate stable structures.

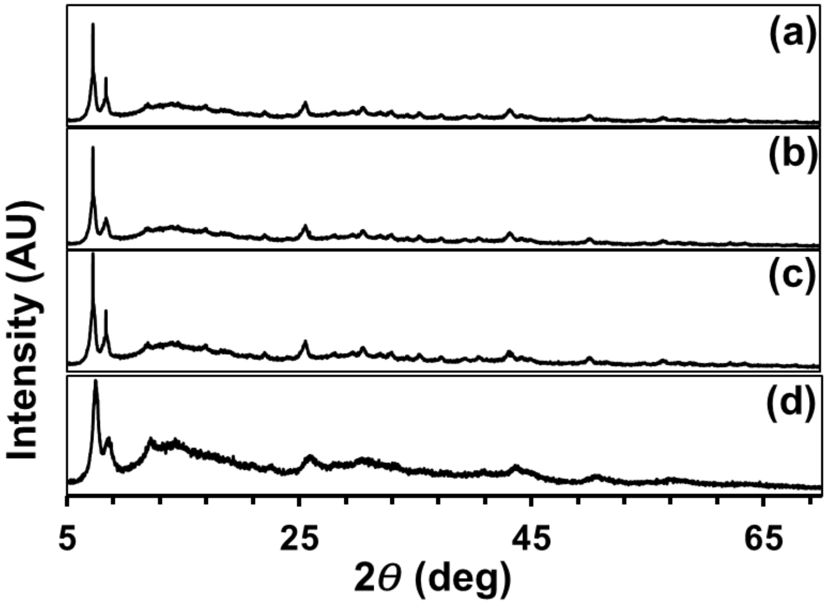

Figure 4.7: The X-ray diffraction (XRD) results of original and functionalised UiO-66 MOFs. Here, (a) UiO-66, (b) N-UiO-66 (c) NH_2-UiO-66, (d) OH-UiO-66.

Thermogravimetric Analysis (TGA)

The thermal stability of the parent and functionalised UiO-66 MOFs are shown in Figure 4.8. The multi-step profiles of TGA provide necessary information on MOFs-porosity, heat resistance and even the water dehydration dynamics. Generally, a three-stage weight loss of all MOFs materials are found from 30 ℃ to 600 ℃. The initial weight loss is attributed to the departure of water molecules and it mainly occurs between the temperatures of 45℃ to 80℃. UiO-66 (Zr) MOF starts the first stage weight loss at the lowest temperature of 45℃ as compared with other samples, suggesting that the physi-bonding interaction between UiO-66 MOF and water molecules is the weakest.

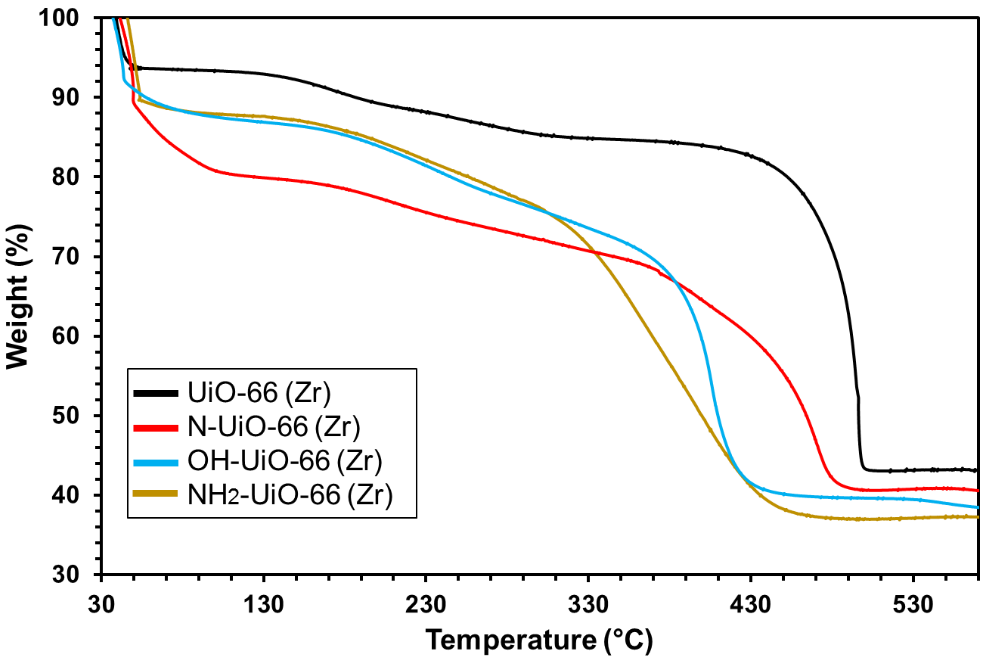

Figure 4.8: TGA analysis for the thermal stabilities of the original and functionalised UiO-66 (Zr) based MOFs adsorbents.

Furthermore, N-UiO-66 MOF shows the highest weight loss (19%) during the first stage, indicating that it generates the largest pore volume among all the functionalised materials, which concurs well with pore size analysis as shown in Table 4.1. Subsequently, the deeper dehydration process takes place and more water molecules are released from the inner pore of adsorbents. The second weight loss process mainly occurs between temperatures 100 ℃ and 135℃, which are higher than the boiling point of water. Another 10% weight loss of functionalised UiO-66 MOFs suggests the plentiful of micro-pores inside the samples. As the temperature increases, the MOF-structure collapses and decomposition takes place. A final weight decrement is observed. Among all the three weight loss stages, it is observed that majority of weight loss occurs at the first stage, which indicates that water vapours are mostly adsorbed in the outer cages of UiO-66 based MOFs structure. In addition, the critical temperature at final stage of weight loss for UiO-66 (Zr), N-UiO-66, OH-UiO-66, and NH_2-UiO-66 are 510.7℃, 479.2 ℃, 429.6 ℃ and 450.1℃, respectively. Hence, the thermal stability of UiO-66 MOF is slightly degraded by the implantation of multiple functional groups. Nonetheless, functionalised UiO-66 MOFs are thermal stabilised materials.

Scanning electron micrography (SEM)

SEM (Scanning Electro-Microscopy) plots are shown in Figure 4.9. The size of the sample is about 1 μm with octahedral shape. Obvious agglomeration behaviours are found for all the nanocrystals, which is similar to another Zr-based MOFs, named MOF-801. Some minor irregular microcrystalline polyhedral are observed for the functionalised UiO-66 MOFs, which may be due to the presence of unreacted terephthalate-based acid within the materials as the purification work was not completed after the functional group implantation process. Nonetheless, the morphologies of the UiO-66 (Zr) MOFs are not destroyed by the introduction of functional group additives.

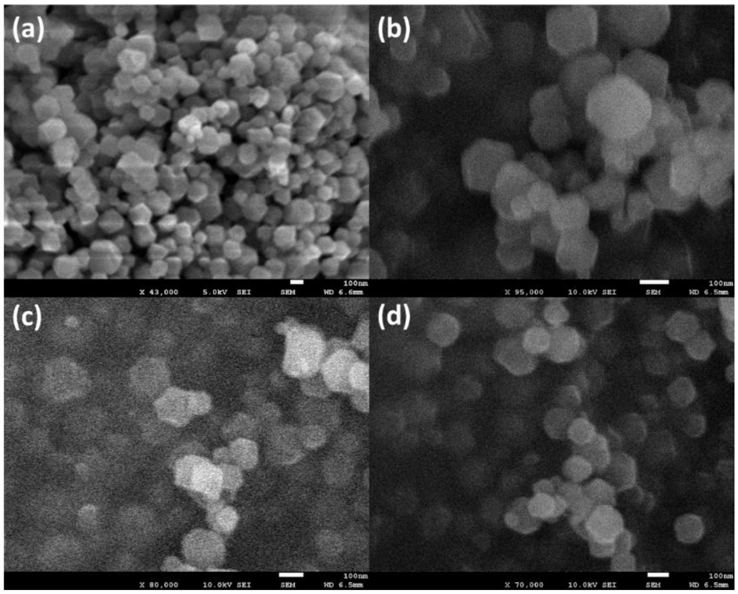

Figure 4.9: Scanning electron micrography (SEM) of functionalised UiO-66 MOFs: (a) UiO-66, (b) N-UiO-66, (c) NH_2-UiO-66 and (d) OH-UiO-66.

N_2 Adsorption for measuring pore size distribution

The porous characteristics such as the BET surface area, average pore size and pore volume of the assorted adsorbents are furnished in Table 4.1. It is found that the BET surface area and the pore volume of the parent UiO-66 (Zr) is decreased with the addition of functional groups. Furthermore, N-UiO-66 (Zr) shows the largest BET surface area and pore volume whilst OH-UiO-66 (Zr) exhibits the smallest among all the functional UiO-66 (Zr) MOFs.

Table 4.1: Surface characteristics (BET surface area, average pore radius and pore volume) of original and functionalised UiO-66 (Zr) based MOFs.

Samples	BET surface area (m^2/g)	Average pore radius (Å)	Pore volume (cm^3/g)
UiO-66 (Zr)	1296.8	10.74	0.54
N-UiO-66 (Zr)	1162.9	10.68	0.46
NH_2-UiO-66 (Zr)	979.2	10.87	0.44
OH-UiO-66 (Zr)	646.0	11.25	0.33

4.4.1.2 Functional MOF-801 (Zr)

Power X-ray diffraction (PXRD)

The PXRD (Powder X-ray diffraction) diagrams for the original and functionalised fumarate-based MOFs are illustrated in Figure 4.10. The functional MOF-801 shows the same XRD trends as compared with the parent adsorbents, which is proposed by Kim et al. [36], which means that the MOFs are synthesised properly and the functional group additives do not destroy MOFs' structure integrity. The distinct reflection is observed at around 8.65° for MOF-801 and $(CH_3)_2$-MOF-801. The peaks correlate the intensity of Zr ions. Few additional peaks at certain angles are observed for the functionalised MOFs and it may be due to the unreacted metallic precursor acid within the adsorbents as inadequate purification work are performed after the synthesisation process. Nonetheless, the adsorbent with methyl functional groups is a stable structure.

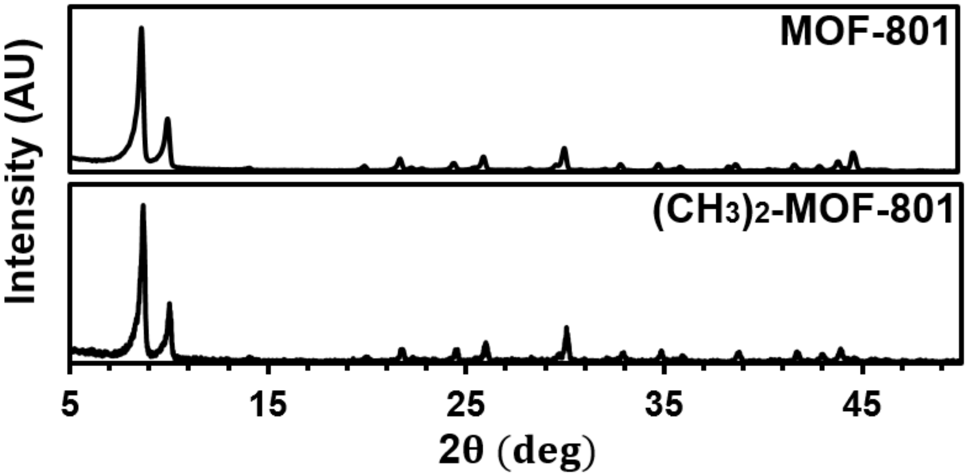

Figure 4.10: The X-ray diffraction (XRD) results of $(CH_3)_2$-MOF-801. The XRD of the original MOF-801 are shown for comparison purpose.

Thermogravimetric Analysis (TGA)

Figure 4.11 shows the TGA profiles of the parent and functionalised MOFs materials. Hence, three stages of weight loss are observed with the increase of temperature. The first stage of weight loss correlates to the departure of water molecules from outer cages of adsorbent and it occurs mainly between the temperatures of 50 and 80 ℃. $(CH_3)_2$-MOF-801 shows the lowest weight loss (14%), suggesting that it has the smaller pore volume, which is consistent with the N_2 adsorption results as shown in Table 4.2. The weight loss of the MOF-801 based adsorbents between 80 to 260 °C is mainly due to the water vapours release from the inner pores. As the temperature keeps increasing (260 to 400 ℃), the decomposition of the linkers occurs [190] and slight weight losses are found for both parent and methyl functionalised MOF-801. Hence, the final major weight loss as a result of the porous material decomposition is observed at higher temperature. The final major weight loss processes of MOF-801 and $(CH_3)_2$-MOF-801 occur at the temperatures of 355 and 380 ^oC, respectively. Hence, the thermal stability of the parent MOF-801 (Zr) is slightly enhanced by the methyl functional group implantation process. It should be noted that the thermal stability test was performed before and after water adsorption test, and same profiles were obtained for both cases.

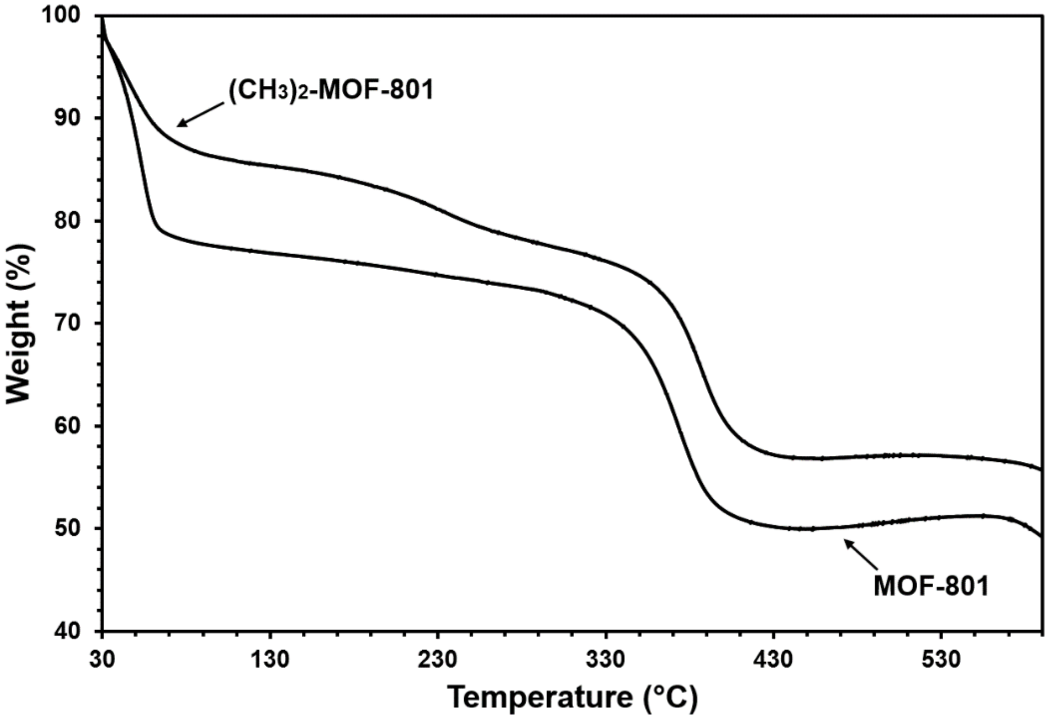

Figure 4.11: TGA analysis for the thermal stabilities of the original and functionalised MOF-801 based MOFs.

Scanning electron micrography (SEM)

Figure 4.12 shows the SEM diagrams for fumarate-based MOFs. The shape and the size of the $(CH_3)_2$-MOF-801 sample are similar to those of the original Al-Fum. In addition, strong agglomeration behaviours are observed for both MOF-801 and $(CH_3)_2$-MOF-801 with typical rounded particle presents. Therefore, the morphologies of the MOFs are not disrupted by the addition of methyl functional groups.

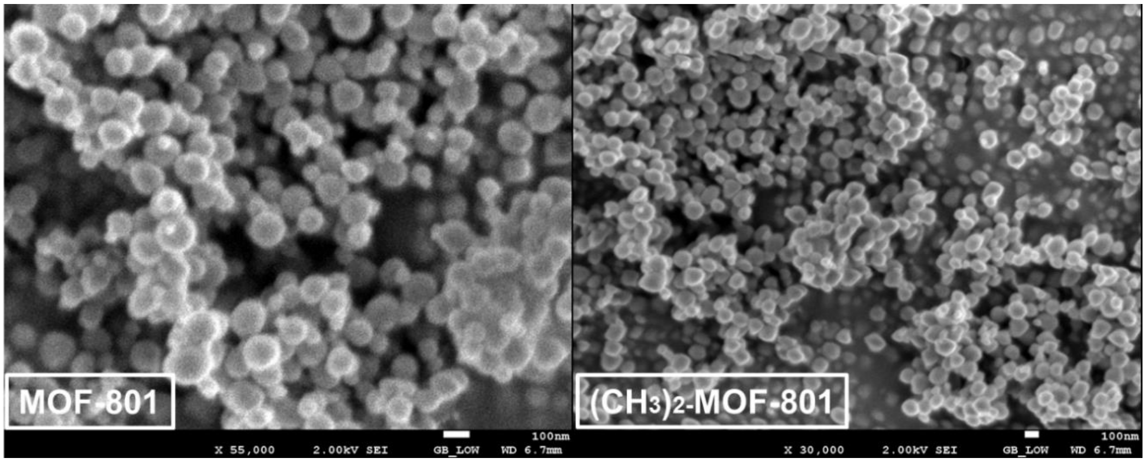

Figure 4.12: Scanning electron micrography (SEM) of functionalised fumarate-based MOFs: MOF-801 and $(CH_3)_2$-MOF-801 (from the left side).

N_2 Adsorption for measuring pore size distribution

Table 4.2 shows the porosities of the original and methyl-functionalised MOF-801 (Zr). It is found that by implanting methyl functional groups into the parent MOF-801 (Zr) structure, the BET surface area decreases from 864.0 m^2/kg to 756.2 m^2/kg and the pore volume decreases from 0.37 cm^3/g to 0.3 cm^3/g.

Table 4.2: N_2 adsorption analysis (BET surface area, pore volume and average pore radius) of original and functionalised MOF-801 (Zr) based MOFs.

Samples	BET surface area (m^2/kg)	Pore volume (cm^3/g)	Average pore radius (Å)
MOF-801	864.0	0.37	10.8
$(CH_3)_2$-MOF-801	756.2	0.30	11.0

4.4.1.3 Al Fumarate and MOF-Zeolite Composites

Thermogravimetric Analysis (TGA)

Figure 4.13 shows the TGA graphs of the 5% doped Li^+, Na^+, K^+ Al-Fum, 30% mixed AFI/CHA-Al-Fum and original aluminium fumarate (Al-Fum) for comparison purposes. Generally, all samples as presented in Figure 4.18 provide three-stages of weight loss for the temperature increasing from 30 °C to 550 °C. The weight loss for the first stage is due to the water vapour release from the outer cage of Al-based adsorbents. The weight loss for the second stage is the result of water vapour release from the sample-inner cage. After that, the final weight decrement is due to the collapse of the material porous structure. The final weight loss process for all the post-synthesis Al-Fum occurs around the temperature range from 400 ℃ to 450 ℃, which is lower as compared with the parent Al-Fum (around 460 ℃). Hence, the post-synthesis process slightly reduced the thermal stability of Al-Fum.

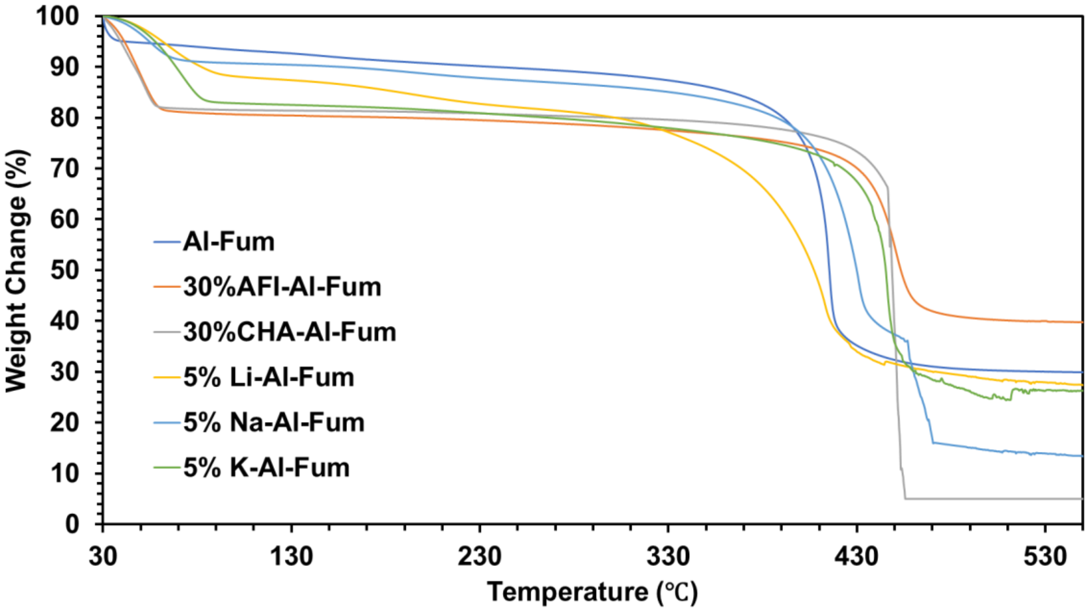

Figure 4.13: TGA analysis for the thermal stability of original and post-synthesis Al-Fum MOF adsorbents.

Scanning electron micrography (SEM)

Figure 4.14 shows the SEM (Scanning Electro-Microscopy) for parent Al-Fum and the post-synthesis Al-Fum (5% doped Li^+, Na^+, K^+ and 10%, 50%, 90% mixed AFI/CHA). The shape and pore size of the alkali metal cations doped samples are similar to the parent Al-Fum samples, which means that the pore structure of Al-Fum is not distorted by the doping process. The coexistence of quadra-hedral and rod-like shape in the 50%AFI/CHA-Al-Fum sample indicates that there is only homogenous physical mixing inside the samples without any chemical reaction.

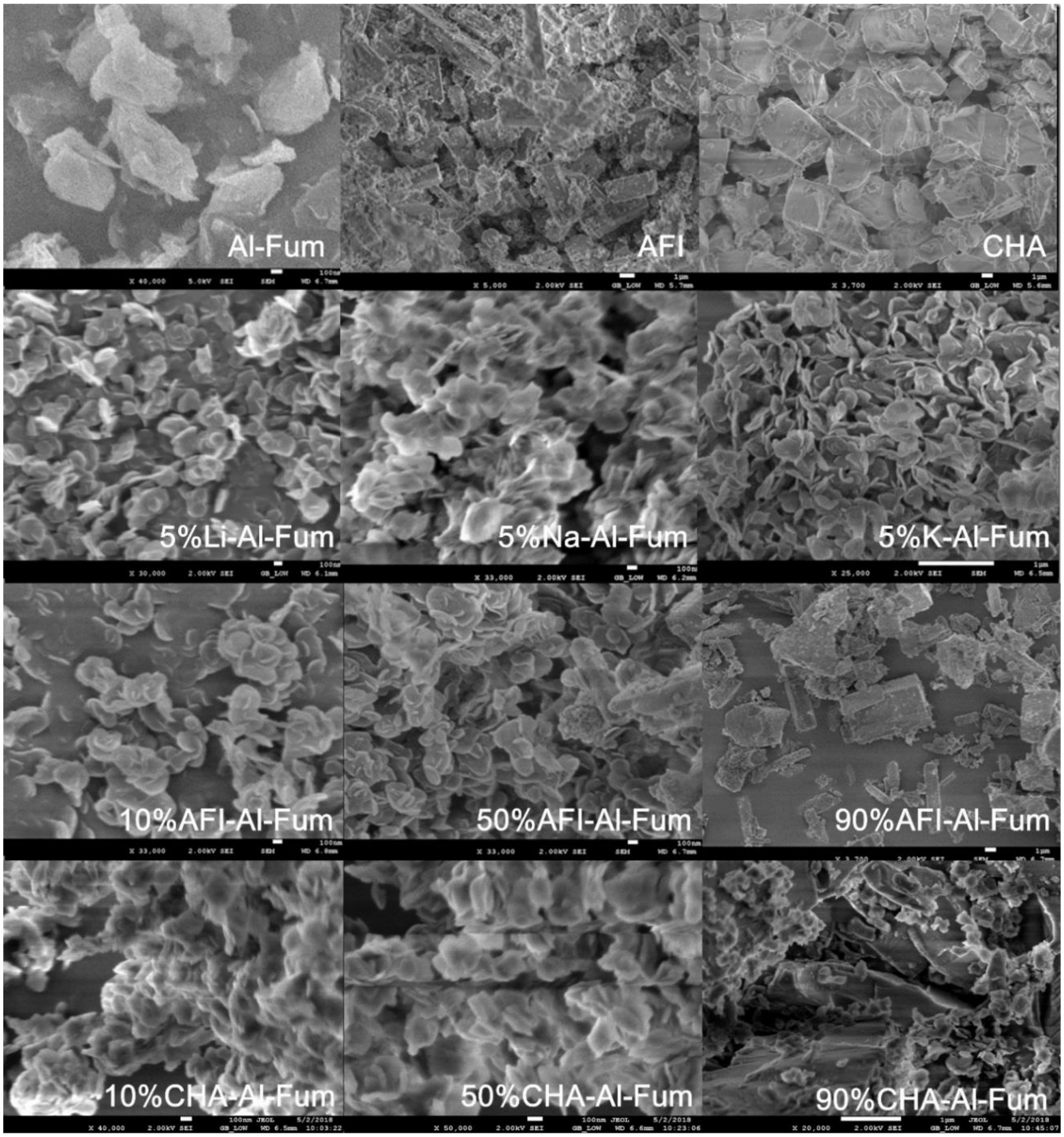

Figure 4.14: Scanning electron micrography (SEM) of Al-Fum (top left), AFI (top middle) and CHA (top right). The second row shows the SEMs of 5% Li^+, Na^+ and K^+ doped Al-Fum (from the left side). The third row shows the SEMs of 10%, 50% and 90% AFI mixed Al-Fum (from left side). The fourth row shows the SEMs of 10%, 50% and 90% CHA mixed Al-Fum (from left side).

N_2 Adsorption for measuring pore size distribution

Based on N_2 adsorption results, the BET surface area, the pore volume and average pore radius of all samples are calculated and listed in Table 4.3. As can be seen from Table 4.3, the micro-structure properties of alkali metal ions doped Al-Fum are nearly the same (BET surface area $\approx$1060 m^2/g, pore volume $\approx$ 0.43 cm^3/g and pore size $\approx$ 11.78 Å). However, mixing different amounts of AFI/CHA zeolite result in different BET surface areas with a range from 598 m^2/g to 1089 m^2/g.

Table 4.3: N_2 adsorption analysis (BET surface area, pore volume and average pore radius) of samples.

Samples	BET surface area (m^2/kg)	Pore volume (cm^3/g)	Average pore radius (Å)
Al-Fum	1093.3	0.93	11.75
Li-Al-Fum (5%)	1061.4	0.43	11.80
Na-Al-Fum (5%)	1061.7	0.44	11.78
K-Al-Fum (5%)	1059.8	0.43	11.78
AFI-Al-Fum (10%)	1089.4	0.45	11.78
AFI-Al-Fum (30%)	822.0	0.34	11.79
AFI-Al-Fum (50%)	598.4	0.25	11.78
CHA-Al-Fum (10%)	1058.7	0.87	11.84
CHA-Al-Fum (30%)	983.5	0.76	11.83
CHA-Al-Fum (50%)	905.8	0.58	11.84

4.4.2 Water adsorption Isotherms and Kinetics

4.4.2.1 Functional UiO-66 (Zr) Plus Water

The amount of water uptakes on functionalised (-N, -OH, -NH_2) and original UiO-66 MOFs at 25 ℃ for the pressures varying from Henry’s region to the capillary condensation zone are shown in Figure 4.15 (a)-(b). Water adsorption experiments are conducted at least three times under same operating conditions for the reliability purpose. Moderate hysteresis behaviours are found and it is caused by the incomplete desorption process with residual water molecules trapped in MOFs inner pores. Hence, the black solid line indicates the parent UiO-66 and the colour dotted lines represent the functionalised materials. As shown in Figure 4.15, the parent UiO-66 provides a typical “S-shaped” isotherm with a relatively high limiting water uptake (q^0) of 0.49 kg/kg (or g/g of adsorbent). However, UiO-66 exhibits extremely long step pressure region ($0 < P/P_s < 0.4$) and very little amount of water vapour is adsorbed in the low pressure region. It is notable that by introducing various functional group additives, all the modified UiO-66 materials present the revised isotherms and capture water molecules in the low pressure region.

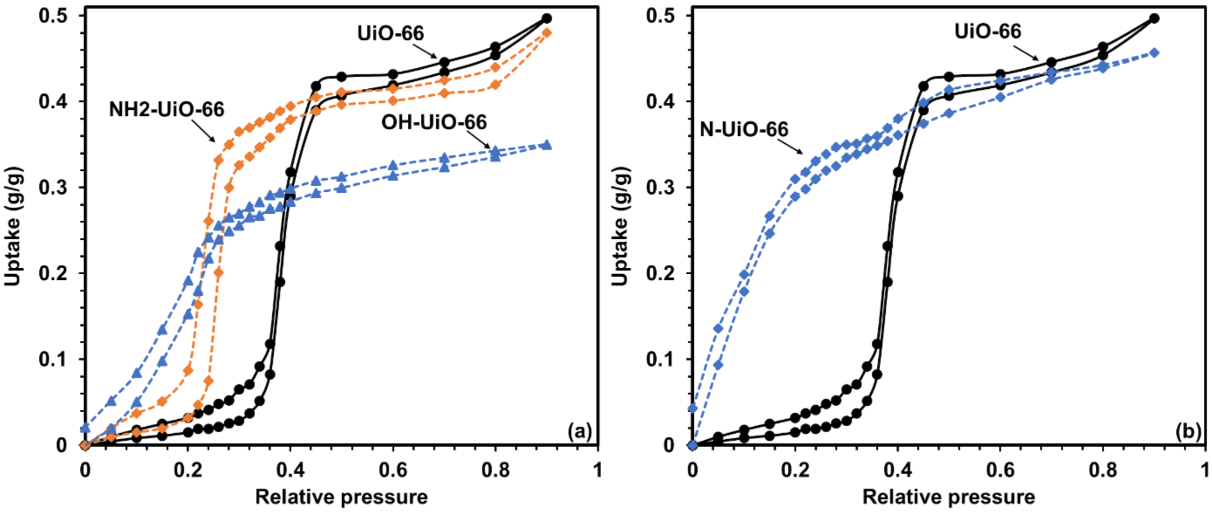

Figure 4.15: Water adsorption-desorption isotherm of functionalised MOFs (a): NH_2-UiO-66 and OH-UiO-66 (b): N-UiO-66 (colour dotted line) at 25 ℃. The original UiO-66 isotherms [both in (a) and (b)] are shown (black solid line) for comparison purpose.

NH_2-UiO-66 (Zr) shows the similar water adsorption isotherm shape as the parent UiO-66 (Zr). However, it provides a shorter hydrophobic length ($P/P_s \approx 0.20$). The isotherm for OH-UiO-66 + water adsorption system is similar to another zirconium-based adsorbent MOF-801, which is studied by Kim et al. [36], which resembles a transition from “type I” to “type V” isotherm with a limiting uptake of 0.34 g/g (of adsorbent). Furthermore, due to the intense hydrophilic adsorbent-adsorbate interaction at $P/P_s < 0.10$, abundant adsorption of water molecules on N-

UiO-66 takes place and a “type I” adsorption isotherm is found, which ties well with previous studies [143]. It is important to highlight here that the maximum water uptakes of all the functionalised materials are smaller as compared with that of the parent UiO-66 (Zr). A reasonable explanation of this phenomenon is that the functional group such as amino additives may cause a smaller pore volume of MOFs and block the water molecules from adsorbed onto the pore site at high pressure region (pore-block effect). This explanation is consistent with $\mathrm{N_2}$ adsorption analysis. All the functionalised UiO-66 MOFs enhance the hydrophilicity and achieve more water uptakes at low pressure region. The reduction of the step pressure region suggests a higher water uptake-offtake difference (Δq) and makes it possible for UiO-66 based MOFs to be used in low temperature heat transmission applications such as adsorption chiller.

The amount of water uptakes on the parent and functionalised ($\mathrm{-N, -OH, -NH_2}$) UiO-66 MOFs are presented in Figure 4.16 (a) – (d) for the temperatures of 25 °C, 35 °C, 45 °C, 60 °C, 75 °C and 80 °C, where the adsorption-desorption process of a thermal compressor (adsorption bed) is plotted. In an ideal thermal compression system (a-b-c-d), the pressure varies from 1 kPa to 5 kPa whilst the temperature swings from 25 °C to 60 °C / 80 °C, from which one can calculate the amount of water transfer, Δq (= $q_{ads} - q_{des}$) per cycle of an AHT. Under adsorption chiller operating conditions (adsorption-triggered-evaporation at 25 ℃ and 1 kPa; desorption-activated-condensation 60 ℃-80 ℃ with 5 kPa), the Δq per thermal compression cycle of the original UiO-66 (Zr) MOF + water system is found the lowest (Figure 4.16 (a)) due to the strong hydrophobic behaviour in UiO-66 (Zr) at lower evapourative pressure (≤ 1 kPa). Therefore, very low cooling power is produced even at higher desorption/regeneration temperature (> 80℃).

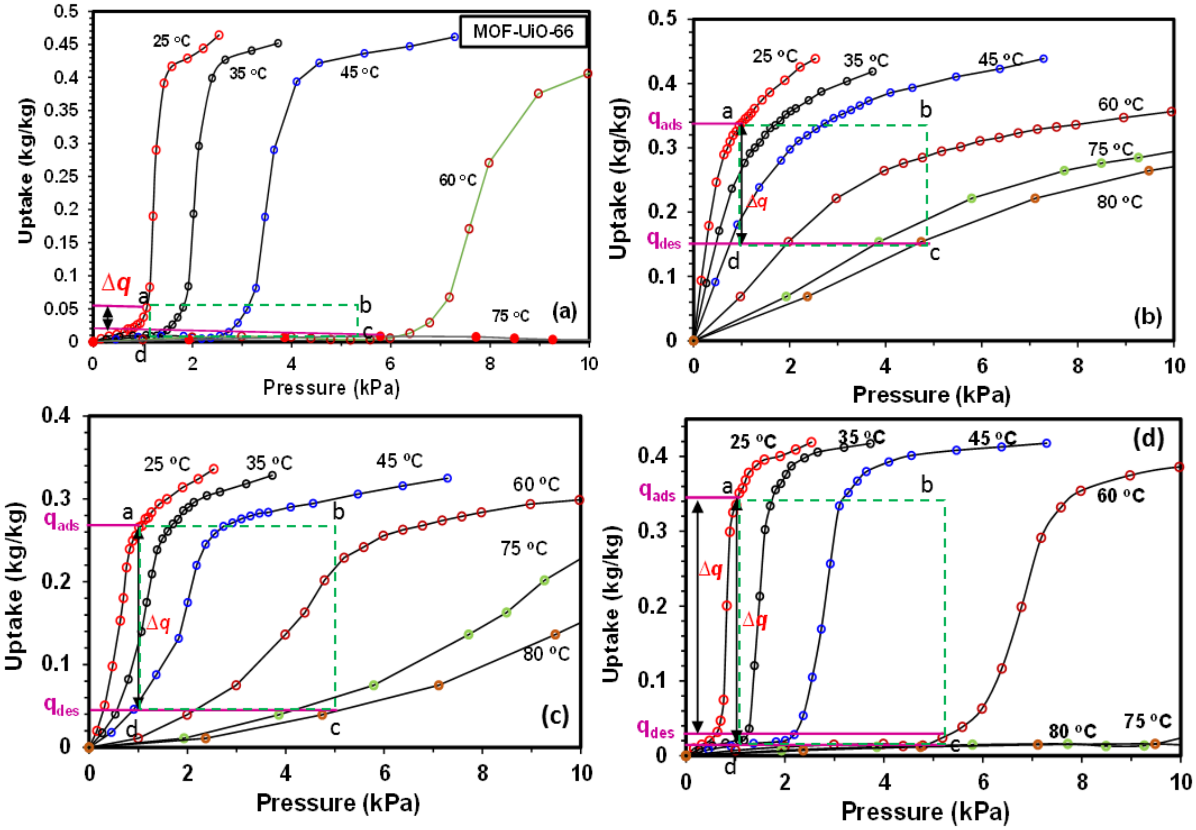

Figure 4.16: Adsorption isotherms of water vapour on (a) UiO-66 (Zr), (b) N-UiO-66 (Zr), (c) OH-UiO-66(Zr) and (d) NH_2-UiO-66 (Zr) MOFs for the temperature ranging from 25℃ to 80 ℃. Here a = adsorption and c = desorption.

The superior Δ*q* results are obtained with the addition of functional groups in MOF structure. As can be seen from Figure 4.16 (b) that at relatively higher desorption temperature (~80 °C), N-UiO-66 (Zr) MOF shows slightly higher Δ*q* as it represents type I isotherm curves. Hence, N-UiO-66 (Zr) MOF delivers considerable Δ*q* at the desorption temperature of 80 ℃. However, the Δq is very small at 60 °C. On the other hand, Figures 4.16 (c) and 4.16 (d) show type V isotherms, when the functional groups –OH and – NH_2 are added to the original UiO-66 (Zr) structure employing hydroxy-terephthalic acid/ amino-terephthalic acid instead of terephthalic acid. Hence, for both OH-UiO-66 (Zr) and NH_2-UiO-66 (Zr) MOFs, a short hydrophobic length is obtained at 298 K (25 °C) with the relative pressures of 0.1 to 0.3. The Δ*q* for –NH_2-UiO-66 is found 0.31 kg/kg (Figure 4.23(d)) at the desorption temperature of 60 ^oC. The main reason is that –NH_2 functional group donates H mole to the framework of the amine functionalised UiO-66 (Zr). Additionally, the amino group provides a positive charge for the interaction with the negatively charged materials plus partially negatively charged ‘O’ of water molecule by the electrostatic interactions. A slightly higher Δq (0.18 kg/kg at 80 ^oC desorption temperature) is found for OH-UiO-66 (Zr) as compared to the parent UiO-66 (Zr) MOFs. Hence, the hydroxyl group (-OH) strengthens the water – MOFs interactions due to the presence of electron donating group. Therefore, the addition of -OH increases the hydrophilic behaviour in UiO-66(Zr) adsorbent i.e. the Δq values are increased sharply under adsorption chiller/heat pump operating conditions.

The experimental data for water uptakes on UiO-66 (Zr) based adsorbents shown in Figure 4.16 could be deduced to the isosteric heat of adsorption. Figure 4.17 shows the isosteric heat of adsorption (Q_{st}) for the original and functionalised UiO-66 (Zr) + water systems based on Clausius - Clapeyron relation $dln(P)/dT = -Q_{st}/RT^2$ [191] with a wide temperature range from 25 ℃ to 75 ℃, where T represents the experiment temperature, P indicates the adsorption pressure and R is the gas constant for water. As shown in Figure 4.17, a rapid increase of Q_{st} for NH_2-UiO-66 (Zr) is found at low water uptake region, which is due to the fast adsorbed process of the water molecules onto the higher energy pore sites of the NH_2-UiO-66 (Zr) framework. A relative steady Q_{st} level is found for the water uptakes from 0.05 kg/kg to 0.3 kg/kg for all the adsorption systems. This is because of that as the adsorption process continues, more water molecules are adsorbed onto lower energy sites. On the other hand, an increase in $\mathrm{Q_{st}}$ is observed for both UiO-66 (Zr), N-UiO-66 (Zr) and NH_2-UiO-66 (Zr) MOFs near the saturation states as the interactions between water molecules are increased. On the other hand, the slight drop of the Q_{st} for OH-UiO-66 (Zr) at the saturated region is related to the combination of meso and macro pore structures.

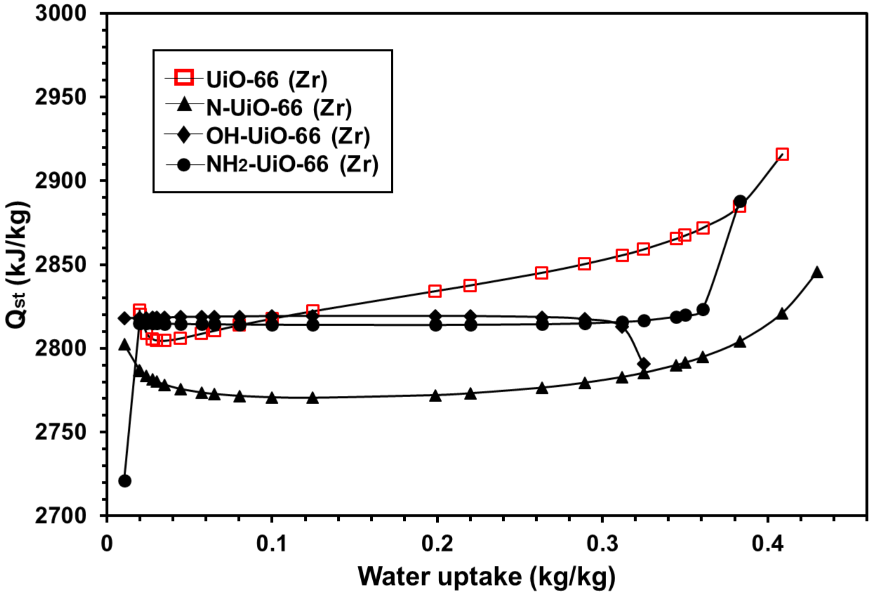

Figure 4.17: Isosteric heats for the adsorption of water on original and functionalised UiO-66 (Zr) for temperature from 25 ℃ to 75 ℃.

The functional group also affects the required time for thermal compression of adsorption-assisted heat transformation system and the plots of water uptakes and offtakes against time for both the parent and functionalised (-N, -OH, -NH_2) UiO-66 MOFs are shown in Figure 4.18 (a – d). Hence the kinetics are presented in terms of the adsorption and desorption conditions of an adsorption cooling system (adsorption –evaporation occurs at 1 kPa and 25℃ and desorption-condensation occurs at 5 kPa and 60℃). For the given MOFs – water systems, the desorption rates are found higher and require less time to reach the equilibrium condition due to faster movement of water molecules at higher temperatures and pressures as compared with the adsorption rates, which is quite slower. As for N-UiO-66 and OH-UiO-66 MOFs, the adsorption kinetics are approximately 1.4 ~ 1.5 times faster as compared to the original UiO-66 (Zr). The adsorption uptake rate of NH_2-UiO-66 is also found 1.2 times higher. The reasons are that with the hydrophilic functional group additives, more micro-pores are formed inside the UiO-66 structure, more intense MOF + water interaction are obtained with faster adsorption kinetics. The overall water adsorption kinetics performance could be summarised as: OH-UiO-66 > N-UiO-66 > NH_2-UiO-66 > UiO-66.

From the isotherms and kinetics results, it is observed that with the implantation of functional group (-N, -OH, $-NH_2$), more micro-pores are generated inside the MOFs structure. Therefore, stronger interatomic and electrostatic interaction potentials for the modified MOFs and water systems are achieved. The use of functional group enhances the electron interaction significantly with the injection of electronic charge into the functionalised MOFs. Secondly, the functional group also decreases the MOF pore openings. From the PSD results, the pore width, surface area and pore volume of functionalised MOFs are found smaller as compared with parent UiO-66 (Zr) MOFs (Table 4.1).

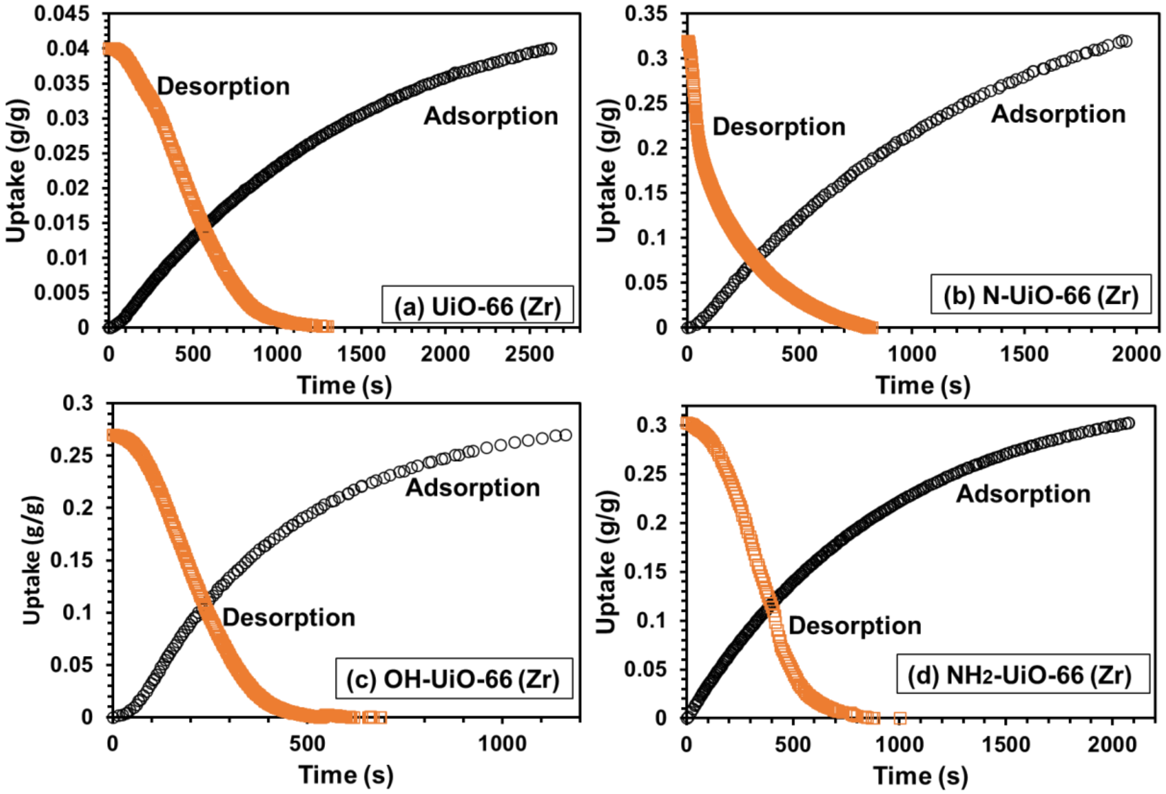

Figure 4.18: Adsorption kinetics under adsorption and desorption conditions of an AHT process in cooling mode (adsorption: 25 °C with 1 kPa and desorption 60 °C with 5 kPa) for water (a) UiO-66 (Zr), (b) N-UiO-66 (Zr), (c) OH-UiO-66 (Zr) and (d) NH_2-UiO-66 (Zr) MOFs.

Employing the gravimetric analyser, the transfer of water vapour on the synthesised NH_2-UiO-66 (Zr) is conducted under cyclic operating conditions consisting of both adsorption and desorption. During experimentation, the relative pressure (P/P_s) varies from 0.1 to 0.9 and the temperature ranges from 25 ^oC to 70 ^oC. The cyclic adsorption-desorption of water vapour on NH_2-UiO-66 (Zr) MOFs are shown in Figure 4.19. Hence the results are presented for more than 300 cycles and each cycle comprises 10 minutes. It is observed that the trends of water uptake and offtake values are nearly same for each cycle, and no evident degradation is observed.

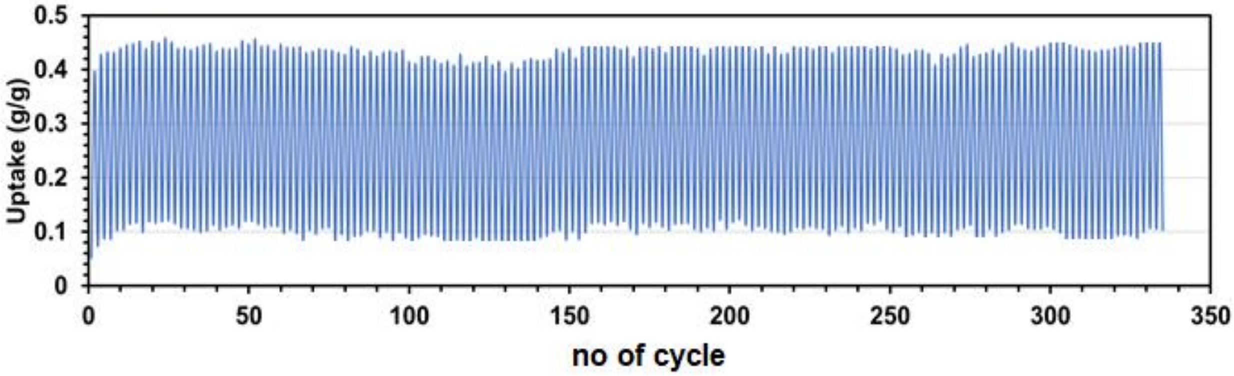

Figure 4.19: Cyclic adsorption-desorption behaviours of NH_2-UiO-66 (Zr) MOFs and water.

4.4.2.2 Functional MOF-801 (Zr) Plus Water

Figure 4.20 shows the water adsorption-desorption plots for water on the parent and $–CH_3$ ligand assisted MOF-801 (Zr) at 25 ℃ with the pressure varying from the low pressure (Henry's region) to the saturated pressure region. Hence, the black solid line represents original MOF-801 and the colour dotted line indicates the methyl functionalised materials. Water adsorption measurements are repeated at least three times for the reliability purposes. As shown in Figure 4.20, the hysteresis phenomenon is found at low pressure region and the isotherm trends are directly in line with findings proposed by Furukawa et al. [172]. Although the limiting uptake of $(CH_3)_2$-MOF-801 (Zr) is decreased as compared with the parent MOF-801 (Zr), the step pressure is substantially enlarged as the hydrophobic length is slightly increased in the low pressure region. Hence the inclusion of two methyl functional groups, $(CH_3)_2$, in MOF-801 (Zr) results in the reduction of the parent MOF-801 (Zr) pore openings and surface area (Table 4.2), which also overrides the influence of methyl group in water - $(CH_3)_2$-MOF-801 interactions.

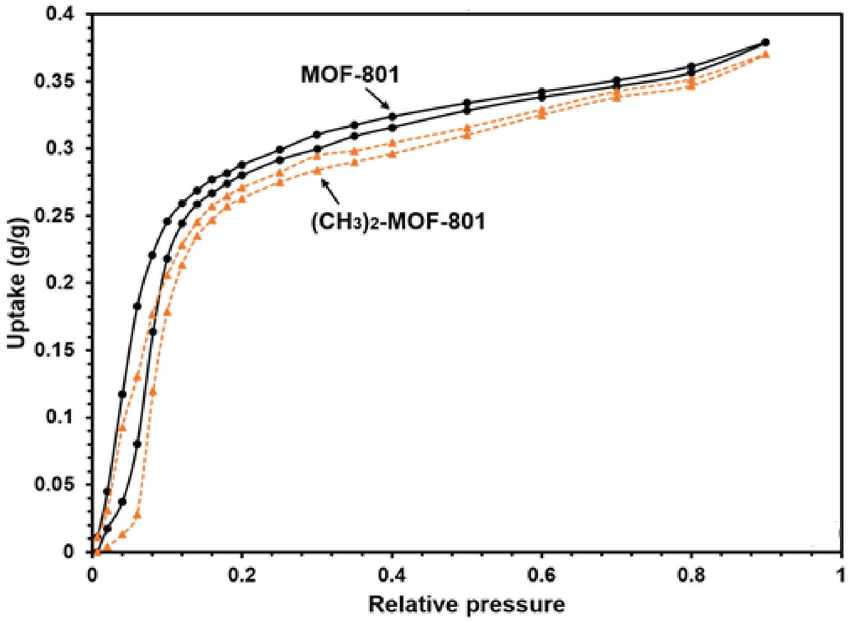

Figure 4.20: Water adsorption-desorption isotherms of the parent MOF-801 (black solid line); functionalised $(CH_3)_2$-MOF-801 (Zr) (colour dotted line) at 25℃.

The experimental results for water adsorption isotherms on original and functionalised MOFs are shown in Figure 4.21 (a)-(b) for a wide temperature conditions (25℃ to 80℃). The performances of adsorption assisted cooling could be predicted based on the water adsorption isotherm, which is calculated in terms of water storage capacity i.e. uptake-offtake difference (Δq) per adsorption – desorption cycle. In Figure 4.21, the Δq $(= q_{ads-}q_{des})$ values for the parent and CH_3-functionalised MOF-801 are shown under the same working conditions (adsorption at 25 ^oC and 1 kPa, and desorption at 80 ^oC and 5 kPa). From the experimental data, the Δq of $(CH_3)_2$-MOF-801 is 25% higher than that of the original MOF-801. This is due to the fact that the strong interactions of water and -CH_3 functionalised MOF dominate the space-loss effects in parent MOF-801. Additionally, small Δq ($\approx$ 0.09 kg/kg) is observed for original MOF-801 + water system at the desorption temperature of 75 ℃. However, $(CH_3)_2$-MOF-801 delivers significantly better Δq ($\approx$ 0.14 kg/kg) results at 75 ^oC desorption temperature. Hence, due to the addition of two –CH_3 functional group in fumaric acid, the pore size and volume of the parent MOF-801 decrease. However, water interaction is increased. The enhancement of water – MOFs interactions are not overrided by the addition of the hydrophobic methyl functional groups. Therefore, the value of water uptake, q decreases significantly at higher temperatures (> 60 ^{o}C), and on the other hand, Δq increases.

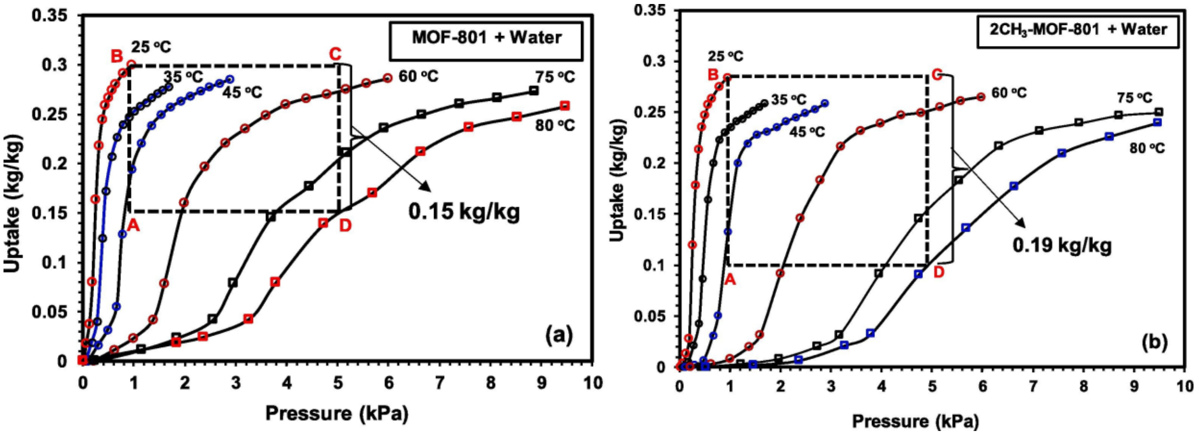

Figure 4.21: Adsorption isotherms for (a) the parent MOF-801 + water and (b) $(CH_3)_2$-MOF-801 + water systems for the temperatures ranging from 25 °C to 80 °C. Hence adsorption-desorption cycle (A-B-C-D) is shown. Hence the thermal compression comprises four thermodynamic processes namely pre-cooling process (C-D), adsorption process (D-A), pre-heating process (A-B) and desorption process (B-C).

The isosteric heat of adsorption (Q_{st}) calculated on the basis of Clausius Clapeyron equation [191] for water adsorption on various fumarate-based MOFs systems are shown in Figure 4.22. A rapid increase in Q_{st} is found for MOF-801 at the low uptake or low pressure region, and it is mainly because that abundant water molecules are adsorbed violently onto the high energy pore site at the beginning of adsorption. As the pressure increases, a continuous decrement of Q_{st} is observed. Similar trends are found for $(\mathrm{CH_3})_2$-MOF-801 except that there is a sudden drop in Q_{st} at the saturation pressure point, which indicates abundant meso and macro pores are available in $(\mathrm{CH_3})_2$-MOF-801 structure. This can also be observed from the PSD distribution curves as shown in $\mathrm{N_2}$ characterisation section. Generally, by implanting the methyl functional group into MOF-801, the water + $(CH_3)_2$-MOF-801 interaction is increased. Therefore, as the pressure (water uptake) increases, the additional interaction between water molecules and MOFs framework will result the increment of Q_{st}.

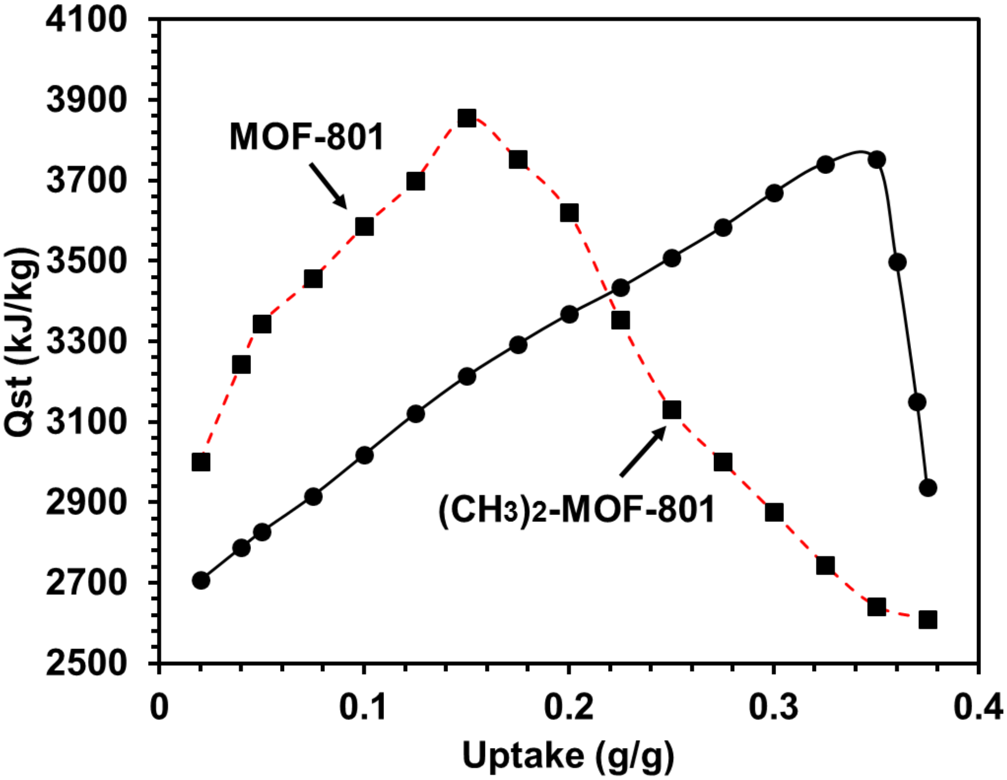

Figure 4.22: Isosteric heat of adsorption for original and functionalised fumarate-based MOFs adsorbents with water. Here, (■) is MOF-801 and (▲) indicates $(CH_3)_2$-MOF-801.

The water uptake rates on the parent and methyl-functionalised-MOF-801 adsorbents for the temperature and pressure under adsorption (30 °C and 1 kPa) and desorption (60 °C and 5 kPa) conditions of an adsorption chiller are shown in Figure 4.23 (a)-(b). The study of adsorption kinetics is presented from t = 0 up to the time when the equilibrium conditions are nearly obtained. It is observed from Figure 4.23 that $(CH_3)_2$-MOF-801 adsorbent exhibits at least two times faster adsorption kinetics (up to 600 s) as compared with the original MOF-801 and reaches the equilibrium within 1000s.

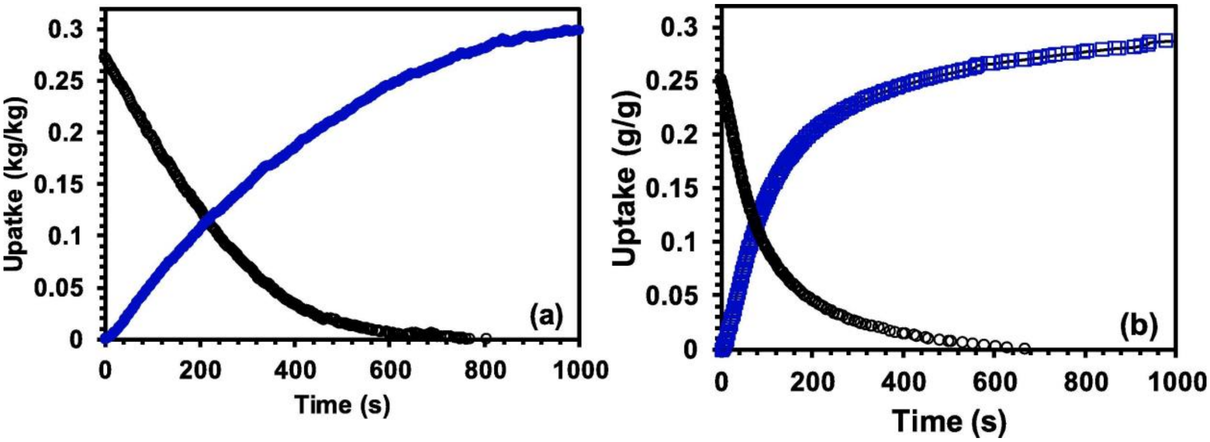

Figure 4.23: Adsorption kinetics for water adsorption on (a) MOF-801 and (b) $(CH_3)_2$-MOF-801 under adsorption (30 °C and 1 kPa) and desorption (60 °C and 5 kPa) conditions of an adsorption chiller.

It is well known that the pore chemistry and topology play important roles in adsorbent + adsorbate interactions [192, 193]. By implanting the methyl functional groups, the pore topologies of the MOF-801 framework is changed, the total pore volume is reduced and more narrow pores are created. Hence, the binding energies between water vapour and the $(CH_3)_2$ - MOF-801 is enhanced inside the narrow pores. This phenomenon could be explained from the basics of interatomic mechanism. As compared with the parent MOF-801 structure, water molecule transfer inside the “methyl functional group-blocked pores” result in higher Lennard-Jones (LJ) potential, electrostatic potential, the induction interaction as well as the high order interactions. Furthermore, the lateral attraction force between adsorbed water molecules is also increased within methyl functional group-blocked pore walls, especially at higher pressure [161]. All these factors will result an overall enhanced interaction between water and methyl functionalised MOF-801 (Zr), as compared to that of the parent MOF-801 (Zr). Therefore, with the implantation of methyl functional group, (i) the pore-blocking effect is resulted, (ii) the stronger interaction potentials are achieved and (iii) the faster adsorption/desorption kinetics are obtained. However, the limiting uptake drops slightly due to the reduction of pore volume.

It is also found that the rate of desorption is faster than that of adsorption due to the fact that the water vapours move in the adsorbent-pores faster under higher temperature and pressures (from the kinetic theory of gas). Under desorption condition as shown in Figures 4.23 (a) and 4.23 (b), the equilibrium is achieved within 600 s, and $–CH_3$-functionalised MOF-801 also shows two times faster desorption up to 200 s. From the PSD results, the pore width, surface area and pore volume of methyl functionalised MOFs are found to be smaller as compared with parent MOFs (Table 4.2).

4.4.2.3 Al Fumarate and MOF-Zeolite Composite Plus Water

The water uptakes on the synthesised adsorbents for various pressures at 30 °C are shown in Figures 4.24 (a – c). The limiting uptake of water on the parent Al-Fum is found to be 0.4 kg/kg as similar to the published data of Teo et al. [40]. The shape of the adsorption isotherm depends on the interaction between water vapour and adsorbent, which is closely related to the porosities of Al-Fum based MOFs. Generally, water vapour is preferentially adsorbed onto the high energy pore sites. However, it does not mean the binding energy between adsorbate and adsorbent is strong. If the pore size of the adsorbent is relatively too big as compared with the size of water molecule, the interactions could be rather small and extremely low water uptakes are expected. For example, strongly hydrophobic behaviours are observed for Al-Fum in the low pressure region which is due to the weak interactions between water vapours and Al-Fum large size pore. As the adsorption pressure increases (up to $P/P_s \approx 0.20$), more water molecules move deeper and interact with the micro-pores of the Al-Fum. Therefore, the binding energy increase dramatically and a sharp increase of water uptakes is observed. As the adsorption continues, some more water molecules are adsorbed onto the sites of lower energy and the adsorbate-adsorbent interactions becomes weaker, hence, the slope of isotherm becomes more gently. The hydrophobic length of Al-Fum – water varies up to the relative pressure of 0.2 ($0 \leq P/P_s \leq 0.2$). Additionally, more micro-pores are created by mixing the original Al-Fum with zeolite-based adsorbents or doping with the lithium ions. Hence, stronger adsorbate-adsorbent interactions are resulted at low pressure region and shorter hydrophobic lengths are found for modified Al-Fum materials. With the addition of AFI/CHA-type zeolites (in weight basis 10%, 30% and 50%) on the parent Al-Fum, the hydrophobic length can be reduced up to $P/P_s = 0.15$. However, the limiting uptake of the composite structure is decreased. The water uptake-offtake difference on composite structure is slightly better at the relative pressure ranging from 0.2 to 0.25 (Figure 4.24 (a)) under chiller operating conditions as compared to that of the parent Al-Fum-MOF. Hence 50% AFI-zeolite and Al-Fum composite shows higher Δq. On the other hand, the similar trends are found for CHA-type zeolite and Al-Fum composites (Figure 4.24 (b)). The effects of alkali ions on MOF structure are shown in Figure 4.24 (c). It is found that 5% Li ions doped adsorbent has higher water uptake under the chiller operating conditions. More adsorbed-water-uptake is found at the pressure regions $0 \leq P/P_S \leq 0.25$ due to the hydrophilic behaviours of Li^+ dopants. It is also found that Na^+ and K^+ dopants do not have much notable effects on the parent MOF for water adsorption due to the fact that the size of Na^+ / K^+ ions is larger than that of Li^+ ions,. Therefore, the hydrophilic features are cancelled by their pore-block-effects.

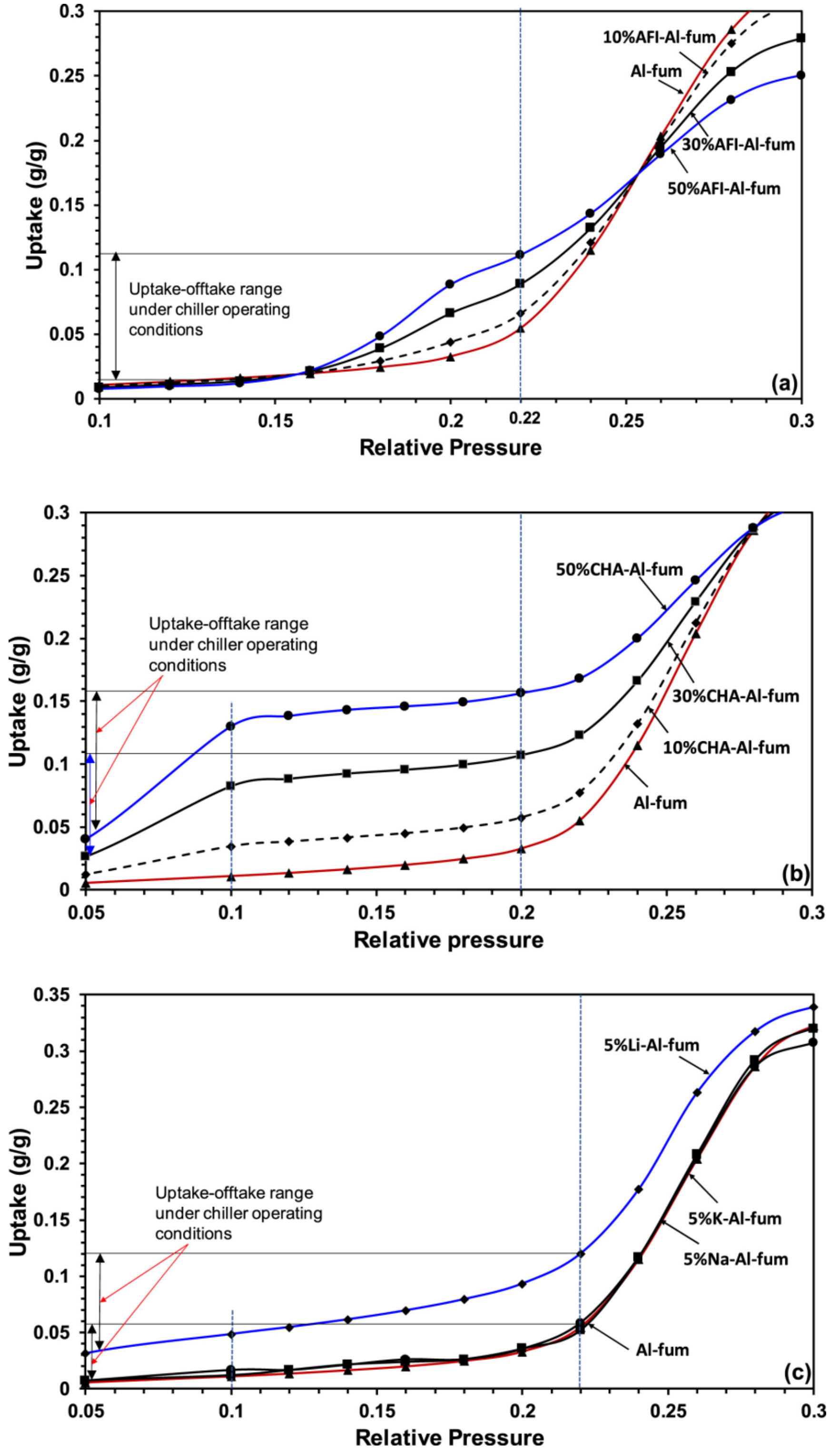

Figure 4.24: Water adsorption isotherms of (a) original and 10%, 30% and 50% AFI mixed Al-fumarate MOFs, (b) original and 10%, 30% and 50% CHA mixed Al-fumarate MOFs, (c) original and 5% Li^+, Na^+ and K^+ doped Al-fumarate MOFs at 30 °C.

The water uptakes data for the original and 5% Li ions doped Al-Fum, AFI- Al-Fum and CHA-Al-Fum composites for the temperatures of 30 ^{o}C – 60 ^{o}C are plotted in Figures 4.25 (a – d). The adsorption-desorption process (A-B-C-D) is also shown in the isotherm curves. Hence, the water uptake – offtake difference (Δq) is calculated for the working pressures between 1 kPa and 5 kPa with the adsorption and the desorption temperatures of 30 ^{o}C and 60 ^{o}C, respectively. It is observed from the experimental data that the Δq for the parent and Li ions doped Al-Fum MOFs are nearly the same under adsorption-chiller-operating conditions (Figure 4.25 (a) and (b)). However, the Δq of CHA / AFI-type zeolite and Al-Fum MOF composite is 12% / 17% lower than that of the parent Al-Fum MOF (Figures 4.25 (c) and (d)). For comparison purposes, the Δq for water adsorption on CHA-type and AFI-type zeolites are found to be 0.05 kg/kg and 0.15 kg/kg, respectively under low temperature driven adsorption chiller conditions (adsorption: 30 ^{o}C and 1 kPa, desorption: 60 ^{o}C and 5 kPa).

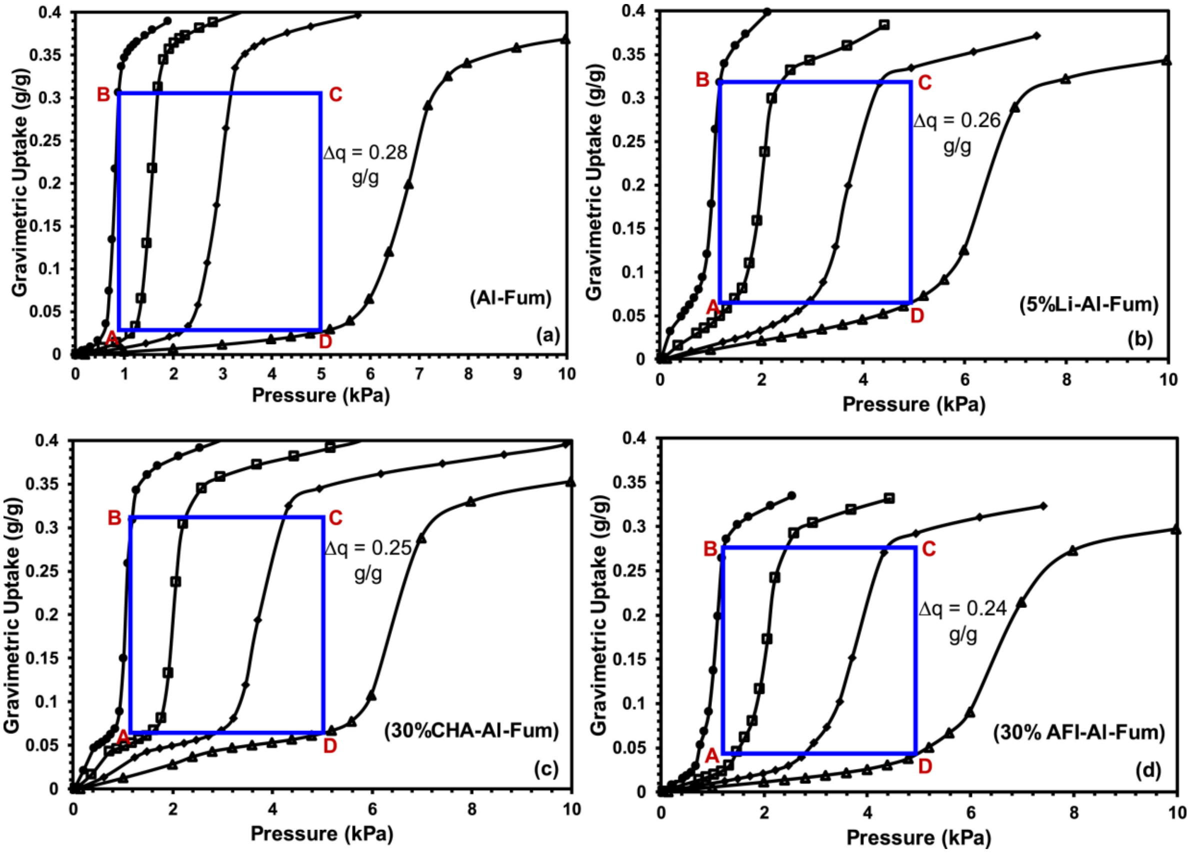

Figure 4.25: Water adsorption isotherms of original and post-synthesised Al-fumarate for the temperatures ranging from 30 °C to 60 °C: (a) parent Al-Fum MOFs, (b) 5% Li^+doped Al-Fum MOFs, (c) 30% CHA mixed Al-Fum MOFs, (d) 30% AFI mixed Al-Fum MOFs. Hence, (●) stands for 30 °C, (□) indicates 40 °C, (◆) is 50 °C and (Δ) represents 60 °C.

The experimental data for water uptakes on Al-Fum based adsorbents are shown in Figure 4.25 for pressures from Henry's regions to the saturated regions and temperatures ranging from 30 ℃ to 60 ℃ (30 ℃, 40 ℃, 50 ℃, 60 ℃), which will be deduced to the adsorption isosteric heat. Figure 4.26 shows the adsorption isosteric heats (Q_{st}) of parent and post-synthesis Al-Fum + water systems based on Clausius -Clapeyron relation $dln(P)/dT = -Q_{st}/RT^2$ with a wide temperature range from 30 ℃ to 60 ℃, where P is the adsorption pressure, T is the experiment temperature and R is the gas constant for water vapour. A sharp increase of Q_{st} for Al-Fum and 5%

Li-Al-Fum is observed at low water uptake region, which is due to the rapid adsorbed process of the water molecules onto the higher energy pore sites.

Therefore, post-synthesis process enhances the sample affinity to water molecules. A relative steady Q_{st} level is found for the water uptakes from 0.1 kg/kg to 0.3 kg/kg for all the adsorption systems. This is due to the fact that as the adsorption process continues, more water molecules are adsorbed onto lower energy sites. On the other hand, an increase in Q_{st} is observed for both 30% CHA-Al-Fum and 30% AFI-Al-Fum MOFs near the saturated regions as the interactions between water molecules are increased.

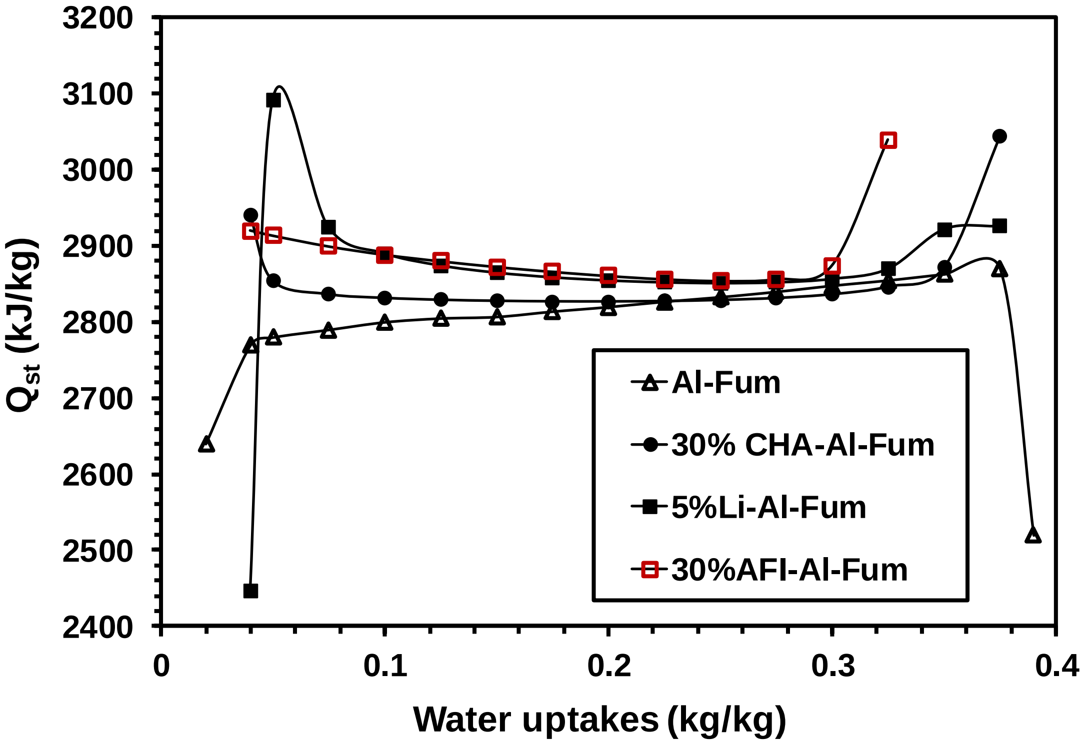

Figure 4.26: Isosteric heats for the adsorption of water on Al-Fum, 5% Li-Al-Fum, 30% AFI-Al-Fum and 30% CHA-Al-Fum for temperature from 30℃ to 60℃.

Figure 4.27 (a – d) shows the kinetics of water uptakes on the synthesised-adsorbents at 30°C and 60°C. For a better analysis of Al-Fum based MOFs kinetics performance, practical adsorption assisted chiller operation criteria are used as reference in the new experiments. First, the adsorption kinetics investigations are taken at 30 ℃, directly from extreme low pressure ($P/P_s \leq 0.05$) to 1.0 kPa ($P/P_s \approx 0.24$). After the adsorption process, the Al Fum based samples are immediately desorbed at 60 ℃, 5.0 kPa ($P/P_s \approx 0.25$). All the experiments are performed three times to minimise uncertainties. These kinetics data are presented up to the equilibrium condition, from which one can understand that the adsorption-desorption periods depend on adsorbent structures. The water uptake rates are greatly improved by zeolite/alkali dopants (in terms of weight basis) addition into the parent MOF material. It should be noted that 30% CHA-MOF composite provides better results in terms of water uptake/offtake rates at 30 ^{o}C and 60 ^{o}C (Figure 4.27) as compared to the parent Al-Fum MOFs. The ranking in terms of kinetics are CHA-Al-Fum > AFI-Al-Fum > Li dope Al-Fum > parent- Al-Fum. The additional CHA/AFI zeolite generates a large number of micro-pores in MOF structure. As a result, more interatomic and electrostatic interaction potentials occur between composite adsorbents and water. Experimentally, it is found that at the temperature of 30°C, (i) the parent- Al-Fum reaches equilibrium at nearly 1900 s (Figure 4.27 (a)), (ii) the post-synthesised Li-doped Al-Fum adsorbent reaches equilibrium at 1790s (Figure 4.27 (b)), (iii) 30% CHA/Al-Fum requires 1214s and 30% AFI/ Al-Fum needs 1702 s for equilibrium conditions (Figures 4.27 (c) and 4.27 (d)), (iv) for practical adsorption chiller operation conditions (half cycle time = 500 s), the parent- Al-Fum could accomplish 49% (0.49) of the whole adsorption process, while 5% Li-doped Al-Fum, 30% CHA-Al-Fum and 30% AFI-Al-Fum could complete 0.55, 0.81 and 0.60 of the whole adsorption process, respectively. Additionally, the desorption rates are faster at higher temperature. All the desorption experiments for Al-Fum based materials could be completed within 1000 s, especially for CHA-Al-Fum (around 500 s). The doubts about whether the experiment reaches the full equilibrated state are mainly caused by the limitation of the apparatus. For one step of the adsorption experiment under certain pressure and temperature, the adsorbents (Al-Fum based materials) will keep adsorbing water and the mass of the adsorbent will keep increasing. The current adsorption step will continue if the increase of the adsorbent mass is detected within the weight change tolerance and short time interval (which depends on the machine's characteristics and could not be changed). However, the adsorption process will automatically move on to the next step if no evident mass change is detected. Therefore, some of the adsorption kinetics curves seem not to be fully equilibrated. Although the qualitative order of the kinetics data shown in Figure 4.27 is correct and all the curves reaching coverage 1 ($\frac{\Delta\theta_t}{\Delta\theta} = 1$) at the end of the adsorption process while the uptake seems to be still increasing. Here, the coverage means surface coverage which is equivalent to uptake/limiting uptake. Nonetheless, the adsorption process should be considered as fully equilibrated. The detailed information about the total experimental duration for all the samples are shown in Table 4.4. Hence the use of alkali dopants and zeolite composite increases the kinetics of parent-Al-Fum MOFs.

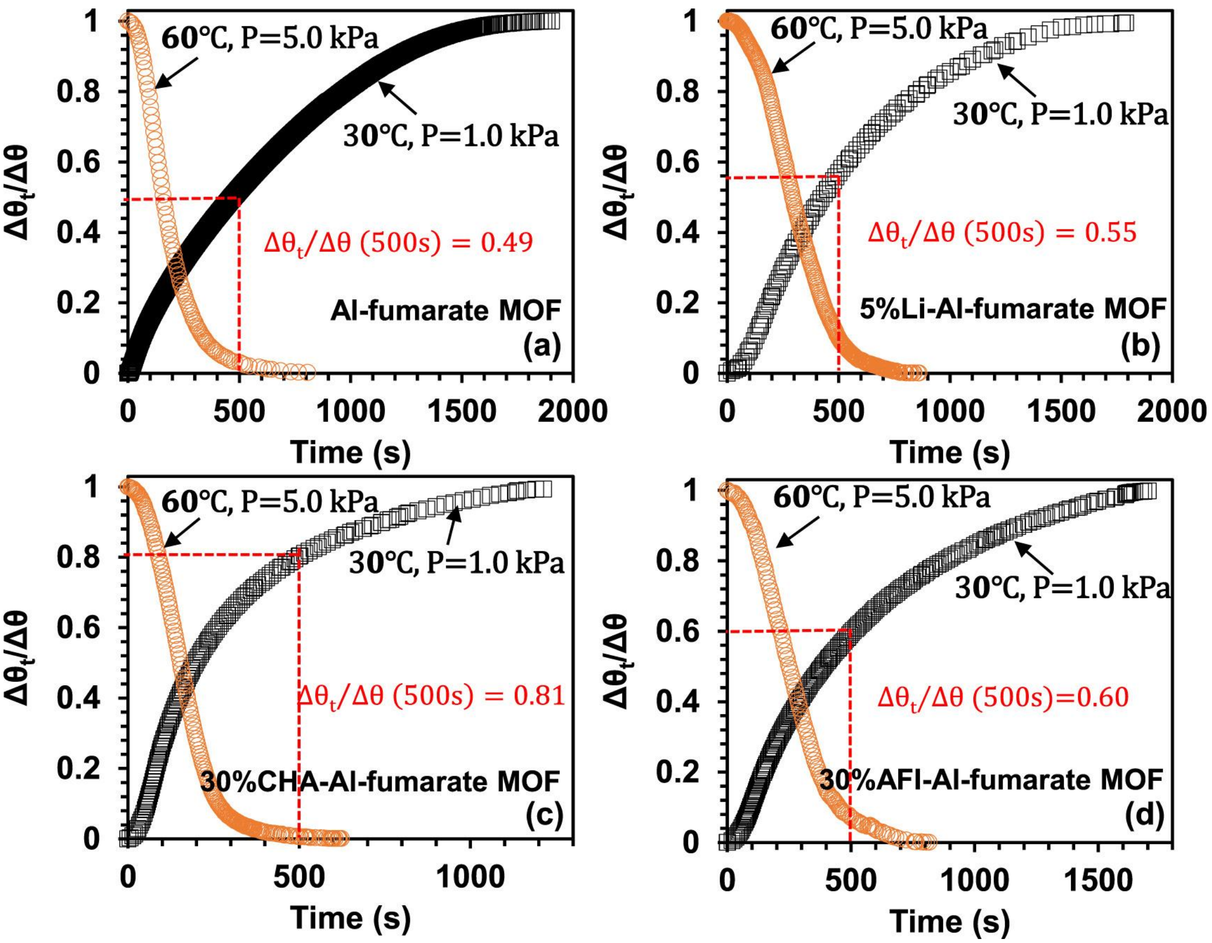

Figure 4.27: The kinetics analysis of water uptakes and offtakes for original and post-synthesised Al-fumarate at temperatures 30 °C and 60 °C. Here (a) parent Al-fumarate MOFs, (b) 5% Li^+ doped Al-fumarate MOFs (c) 30% CHA mixed Al-fumarate MOFs, and (d) 30% AFI mixed Al-fumarate MOFs.

Table 4.4: Total experimental duration (hours) per adsorption-desorption loop for original and post-synthesised Al-Fum samples.

Samples	30 ℃	40 ℃	50 ℃	60 ℃
Al-fumarate MOF	94.2	77.9	63.2	43.1
Li-Al-fumarate MOF (5%)	90.2	72.8	59.3	30.7
AFI-Al- fumarate MOF (30%)	84.0	60.3	43.2	36.1
CHA-Al- fumarate MOF (30%)	29.2	26.3	18.7	12.5

4.5 Summary

This chapter describes the experimental synthesis methods for original MOFs namely UiO-66 (Zr), MOF-801 (Zr) and Al Fumarate (Al-Fum). The water adsorption performance of these original MOFs are generalised and the defects are pointed out. In order to rectify these problem, well-defined MOFs modification methods are elaborated including mixing with conventional adsorbent, doping with alkali ions and organic ligand functionalisation. Furthermore, a variety of characterisation techniques are introduced to test the topologies, morphologies, porosities and water adsorption behaviours for parent and modified MOFs. The next chapter begins with the thermodynamic-framework of MOFs + water based AHT system.

Chapter 5. Energy and Entropy Analyse of Adsorption Heat Transformation Systems

Chapter 5 starts with the introduction of AHT (adsorption heat transformation) operation mechanisms, followed by the static and dynamic modelling of a two-bed AHT system (adsorption chiller, heat pump and desalination). The thermodynamic frameworks of the entropy generation are also proposed. Based on the experimentally confirmed adsorption isotherms and kinetics, the entropy behaviours as well as the performances of the AHT systems are presented.

5.1 Adsorption assisted heat transformation (AHT) system

A two-bed AHT system is constructed by a condenser, an evaporator and a pair of adsorption/desorption beds. For a complete AHT operation cycle, four steps namely isosteric cooling, isobaric adsorption, isosteric heating and isobaric desorption are involved. By monitoring the valve states and the direction of cooling/hot water supply, the adsorbent beds are refreshed, and the continuous cooling, heating and water production are achieved. The adsorption-triggered-evaporation and the desorption-activated-condensation in terms of heat and mass transfer are shown schematically in Figures 5.1 and 5.2, respectively. Hence, the specific amounts of solid porous adsorbents (original or modified MOFs) are housed in finned-tube heat exchangers called adsorption beds.

As shown in Figure 5.1, when valve V1 is opened whilst valve V2 is closed, cooling water is supplied to the adsorption-bed. For the adsorption process, due to the supply of chiller water with an inlet temperature of 14.8 °C (cooling load, Q_{evap}) to the evaporator, the refrigerant (water here) evaporates from the evaporator and is adsorbed by the porous adsorbent housed in adsorption-bed (i.e. mass transfer from the evaporator to the bed). It is noted here that the term "mass transfer" used in this chapter is particularly referred to the movement of water vapour through the major components (i.e. evaporator, condenser and sorption-beds) of the AHT system, it is not relevant to the mass movement due to a concentration gradient. The adsorption heat (Q_{ads}) is removed by the circulating cooling water. The supply of cooling water through the heat exchanger tubes increases the adsorption capacity. When the pressure of the adsorption-bed equals to that of the evaporator, the water vapour transfer stops.

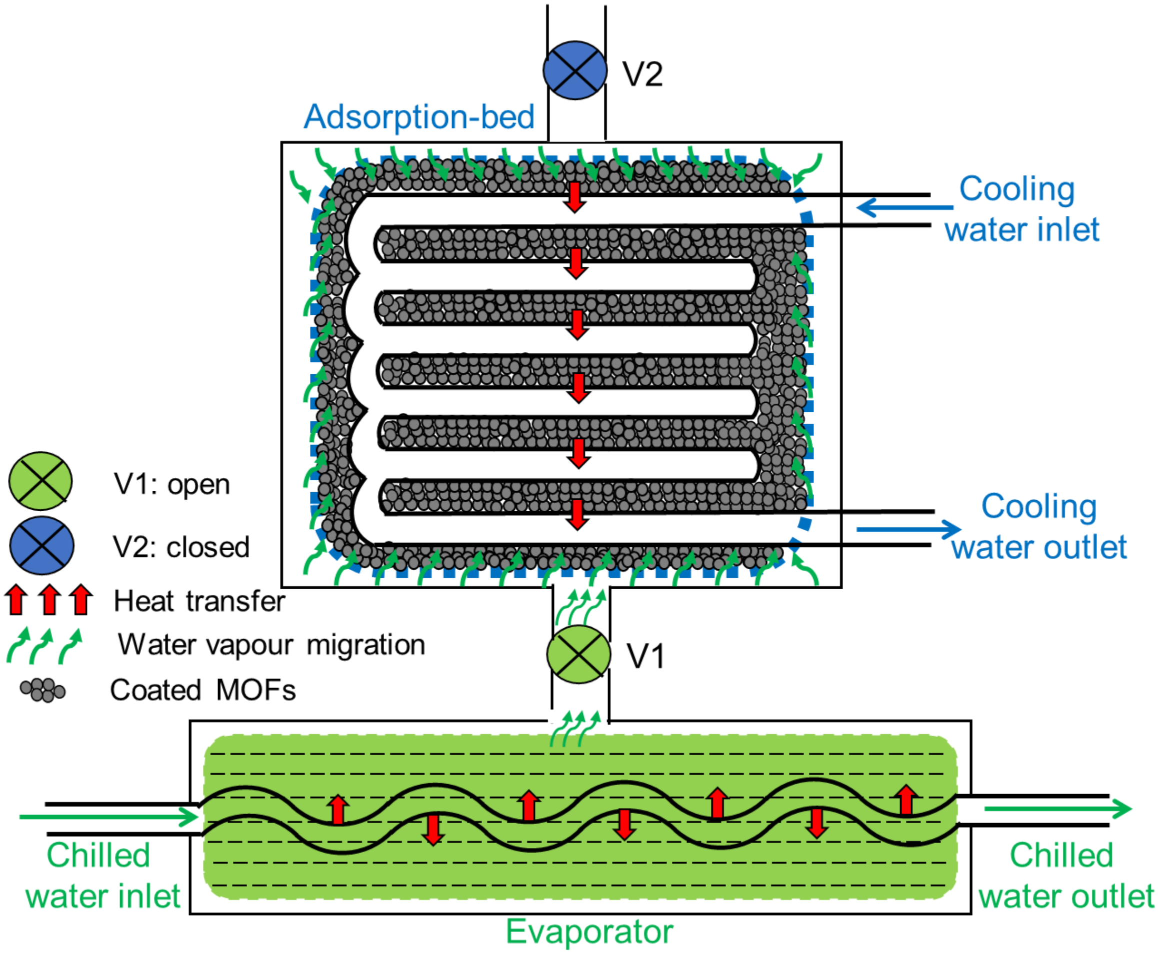

Figure 5.1: Schematic diagram of adsorption-triggered-evaporation process of the MOFs - water based adsorption assisted heat transformation (AHT) system.

During desorption period as shown in Figure 5.2, valve V3 is closed and valve V4 is opened. By the supply of heating water to the heat exchanger tubes in the bed, desorption-bed is constantly heated up and the bed-temperature increases up to the desorption temperature T_{des}. Therefore, the water vapour is dehydrated from the porous adsorbent with the heat source of Q_{des}. The desorbed water vapour enters into the condenser and condenses at the pressure and temperature of P_{cond} and T_{cond}, respectively. The heat Q_{cond} due to condensation is removed by the supply of cooling water into the tubes of condenser heat-exchanger. Hence, the evaporator pressure is maintained lower than that of the condenser pressure via the expansion valve.

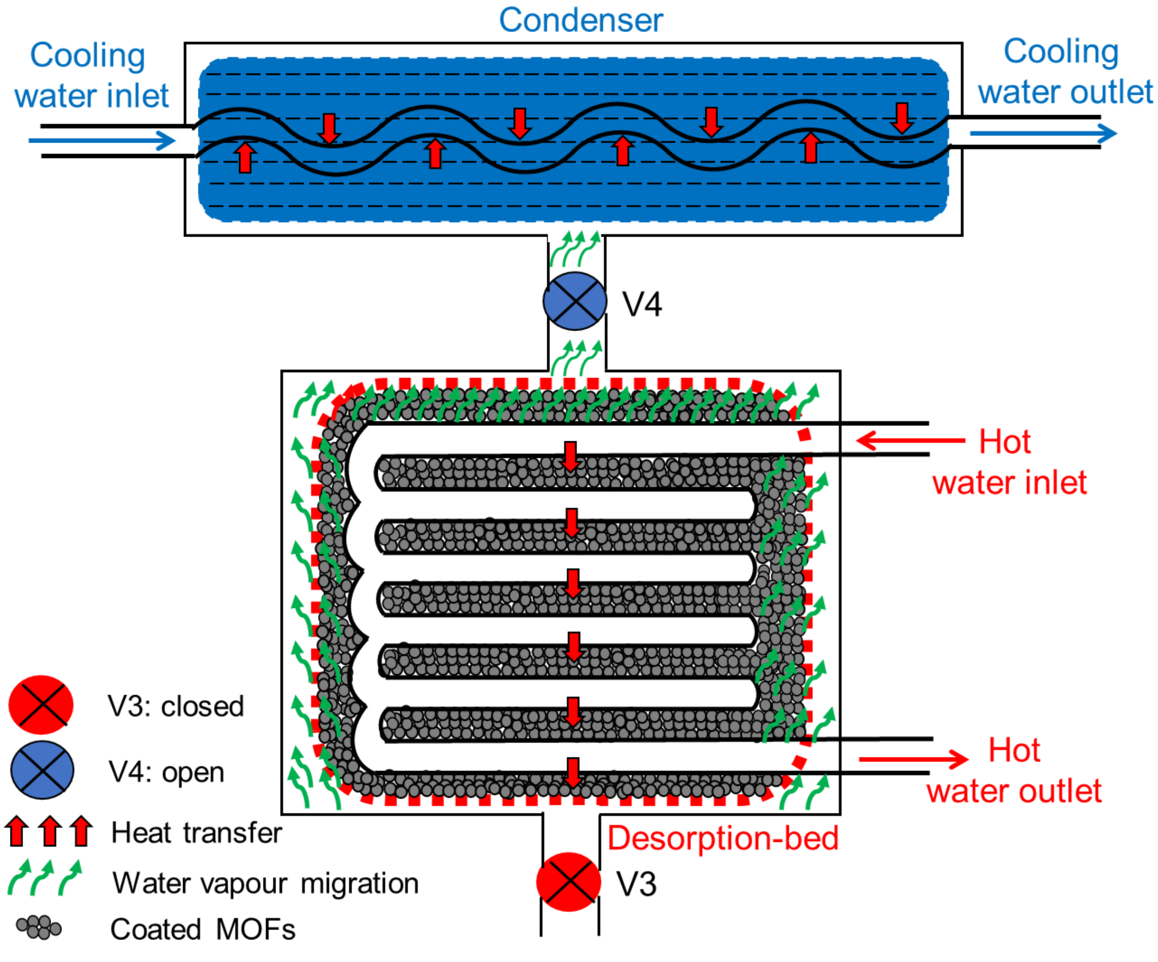

Figure 5.2: Schematic diagram of desorption-activated-condensation process of the MOFs - water based adsorption assisted heat transformation (AHT) system.

After adsorption and desorption, both beds are refreshed during switching periods by changing the direction of heating and cooling fluids to the subsequent bed. During that periods, all the four valves are closed and no mass transfer is occurred. The adsorption-desorption continues after the switching periods. It is noted here that there may be ‘reverse-desorption’ in the bed (i.e, water vapours transfer from the bed to the evaporator) at the beginning of adsorption periods due to short pre-cooling time. On the other hand, if the preheating/desorption time is too long, ‘reverse-adsorption’ may be found in desorption mode. In an AHT cycle, the enthalpy of evaporation is used for cooling purpose. The combined effects of enthalpies of condensation and adsorption are used as heating pumping effects. Furthermore, as sea water is provided into the evaporator, the condensed liquid could be stored as the desalinated water.

5.2 AHT modelling

A good number of papers describing the thermodynamic frameworks of adsorption-desorption process for various heat transformation applications such as heat pump, cooling and desalination/distillation are available in literature. For simplicity, the lumped thermal capacity model is considered. It is assumed that in the modelling, the temperature of each component of AHT system is a function of time only, which means that the temperature is assumed to be spatially (related to space and position of bed) independent. In addition, it is assumed that the heat transfer through the fin is one dimensional. The limitations of the thermodynamic modelling are (i) the adsorption bed temperature depends on time only and (ii) the simulation domain begins with initial conditions and stops by setting a tolerance or error between the last two values as a function of time.

It should be noted here that (i) the supply of chilled water through the copper tubes in the evaporator, and (ii) the high temperature cooling water (> 25 °C) generating from the TES (thermal energy storage) provide the extra cooling loads to the AHT system. For the generation of continuous cooling, heating and desalination, the refrigerant (hence water vapour) under low pressure conditions is evaporated and flows into the porous adsorbents of bed. The combination of sensible and latent heat flow is involved in the evaporator by (i) the transfer of heat from chilled/cooling – water to the refrigerant through the heat exchanger tubes and (ii) energy transmission from the evaporated water vapour to the adsorption bed. Both the mass and heat interactions between the evaporator and the adsorption bed evolve the energy balance within the evaporator as given by the following equation

$$\left(Mc_p\right)_e \frac{dT_e}{dt} = -h_{fg} M_s \frac{dq_a}{dt} + (UA)_e \frac{1}{N} \sum_{i=1}^{N} (T_e - T_i) - h_f M_s \frac{dq_d}{dt}, \tag{5.1}$$

The adsorption and desorption rates $\frac{dq_a}{dt}$ and $\frac{dq_d}{dt}$ are calculated by the adsorption isotherms and kinetics models. Hence, the heat capacity of copper tube-heat exchanger as presented in the left hand side of Eq. (5.1) becomes $\left(Mc_p\right)_e \left[= M_{ehx} c_{p,ehx} + M_w c_{p,w}\right]$. The first item of the right-hand-side of Eq. (5.1) shows the latent heat involved during evaporation, the second term presents the heat transfer between the chilled water and the evaporator, and the third term stands for the load generating from the supply of chilled/warm/cooling water. The chilled water temperature for each segment of the heat exchanger tube (T_i) becomes

$$\frac{V_e (\rho c_p)_{cw}}{N} \frac{dT_i}{dt} = (\dot{m} c_p)_{cw} (T_{i-1} - T_i) + \frac{(UA)_e}{N} (T_e - T_i). \tag{5.2}$$

The heat is evolved as the water vapour enters into the bed during adsorption. The generated heat in the bed-heat-exchanger is removed by flowing cooling water through the heat exchanger tubes. On the other hand, during pre-heating and desorption periods, the hot water is transferred to the heat-exchanger-tubes of the bed. Therefore, the water vapour is rejected from the surface of porous adsorbents i.e. mass transfer of water vapour occurs. All these phenomena as observed in the adsorption bed can be expressed mathematically by

$$\left(Mc_p\right)_b \frac{dT_{b,k}}{dt} = \psi . M_s \frac{dq_{b,k}}{dt} \Delta H - \frac{(UA)_{b,k}}{N} \sum_{j=1}^{N} \left(T_{b,k} - T_j\right), \tag{5.3}$$

where k shows either adsorption or desorption condition with flag ψ = 1 (for adsorption) and ψ = -1 (for desorption). The left hand side of Eq. (5.3) represents the thermal heat capacity of the bed, e.g. $\left(Mc_p\right)_b = \left[M_{bhx}c_{p,bhx} + M_s\left(c_{p,s} + q.c_{p,a}\right)\right]$. On the other hand, the right hand side of Eq. (5.3) is related to the amount of energy input and output in the bed control volume, in which the first term represents the latent-heat transfer due to the heat of adsorption, and the second term indicates the rejection of heat energy from the bed to the cooling water (during adsorption and pre-cooling periods) or the addition of heat to the bed by the driving heat source (hot water) during pre-heating and desorption periods. The amount of water vapour in the bed is calculated with respect to the bed temperature and evaporator/condenser pressure. The valves effects are considered to calculate the bed pressure under adsorption and desorption conditions. However, the bed pressure is based on isosteric conditions during pre-heating and pre-cooling periods. All these phenomena as mentioned above depends on the flow rates and temperature of the heat transfer fluid. Hence the temperature, T_i of the heat transfer fluid (hence hot and cooling water) for N segment of heat-exchanger tubes is calculated by the following equation

$$\frac{V_b(\rho c_p)_f}{N}\frac{dT_j}{dt} = (\dot{m}c_p)_f\left(T_{j-1} - T_j\right) + \frac{(UA)_{b,k}}{N}\left(T_b - T_j\right). \qquad (5.4)$$

The term $V_b(\rho c_p)_f$ as shown in left-hand side defines the total heat capacity of cooling/heating water passing through the tubes. On the other hand, the right-hand side relates to the heat input and output involved in fluid control volume in tubes. The water vapour is desorbed from the porous adsorbents by the supply of heating fluid to the heat exchanger tubes of bed. The desorbed water vapour enters into the condenser and condensation occurs. Cooling water flows through the condenser tubes and heat is rejected to the environment at the same time. Finally, the condensed fluid reflux-back to the evaporator via a U-tube or an expansion valve, which maintains the pressure difference between the condenser and the evaporator. In the present modelling, it is assumed that the condenser tube holds some liquid condensate. Therefore, the energy balance in the condenser is calculated on the basis of (i) heat input from the desorbed water vapour as shown in the first term of right-hand side of Eq. (5.5), (ii) the heat transfer from the condenser to the heat sink as indicated by the second term of the right-hand side, and (iii) the transfer of warm condensate through the expansion valve (third term of Eq. (5.5)). The condenser temperature (T_c) is calculated by

$$\left(Mc_p\right)_c \frac{dT_c}{dt} = -h_{fg} M_s \frac{dq_d}{dt} + \frac{(UA)_c}{N} \sum_{i=1}^{N} (T_i - T_c) + h_f M_s \frac{dq_d}{dt} \tag{5.5}$$

Hence $\left(Mc_p\right)_c$ is the total heat capacity of condensed water and heat exchanging tubes of condenser and is defined by $\left[M_{chx} c_{p,chx} + M_w c_{p,w}\right]$. The cooling water temperature at each segment (total *N* segment) of condenser heat exchanger tube is calculated by the following equation

$$\frac{V_c (\rho c_p)_c}{N} \frac{dT_i}{dt} = (\dot{m} c_p)_{cw} (T_{i-1} - T_i) + \frac{(UA)_c}{N} (T_c - T_i). \tag{5.6}$$

The amount of water vapour per adsorption-desorption cycle is obtained by the mass interaction during adsorption-desorption operation and the switching periods. The sea water in the evaporator decreases as the evaporation of water vapour continues. Therefore, the mass balance in the evaporator becomes $\frac{dM_{sw}}{dt} = \dot{m}_{sw,i} - M_s \frac{dq_a}{dt} - \dot{m}_{br,o}$, where M_{sw} is the amount of sea water, $\dot{m}_{sw,i}$ is the mass flow rate of feed sea water and $\dot{m}_{br,o}$ is the flow rate of concentrated brine solution drained from the evaporator. The water vapour is evaporated and adsorbed into the adsorbents. The salt rests in the evaporator and the concentration of brine solution (X_{sw}) increases, which is represented by the following equation

$$M_{sw} \frac{dX_{sw}}{dt} = X_{sw,i} \dot{m}_{sw,i} - X_{sw} \dot{m}_{br,o} - \left(\frac{dq_a}{dt} + \frac{dq_d}{dt}\right) M_s, \tag{5.7}$$

where M_s is the mass of adsorbent, $X_{sw,i}$ and X_{sw} are the concentrations for the inlet feed water and the remaining water in the evaporator.

Hence the TES (thermal energy storage) is used to store energy, which could be further used for pumping heat or increasing evaporation rate in the evaporator for desalination purposes. In the TES system, the energy balance of the thermal storage system for mass recovery is written as $\left(Mc_p\right)_{ts}\frac{dT_{ts}}{dt}=\alpha.M_s\frac{dq_{ts}}{dt}\Delta H$, where α is the flag. α = 1 for adsorption and -1 for desorption. During the switching period, the valve connected the adsorber and desorber is open and the initial conditions are T_{ts} (t = 0) = $T_{ads,initial}$ and T_{des} (t = 0) = $T_{des,initial}$. The boundary condition is that the valve is closed when P_{ads} = P_{des}. The energy and mass balance equations are solved numerically and a finite difference method is applied with the initial and boundary conditions. The computational region is discretised into many discrete elements having equal steps. In the programming code, the fins and MOFs adsorbents are considered as a control volume and considered as the same temperature at initial condition. In the modelling, the heat conduction along the fin is assumed one dimensional. Figure 5.3 shows the schematic layout of adsorption bed for net distribution of tube-fin-MOF in the bed structure [22]. The temperature difference in the heat-exchanging tubes is approximated by a forward difference scheme. The adsorption isotherms and kinetics are correlated by a series of subroutines. Double precision is applied with the tolerance of 1×10^{-6}. The simulated variables such as the water vapour uptake-offtake, temperature of sorption beds are continuously updated by numerical integration momentarily. The overall simulation of the AHT system begins with the initial conditions and subsequent simulation automatically, from the transient to the cyclic steady state.

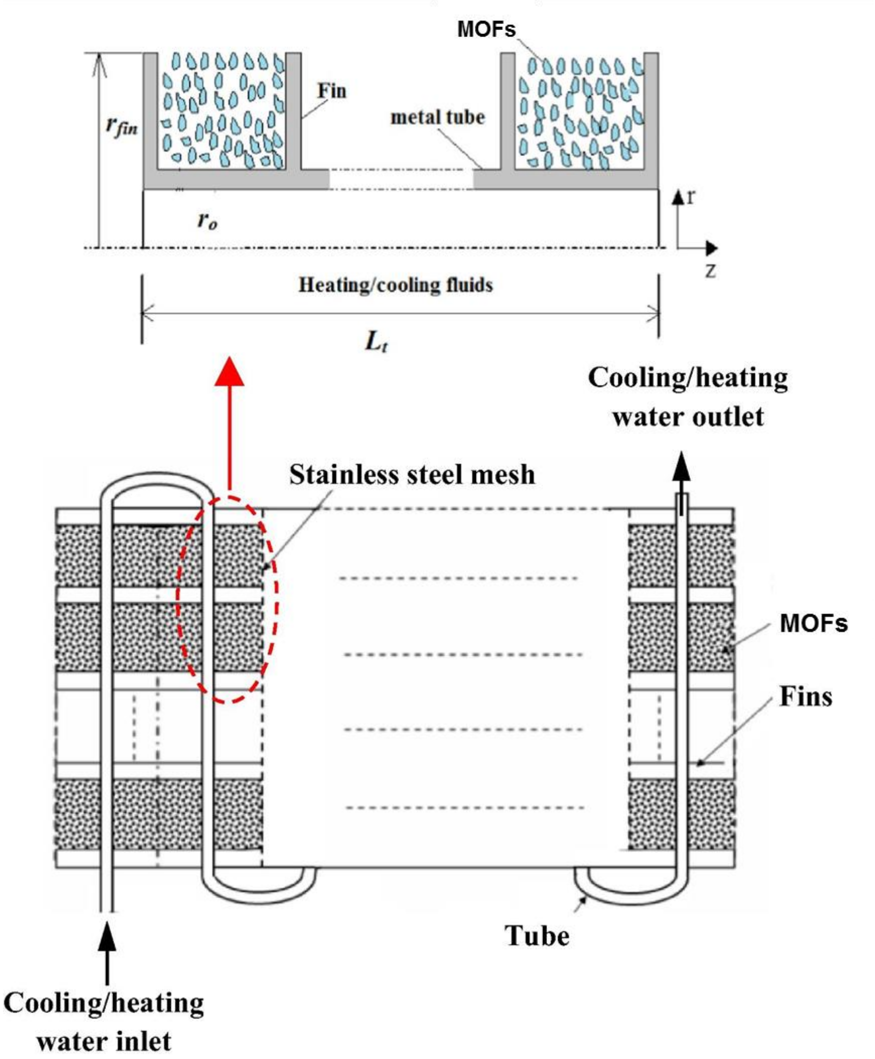

Figure 5.3: Schematic diagram of adsorption bed for net distribution of tube-fin-MOF in the bed structure [22].

The parameters [22, 194] for energy and mass balance equations are furnished in Table 5.1.

Table 5.1: Key parameters for the simulation of MOFs plus water assisted heat transformation system.

Parameter	Numerical description
c_p	750 $(\mathrm{J/kg \cdot K})$ at 300 K
M_s	18 kg
$(Mc_p)_{\boldsymbol{b}}$	184.1 $\mathrm{W/(m^2 \cdot K)}$ [38]
$(Mc_p)_{\boldsymbol{c}}$	(24 kg × 386 $\mathrm{J/(kg \cdot K)}$ + 5 kg× 4180 $\mathrm{J/(kg \cdot K)}$) [38]

$(Mc_p)_e$	(8.9 kg × 386 $\mathrm{J/(kg \cdot K)}$ + 40 kg×4180 $\mathrm{J/(kg \cdot K)}$) [38]
T_f^i	30 ℃
T_f^j	60 ~ 80 ℃
T_{chill}^{in}	14.8 ~ 30 ℃ (Maintained by TES)
$(UA)_e$	(2557 $\mathrm{W/(m^2 \cdot K)}$ × 1.37 $\mathrm{m^2}$) [22]
$(UA)_c$	(4115 $\mathrm{W/(m^2 \cdot K)}$ × 3.71 $\mathrm{m^2}$) [22]
$(UA)_a$	10.3 kW/K (experimental investigation)
$(UA)_d$	9.85 kW/K (experimental investigation)
u_{cw}	0.20 $\mathrm{m/s}$
u_{cw}	0.15 $\mathrm{m/s}$ (chilled water)
u_f	0.20 $\mathrm{m/s}$ (for heating)
$V_b = \pi r_0^2 L_t$	r_0= 8.6 mm, L_t= 2.5 m
$V_e = \pi r_0^2 L_e$	L_e = 2.0 m, r_0= 8.6 mm
$V_c = \pi r_0^2 L_c$	L_c = 2.0 m, r_0= 8.6 mm
$\dot{m}_f$	2.08 kg/s for both beds
$\dot{m}_{cw}$	1.4 kg/s

Under cyclic steady state conditions, the performance parameters such as SCP, SHP, SDWP and COP are calculated on the basis of the cycle time (t_{cycle}) consisting of adsorption-desorption operation and pre-cooling/pre-heating time. The energy involved in evaporation (Q_e) and desorption (Q_h) are calculated by the following equations

$$Q_e = \int_0^{t_{cycle}} \frac{(\dot{m}c_p)_{cw}\,(T_{cw,i}-T_{cw,o})dt}{t_{cycle}} \tag{5.8}$$

$$Q_h = \int_0^{t_{cycle}} \frac{(\dot{m}c_p)_{hw}\,(T_{hw,i}-T_{hw,out})dt}{t_{cycle}} \tag{5.9}$$

The specific cooling power (SCP) and the coefficient of performance (COP) are written as

$$SCP = \int_0^{t_{cycle}} \frac{(\dot{m}c_p)_{cw}}{M_s} \frac{(T_{cw,i}-T_{cw,o})dt}{t_{cycle}} \tag{5.10}$$

$$COP = \frac{Q_e}{Q_h} \tag{5.11}$$

The performance of the AHP (adsorption heat pump) is assessed in terms of cycle average specific heating power (SHP) and heating coefficient of performance (COP_h) as defined by

$$SHP = \int_0^{t_{cycle}} \frac{(\dot{m}c_p)_{ad}}{M_s}\frac{(T_{ad,o}-T_{ad,i})dt}{t_{cycle}} + \int_0^{t_{cycle}} \frac{(\dot{m}c_p)_{con}}{M_s}\frac{(T_{con,o}-T_{con,i})dt}{t_{cycle}} \tag{5.12}$$

$$COP_h = \frac{(\dot{m}c_p)_{ad}\displaystyle\int_0^{t_{cycle}} \frac{(T_{ad,o}-T_{ad,i})dt}{t_{cycle}} + (\dot{m}c_p)_{con}\displaystyle\int_0^{t_{cycle}} \frac{(T_{con,o}-T_{con,i})dt}{t_{cycle}}}{(\dot{m}c_p)_{hw}\displaystyle\int_0^{t_{cycle}} \frac{(T_{hw,i}-T_{hw,out})dt}{t_{cycle}}} \tag{5.13}$$

Furthermore, the performance of the AD (adsorption desalination) system is evaluated in terms of the specific daily water production (SDWP) [6] i.e.

$$SDWP = N\int_0^{t_{cycle}} \frac{Q_{con}}{h_{fg}(T_c)M_s}dt \tag{5.14}$$

where N is the total number of cycle operated by the AD plant daily and energy involved during condensation $Q_{con} = \left(\dot{m}c_p\right)_{con}(T_{con,o} - T_{con,i})$.

5.3 Entropy flow and entropy generation modelling

The entropy change (dS) of any system consists of two terms i.e. $dS = dS_{flow} + dS_{gen}$, where the first term dS_{flow} indicates the transfer of entropy across the boundaries of the system, and the second term dS_{gen} defines the entropy production within the system [195]. The Second Law of Thermodynamics states that for an isolated system or the thermodynamics universe (system + surroundings), the entropy production inside the system is positive or zero, $dS_{gen} \geq 0$. Therefore, the rate of entropy change can be expressed by

$$\frac{dS}{dt} = \frac{dS_{flow}}{dt} + \frac{dS_{gen}}{dt} \tag{5.15}$$

The entropy generation for each component of AHT system is furnished in Table 5.2.

Table 5.2: Entropy flow and entropy generation models for AHT.

Components	Entropy flow and generation model
Evaporator	The transfer of entropy due to heat and water vapour flow inside the evaporator (outside the chilled water contained heat-exchanging tubes) becomes $\frac{dS_{flow,evap}}{dt} = -M_s \cdot \frac{dq_{ads}}{dt} \cdot \left\{\frac{h_g(P_{evap},T_{ads}) - h_g(P_{evap})}{T_{evap}}\right\} - M_s \cdot \frac{dq_{des}}{dt} \cdot \left\{\frac{h_f(T_{con}) - h_f(P_{evap})}{T_{evap}} + \left(\frac{UA}{N}\right)_{evap} \cdot \sum_{i=1}^{N} \frac{(T_i - T_{evap})}{T_{evap}}\right\}$ (5.16) where the first term of the right-hand side defines the energy flow related to the transfer of water vapour migrating from the evaporator to the adsorption-bed; the second term shows the entropy flow of liquid water from the condenser to the evaporator for de-superheating process, and the third term relates to the entropy flow due to heat transfer from N segments of evaporator tube to the evaporator. Employing Eq. (5.15), the entropy generation inside the evaporator and the chilled water inside the tube are calculated as $\frac{dS_{gen,evap}}{dt} = -M_s \cdot \frac{dq_{ads}}{dt} \cdot \left\{s_g(P_{evap}, T_{ads}) - s_g(P_{evap})\right\} + M_s \cdot \frac{dq_{ads}}{dt} \cdot \left\{\frac{h_g(P_{evap},T_{ads}) - h_g(P_{evap})}{T_{evap}}\right\} - \left(\frac{UA}{N}\right)_{evap} \cdot \sum_{i=1}^{N} \frac{(T_i - T_{evap})}{T_{evap}} + M_s \cdot \frac{dq_{des}}{dt} \cdot \left\{s_f(T_{evap}) - s_f(T_{cond})\right\} + M_s \cdot \frac{dq_{des}}{dt} \cdot \left\{\frac{h_f(T_{con}) - h_f(P_{evap})}{T_{evap}}\right\}$ (5.17) $\frac{dS_{gen,chill}}{dt} = \frac{\dot{m}_{chilled}}{N} \cdot \sum_{i=1}^{N} \left[\frac{h_f(T_{i-1}) - h_f(T_i)}{T_i} - \left\{s_f(T_{i-1}) - s_f(T_i)\right\}\right]$ (5.18) Combining these two equations, the total entropy generation in the evaporator of AHT can be written by $\frac{dS_{gen,evap,tot}}{dt} = \dot{S}_{g,evap,MT} + \dot{S}_{g,evap,HT} + \dot{S}_{g,evap,DS} + \dot{S}_{g,evap,FH}$, where the entropy generation inside the evaporator due to (i) mass transfer during adsorption ($\dot{S}_{g,evap,MT}$) and desuper-heating during desorption ($\dot{S}_{g,evap,DS}$), (ii) heat transfer into the evaporator ($\dot{S}_{g,evap,HT}$) and (iii) the flushing of chilled water ($\dot{S}_{g,evap,FH}$) inside the tube. $\dot{S}_{g,evap,MT} = -M_s \cdot \frac{dq_{ads}}{dt} \cdot \left\{s_g(P_{evap}, T_{ads}) - s_g(P_{evap})\right\} + M_s \cdot \frac{dq_{ads}}{dt} \cdot \left\{\frac{h_g(P_{evap},T_{ads}) - h_g(P_{evap})}{T_{evap}}\right\}$ (5.19) $\dot{S}_{g,evap,DS} = M_s \cdot \frac{dq_{des}}{dt} \cdot \left\{s_f(T_{evap}) - s_f(P_{cond})\right\} + M_s \cdot \frac{dq_{des}}{dt} \cdot \left\{\frac{h_f(T_{con}) - h_f(P_{evap})}{T_{evap}}\right\}$ (5.20) $\dot{S}_{g,evap,HT} = \left(\frac{UA}{N}\right)_{evap} \cdot \sum_{i=1}^{N} (T_{evap} - T_i) \cdot \left(\frac{1}{T_i} - \frac{1}{T_{evap}}\right)$ (5.21) $\dot{S}_{g,evap,FH} = \frac{\dot{m}_{chilled}}{N} \cdot \sum_{i=1}^{N} \left[\frac{h_f(T_{i-1}) - h_f(T_i)}{T_i} - \left\{s_f(T_{i-1}) - s_f(T_i)\right\}\right]$ (5.22)

Condenser	The entropy flow in the condenser occurs as a result of heat and water vapour transfer inside the condenser as given by $\frac{dS_{flow,cond}}{dt} = -M_s \cdot \frac{dq_{des}}{dt} \cdot \left\{\frac{h_g(P_{cond},T_{des}) - h_g(P_{cond})}{T_{cond}}\right\} - \left(\frac{UA}{N}\right)_{cond} \cdot \sum_{j=1}^{N} \frac{(T_{cond}-T_j)}{T_{cond}} + M_s \cdot \frac{dq_{des}}{dt} \cdot \left\{\frac{h_f(T_{con}) - h_f(P_{evap})}{T_{cond}}\right\}$ (5.23) where the first term of the right-hand side defines the energy flow related to the transfer of water vapour from the bed to the condenser, the second term indicates the entropy flow due to heat transfer from the desorbed water vapour to cooling water inside the condenser tubes, and the third term shows the entropy flow of liquid water from the condenser to the evaporator. Employing Eq. (5.15), the entropy generation inside the condenser and cooling water in tubes are given by $\frac{dS_{gen,cond}}{dt} = -M_s \cdot \frac{dq_{des}}{dt} \cdot \left\{s_g(P_{cond},T_{des}) - s_g(P_{cond}) - \frac{h_g(P_{cond},T_{des}) - h_g(P_{cond})}{T_{cond}}\right\} + \left(\frac{UA}{N}\right)_{cond} \cdot \sum_{j=1}^{N} \frac{(T_{cond}-T_j)}{T_{cond}} - M_s \cdot \frac{dq_{des}}{dt} \cdot \left\{\frac{h_f(T_{con}) - h_f(P_{evap})}{T_{cond}} - [s_f(T_{cond}) - s_f(T_{evap})]\right\}$ (5.24) $\frac{dS_{gen,cooling}}{dt} = \frac{\dot{m}_{cooling}}{N} \cdot \sum_{j=1}^{N} \left[\frac{h_f(T_j) - h_f(T_{j-1})}{T_j} - \{s_f(T_j) - s_f(T_{j-1})\}\right]$ (5.25) Combining $\frac{dS_{gen,cond}}{dt}$ and $\frac{dS_{gen,cooling}}{dt}$ the total entropy generation in the condenser is written as $\frac{dS_{gen,cond}}{dt} = \dot{S}_{g,cond,MT} + \dot{S}_{g,cond,HT} + \dot{S}_{,cond,FH}$ where the entropy generation inside the condenser is observed here for (i) the transfer of water vapour mass during desorption ($\dot{S}_{g,cond,MT}$) and desuper-heating during desorption ($\dot{S}_{g,cond,DS}$), (ii) heat transfer into the condenser tube ($\dot{S}_{g,evap,HT}$) and (iii) the flushing of chilled water ($\dot{S}_{g,evap,FH}$) inside the tube. $\dot{S}_{g,cond,MT} = -M_s \cdot \frac{dq_{des}}{dt} \cdot \left\{s_g(P_{cond},T_{des}) - s_g(P_{cond}) - \frac{h_g(P_{cond},T_{des}) - h_g(P_{cond})}{T_{cond}}\right\}$ (5.26) $\dot{S}_{g,cond,DS} = -M_s \cdot \frac{dq_{des}}{dt} \cdot \left\{\frac{h_f(T_{con}) - h_f(P_{evap})}{T_{cond}} - [s_f(T_{cond}) - s_f(T_{evap})]\right\}$ (5.27) $\dot{S}_{g,cond,HT} = \left(\frac{UA}{N}\right)_{cond} \cdot \sum_{j=1}^{N}(T_{cond} - T_j) \cdot (\frac{1}{T_j} - \frac{1}{T_{cond}})$ (5.28) $\dot{S}_{g,cond,FH} = \frac{\dot{m}_{cooling}}{N} \cdot \sum_{j=1}^{N} \left[\frac{h_f(T_j) - h_f(T_{j-1})}{T_j} - \{s_f(T_j) - s_f(T_{j-1})\}\right]$ (5.29)
Adsorption-bed	Employing the basic equation as presented in (5.15), the entropy flow and generation in the bed during adsorption process are given by $\frac{dS_{flow,ads}}{dt} = M_s \cdot \frac{dq_{ads}}{dt} \cdot \frac{\overline{\Delta H}}{T_{ads}} - \left(\frac{UA}{N}\right)_{ads} \cdot \sum_{k=1}^{N} \frac{(T_{ads}-T_k)}{T_{ads}}$ (5.30)

	$\frac{dS_{gen,ads}}{dt} = M_s \cdot \frac{dq_{ads}}{dt} \cdot \left[\frac{\overline{\Delta H}}{T_{ads}} - \left\{s_g\left(P_{evap}, T_{ads}\right) - s_f\left(P_{evap}\right)\right\}\right] + \left(\frac{UA}{N}\right)_{ads} \cdot \sum_{k=1}^{N} \frac{(T_{ads}-T_k)}{T_{ads}}$ (5.31) $\frac{dS_{gen,cool}}{dt} = \frac{\dot{m}_{cooling}}{N} \cdot \sum_{k=1}^{N} \left[\frac{h_f(T_k)-h_f(T_{k-1})}{T_k} - \left\{s_f(T_k) - s_f(T_{k-1})\right\}\right]$ (5.32) $\frac{dS_{gen,ads,tot}}{dt} = M_s \cdot \frac{dq_{ads}}{dt} \cdot \left[\frac{\overline{\Delta H}}{T_{ads}} - \left\{s_g\left(P_{evap}, T_{ads}\right) - s_f\left(P_{evap}\right)\right\}\right] + \left(\frac{UA}{N}\right)_{ads} \cdot \sum_{k=1}^{N} \frac{(T_{ads}-T_k)}{T_{ads}} + \frac{\dot{m}_{cooling}}{N} \cdot \sum_{k=1}^{N} \left[\frac{h_f(T_k)-h_f(T_{k-1})}{T_k} - \left\{s_f(T_k) - s_f(T_{k-1})\right\}\right]$ (5.33) $or, \quad \frac{dS_{gen,ads,tot}}{dt} = \dot{S}_{g,ads,MT} + \dot{S}_{g,ads,HT} + \dot{S}_{g,ads,FH},$ where the total entropy generation in the bed during adsorption process are due to (i) mass transfer into the porous materials ($\dot{S}_{g,ads,MT}$), (ii) the heat transfer between the adsorption bed and the cooling water inside the heat exchanger tube ($\dot{S}_{g,ads,HT}$), and (iii) the mass transfer of cooling water in and out of the tubes ($\dot{S}_{g,ads,FH}$). These terms are separately written as $\dot{S}_{g,ads,MT} = M_{MOFs} \cdot \frac{dq_{ads}}{dt} \cdot \left[\frac{\overline{\Delta H}}{T_{ads}} - \left\{s_g\left(P_{evap}, T_{ads}\right) - s_f\left(P_{evap}\right)\right\}\right]$ (5.34) $\dot{S}_{g,ads,HT} = \left(\frac{UA}{N}\right)_{ads} \cdot \sum_{k=1}^{N} \frac{(T_{ads}-T_k)}{T_{ads}}$ (5.35) $\dot{S}_{g,ads,FH} = \frac{\dot{m}_{cooling}}{N} \cdot \sum_{k=1}^{N} \left[\frac{h_f(T_k)-h_f(T_{k-1})}{T_k} - \left\{s_f(T_k) - s_f(T_{k-1})\right\}\right]$ (5.36)
Desorption-bed	Similarly, employing the basic equation (5.15), the entropy flow and generation in the bed during desorption process are given by $\frac{dS_{flow,des}}{dt} = M_s \cdot \frac{dq_{des}}{dt} \cdot \frac{\overline{\Delta H}}{T_{des}} + \left(\frac{UA}{N}\right)_{des} \cdot \sum_{m=1}^{N} \frac{(T_{des}-T_m)}{T_{des}}$ (5.37) $\frac{dS_{gen,des}}{dt} = -M_s \cdot \frac{dq_{des}}{dt} \cdot \left[\frac{\overline{\Delta H}}{T_{des}} - \left\{s_g(P_{cond}, T_{des}) - s_f(P_{cond})\right\}\right] + \left(\frac{UA}{N}\right)_{des} \cdot \sum_{m=1}^{N} (T_m - T_{des}) \cdot \left(\frac{1}{T_{des}} - \frac{1}{T_m}\right)$ (5.38) $\frac{dS_{gen,hot}}{dt} = \frac{\dot{m}_{hot}}{N} \cdot \sum_{k=1}^{N} \left[\frac{h_f(T_{m-1})-h_f(T_m)}{T_m} - \left\{s_f(T_{m-1}) - s_f(T_m)\right\}\right]$ (5.39) $\frac{dS_{gen,des,tot}}{dt} = -M_s \cdot \frac{dq_{des}}{dt} \cdot \left[\frac{\overline{\Delta H}}{T_{des}} - \left\{s_g(P_{cond}, T_{des}) - s_f(P_{cond})\right\}\right] + \left(\frac{UA}{N}\right)_{des} \cdot \sum_{m=1}^{N} (T_m - T_{des}) \cdot \left(\frac{1}{T_{des}} - \frac{1}{T_m}\right) + \frac{\dot{m}_{hot}}{N} \cdot \sum_{k=1}^{N} \left[\frac{h_f(T_{m-1})-h_f(T_m)}{T_m} - \left\{s_f(T_{m-1}) - s_f(T_m)\right\}\right]$ (5.40) $\frac{dS_{gen,des}}{dt} = \dot{S}_{g,des,MT} + \dot{S}_{g,des,HT} + \dot{S}_{g,des,FH}$

	where the total entropy generation in the bed during desorption process occurs by (i) mass transfer out of the porous materials ($\dot{S}_{g,des,MT}$), (ii) the heat transfer between the adsorption bed and the hot water inside the heat exchanger tube ($\dot{S}_{g,des,HT}$), and (iii) the mass transfer of hot water in and out of the tubes ($\dot{S}_{g,des,FH}$). These terms are separately written as $\dot{S}_{g,des,MT} = -M_s \cdot \frac{dq_{des}}{dt} \cdot \left[\frac{\overline{\Delta H}}{T_{des}} - \left\{s_g(P_{cond}, T_{des}) - s_f(P_{cond})\right\}\right] \qquad (5.41)$ $\dot{S}_{g,des,HT} = \left(\frac{UA}{N}\right)_{des} \cdot \sum_{m=1}^{N}(T_m - T_{des}) \cdot \left(\frac{1}{T_{des}} - \frac{1}{T_m}\right) \qquad (5.42)$ $\dot{S}_{g,des,FH} = \frac{\dot{m}_{hot}}{N} \cdot \sum_{k=1}^{N}\left[\frac{h_f(T_{m-1}) - h_f(T_m)}{T_m} - \left\{s_f(T_{m-1}) - s_f(T_m)\right\}\right] \qquad (5.43)$

5.4 Adsorption isotherms and kinetics

The water uptake, q as a function of pressure (P) and temperature (T) under equilibrium condition is calculated by [196] $q = q^0 \frac{\alpha \exp[m(Q_{st}^* - h_{fg})/RT] . \left(\frac{P}{P_s}\right)^m}{1 + \left(\alpha \exp[m(Q_{st}^* - h_{fg})/RT] - 1\right) . \left(\frac{P}{P_s}\right)^m}$, where q^0 is the limiting uptake, α defines the pre-exponential coefficient, m denotes the heterogeneous coefficient, Q_{st}^* represents the isosteric heat at zero coverage and h_{fg} stands for the evaporation-enthalpy. In addition, R is the universal gas constant. On the other hand the uptake rates are estimated by [98] $\frac{dq}{dt} = k_{ads}\,(1 - q)\left(\frac{P}{P_s}\right)^m - k_{des}\, q\left[1 - \left(\frac{P}{P_s}\right)^m\right]$, where the isotherm coefficient $K = k_{ads}/k_{des}$ and $k_{ads} = \frac{MP}{\sqrt{2\pi MRT}}\beta_0 \exp\,(E_a/RT) A_s$. Here A_s is the specific surface area, β_0 is the frequency factor; E_a represents the activation energy and M is the adsorbate molecular weight. Both the isotherms and kinetics equations are fitted with experimentally confirmed data of MOFs + water systems and the curve fitting parameters for isotherms and kinetics are furnished in Table 5.3 and Table 5.4. The errors of experimental data range from 2 to 10%. It is noted that the frequency factor β_0 is equivalent to 1 since a thin adsorbent layer is considered for modelling purposes.

Table 5.3: Adsorption isotherms parameters for assorted MOFs + water systems.

System	q^0 (kg/kg)	Q_{st}^* (kJ/kg)	m	α
Al-Fum+Water	0.40	2786.5	6.8	9.98×10^{-5}
5%Li-Al-Fum+Water	0.41	2861.4	5.7	1.86×10^{-5}
30%AFI-Al-Fum+Water	0.34	2877.5	5.6	1.12×10^{-5}
30%CHA-Al-Fum+Water	0.39	2781.2	5.9	3.49×10^{-4}
UiO-66 +Water	0.45	2566.5	8.0	4.41×10^{-1}
N-UiO-66 +Water	0.38	2723.4	2.2	9.15×10^{-1}
OH-UiO-66 +Water	0.19	2974.1	2.1	2.93×10^{-2}
NH_2-UiO-66 +Water	0.41	2601.8	6.3	9.49×10^{-1}
MOF-801+Water	0.31	3132.5	3.2	4.54×10^{-3}
$(CH_3)_2$-MOF-801+Water	0.30	3110.5	3.3	7.78×10^{-4}

Table 5.4: Parameters of adsorption kinetics equations for assorted MOFs + water systems.

System	k_{ads}(1/s)	$E_{a@30℃}$(J/mol)	β_0	k_{des}(1/s)	$E_{a@60℃}$(J/mol)
Al-Fum+Water	1.177	41200	1	0.0041	40100
5%Li-Al-Fum+Water	1.183	41100	1	0.0039	43500
30%AFI-Al-Fum+Water	1.122	42700	1	0.0052	42600
30%CHA-Al-Fum+Water	2.177	39500	1	0.0068	40780
UiO-66 +Water	0.645	43200	1	0.0017	43000
N-UiO-66 +Water	0.135	46800	1	0.0055	47600
OH-UiO-66 +Water	0.334	43100	1	0.0062	46400
NH_2-UiO-66 +Water	0.774	42050	1	0.0019	41000
MOF-801+Water	1.694	39800	1	0.0037	43300
$(CH_3)_2$-MOF-801+Water	3.193	37900	1	0.0061	42000

5.5 Temperature-entropy Analysis

The entropy generation for each component of AHT system for cooling/heat pump and desalination systems are presented from transient to cyclic steady state. The operational behaviour is reflected by the change in internal storage temperature of each component as well as the thermal source and sink temperatures of the AHT system. The inlet temperature of hot water is one variable ranging from 60 °C to 80 °C, and the other variable is cooling water inlet temperature as 30 ^{o}C whereas the chilled water outlet temperature is maintained at 12 ^{o}C for cooling/heat pump operations. The other key parameter to be analysed is the adsorption/desorption cycle time, which ranges from 150 s to 1000 s.

From the $\dot{S}_{gen}$ analysis, one can easily know the following information:

(i) which component (desorber, adsorber, condenser or evaporator) generates the highest proportion of the entropy change and which component generates the least;

(ii) which operation process (mass transfer, heat transfer, flushing or de-superheating) generates the highest proportion of the entropy change and which operation process generates the least;

(iii) the optimum operation cycle time and regeneration temperature which result in the least $\dot{S}_{gen}$.

Because of that $\dot{S}_{gen}$ is directly related to the dissipative losses during the AHT operation process and it has a significant effect on the performance of AHT system. These $\dot{S}_{gen}$ information provide valuable references on the AHT system design and AHT performance improvement. For example, based on the information of $\dot{S}_{gen}$ inside each component, re-implementation works can be performed to multiple adsorber-desorber beds [197]. From the information of $\dot{S}_{gen}$ raises from each process, specific heat and mass recovery schemes could be applied for AHT operation [198]. In addition, by analysing the effect of cycle time and regeneration temperature on $\dot{S}_{gen}$, optimised cycle time allocations and heat input can be selected [199]. Furthermore, by comparing the $\dot{S}_{gen}$ among different MOF materials, adsorbents with the strongest host-guest interaction and least $\dot{S}_{gen}$ can be tailored and fabricated.

5.5.1 Al-Fum/composites + water systems

The temporal history of entropy generation (W/K) for each component of AHT system under batch operating condition is shown in Figure 5.4. Hence, the results are presented for various assorted matrials such as parent aluminium fumarate (Al-fum) and Al-fum/zeolite composites plus water systems. These results are simulated for the operating conditions of 14.8 °C, 30 °C and 80 °C as the chilled water, the cooling water, and the hot water inlet temperature, respectively. Secondly, the adsorption-desorption time and the switching time are considered 500 s and 25 s. It is observed that the desorption-bed generates the most percentage of the entropy, followed by the adsorption-bed, evaporator, and condenser in the descending order. The entropy generation ($\dot{S}_{gen}$) inside the sorption heat exchanger is mainly due to the heat transfer (cooling/heating surge) from external source and the mass transfer (water vapour during adsorption/desorption) from the evaporator or to the condenser. Furthermore, the $\dot{S}_{gen}$ in the evaporator is the results of (i) heat transfer to the chill-water, (ii) mass transfer to the bed, (iii) flushing of fluids inside the evaporator tubes and (iv) mass transfer from the condenser to the evaporator. On the other hand, the $\dot{S}_{gen}$ in the condenser is due to (i) the heat transfer from desorbed water vapour to the cooling water through the condenser tubes, (ii) the mass transfer from the bed, (iii) the flushing of liquid fluid in the condenser tubes and (iv) the mass transfer from the condenser. The various effects of entropy generation for each component of AHT system are also provided in the Appendix. It is found that the entropy generation in each thermal storage component increases at the beginning of adsorption/desorption due to the transfer of more water vapour as latent heat, and the enthalpy of adsorption is found higher at the beginning of adsorption. For both adsorption and desorption beds, the entropy generation drops slightly when adsorption/desorption progresses as the adsorption/desorption rate decreases. It is also found that the most entropy generation is attributed to the heat and mass transfer during adsorption and desorption processes whilst the fluid flushing inside the tubes does not contribute significantly to the entropy generation. It should be noted here that the entropy generation reflects the batch-operation process of the AHT cycle and there is a sudden surge in the entropy generation during the switching process.

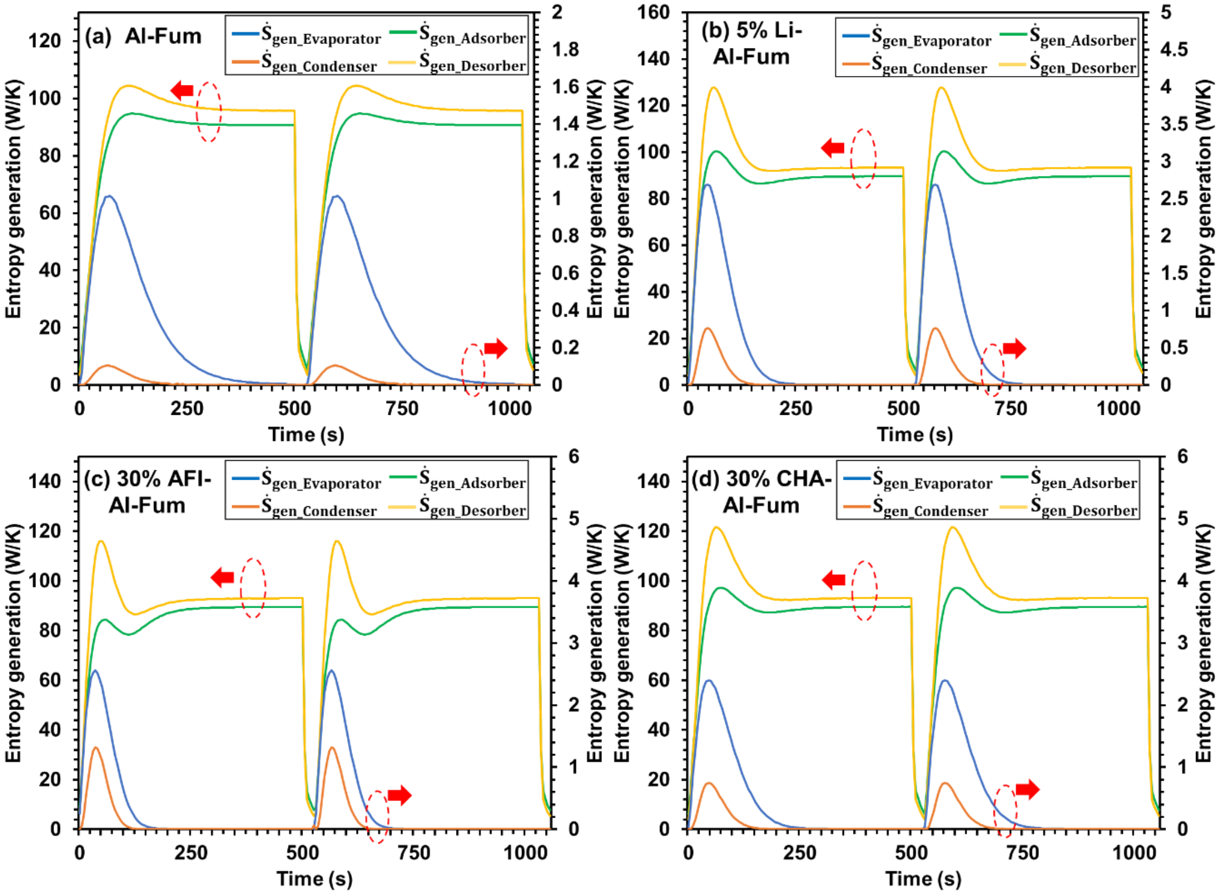

Figure 5.4: The entropy generation ($\dot{S}_{gen}$) for the main components of the Al-Fum + water based AHT system at the regeneration temperature of 80 °C: (a) Al-Fum; (b) 5% Li-Al-Fum; (c) 30% AFI-Al-Fum and (d) 30% CHA-Al-Fum.

The higher entropy generation obtained in the bed are ranked as: 5% Li-Al-Fum (Fig. 5.4b) > 30% CHA-Al-Fum (Fig. 5.4d) > 30% AFI Al-Fum (Fig. 5.4c) > parent Al-Fum (Fig. 5.4a). The parent Al-Fum based AHT provides the least $\dot{S}_{gen}$ as compared with the modified materials, which is due to its poor interaction with water or longer hydrophobic length at the beginning of adsorption. On the other hand, for evaporator and condenser cases, relatively higher entropy generation is entailed at the beginning of each cycle. This is due to the fact that more water vapour is adsorbed into the unsaturated adsorbent during adsorption-triggered-evaporation as well as desorbed from the saturated adsorbent during desorption-activated-condensation. The entropy generation detects the nature of heat and mass transfer inside the evaporator and the condenser. However, these contributions are very small as compared with those found in the adsorber and the desorber. For example, the highest $\dot{S}_{gen}$ in the evaporator, condenser, adsorber and desorber is 0.99 W/K, 0.50 W/K, 94.68 W/K and 104.01 W/K for the parent Al-Fum, respectively. By adding the hydrophilic lithium dopants or AFI/CHA type zeolite into the structure of the Al-Fum, the hydrophobic length is decreased with the increase in adsorption kinetics, which enhances the interactions of water vapour into the porous adsorbents. Therefore, the entropy flow and generation increase in each component of the AHT. The simulation results show that the $\dot{S}_{gen}$ in the evaporator, condenser, adsorber and desorber of 5% Li-doped AL-Fum MOFs based AHT are increased up to 2.68 W/K, 1.55 W/K, 107.77 W/K and 127.21 W/K, respectively.

Figure 5.5 (a – d) shows the $\dot{S}_{gen}$ for each component of the parent Al-Fum, Li-doped and zeolite-Al-Fum composites + water based adsorption heat transformation systems in which the regeneration temperatures vary from 60 to 80 ℃ with the optimum half cycle time of 500 s. With the increase in regeneration temperature, the $\dot{S}_{gen}$ increases for each component of AHT systems. The higher regeneration temperature in the thermal compressor results in the greater temperature gap between the adsorption and the desorption beds. Therefore, the pressure difference also increases during batch operation of AHT and the irreversibility increases. In other words, with the input of higher thermal energy, the enhanced heat and mass transfer leads to larger entropy production in adsorbed water vapour, especially at the initial stage of adsorption/desorption. Additionally, the $\dot{S}_{gen}$ by the desorption-bed is the highest followed by the adsorption-bed, the evaporator, and the condenser in descending order. Furthermore, the entropy generation in every component escalates with the increase of hot water inlet temperature along with the cooling capacity, which is because of that the cooling capacity is an increasing function of hot water inlet temperature. At the regeneration temperatures ranging from 60 °C to 80 ^{o}C, the overall $\dot{S}_{gen}$ for the parent Al-Fum, Li-doped and Al-Fum/zeolite composites are summarised as: 5% Li-Al-Fum > 30% AFI-Al-Fum > 30% CHA-Al-Fum > Al-Fum. This is due to the fact that with the addition of lithium ions or zeolite adsorbents into the parent aluminium fumarate MOF, the hydrophilicity at low pressure region is enhanced. Therefore, more water vapours are adsorbed at the beginning of adsorption with higher enthalpy of adsorption, and the entropy generation in the bed increases. In addition, the higher hot water inlet temperature enhances the desorption rates which provides more de-super-heating process inside the evaporator and the condenser and results in higher entropy generation. Furthermore, the higher regeneration temperature provides large temperature lift (ΔT) inside the adsorption bed resulting in higher $\dot{S}_{gen}$ in both adsorption and desorption beds. At 60 °C, the maximum $\dot{S}_{gen}$ values for water adsorption on 5% Li-Al-Fum, 30% AFI-Al-Fum, 30% CHA-Al-Fum and the parent Al-Fum are found to be 34.11 W/K, 33.16 W/K, 33.64 W/K, and 32.98 W/K), respectively. It should also be noted here that the entropy generations for the modified MOFs and composite structures are found due to higher adsorption/desorption kinetics. As the regeneration temperature increases up to 80 °C, the overall $\dot{S}_{gen}$ of all the Al-Fum based MOFs could be ranked as: 5% Li-Al-Fum > 30% CHA-Al-Fum > 30% AFI-Al-Fum > Al-Fum. The higher $\dot{S}_{gen}$ also relates to the higher uptake-offtake difference per cycle (understanding from isotherm graphs). For example, 5% Li-Al-Fum delivers the most water vapour (Δq) whilst Al-Fum transfers the least Δq per operation cycle.

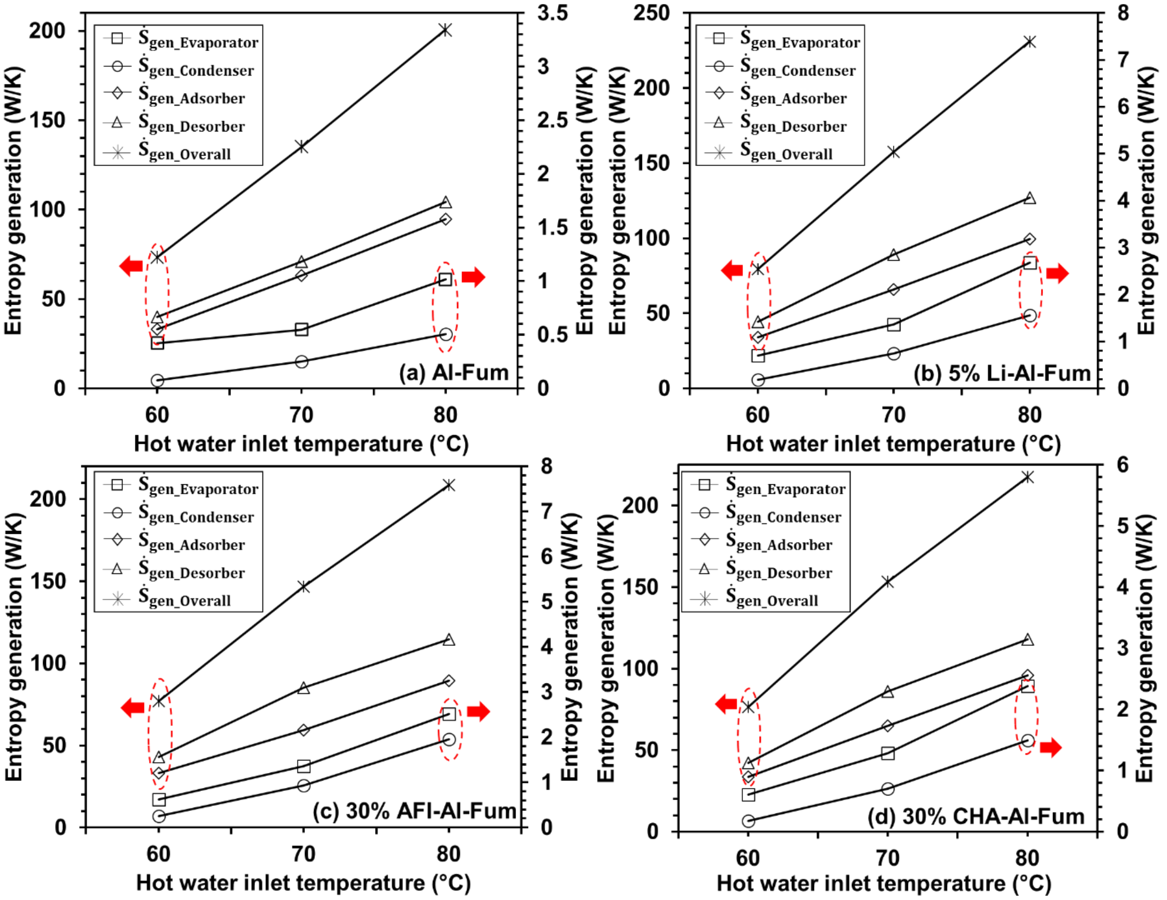

Figure 5.5: Entropy generation analysis for each component (evaporator, condenser, adsorber and desorber) of original and modified Al-Fum based AHT operation cycle at various regeneration temperatures: (a) Al-Fum; (b) 5% Li-Al-Fum; (c) 30% AFI-Al-Fum and (d) 30% CHA-Al-Fum. (The AHT working conditions: 25 s/500 s/14.8 °C/30 °C/60 °C - 80 °C)

5.5.2 Functional-UiO-66 (Zr) MOFs + water systems

The effects of the regeneration temperature on entropy generation for UiO-66 (Zr) based AHT systems are presented in Figure 5.6, where the chilled water and the cooling water inlet are maintained 14.8 and 30 ^{o}C, respectively whilst the operation and the switching times are 500 s and 25 s. It is found that the $\dot{S}_{gen}$ (entropy generation) for all the major components increases monotonically with the increase in regeneration temperature due to the fact that the heat exchange between the heat exchanger and adsorbent materials is enhanced with the increase of irreversibility and the $\dot{S}_{gen}$ inside the adsorption bed is increased. Additionally, the higher regeneration temperature also leads to the generation of more water vapour through the desorption process. Therefore, larger mass transfer of water vapour are resulted during desorption-activated-condensation process plus liquid water during condenser-evaporator interaction process, which increase the entropy generation for each component of the AHT. On the other hand, at very high regeneration temperature, the water vapour transfer per AHT cycle is not increased due to the structural capacity of adsorbent materials. As a result, the extra heating energy is not properly utilised, which also increases the entropy generation of the bed. Hence, higher $\dot{S}_{gen}$ are observed in all the major parts of the AHT system. At the regeneration temperature of 60 °C – 80 °C, the total $\dot{S}_{gen}$ could be ranked as: parent UiO-66 > NH_2-UiO-66 > N-UiO-66 > OH-UiO-66. The maximum $\dot{S}_{gen}$ as found in the parent UiO-66 (Zr) based AHT system is due to its super-hydrophobic behaviours as well as the slow adsorption kinetics with water adsorption. In addition, the weak interactions between water vapour and adsorbent materials lead to the waste of the thermal input (in terms of cooling and heating) in the adsorption beds, as the water uptake-offtake difference per cycle is not improved even though more heating and cooling are provided to the beds. Higher entropy generation for the parent UiO-66 (Zr) + water systems results in the lower performances in terms of cooling and heat pumping capacities. After implanting the hydrophilic functional groups onto the UiO-66 (Zr) structure, the shorter hydrophobic length in low pressure region is obtained, which results in the faster adsorption kinetics with stronger affinity to the water vapour. Therefore, for functional-

UiO-66 (Zr) MOFs + water assisted AHT systems, the thermal input to the thermal compressor is utilised more efficiently, which results in the lower entropy generation with higher cooling or heating capacity and the COP. For example, at the regeneration temperature of 60 °C, the total entropy generation (i.e. the summation of all components of AHT system) $\dot{S}_{gen\_overall}$ for UiO-66 (Zr), NH_2-UiO-66 (Zr), N-UiO-66 (Zr) and OH-UiO-66 (Zr) are calculated 73.07 W/K, 71.47 W/K, 70.28 W/K and 68.82 W/K, respectively. On the other hand, the $\dot{S}_{gen\_overall}$ are found evident at higher regeneration temperature of 80 °C and the $\dot{S}_{gen\_overall}$ is found to be 191.22 W/K, 188.03 W/K, 180.86 W/K and 178.26 W/K for UiO-66 (Zr), NH_2-UiO-66 (Zr), N-UiO-66 (Zr) and OH-UiO-66 (Zr), respectively.

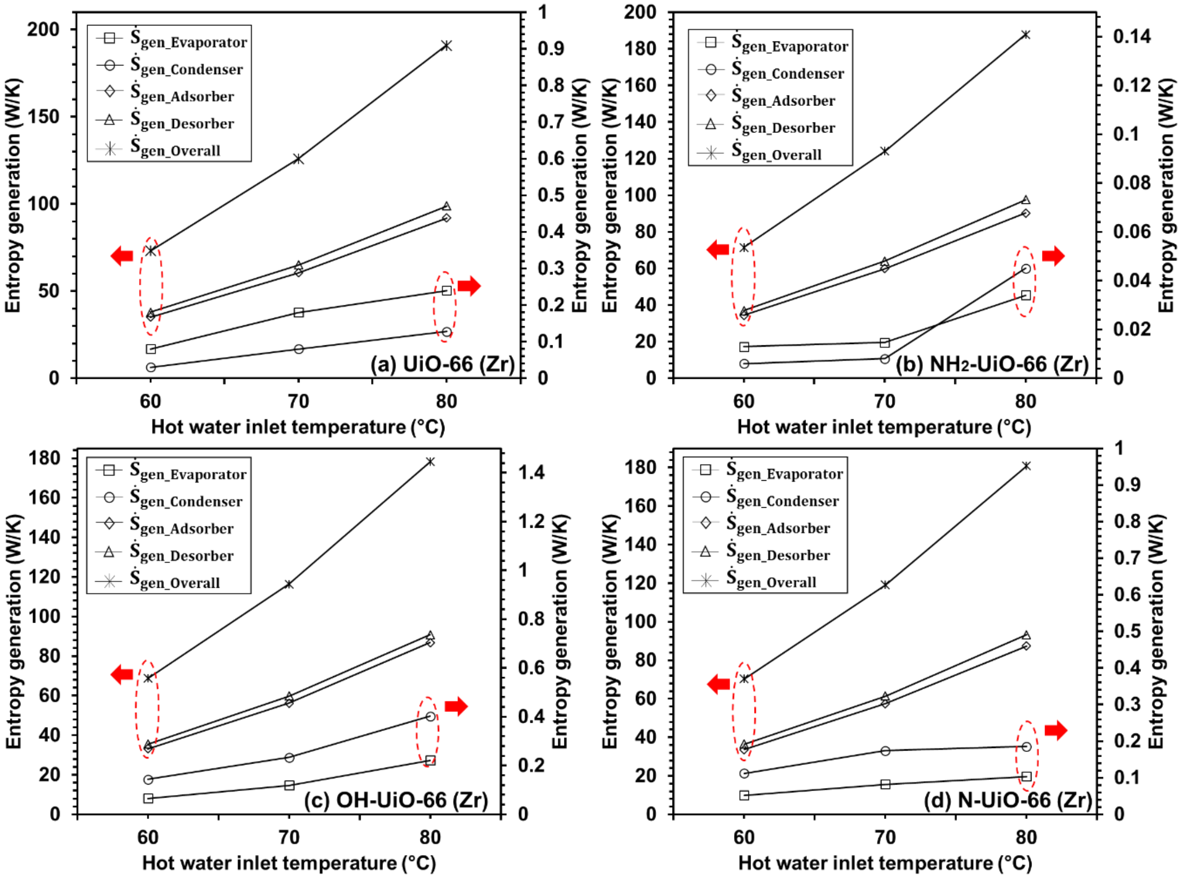

Figure 5.6: Entropy generation analysis for each components (evaporator, condenser, adsorber and desorber) of original and functionalised UiO-66 (Zr) based AHT operation cycle at various

regeneration temperatures: (a) UiO-66 (Zr); (b) NH_2-UiO-66 (Zr); (c) OH-UiO-66 (Zr) and (d) N-UiO-66 (Zr). (The AHT working conditions: 25 s/500 s/14.8 °C/30 °C/60 °C-80 °C)

The entropy generation ($\dot{S}_{gen}$) profiles under steady state conditions for each component (evaporator, condenser, adsorption-bed and desorption-bed) of NH_2-UiO-66 (Zr) – water based AHT (for cooling conditions) are shown in Table 5.5. At the beginning of the half cycle period (i.e. switching time + operation time), the entropy generation inside the evaporator increases, which is related to the displacement of the water vapour from evaporator to the adsorption-bed. The same phenomenon is found in the condenser, where the desorbed water vapour is transferred for condensation. Furthermore, the entropy due to de-superheating of the evaporator is caused by the returning of condensed water from condenser to evaporator. The increases in $\dot{S}_{gen}$ due to heat transfer are found during the pre-heating and pre-cooling stages for both adsorption and desorption beds, which indicate that the temperature gap between the adsorption bed and the thermal fluid is the main reason for entropy production inside the AHT system. The evident mass transfer suggests an increased randomness at the adsorbate - adsorbent interface during water adsorption/desorption process, which is related to the displacement of water vapour on the pores of NH_2-UiO-66 (Zr) MOF. The overall $\dot{S}_{gen}$ inside the desorption-bed is higher than that of the adsorption-bed, which is because of the fact that at the beginning of pre-heating process, the pores of the NH_2-UiO-66 (Zr) are assumed to be filled with water vapour, and the heat applied to adsorbents is not completely used. Therefore, a large amount of entropy is produced due to the significant temperature difference (ΔT) between the adsorption bed and the heating source, as well as the intense mass transfer of water vapour caused by ΔT. Concomitantly, a continuous decrease of $\dot{S}_{gen}$ is observed when the adsorption bed approaches the heat source temperature and desorbed phase saturation, hence, the irreversibility of the AHT system is reduced, and the relatively steady generation of entropy is found.. The present analysis shows that the overall $\dot{S}_{gen}$ of each component is summarised as: $\dot{S}_{gen-desorption}$ > $\dot{S}_{gen-adsorption}$ > $\dot{S}_{gen-evaporator}$ > $\dot{S}_{gen-condenser}$.

From Table 5.5, it is observed that for NH_2-UiO-66 (Zr) and water assisted AHT system (i) the mass transfer is the main entropy generation source (around 80%) for the evaporator and condenser, whilst the entropy generation inside the sorption-beds is dominated by the heat transfer (> 95%); (ii) the effect of the entropy generation inside the evaporator and condenser is small as compared to that of the sorption-bed; (iii) the mass transfer (liquid water) during the evaporation–adsorption process produces the least entropy generation; and (iv) the flushing $\dot{S}_{gen}$ inside the heat-exchanger tubes for all the components are found negligible (< 0.01 W/K). Hence, these founding suggests that the major $\dot{S}_{gen}$ is attributed to the internal entropy generation (mass transfer and heat transfer) rather than the external ones (fluid flushing).

Table 5.5: Entropy generation ($\dot{S}_{gen}$) study on the major components of the NH_2-UiO-66 (Zr) MOFs based AHT systems with the highlighting of the contributions by processes*.

	$\dot{S}_{gen,MT}$ (W/K)	$\dot{S}_{gen,HT}$ (W/K)	$\dot{S}_{gen,FH}$ (W/K)	$\dot{S}_{gen,DS}$ (W/K)	$\dot{S}_{gen,overall}$ (W/K)
Evaporator	0.019	0.003	0.003	0.013	0.038
Condenser	0.023	0.028	0.002	-	0.053
Adsorber	0.47	90.93	12.81	-	104.21
Desorber	0.29	97.50	16.13	-	113.92

* Operating conditions: switching time/ operating time = 25 s/ 500 s; chilled water inlet/cooling water inlet/regeneration temperature = 14.8 °C/30 °C/80 °C.

5.5.3 MOF-801 (Zr) + water systems

Figure 5.7 shows the effects of the regeneration temperatures on the entropy generation for both functional and parent MOF-801 (Zr) + water based AHT systems. The major $\dot{S}_{gen}$ are found in thermal heat exchanger per adsorption-desorption cycle whereas the minimum $\dot{S}_{gen}$ effects are captured in evaporation/condensation processes (< 1.0 W/K). The $\dot{S}_{gen}$ for each component increases with temperature. The present formulation shows that the total $\dot{S}_{gen}$ of parent MOF-801 (Zr) > $(CH_3)_2$-MOF-801 (Zr). At the regeneration temperature of 60 °C, 70 °C and 80 °C, the $\dot{S}_{gen\_overall}$ for the parent MOF-801 (Zr) are 72.53 W/K, 120.17 W/K and 183.0 W/K, respectively. For $(CH_3)_2$-MOF-801 (Zr), these values are 70.11 W/K, 113.86 W/K and 166.38 W/K, respectively. As the regeneration temperature increases, the $\dot{S}_{gen\_overall}$ differences between the parent and functional MOF-801 (Zr) becomes bigger, which indicates that the thermal input is better utilised in $(CH_3)_2$-MOF-801 (Zr) at higher regeneration temperatures and therefore, better AHT performances are expected in terms of cooling/heating capacities, COP and daily water production.

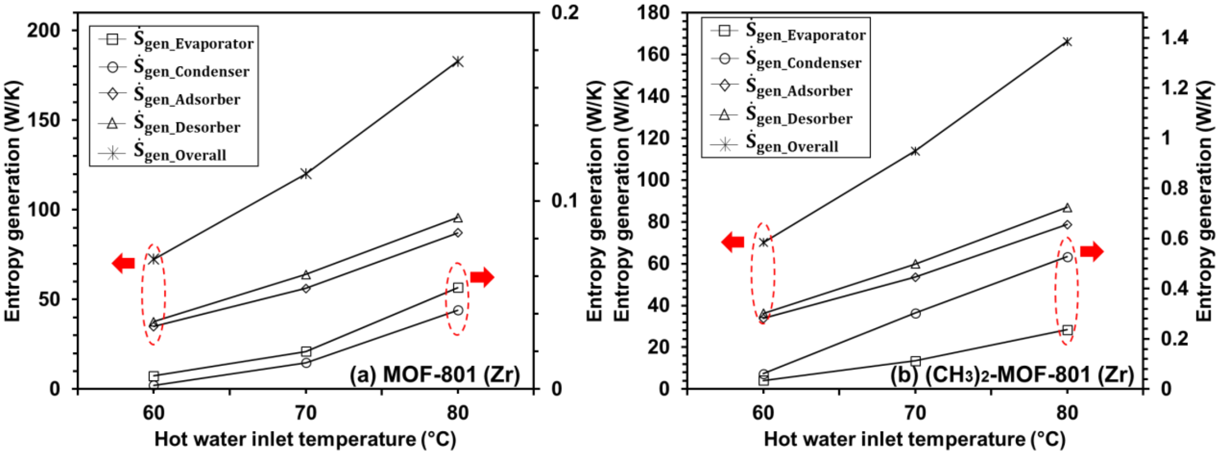

Figure 5.7: Entropy generation analysis for each component (evaporator, condenser, adsorber and desorber) of original and modified MOF-801 (Zr) based AHT operation cycle at various regeneration temperatures: (a) MOF-801 (Zr) and (b) $(CH_3)_2$-MOF-801 (Zr). (The AHT working conditions: 25 s/500 s/14.8 °C/30 °C/60 °C-80 °C)

The factors of $\dot{S}_{gen}$ for each component of the synthesised $(CH_3)_2$-MOF-801 (Zr) + water systems are furnished in Table 5.6, from which one can analyse the $\dot{S}_{gen}$-contribution of each process. Hence, the switching time, half-cycle time, chilled water inlet, cooling water inlet and hot water inlet temperature are 25 s, 500 s, 14.8 °C, 30 °C and 80 °C, respectively. The $\dot{S}_{gen}$ raised in the evaporator is mainly caused by the mass transfer and the de-superheating of water vapour generated from the condenser. The main contribution to entropy generation inside the bed is due to the heat transfer. In condenser, the heat-transfer contributions for $\dot{S}_{gen}$ are higher as compared to that of the evaporator.

Table 5.6: Entropy generation ($\dot{S}_{gen}$) study on the major components of the $(CH_3)_2$-MOF-801 (Zr) MOFs based AHT systems with the highlighting of the contributions by processes*.

	$\dot{S}_{gen,MT}$ (W/K)	$\dot{S}_{gen,HT}$ (W/K)	$\dot{S}_{gen,FH}$ (W/K)	$\dot{S}_{gen,DS}$ (W/K)	$\dot{S}_{gen,overall}$ (W/K)
Evaporator	0.17	0.021	0.002	0.041	0.23
Condenser	0.074	0.46	0.002	-	0.54
Adsorber	4.21	77.96	10.31	-	92.48
Desorber	9.04	81.86	13.22	-	104.12

* Operating conditions: switching time/ operating time = 25 s/ 500 s; chilled water inlet/cooling water inlet/regeneration temperature = 14.8 °C/30 °C/80 °C.

5.6 Temperature-entropy maps

Temperature-entropy **for adsorption cooling/heat pump**

The temperature-entorpy (*T*-*s*) diagrams for the operating conditions of each component of adsorption cooling/heat pump are shown in Figure 5.8. To understand the MOFs' performances, the functional adsorbents such as 30% CHA-Al-Fum, $(CH_3)_2$-MOF-801 (Zr) and NH_2-UiO-66 (Zr) plus water systems are added in Figure 5.8. These results are presented on the operating conditions of the chilled water/cooling water/hot water inlet temperature of 14.8 °C/30 °C/80 °C. The *T*-*s* maps are plotted here under the optimal operation conditions of maximum heating/cooling power, where the half cycle times for $(CH_3)_2$-MOF-801 (Zr), 30% CHA-Al-Fum and NH_2-UiO-66 (Zr) are optimised 500 s, 700 s and 1000 s, respectively. From the *T*-*s* diagrams, one can see that closed loops are formed (Fig. 5.8a, Fig. 5.8b and Fig. 5.8c) at all the internal energy storage components. From Figure 5.8 (a), it is found that during the switching period, the evaporator temperature rises from 13.3 °C to 14.6 °C for the $(CH_3)_2$-MOF-801 (Zr) AHT system whilst the $\dot{S}_{gen}$ increases from 0 up to 0.306 W/K. Similar profiles are observed for 30% CHA-Al-Fum and NH_2-UiO-66 (Zr) AHT systems where larger $\dot{S}_{gen}$ (0.40 W/K, 0.72 W/K, respectively) are obtained within the similar temperature ranges. For *T*-*s* maps of condenser as shown in Figure 5.8 (b), NH_2-UiO-66 (Zr) AHT system exhibits the largest $\dot{S}_{gen}$ (0.94 W/K) with a larger temperature gap (29.9 °C to 32.8 °C). On the other hand, smaller temperature changes are found for $(CH_3)_2$-MOF-801 (Zr) and 30% CHA-Al-Fum AHT systems during the swtiching period where the highest temperature of the condenser is around 32.1 °C, and the highest $\dot{S}_{gen}$ values are 0.37 W/K and 0.71 W/K, respectively. Furthermore, as shown in Figure 5.8 (c), it is found that during the pre-heating + desorption processes (for the temperature ranges from 30 °C to 80 °C), the NH_2-UiO-66 (Zr) AHT system generates the largest $\dot{S}_{gen}$ (97.43 W/K) whilst the $(CH_3)_2$-MOF-801 (Zr) + water system provides lower $\dot{S}_{gen}$ (89.29 W/K). As can be seen from Figure 5.8 (c), the temperautre difference between the hot water inlet and the desorption bed for $(CH_3)_2$-MOF-801 (Zr) is higher as compared with 30% CHA-Al-Fum or NH_2-UiO-66 (Zr) + water systems due to the strong hydrophilic behaviours of MOF-801(Zr) adsorbent. Therefore, large amounts of the heating energy are required to desorb the water vapour from the pores of the $(CH_3)_2$-MOF-801 (Zr) structure. On the contrary, the desorption process could be completed under lower desorption temperature for the materials with longer hydrophobic length such as 30% CHA-Al-Fum, and NH_2-UiO-66 (Zr) + water systems. The overall $\dot{S}_{gen}$ is summarised as: NH_2-UiO-66 (Zr) > CHA-Al-Fum > $(CH_3)_2$-MOF-801 (Zr), which suggest that $(CH_3)_2$-MOF-801 (Zr) can achieve relatively higher SCP under moderate half cycle time.

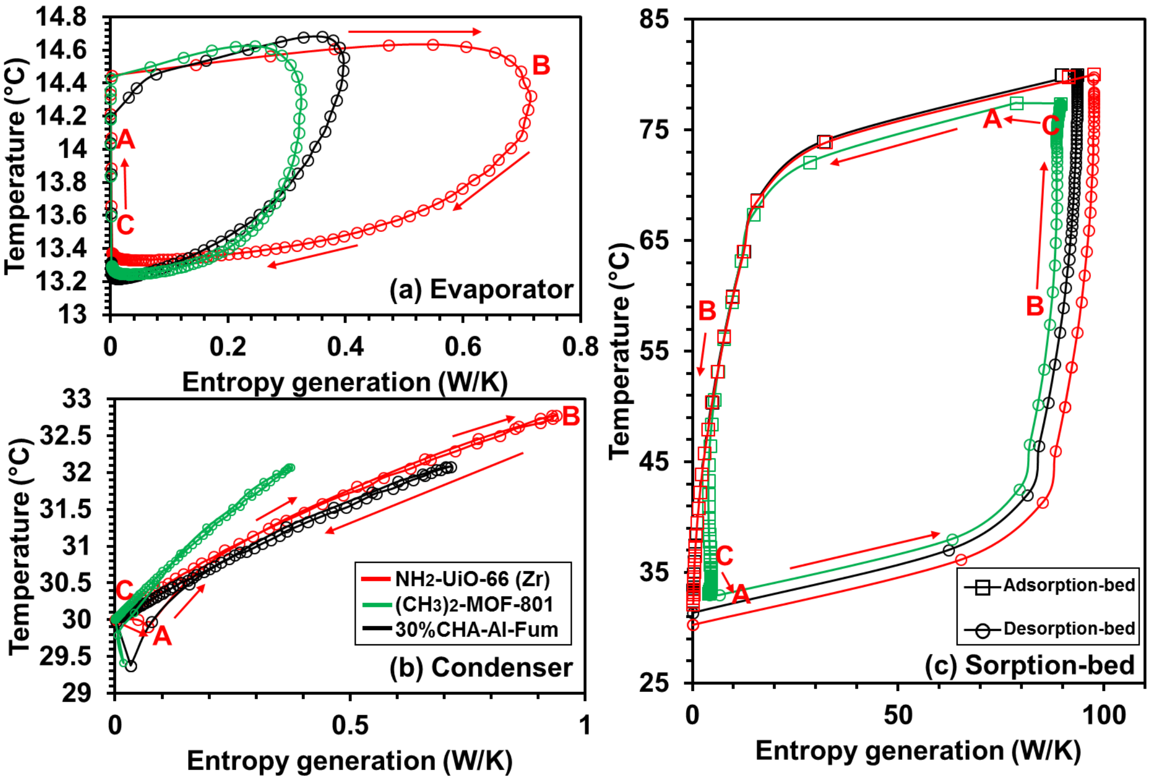

Figure 5.8: Temperature-entropy (T-s) maps of 30% CHA-Al-Fum composite vs $(CH_3)_2$-MOF-801 (Zr) vs NH_2-UiO-66 (Zr) system under cyclic-steady-state: (a) Evaporator; (b) Condenser and (c) Adsorption/Desorption-bed. Here, A→B represents the switching period (pre-cooling or pre-heating) process and B→C indicates the half-cycle-operation (adsorption/desorption) process under adsorption cooling condition. Here, the red line indicates the NH_2-UiO-66 (Zr), the green line is the $(CH_3)_2$-MOF-801 (Zr) and the black line represents the 30% CHA-Al-Fum.

Temperature-entropy for adsorption desalination

The temperature-entropy (*T*-*s*) maps for understanding the operating principle of adsorption desalination is shown in Figure 5.9. Hence the entropy generation results for 30% CHA-Al-Fum, $(CH_3)_2$-MOF-801 (Zr) and N-UiO-66 (Zr) plus water systems are presented for comparison purposes. The entropy generation ($\dot{S}_{gen}$) are calculated for the chilled water, cooling water and hot water inlet temperature of 30 °C, 30 °C and 80 °C, respectively with the optimal cycle time (in terms of maximum water production) of 500 s for 30% CHA-Al-Fum composite and 300 s for $(CH_3)_2$-MOF-801 (300 s) and N-UiO-66 (300 s) MOFs based AHT systems. As shown in Figure 5.9.(a), the *T-s* maps of the evaporator for adsorption desalination process exhibit different profiles as compared with those for the adsorption cooling process. During the switching period of the evaporator, 30% CHA-Al-Fum composite shows the largest $\dot{S}_{gen}$ (from 0 to 0.55) whilst the evaporator temperature fluctuates within a small range (26.7 °C to 28.9 °C). On the other hand, the evaporator temperature of the $(CH_3)_2$-MOF-801 (Zr) + water changes tremendously (from 22.2 °C to 29.7 °C) with smaller $\dot{S}_{gen}$ (0.32 W/K). In addition, N-UiO-66 (Zr) generates the lowest $\dot{S}_{gen}$ (0.17 W/K). Similar results are found for the condenser, where the $\dot{S}_{gen}$ increases to the maximum during the switching period and decreases to zero during the adsorption processes. Additionally, as the temperature of the condenser increases during the pre-heating and pre-cooling process, 30% CHA-Al-Fum composite achieves the largest $\dot{S}_{gen}$ (1.59 W/K), followed by the $(CH_3)_2$-MOF-801 (0.77 W/K) and N-UiO-66 (0.60 W/K). Although 30% CHA-Al-Fum composite provides higher $\dot{S}_{gen}$ within the condenser and evaporator as compared with the $(CH_3)_2$-MOF-801 (Zr) and N-UiO-66 (Zr), it provides narrower loop per cycle. For example, during the pre-heating and desorption process, the temperature of the 30% CHA-Al-Fum composite based desorption-bed increases from 37 °C to 79 °C, and the $\dot{S}_{gen}$ reaches the maximum value of 72.69 W/K. The entropy generation for 30% CHA-Al-Fum + water system is smaller than that of N-UiO-66 + water (76.91 W/K) /$(CH_3)_2$-MOF-801 + water (98.59 W/K) systems. These results also indicate that the modified MOFs with shorter hydrophobic length generate larger $\dot{S}_{gen}$ within the adsorption-beds, which contributes to the majority of the overall

$\dot{S}_{gen}$. The overall $\dot{S}_{gen}$ of these three modified MOFs for adsorption desalination purpose are ranked as: $(CH_3)_2$-MOF-801 (99.68 W/K) > N-UiO-66 (77.68 W/K) > 30% CHA-Al-Fum (74.83 W/K). The maximum SDWP (in terms of m^3 per tonne of MOF per day) of all the modified MOFs is summarised as: N-UiO-66 (37.6) > 30% CHA-Al-Fum (33.19) > $(CH_3)_2$-MOF-801 (25.02). Collectively, N-UiO-66 (Zr) achieves the highest SDWP with shorter operation half cycle time as it provides relatively lower $\dot{S}_{gen}$ in the adsorption beds Hence, N-UiO-66 (Zr) MOF is the most promising material for adsorption desalination application.

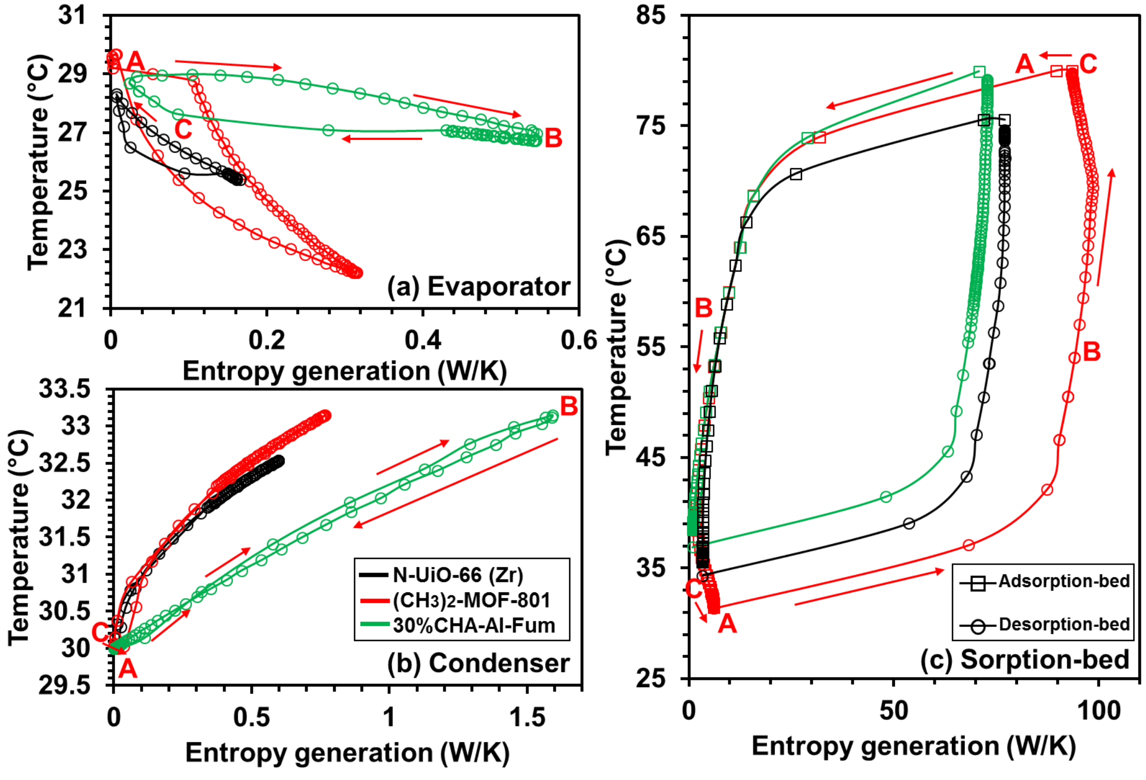

Figure 5.9: Temperature-entropy (T-s) maps of 30% CHA-Al-Fum composite vs $(CH_3)_2$-MOF-801 (Zr) vs N-UiO-66 (Zr) system under cyclic-steady-state: (a) Evaporator; (b) Condenser and (c) Adsorption/Desorption-bed. Here, A→B represents the switching period (pre-cooling or pre-heating) process and B→C indicates the half-cycle-operation (adsorption/desorption) process under adsorption desalination condition. Here, the black line represents the N-UiO-66 (Zr), the red line indicates the $(CH_3)_2$-MOF-801 (Zr) and the green line stands for the 30% CHA-Al-Fum.

5.7 Performance Analysis

5.7.1 Al-Fum/composites + water systems

Employing the AHT modelling, Figure 5.10 demonstrates the performance of original and modified Al-Fum based MOFs – water adsorption chiller/heat pump at different half cycle time ($t_{half\ cycle}$) for the heat source (hot water) temperature of 60 ℃ and the heat sink (cold water) temperature of 30 ℃. As shown in Figure 5.10(a.1), the COP increases monotonically with $t_{half\ cycle}$ for all the adsorbents. The reason is that with a shorter cycle time, the water vapour is not completely desorbed because of the poor utilisation of the heating energy, which leads to the low uptake – offtake difference (Δq) per adsorption cooling cycle, therefore, low COP is caused. As the cycle time increases, the consumption of the heat energy is reduced significantly as compared with the reduction in the production of the cooling power, which results in a favourable impact on the COP. Hence, higher COP is obtained. From this standpoint, saturated COP is excepted when a relatively long cycle time is considered. For Al-Fum-based adsorbent system, the largest COP ($t_{half\ cycle}$ = 1000 s) for Al-Fum, 5% Li-Al-Fum, 30% AFI-Al-Fum and 30% CHA-Al-Fum is 0.45, 0.476, 0.54 and 0.56, respectively. As shown in Figure 5.10(b.1), similar trends are found for AHP system, where all the adsorbents obtain the lowest COP_h at shorter half cycle time ($t_{half\ cycle}$ = 150 s) and highest COP_h at longer half cycle time ($t_{half\ cycle} \geq$ 900s), except for 30% AFI-Al-Fum. 30% AFI-Al-Fum achieves the best COP_h at $t_{half\ cycle}$ = 800 s, which means that redundant heating energy provided at longer operation period results unfavourable effect on the overall performance of 30% AFI-Al-Fum – water AHP system. The maximum COP_h for all the system with various Al-Fum based MOFs is summarised as: Al-Fum, 5% Li-Al-Fum, 30% AFI-Al-Fum and 30% CHA-Al-Fum is 1.67 ($t_{half\ cycle}$ = 1000 s), 1.66 ($t_{half\ cycle}$ = 1000 s), 1.65 ($t_{half\ cycle}$ = 800 s) and 1.67 ($t_{half\ cycle}$ = 900 s), respectively.

Unlike COP, the SCP delivers the non-monotonic behaviours with the change of $t_{half\ cycle}$ for majority of the adsorbents (Figure 5.10(a.2)). For Al-Fum-based ADC system, SCP increases steeply up to 300 s and the effect of τ becomes weak when longer half cycle time is applied. Hence, the highest SCP is labelled in red colour and the lowest SCP is marked in green. At shorter half cycle time (150 to 300 s), the insufficient cooling and heating of the beds result in the reduced level of adsorption and desorption, which will lead to the lower Δq and SCP. At longer half cycle time, more heat energy is utilised in the adsorption beds and all the Al-Fum based adsorbents approaches their adsorption limit. In addition, due to the strong interaction between the lithium dopants and CHA type zeolite framework with water, adsorption may also occur if longer desorption periods are applied. These constraints will result in poor cooling capacity and unfavourable SCP. Hence, a decrease of SCP is found for 5% Li-Al-Fum and 30% CHA-Al-Fum when longer half cycle time is applied ($t_{half\ cycle}$ > 700 s). The highest SCP for all the system with various MOF adsorbents is summarised as: Al-Fum, 5% Li-Al-Fum, 30% AFI-Al-Fum and 30% CHA-Al-Fum is 0.35 ($t_{half\ cycle}$ = 1000 s), 0.39 ($t_{half\ cycle}$ = 1000 s), 0.47 ($t_{half\ cycle}$ = 800 s) and 0.55 ($t_{half\ cycle}$ = 700 s), respectively. On the other hand, it is found in Figure 5.9(b.2) that SHP decreases monotonically with the increase of $t_{half\ cycle}$. For example, for 30% CHA-Al-Fum, the SHP drops from 1.15 kW/kg to 0.98 kW/kg when the half cycle time increases from 150 s to 1000 s. It is because of this at the beginning of adsorption, water vapour will preferentially be adsorbed onto the Al-Fum based MOF high energy pore sites and this intense process will generate significant adsorption heat. As the time increases, the interaction between water and porous structures become weak and less heat is delivered. In addition, once the desorption limit is reached, there is no more water vapour transferred to the condenser even at longer operation time, therefore, no more condensation heat is produced and the SHP will drop.

These results suggest that short $t_{half\ cycle}$ should be considered when the combined effects of enthalpies of condensation and adsorption are used for heat-pumping applications.

The results demonstrate that the performance of AC system could be enhanced significantly by employing the modified Al-Fum as adsorbent as compared with the original MOF. For example, among the four Al-Fum based adsorbents, original Al-Fum shows the poorest AC performance (COP and SCP) for its strong hydrophobic behaviours at low pressure region as well as the slow adsorption kinetics. By mixing the parent Al-Fum with the AQSOA-Z02 (CHA type) zeolite, the modified 30% CHA-Al-Fum delivers the best ADC performance with a highest COP of 0.56 ($t_{half\ cycle}$ = 1000 s) and SCP of 0.55 ($t_{half\ cycle}$ = 700 s). Evident improvements are also observed for 5% Li-Al-Fum and 30% AFI-Al-Fum for their enhanced hydrophilicity, higher Δq and faster kinetics. For example, at half cycle time of 300 s, a 14.3% larger COP and 18.8% higher SCP are found for 30% AFI-Al-Fum as compared with the original Al-Fum. Even better results are obtained for 5% Li-Al-Fum (+35.0% COP and +44.7% SCP) and 30% CHA-Al-Fum (+35.0% COP and +44.7% SCP). At other half cycle times such as 500 s, obvious enhancements of AC performance are also found, which is shown in Figure 5.10(a.1) and 5.10(a.2). The overall performance for different Al-Fum based adsorbent – water AC in terms of COP and SCP could be summarised as: 30% CHA-Al-Fum > 5% Li-Al-Fum > 30% AFI-Al-Fum > Al-Fum. On the other hand, as shown in Figure 5.10(b.1) and 5.10(b.2), improved SHP are found for all the modified Al-Fum based MOFs while no obvious COP_h enhancements are observed. For example, at half cycle time of 500 s, 13.4% higher of SHP are found for 30% AFI-Al-Fum as compared with the parent Al-Fum while only 0.24% larger COP_h is obtained. Additionally, it is also found that at the half cycle time of 500 s, all the Al-Fum based MOFs – water AC or AHP system could reach 80% of their optimal performance.

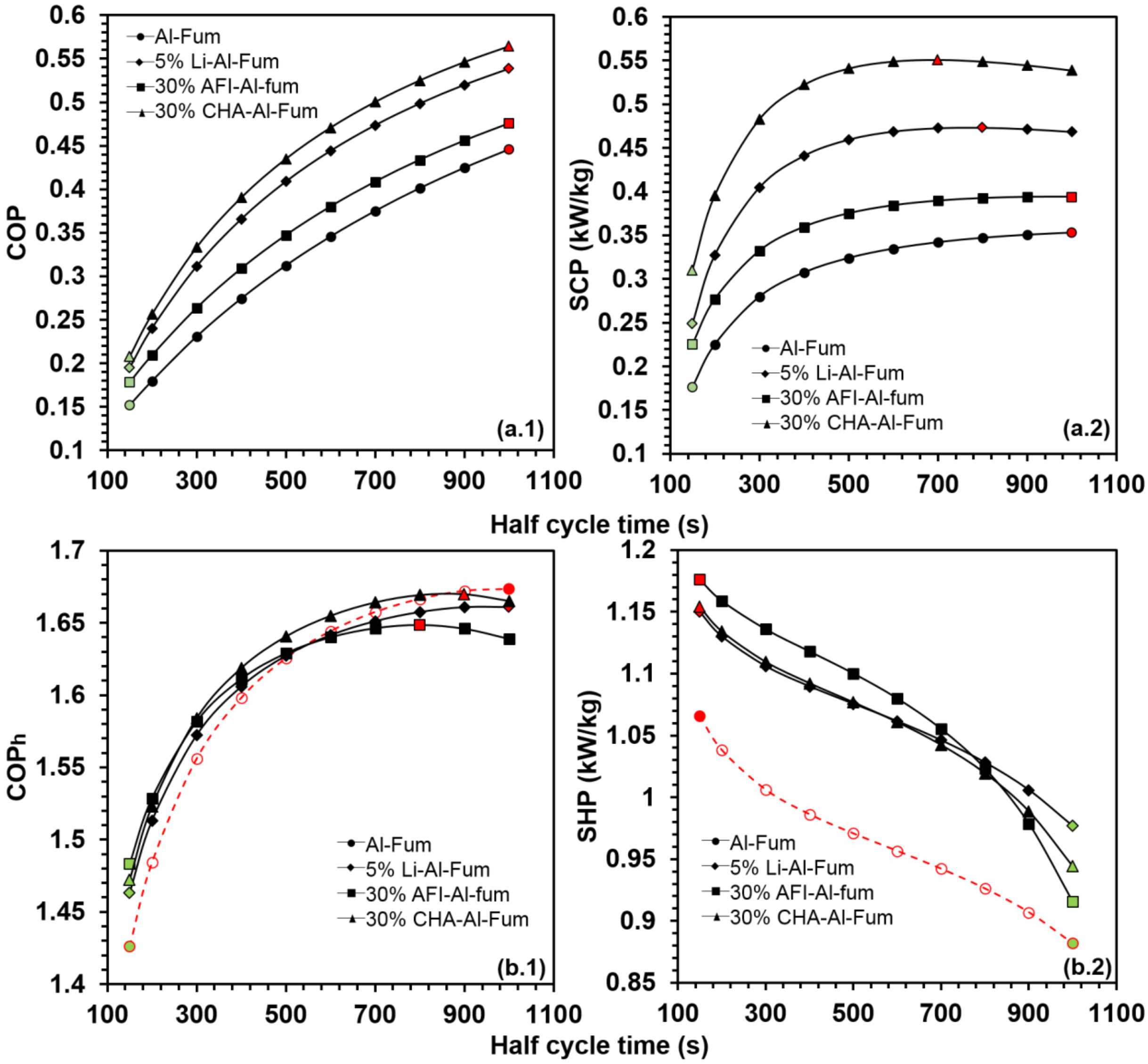

Figure 5.10: Effects of half cycle time on: (a.1-a.2) the performance of AC (in terms of COP and SCP (kW/kg)); (b.1-b.2) AHP (in terms of COP_h and SHP (kW/kg)) for original Al-Fum, alkali-ions doped Al-Fum and Al-Fum + zeolite composites based MOFs – water AHT systems.

The hot water (driving heat source) inlet temperature (55 – 90 ℃) effects on the performance for various original and modified Al-Fum based AC or AHP systems are shown in Figure 5.11. Here, the cooling water inlet temperature is 30 ℃ and the half cycle time is fixed at 500 s. For all the Al-Fum based adsorbent – water AC system, the highest COP and COP_h is found at the hot water inlet temperatures between 55 ℃ and 60 ℃. The COP and COP_h starts to drop when the heat source temperature is higher than 60 ℃. The reason is that all the Al-Fum based adsorbents exhibit "S-shaped" isotherms for water adsorption and the hydrophobic length is smaller than 0.22 ($P/P_s \leq 0.22$), therefore, no significant increase of the water vapour transfer per adsorption-desorption cycle is yielded at $T_{des} > 60℃$. As shown in Figure 5.11(a.1), the maximum COP for 30% CHA-Al-Fum is 0.390 ($T_{des} = 60℃$) while the largest COP for 5% Li-Al-Fum, 30% AFI-Al-Fum and Al-Fum is 0.37, 0.32 and 0.28, respectively ($T_{des} = 55$ ℃). It is also found in Figure 5.11(b.1) that all the adsorbents achieve the largest COP_h at $T_{des} = 60$ ℃, which is 1.63, 1.63, 1.63 and 1.64 for Al-Fum, 5% Li-Al-Fum, 30% AFI-Al-Fum and 30% CHA-Al-Fum, respectively.

Figure 5.11(a.2) shows that the SCP rises quickly between the regeneration temperatures of 55 ℃ and 60 ℃ for the increase of the water vapour delivery per adsorption cooling cycle. It begins to drop when $T_{des} > 65℃$ due to the incompletely utilisation of the applied heat to the desorption bed. The maximum SCP for all the four Al-Fum based adsorbents are found at 65 ℃ with the value of 0.54, 0.45, 0.37 and 0.31 kW/kg for 30% CHA-Al-Fum, 5% Li-Al-Fum, 30% AFI-Al-Fum and Al-Fum, respectively. On the other hand, it is found that the highest SHPs are obtained at higher regeneration temperature (Figure 5.10(b.2)). It is because of that at higher regeneration temperature, the desorption process could be finished more completely, this process results drier adsorbents and more water vapour is transferred to the condenser. In the next cycle, more water is adsorbed on the drier porous adsorbents and intense adsorption heat is generated. Hence, the enthalpies of both the adsorption and condensation process are enhanced and larger SHP is achieved.

These results indicate that all the modified MOFs present substantially better results as compared with the original MOFs. For example, under the low regeneration temperature (60 ℃) condition, a 42.3% higher COP and 70.0% larger SCP are found for 30% CHA-Al-Fum as compared with the parent Al-Fum while similar results are also found for 5% Li-Al-Fum (+33.3% COP and +43.5% SCP) and 30% AFI-Al-Fum (+12.6% COP and +17.0% SCP). Hence, impressive AC performance enhancements are obtained by the post-modification works on the original MOF materials. Furthermore, slightly superior performances are achieved for AHP system when modified Al-Fum MOFs are used. By balancing the AC and AHP performance, the outcomes described above suggest an optimal regeneration temperature between 55 ℃ and 65 ℃ for Al-Fum based AHT systems, which means the modified Al-Fum based MOFs AHT systems could be readily driven by the low-grade heat source such as solar energy.

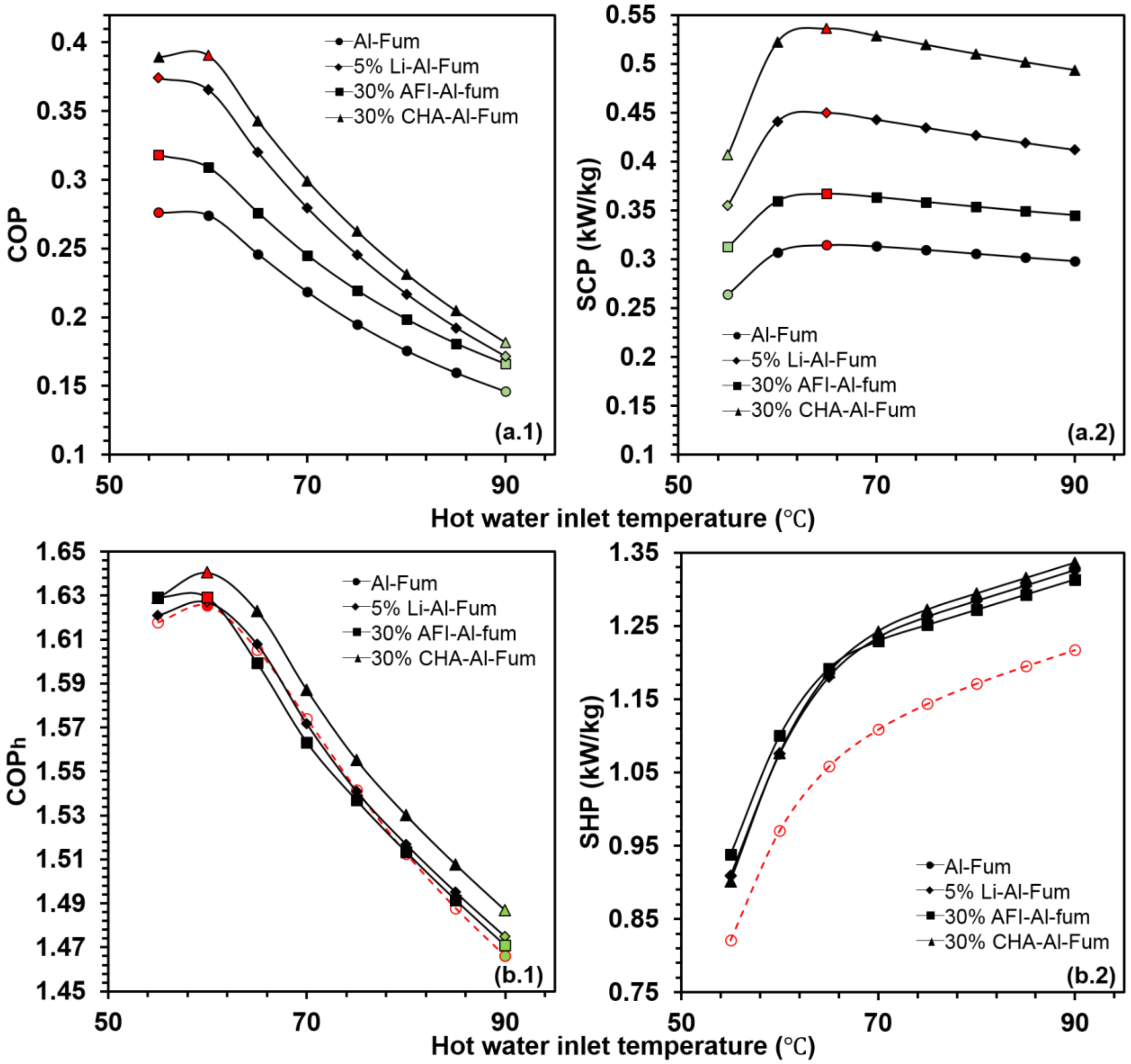

Figure 5.11: Effects of hot water inlet temperature on: (a.1-a.2) the performance of AC (in terms of COP and SCP (kW/kg)); (b.1-b.2) AHP (in terms of COP_h and SHP (kW/kg)) for original and modified Al-Fum based MOFs – water AHT systems.

Figure 5.12 (a.1-a.2) shows the effect of cold water inlet temperature (20 – 35 ℃) on the AC performance for all the MOFs based adsorption chiller. Generally, the cooling water inlet temperature plays a key role in the adsorption process as well as the condensation process. As shown in Figure 5.12 (a.1-a.2), both the COP and SCP drops monotonically for all the MOF adsorbents with the cooling water inlet temperature increases. This is because that a higher cooling water inlet temperature will lead to a higher temperature in the adsorption bed and condenser. Hence, adsorption process degrades, refrigerating energy is wasted and low AC performance (COP and SCP) is caused. Normally, water at room temperature is used as the heat sink for energy saving purpose. At 25 ℃, the original Al-Fum MOF results in a moderate performance with the COP of 0.39 and SCP of 0.43 kW/kg. By doping the lithium ions onto the Al-Fum structure, a 17.5% higher COP (0.46) and 23.9% larger SCP (0.54 kW/kg) is obtained for 5% Li-Al-Fum. In addition, 30% AFI-Al-Fum shows a 4.7% higher COP (0.41) and 17.5% larger SCP (0.49 KW/kg) as compared with the original Al-Fum. The best performance is found for 30% CHA-Al-Fum – water adsorption chiller, where the COP is 0.483 (+24.1%) and SCP is 0.594 kW/kg (+37.6%).

Figure 5.12 (b.1-b.2) shows the effects of chilled water inlet temperature on AHP system performances. It is found that both the COP_h and SHP increase monotonically with the increase of chilled water inlet temperature. Generally, chilled water flow with high inlet temperature will result high evaporator temperature. Hence, more water vapour is transferred to the adsorption bed with faster evaporation kinetics. This process induces more adsorption heat generation and better AHP performance. For example, at 15 ℃, the COP_h and SHP for parent Al-Fum are only 1.21 and 0.27 KW/kg, respectively. As the chilled water inlet temperature increases to 30 ℃, a 134.5% larger COP_h (1.625) and 3.5 times higher SHP (0.971 KW/kg) are obtained. All the modified Al-Fum based MOFs provide similar AHP performances where superior COP_h (1.62–1.64) and SHP (1.08–1.10 KW/kg) are obtained.

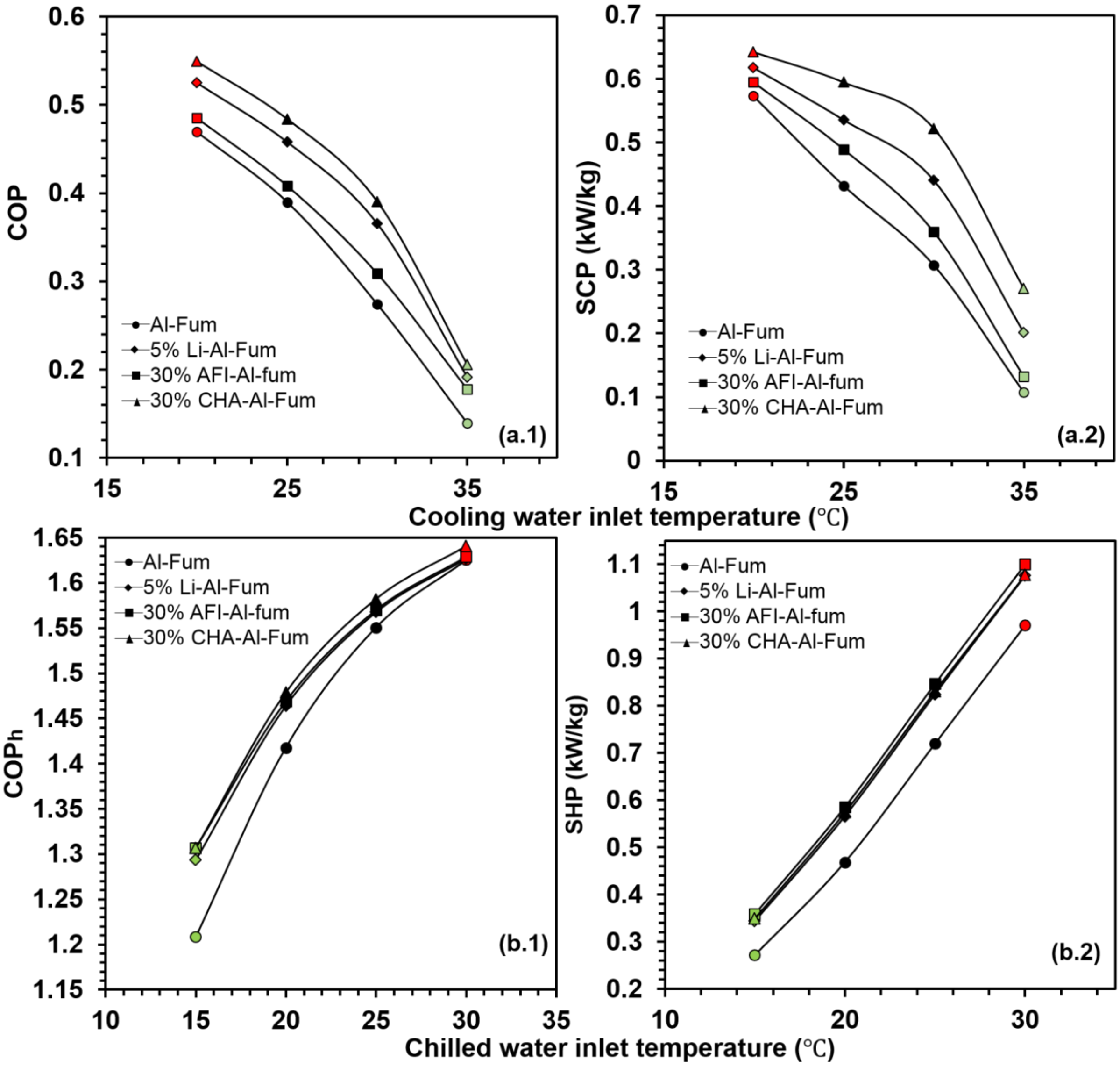

Figure 5.12: (a.1-a.2) Effect of cooling water inlet temperature on the performance of AC (in terms of COP and SCP (kW/kg)); (b.1-b.2) the effect of chilled water inlet temperature on the performance of AHP (in terms of COP_h and SHP (kW/kg)) for original and modified Al-Fum based MOFs – water AHT systems.

The effects of half cycle time on SDWP of adsorption desalination performance are shown in Figure 5.13. Here, SDWP profiles for all the parent and modified Al-Fum based MOFs are shown under different regeneration temperatures (60 - 80 ℃) for comparison purpose. Hence, the highest SDWP is marked in red colour and the lowest SDWP is labelled in green. It is found that there exists an optimal $t_{half\ cycle}$ ranging from 400 s to 600 s. At lower half cycle time, the desorption process could not be completed and low water vapour transformation per adsorption-desorption cycle (Δq) are compromised. Hence, poor SDWP performance is obtained. As the operation time increases, more water vapour is desorbed from the porous Al-Fum based materials and higher Δq as well as larger SDWP are achieved. Once the AD system reaches the adsorption/desorption limit, there is no more Δq could be delivered no matter how long the half cycle time it is. Hence, at longer $t_{half\ cycle}$, heating energy input is wasted, total daily desalination cycles are reduced and decrease of SDWP is observed. Furthermore, it is found that for all the materials at different regeneration temperatures, the overall SDWP performance could be summarised as: SDWP (70 ℃) > SDWP (80 ℃) > SDWP (60 ℃). The reason is that for Al-Fum based MOFs with “S-shaped” isotherm ($P/P_s \leq 0.22$), a completed desorption process could be achieved under regeneration temperature of around 70 ℃. Either too low regeneration temperature (incomplete offtake) or too high regeneration temperature (waste of thermal energy input) will lead to unfavourable results on SDWP. At the regeneration temperature of 70 ℃, the highest SDWP achieved by Al-Fum, 5% Li-Al-Fum, 30% AFI-Al-Fum and 30% CHA-Al-Fum is 29.92 ($t_{half\ cycle}$ = 600 s), 33.02 ($t_{half\ cycle}$ = 400 s), 32.78 ($t_{half\ cycle}$ = 400 s) and 33.85 ($t_{half\ cycle}$ = 400 s), respectively. Hence, AD systems employing modified Al-Fum shows higher SDWP with faster water production rates as compared with original Al-Fum.

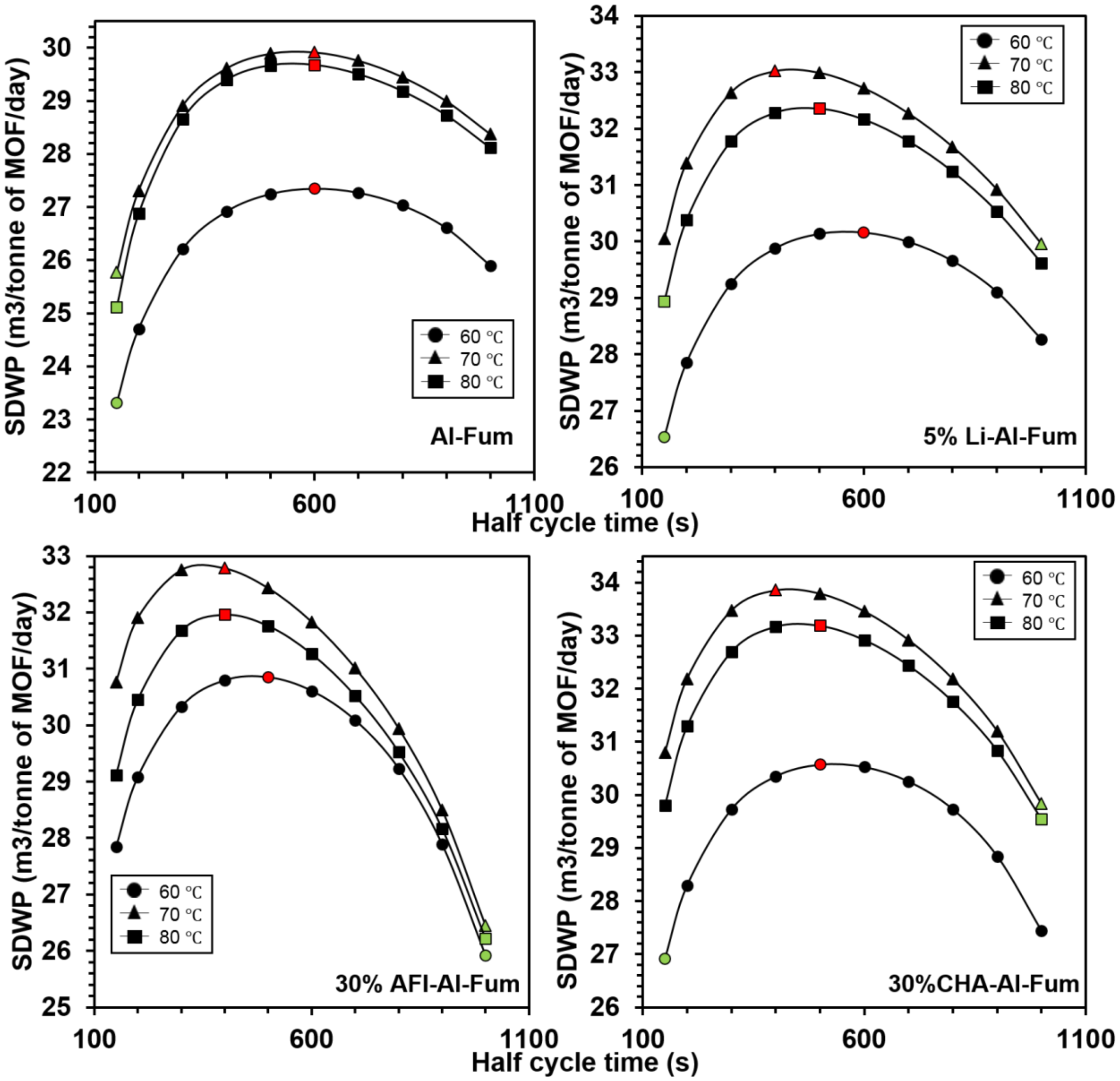

Figure 5.13: Effects of half cycle time on SDWP (in terms of m^3 per tonne of MOF per day) for original Al-Fum, alkali-ions doped Al-Fum and Al-Fum + zeolite composites based MOFs - water adsorption desalination systems under various regeneration temperatures.

5.7.2 Functional UiO-66 (Zr) MOFs + water systems

Employing the adsorption chiller modelling, the simulation is carried for the cooling water and chilled water inlet temperatures of 30 °C and 14.8 °C. Figure 5.14 demonstrates the COP and the SCP of the parent and functionalised UiO-66 + water assisted adsorption chiller at different half cycle time ($t_{half\ cycle}$) for the heat source (hot water) temperature ranging from 60 ℃ to 80 ℃ and the heat sink (cooling water) temperature of 30 ℃. As shown in Figure 5.14, the COP increases monotonically with $t_{half\ cycle}$. The main reason is that with a shorter cycle time, the water vapour is not completely desorbed because of the poor utilisation of the heating energy, which leads to the lower uptake – offtake difference (Δq) per adsorption cooling cycle, therefore, low COP results. On the other hand, at longer cycle time, the heat energy is fully utilised to release water vapour from the adsorbents, which results the higher COP. Hence the functional-UiO-66 (Zr) shows higher COP as compared with the parent UiO-66 (Zr).

Unlike COP, the SCP delivers the non-monotonic behaviours with the change of cycle time (Figure 5.14). For the parent UiO-66 (Zr) MOFs, the SCP increases steeply up to 400 s and the slope becomes gently for the half cycle time above 500 s. For N-UiO-66 and OH-UiO-66 + water assisted adsorption chiller, at shorter half cycle time (150 to 400 s), the insufficient cooling and heating of the beds result in the reduced level of adsorption and desorption effects, which lead to the lower Δq. As a result, the lower SCP is obtained. At longer half cycle time, more heat energy is utilised for desorption purposes and all the UiO-66 (Zr) based adsorbents approach to their adsorption limit. In addition, due to the strong interaction between N-UiO-66/OH-UiO-66 adsorbent with water, adsorption may also occur if longer desorption periods are applied. These constraints will result poor and unfavourable SCP. Therefore, a decreasing trend of SCP is the result for longer half cycle time ($t_{half\ cycle} > 500$ s).

The performance of adsorption chiller also depends on the regeneration temperature. Both the COP and the SCP increase at higher regeneration temperature due to higher Δq and faster kinetics. For the hot water inlet temperature of 60 ℃, the maximum COP for UiO-66, N-UiO-66, OH-UiO-66 and NH_2-UiO-66 are found to be 0.15, 0.47, 0.42 and 0.82, respectively. Hence, the

COP of all functionalised adsorbents are found higher as compared with that of parent UiO-66 (Zr) MOFs. This is due to the fact that as compared with other functional materials, OH-UiO-66 (Zr) and NH_2-UiO-66 exhibit impressively fast water adsorption kinetics and could complete about 80% of equilibrium state within 700 s. Hence, no significant COP enhancement is observed for longer cycle time operation cases ($700 < t_{half\ cycle} < 1000$ s) as the uptake-offtake difference per adsorption cooling cycle is not improved significantly. Furthermore, it is observed that as compared with the parent UiO-66 (Zr), all the functionalised materials show higher COP. The main reasons are higher uptake-offtake difference per adsorption-desorption periods and faster kinetics. With the enhanced hydrophilic behaviours at the low pressure region as well as the faster adsorption-desorption rates, the functionalised UiO-66 (Zr) MOFs utilise the applied heating energy completely to drive the AHT system, which therefore leads to restively higher SCP and COP.

The effects of regeneration temperature (60 – 80 ℃) on the AC performances are also plotted in Figure 5.14. For the parent UiO-66 (Zr) and NH_2-UiO-66 (Zr) MOFs, the COP decreases with the increase of regeneration temperature while the SCP remains almost unchanged. The reason is that these two adsorbents exhibit “S-shaped” isotherms for water adsorption and the hydrophobic length is smaller than 0.4 ($P/P_s \leq 0.4$), therefore, no significant increase in the water vapour transfer per adsorption cooling cycle is yielded at higher desorption temperatures (> 70 ℃) even though more heating energies are consumed at higher hot water inlet temperature.

On the other hand, N-UiO-66 and OH-UiO-66 MOFs exhibit the hydrophilic behaviours at low pressure region and higher regeneration temperatures are needed to achieve complete desorption processes. Hence, the higher COP and SCP are observed at higher hot water inlet temperature.

The overall performances of different UiO-66 (Zr) MOFs + water based adsorption chiller could be ranked as: NH_2-UiO-66 > OH-UiO-66 > N-UiO-66 > UiO-66.

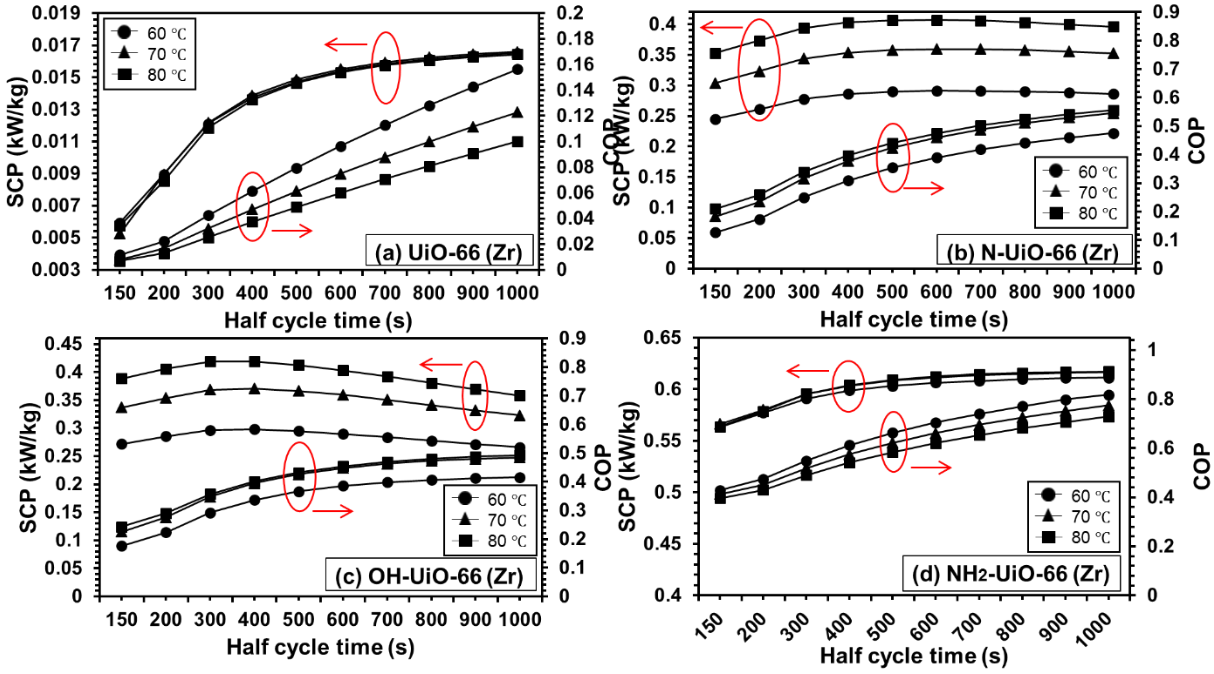

Figure 5.14: The COP and SCP (in terms of kW/kg) in terms of half cycle time under various regeneration temperatures (60 – 80 °C) for (a) UiO-66, (b) N-UiO-66, (c) OH-UiO-66 and (d) NH_2-UiO-66 and water based adsorption chillers.

Figure 5.15 shows the effects of $t_{half\ cycle}$ on COP_h and SHP for various heat source (here hot water) temperatures ranging from 60 ℃ to 80 ℃. Hence, the heat sink or cooling water temperature and the chilled water temperature are considered 30 ℃ and 14.8 ℃, respectively. For all the parent and functionalised UiO-66 (Zr) MOFs adsorbents, monotonic increase of COP_h and the decrease of SHP are found with the increase of half cycle time. At shorter half cycle time, the water vapour is not completely adsorbed and it leads to the poor uptake – offtake difference (Δq), hence, low COP_h is obtained. When the half cycle time increases, the adsorption-desorption process could be fully completed resulting higher COP. However, the effect of the cycle time on

COP_h becomes insignificant for the longer cycle time ($t_{half\ cycle}$ > 800 s) due to the requirement of more heat. On the other hand, all the adsorbents provide higher SHP at very short half cycle time (150 – 200 s) and then decreases at higher $t_{half\ cycle}$. This finding suggests that for the AHP system, the heating power is mainly generated at the beginning of the adsorption – desorption process as well as the switching period (mass – heat recovering process). This phenomenon also conforms to the adsorption mechanism i.e. water vapour will preferentially be adsorbed onto the high energy pore sites at first and delivers significant adsorption heat. As the time increases, the adsorption process becomes less intense, less heating power is generated and the SHP decreases. Additionally, the superior heat pumping effects are found for functionalised UiO-66 (Zr) adsorbents as compared with the parent UiO-66 (Zr) adsorbent. Hence, the parent UiO-66 (Zr) shows the lowest efficiency in terms of COP_h and SHP due to its strong hydrophobic behaviours at low pressure region and the slow adsorption kinetics.

At the hot water temperature of 80 ℃, N-UiO-66 shows the best AHP performance with the COP_h of 1.46 (at $t_{half\ cycle}$ =1000 s) and the SHP of 1.1 kW/kg (at $t_{half\ cycle}$ = 700 s). Evident improvements are also observed for OH-UiO-66 due to its enhanced hydrophilicity, higher Δq and faster kinetics. For example, at the half cycle time of 1000 s, (i) NH_2-UiO-66 (Zr) shows 13.7% higher COP_h, and (ii) OH-UiO-66 (Zr) provides 28.9% higher COP_h and 37.4% higher SHP as compared with that of the parent UiO-66 (Zr).

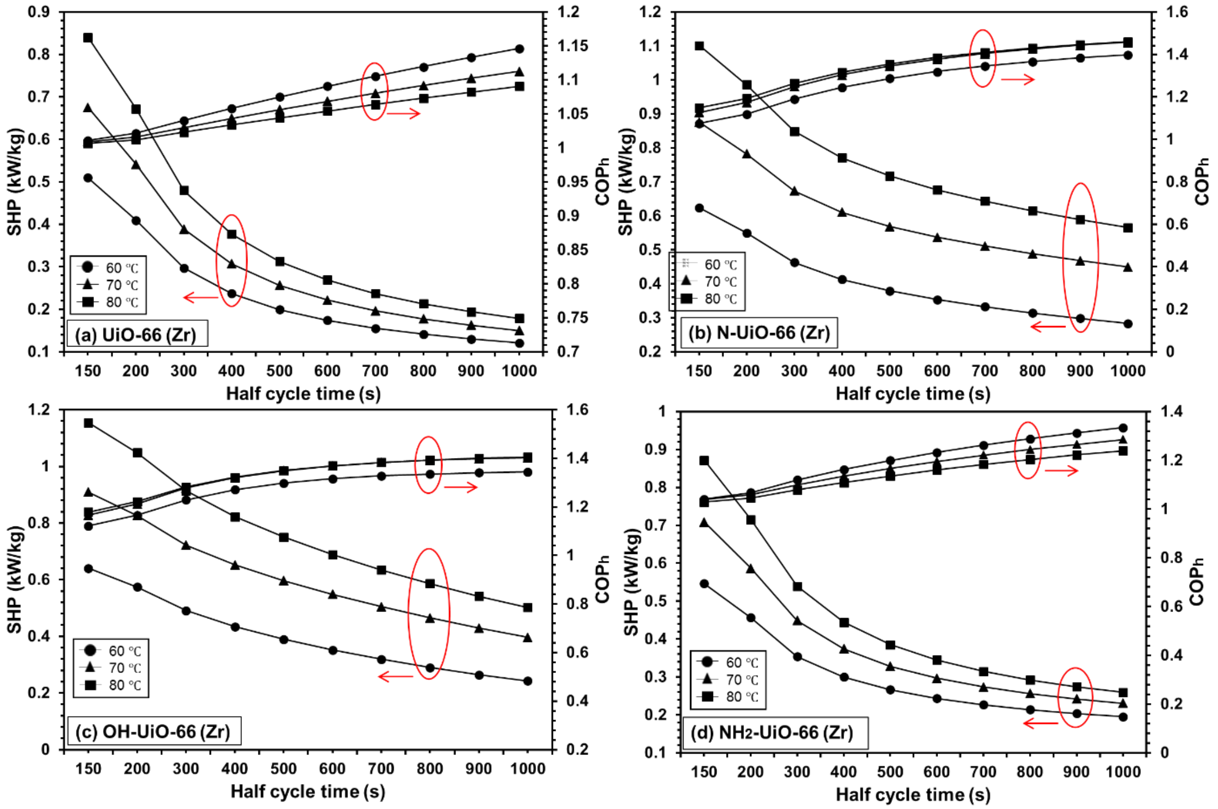

Figure 5.15: The COP$_h$ and SHP (in terms of KW/kg) are presented in terms of half cycle time under various regeneration temperatures of (a) UiO-66, (b) N-UiO-66, (c) OH-UiO-66 and (d) NH$_2$-UiO-66 and water based adsorption heat pump.

Figure 5.16 shows the effects of chilled water (load) inlet temperature (15 – 30 ℃) on the AHP performance. Generally, the load temperature (generating from the supply of chilled water or the heat source of the TES) plays a key role in the evaporation process. As shown in Figure 5.16, both the COP and SCP increase monotonically with the increase in load temperature due to the fact that the evaporation rate increases and more water vapour is transferred to the adsorption bed, which also increases the adsorption uptake rates. Therefore, the amount of total heat release from the adsorption bed is increased and higher AHP performances in terms of COP$_h$ ad SHP are obtained. At 15 ℃, the original UiO-66 MOF results a moderate performance with the COP$_h$ of 0.7 and SHP of 0.2 kW/kg. By implanting amine functional group onto the UiO-66 structure, a

12.8% higher COP_h (1.21) and 34.7% more SHP (0.27 kW/kg) are obtained for NH_2-UiO-66. The best performance is found for N-UiO-66 + water adsorption heat pump, where the COP_h is 1.36 (25.8% higher) and SHP is 0.73 kW/kg (3.6 times more). As the chilled water inlet temperature increases up to 30 ℃, the AHP performance is improved for all types of UiO-66 (Zr) MOFs. For example, UiO-66 (Zr) based AHP yields high COP_h (1.55) and SHP (1.39 kW/kg) at chilled water inlet temperature of 30 ℃.

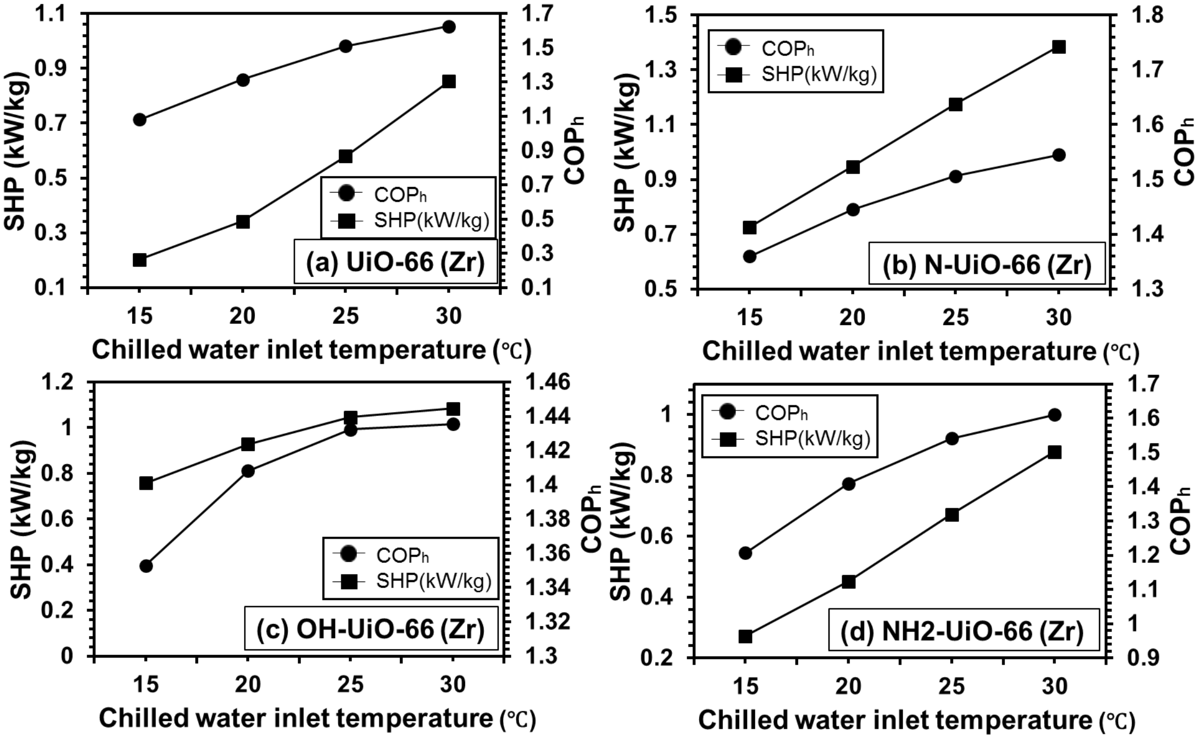

Figure 5.16: Effects of chilled water inlet temperature on COP_h and SHP for (a) UiO-66, (b) N-UiO-66, (c) OH-UiO-66 and (d) NH_2-UiO-66 and water based adsorption heat pump under optimal regeneration temperature/cycle time conditions.

Figure 5.17 (a – d) shows the effects of SDWP on cycle time for various hot water inlet temperatures. Hence, the cooling water inlet temperature and the chilled water inlet temperature are kept at 30 ℃. Overall, non-monotonic profiles are observed. The SDWP first increases then decreases with the increase of half cycle time. Generally, both adsorption and desorption processes are not completed within short half cycle time. Therefore, at shorter cycle time, the incomplete regeneration process leads to poor water transfer (i.e. lower uptake-offtake difference or Δq) per desalination cycle, which results lower SDWP. However, very long cycle time may also generate poor SDWP especially for the adsorbents with faster adsorption kinetics, such as N-UiO-66 and OH-UiO-66. This is due to the fact that superfluous thermal energy input is applied into the AD system while the regenerative process already completed. With the longer half cycle time, the input-energy is wasted. Therefore, the total daily numbers of operation cycles are dampened and lower SDWP results. The simulation results show that the maximum SDWP (m^3 per tonne of MOFs per day) for UiO-66, N-UiO-66, OH-UiO-66 and NH_2-UiO-66 are calculated as 24.9 ($t_{half\ cycle}$ = 700 s), 37.6 ($t_{half\ cycle}$ = 300 s), 35.5 ($t_{half\ cycle}$ = 200 s) and 30.0 ($t_{half\ cycle}$ = 500 s), respectively. In addition, the SDWP increases with the hot water temperature due to the fact that the desorption process is completed with shorter cycle time interval at higher regeneration temperature. The increase in hot water temperature improves desorption processes, thanks to which the adsorbent is better prepared for the next stage of adsorption. For example, for N-UiO-66 + water AD systems, the maximum SDWP at different regeneration temperature are 19.9 (60 ℃), 29.7 (70 ℃) and 37.6 (80 ℃) m^3 of water per tonne of adsorbent per day.

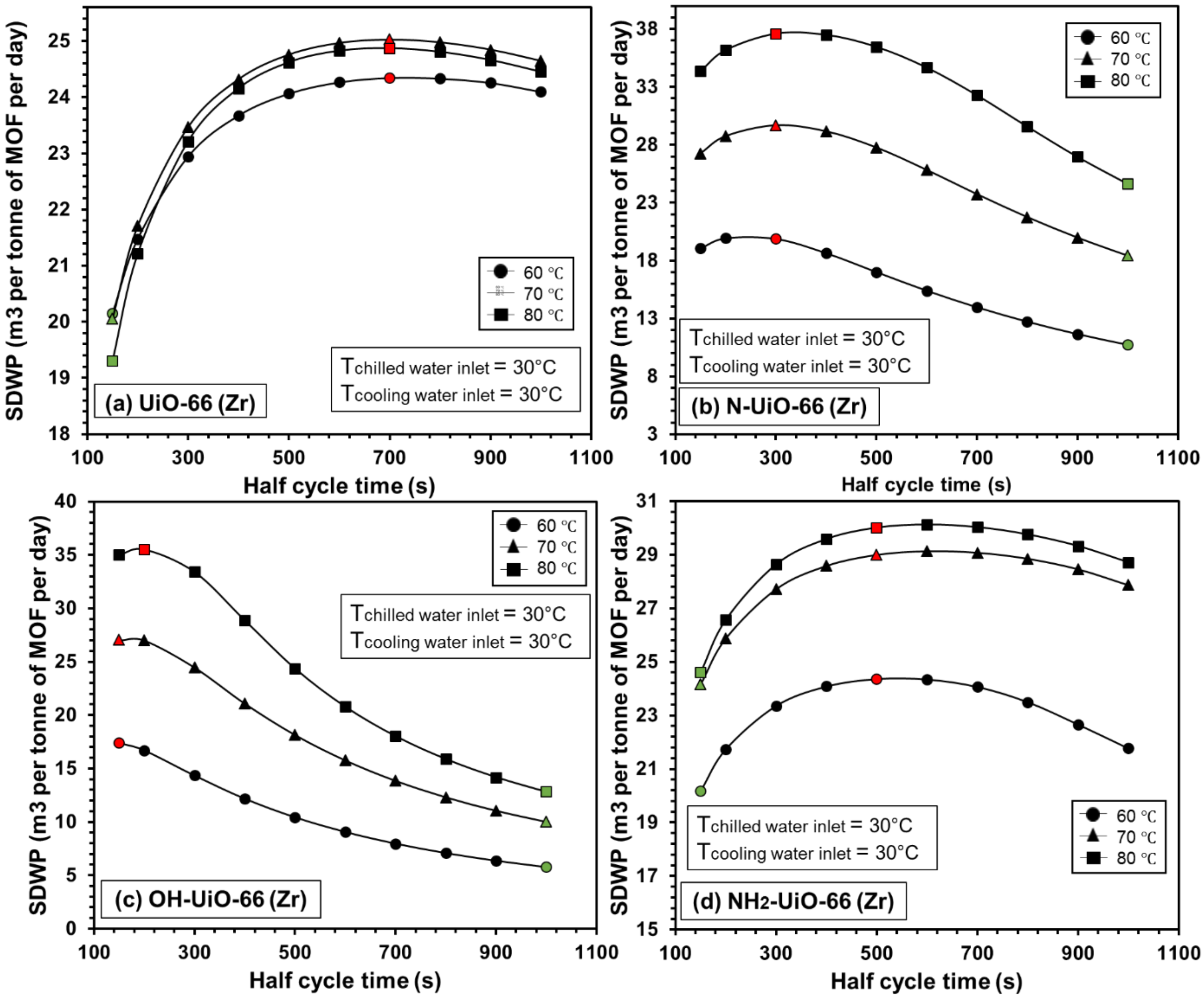

Figure 5.17: Effects of half cycle time on SDWP (in terms of m^3 per tonne of MOF per day) for (a) UiO-66, (b) N-UiO-66, (c) OH-UiO-66 and (d) NH_2-UiO-66 and water based adsorption desalination under various regeneration temperatures. Hence, the cooling water and the chilled water inlet temperature are kept at 30 °C.

5.7.3 Functional MOF-801 (Zr) + water systems

The SCP and the COP of the parent and CH_3 functionalised MOF-801 (Zr) + water assisted adsorption chiller are shown in Figures 5.18(a-b). Hence the COP and the SCP are presented in terms of half cycle time for various hot water temperature ranging from 60 °C to 80 °C with the cooling water (hence the heat sink) temperature of 30 °C. The chilled water inlet temperature is fixed at 14.8 ^{o}C. Both the COP and the SCP are observed as increasing function of the driving heat source/hot water temperature.

At first, the SCP increases with the increase in cycle time, and reaches its maximum value. Later, the SCP drops with longer cycle time. At shorter cycle time, the Δq is found lower due to incomplete adsorption and desorption of water vapour. At longer cycle time, the uptake and offtake difference is not changed significantly i.e. Δq is nearly the same. At very long cycle time, momentarily adsorption of water vapour occurs in the bed during desorption periods. As a result, the offtake increases and the Δq per adsorption cooling cycle decreases. In addition, the heat transfer losses from the condenser to the evaporator are increased during longer cycle time. Therefore, the SCP is found lower.

The COP and SCP of the CH_3-functionalised MOF-801(Zr) adsorbent are found higher as compared to those of the parent MOF-801 (Zr), which is due to the fact that the adsorption/desorption rate of $(CH_3)_2$-MOF-801 (Zr) is two times faster than the parent MOF. For the parent MOF-801 (Zr) + water system, the maximum SCP is 0.54 kW/kg at the hot water inlet temperature of 80 °C. The optimum SCP is found 0.78 kW/kg for $(CH_3)_2$-MOF-801 (Zr) + water based adsorption chiller. This means the SCP is improved 40% employing CH_3 ligand on the parent MOF-801 adsorbent, which is the key finding of this research. On the other hand, the COP also increases from 0.5 to 0.65, which is 30% higher as compared with the parent MOF-801 (Zr) + water assisted adsorption chiller. It is also observed that the modified $(CH_3)_2$-MOF-801(Zr) works well at the desorption temperature of 60 °C for cooling applications.

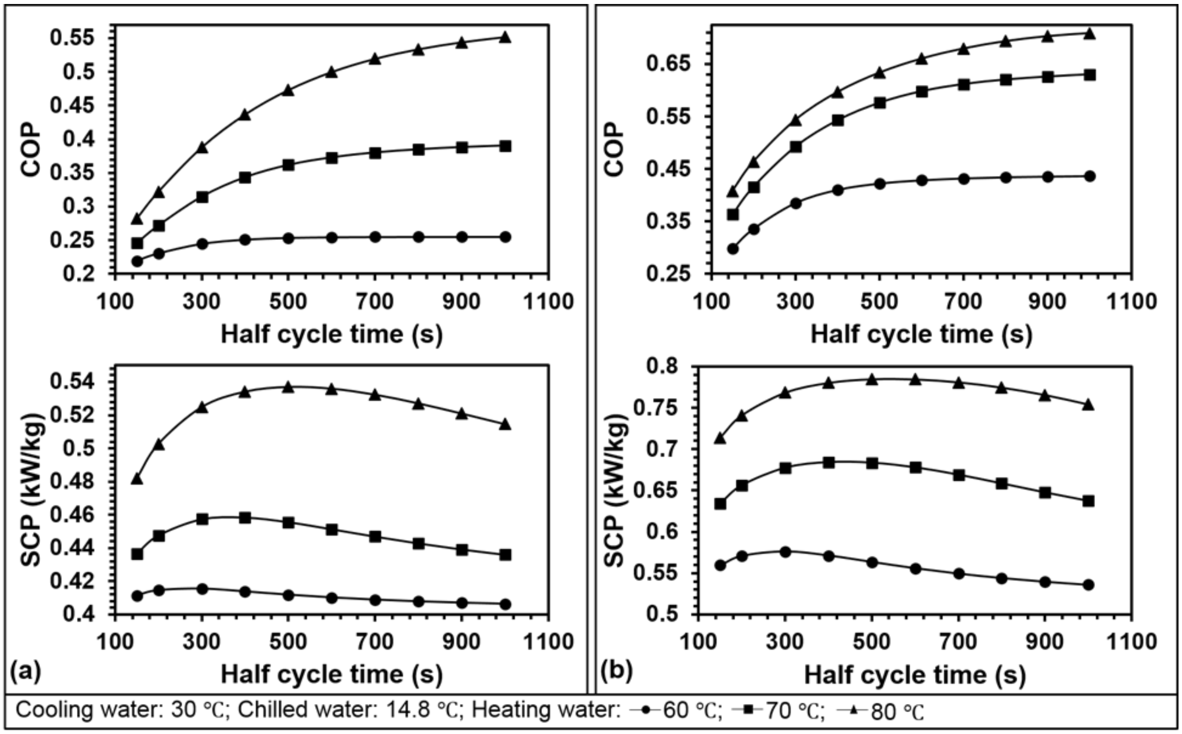

Figure 5.18: Effects of half cycle time on COP and SCP (KW/kg) for (a) MOF-801 (Zr) and (b) $(CH_3)_2$-MOF-801 (Zr) + water based adsorption chillers at the cooling water temperature of 30 °C, chilled water temperature of 14.8 °C and hot water temperature ranging from 60 °C to 80 °C.

Figure 5.19 shows the effects of the half cycle time on COP_h and SHP (KW/kg) for the parent and functionalised MOF-801 + water based adsorption heat pump at various regeneration temperatures (60 °C to 80 °C). It is found that for both the MOF-801 (Zr) and $(CH_3)_2$-MOF-801 (Zr): (i) the COP_h increases and SHP decreases monotonically with increases of the half cycle time; (ii) higher AHP performances in terms of COP_h and SHP are obtained at higher regeneration temperature (where the mechanism has been explained in the previous section). For the parent MOF-801 (Zr), the best performance is obtained at the regeneration temperature of 80 °C with the COP_h of 1.21 ($t_{half\ cycle}$ = 1000 s) and SHP of 1.0 kW/kg ($t_{half\ cycle}$ = 100 s). With the implanting of methyl functional groups into the MOF-801 framework, the best COP_h of

$(CH_3)_2$-MOF-801 is 1.41 and the best SHP is 1.07 kW/kg, which is 17.0% and 7.3% higher than those of the original MOF-801 (Zr).

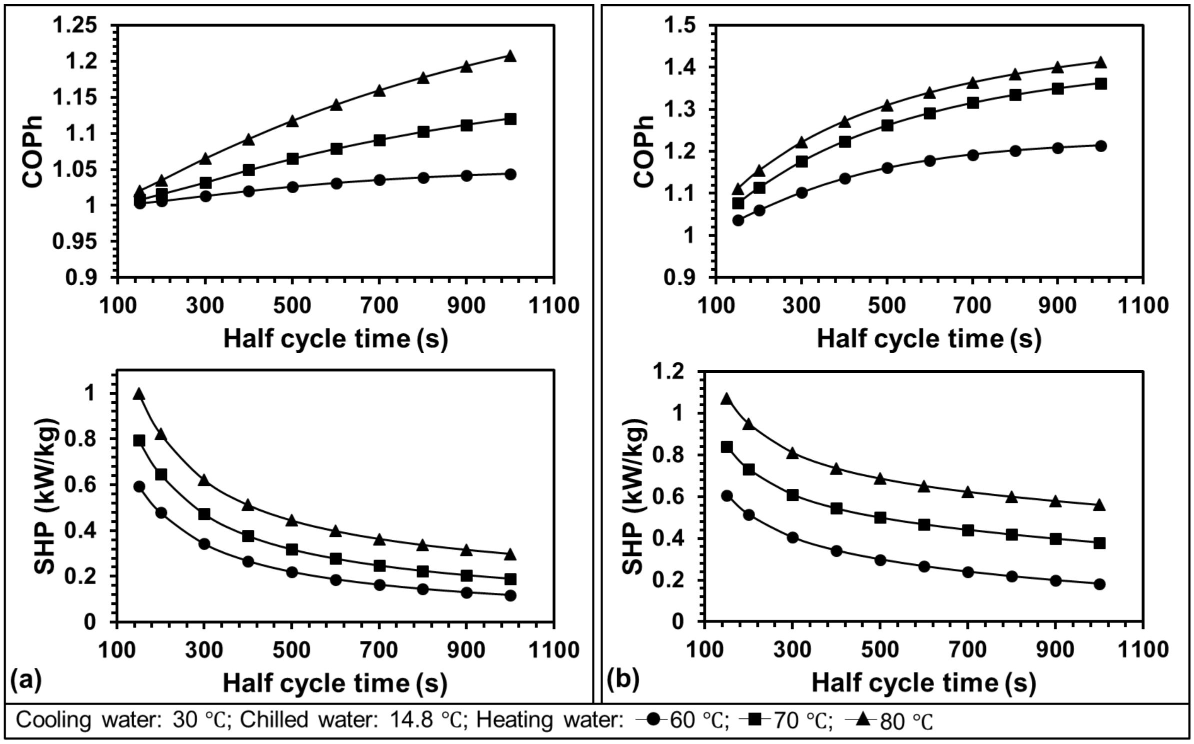

Figure 5.19: Effects of half cycle time on COP_h and SHP (KW/kg) for (a) MOF-801 (Zr) and (b) $(CH_3)_2$-MOF-801 (Zr) + water based adsorption heat pumps at the cooling water temperature of 30 °C, chilled water temperature of 14.8 °C and hot water temperature ranging from 60 °C to 80 °C.

The performances of the parent and original MOF-801 + water based adsorption desalination systems are shown in Figure 5.20 under various regeneration temperatures for the half cycle time ranging from 150 s to 1000 s. It is found that the SDWP (m^3 per tonne of MOFs per day) increases monotonically with the increases of the regeneration temperatures. In addition, for both the MOF-801 (Zr) and $(CH_3)_2$-MOF-801 (Zr), different optimal $t_{half\ cycle}$ is observed at various regeneration temperature. For example, the parent MOF-801 achieved the maximum SDWP at 300 s, 400 s and 500 s with the regeneration temperatures of 60 °C, 70 °C and 80 °C, respectively. In addition, due to the faster adsorption kinetics as compared with the original MOF-801, $(CH_3)_2$-MOF-801 (Zr) could achieve the best SDWP within 300 s for all the regeneration temperatures. The highest SDWP for the parent MOF-801 is 4.97 (m^3 per tonne of MOFs per day) and this number increases up to 25.02 (m^3 per tonne of MOFs per day) for the methyl functionalised MOF-801, which is four times bigger. It is also found that even low regeneration temperature of 60 °C, $(CH_3)_2$-MOF-801 (Zr) could achieve higher SDWP of 5.46 within a shorter half cycle time of 200 s, as compared to that of the highest SDWP for the parent MOF-801.

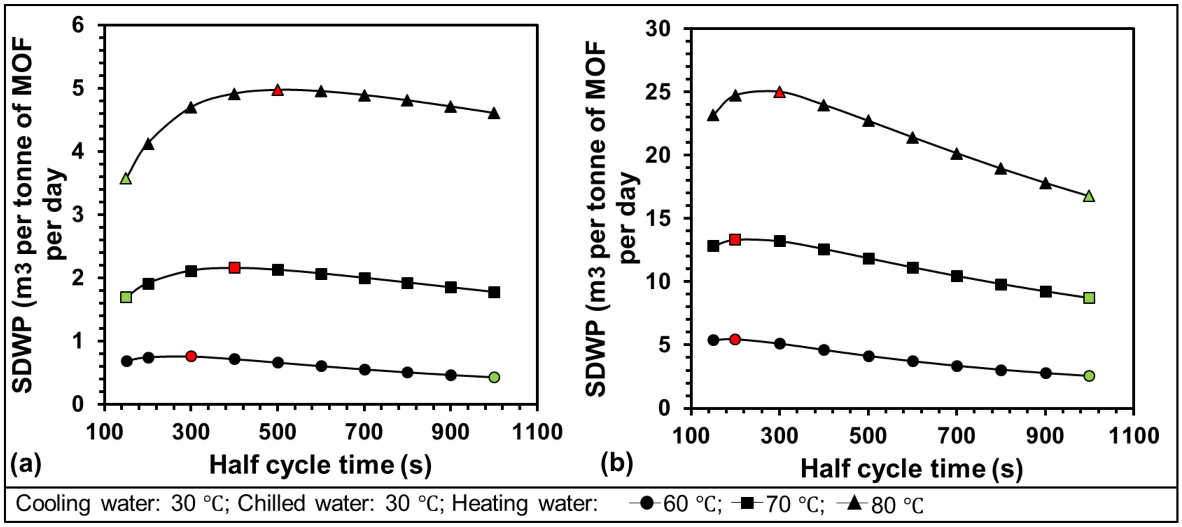

Figure 5.20: Effects of half cycle time on SDWP (in terms of m^3 per tonne of MOF per day) for (a) MOF-801 (Zr) and (b) $(CH_3)_2$-MOF-801 (Zr) and water based adsorption desalination under various regeneration temperatures (60 – 80 °C). Hence, the cooling water and the chilled water inlet temperature are kept at 30 °C.

5.8 Comparison study

The overall AHT performances in terms of SCP, SHP and SDWP for the parent and modified MOFs are presented in Figure 5.21. The performances of AHT system based on silica gel (type RD) and zeolite (types AQSOA-Z01 and Z02) [22] plus water are also provided here (Figure

5.20) for comparison purposes. Here, the regeneration temperature, the heat sink (both the condenser and adsorption bed) temperature and the chilled water inlet temperature are kept at 80 ℃, 30 ℃ and 14.8 ℃, respectively for the calculations of SCP and SHP. The load (e.g. the cooling water supply to the evaporator tube) temperature is considered 30 ^{o}C for the calculation of SDWP. It is found that the SDWP for both the UiO-66 (Zr) based MOFs are higher than that of silica gel and zeolites due to higher evaporation pressure i.e. more water transfer ($M_s \times \Delta q$) per adsorption desorption cycle. Secondly, both the SHP and the SCP of AQSOA-Z01 and Z02 are observed to be relatively lower. It should be noted here that silica gel based AHT system provides relatively higher SCP and SHP than those of the parent Al-Fum and UiO-66 (Zr) MOF. This due to the fact that the original Al-Fum and UiO-66 (Zr) MOF possesses the longer hydrophobic length. By doping lithium ions or mixing with zeolite composites, the performances of the Al-Fum based MOFs AHT system is improved dramatically, especially in terms of SHP and SDWP. In addition, the functional (based on OH, NH_2 and N) UiO-66 (Zr) MOFs show the higher SHP and SCP as compared with those of silica gel and zeolite adsorbents. With the addition of functional groups, the hydrophilicity of the parent UiO-66 (Zr) is enhanced. Furthermore, the SHP and SDWP of the parent MOF-801 (Zr) are observed relatively lower than those of the conventional adsorbents as a result of the low water transfer ($M_s \times \Delta q$) per adsorption-desorption cycle, which is due to the stronger hydrophilic behaviour of the parent MOF-801 (Zr) at low pressure region (uptake of 0.25 g/g at the relative pressure of 0.1). By tailoring the hydrophobic length with methyl-functional group, the hydrophobicity of the parent MOF-801 at Henry's region is enhanced. Higher SCP, SHP and SDWP are found for methyl-functionalised MOF-801 as compared with those of conventional adsorbents and original MOF-801 (Zr).

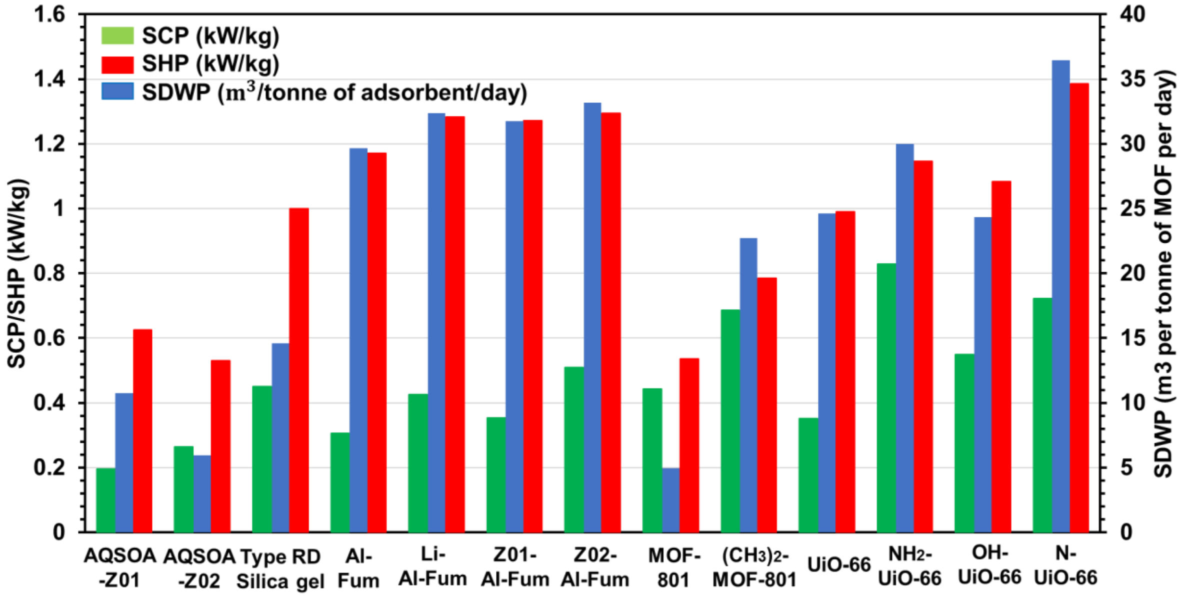

Figure 5.21: Representation of various adsorbents + water based AHT-system-performances in terms of SCP, SHP and SDWP at optimum working conditions.

For adsorption cooling application, the volumetric cooling power (i.e. cooling power per unit volume) is related to the density (ρ) of the adsorbent. It is known that the specific cooling power SCP = (Cooling power)/Mass$_{MOF}$ (kW/kg). Hence, the volumetric cooling power VCP = (Cooling power)/Mass$_{MOF}$ *ρ (kW/m^3). Currently, due to the equipment limitation, the bulk density of fabricated adsorbents such as UiO-66 (Zr) based MOFs are not conducted. However, many works have been proposed to investigate the density of UiO-66 (Zr) MOFs. For example, Dhainaut et al. [200] reported that the bulk density of UiO-66 (tablet form) is 0.43 g/cm^3. By implanting functional groups inside the MOF, the density of NH_2-UiO-66 is increased to 0.93 g/cm^3. In another work, Khabzina et al. [201] showed that the density of COOH-UiO-66 ranges from 0.62 g/cm^3 (pellet form) to 1.04 g/cm^3 (extrudate form). Therefore, it could be predicted that the density of the functionalised UiO-66 (Zr) is higher than that of the conventional adsorbents such as silica gel (≈ 0.7 g/cm^3) and comparable to that of the zeolite (≈ 1.0 g/cm^3). The synthesis of the original UiO-66 (Zr) and NH_2-UiO-66 (Zr) in this work is similar with those proposed in these papers. Hence, reported densities of these materials could be used to predict the VCP. From Figure 5.20, the optimal SCP for zeolite (AQSOA-Z02), silica gel (type RD), UiO-66 (Zr) and NH_2-UiO-66 (Zr) is 0.27 KW/kg, 0.45 KW/kg, 0.35 KW/kg and 0.83 KW/kg, respectively. Hence, their optimal VCP is calculated as 270 kW/m^3, 315 kW/m^3, 150.5 kW/m^3 and 771.9 kW/m^3, respectively. Although no evident VCP improvement is found for the original UiO-66 (Zr), it is observed that the VCP of the amine-functionalised UiO-66 (Zr) based adsorption chiller is much higher as compared with that of the zeolite and silica gel. Therefore, it could be concluded that the functionalised MOF is qualified for adsorption cooling application in terms of both SCP and VCP. Hence, the comparison Figure of volumetric cooling power (VCP) and specific cooling power (SCP) of conventional adsorbent (zeolite and silica gel) and UiO-66 (Zr) based MOFs (original and NH_2-UiO-66) under optimal AAHT operation conditions is shown in Figure 5.22.

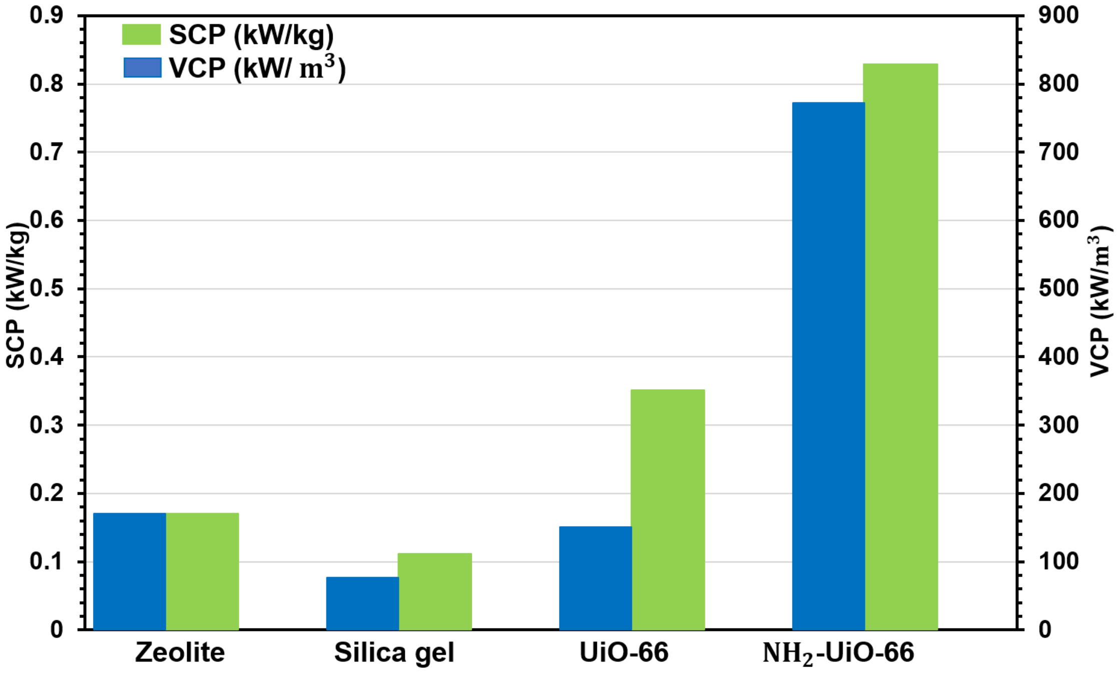

Figure 5.22: Comparison study of various adsorbents + water based AAHT-system-performances in terms of VCP and SCP at regeneration temperature and optimum cycle time.

The simulation results can also be compared with other published works. For example, Kim et al. [6] pointed out that silica gel based two-bed AD could yield maximum 8.2 m^3/tonne of silica gel per day and this number could be increased up to about 8.9 m^3/tonne of silica gel per day (at hot water/cooling water/chilled water inlet = 85/29.8/30 °C). Youssef et al. [21] showed that zeolite (AQSOA-Z02) could only produce 6.2 m^3/tonne of adsorbent per day under low chilled water temperature (at hot water/cooling water/chilled water inlet = 85/30/10 °C). which is much lower as compared with Al-Fum and UiO-66 (Zr) MOFs based AD system. Furthermore, Ahmed et al. [10] proposed one solar-energy driven ADC hybrid system where the average COP of 0.45 and SCP of 0.112 kW/kg with SDWP of 4.0 m^3/tonne of silica gel per day (at hot water/cooling water/chilled water inlet = 85/25/15 °C). By coating SAPO-34 type zeolite onto the solar evacuated tube, Du et al. [202] achieved a relatively lower SCP of 0.170 KW/kg(at hot water/cooling water/chilled water inlet = 60/31/15 °C). In addition, it is found that original silica gel could achieve a moderate SCP (0.2 kW/kg) at the regeneration temperature of 82.1 ℃ [203]. Evident improvements are obtained when activated carbon + silica/$CaCl_2$ composites are applied, where 90% of increment is resulted for the SCP as compared with type RD silica gel. However, a higher regeneration temperature is required (85 ℃) [204]. As compared with zeolite FAM Z01 [29], the parent MOF-801 (Zr) delivers the higher SCP (0.54 > 0.51 kW/kg). In addition, Melkon and Ayse [9] studied the metal mass effect on the performance of one zeolite 4A based adsorption heat pump and the highest AHP of 0.43 kW/kg is obtained with the heat exchanger tubes' wall thickness of 0.1 mm . However, higher hot water temperature of 150 ℃ is needed for driving the desorption bed (at hot water/cooling water/chilled water inlet = 150/20/2 °C). Aristov et al. [12] conducted AHP experiments using SWS-1L ($CaCl_2$ in silica) as adsorbent and over 1.0 kW/kg of SHP is obtained under optimal conditions (at hot water/cooling water/chilled water inlet = 90/30/10 °C). These findings highlight that the modified Al-Fum/MOF-801 (Zr)/UiO-66 (Zr) based adsorbent + water AHT systems have enormous potential in adsorption cooling, heat pump and desalination applications.

5.9 Summary

In this chapter, the entropy balance analysis of AHT system is established, and the performance results are presented in terms of cooling/heating capacity, COP and the specific daily water production. The entropy generation indicates the selection of suitable MOFs for various application with the use of lower hot water inlet temperature. The entropy analysis is explained here employing two important concepts namely entropy flow and generation for the first time. It is observed that all the modified MOFs show enhanced AHT performance as compared with that of the original MOFs. In addition, combing the study of entropy generation and AHT performance, it is found that the functionalised $(CH_3)_2$-MOF-801 (Zr) shows the promising adsorbent for adsorption cooling application and N-UiO-66 (Zr) is found suitable for the development of adsorption desalination system.

Chapter 6. Conclusions and Recommendations for Future Work

6.1 Conclusions

The thesis presents comprehensive studies for water adsorption on metal-organic frameworks (MOFs). Firstly, Grand Canonical Monte Carlo (GCMC) simulations are conducted to predict water adsorption uptakes on designed functional MOFs and composites under AHT-operating conditions. Secondly, based on the simulation results, the MOFs (such as Al-Fum, MOF-801 (Zr) and UiO-66 (Zr)) and MOFs/zeolite composites are synthesised and modified via alkali ions doping, conventional adsorbent mixing and functional group implanting approaches. Thirdly, the synthesised adsorbents are characterised by XRD, SEM, TGA and N_2 adsorption, and water adsorption on modified MOFs are measured. Finally, a thermodynamic model is developed for analysing the performances of AHT (adsorption assisted heat transformation) for various operating conditions with the basic concept of entropy generation. The performance parameters are shown here in terms of COP, SCP, COP_h, SHP and SDWP. The key findings of this thesis are as follows:

The selection of suitable MOFs and composite adsorbents are obtained from the screening of various MOFs employing GCMC simulation. The present simulation results suggest that the post-synthetisation methodology such as doping or organic-linker modification changes the MOF-structure with shorter hydrophobic length and faster kinetics with water adsorption. Based on simulation, the functional MOFs and composite adsorbents are designed and fabricated for cooling, heating and desalination applications.

The contributions from this thesis are:

1. Based on surface characterisation results, the modified MOFs shows higher micro-pore distributions with enhanced structural and thermal stability as compared with conventional MOFs. In addition, the pore structure of the MOFs and composite adsorbents are not distorted by the alkali ions doping, zeolite mixing or functional group implanting process.
2. Experimentally, the post-synthesised Al-Fum MOFs deliver higher hydrophilicity, which agrees well with the GCMC simulation results. Al-Fum based adsorbents can also be ranked with respect to kinetics and these are 30% CHA-Al-Fum composite > 30% AFI-Al-Fum composite > 5% Li-Al-Fum-MOF > parent Al-Fum-MOF. Additionally, it is also found that Na^+ and K^+ dopants with larger sizes are not suitable for increasing the hydrophilicity of Al-Fum MOFs.
3. The hydrophobic length of functional $(CH_3)_2$-MOF-801 (Zr) is increased as compared with original MOF-801 (Zr) adsorbent. The higher water vapour transfer per thermal compression cycle (Δq) with faster kinetics are obtained for $(CH_3)_2$-MOF-801 (Zr). Experimentally, 25% higher Δq with two-times faster uptake/offtake rates are found for $(CH_3)_2$-MOF-801 (Zr) adsorbents, which is one of the key findings as compared with the literature review.
4. The linker functionalisation on MOFs has significant effects on water adsorption behaviours. As compared with original UiO-66 (Zr) MOFs, NH_2-UiO-66 (Zr) shows the similar “S-shaped” isotherm with a shorter hydrophobic length ($P/P_S \approx 0.20$) and negligible water transfer per cycle. OH-UiO-66 (Zr) resembles a transition from “type I” to “type V” isotherm with a limiting uptake of 0.34 g/g (of adsorbent). N-UiO-66 (Zr) exhibits “type I” isotherm due to the intense hydrophilic adsorbent-adsorbate interaction

at $P/P_s < 0.1$. Among all the UiO-66 (Zr) based MOFs, NH_2-UiO-66 (Zr) adsorbent exhibits the best performance, where substantial Δq (0.21) is achieved at the lower desorption temperature of 60℃ and relatively higher Δq (0.33) is observed when the desorption temperature increases up to 70℃.

5. Based on the numerical simulation of AHT systems, among all Al-Fum based MOFs, 5% Li-Al-Fum delivers the maximum water uptake/offtake difference (Δq) per AHT operation cycle. 30% CHA-Al-Fum exhibits the best cooling performance in terms of cooling capacity and COP. For the regeneration temperature of 60 ℃ and the cooling water inlet temperature of 30 ℃, 30% CHA-Al-Fum presents a promising COP of 0.39 and the SCP of 0.52 kW/kg, which is 42.3% and 70% higher as compared with the parent Al-Fum MOFs. In addition, at shorter half cycle time, higher SDWP are obtained for modified Al-Fum MOFs.
6. For $(CH_3)_2$ - MOF-801 (Zr) + water system, the optimum SCP is found 0.78 KW/kg, which is 40% higher as compared with parent MOF-801 (Zr) adsorbent. Furthremore, $(CH_3)_2$ - MOF-801 (Zr) achieves 17.0%, 7.3% and 40.4% higher in terms of COP_h, SHP and SDWP as compared with those of the original MOF-801 (Zr).
7. As compared with parent UiO-66 (Zr), NH_2-UiO-66 (Zr) yields over four times higher of COP in cooling applications; whereas OH-UiO-66 (Zr) and N-UiO-66 (Zr) could produce 10.6 and 12.7 m^3 more desalinated water per tonne of adsorbent per day, respectively. Employing the proposed functional UiO-66 (Zr) adsorbents, the thermal compressor can be operated with the driving heat source temperature of 60 ^oC or even lower for higher cooling/heating performances, COP and SDWP. The lower regeneration temperature also provides lower entropy generation.

8. The present results show that the smaller entropy generation ($\dot{S}_{gen}$) of AHT system is excepted under lower regeneration temperature and shorter half cycle time, which leads to the reduction of system irreversibility and the improvement of system-efficiency. By analysing temperature-entropy maps for each component of adsorption heat transformation process, the functionalised $(CH_3)_2$-MOF-801 (Zr) shows the promising adsorbent for adsorption cooling and N-UiO-66 (Zr) is found suitable for adsorption desalination application.

These findings confirm that the performances of adsorption heat transformation depend on water adsorption behaviours on adsorbents, which are mainly governed by interactions between adsorbate and adsorbent. The GCMC simulation is a reliable method to predict the water adsorption performances on various MOFs and composite adsorbents. Furthermore, the hydrophobic length for water adsorption on MOFs is controlled by modifying the micro-structures of MOFs with alkali ions doping, zeolite addition and functional group implanting on organic linker. Additionally, $\dot{S}_{gen}$ reflects the irreversibilities of the AHT system. The temperature-entropy maps could be used to analyse the $\dot{S}_{gen}$ with the change of temperature in each component of the AHT system, which could be used as a tool to enhance the performances of the AHT system. These contributions provide a benchmark for new MOFs design, fabrication and the optimisation of adsorption assisted cooling/heat pump and desalination systems.

6.2 Recommendations for Future Work

Novel MOFs design and modification

Theoretically, the number of self-assembly combinations of metal ions and organic ligands is limitless. Key parameters such as temperature, pressure, concentration of the reagent, acidity or alkalinity may affect the crystalline network significantly, even same metal-organic-precursors are used [123]. Hence, there is still enormous potential in novel MOFs design. To achieve that, detailed research activities such as the functionality of multitopic organic ligands, the critical formation conditions of metal building blocks, the possible morphologies as well as the nucleation kinetics are required for future exploration. Additionally, as described in this thesis, the adsorption behaviours of MOFs could be tailored to fulfill the requirements of a specific task. The main objective of MOFs modification (direct or post-synthesis) is to create the formation conditions that lead to the desired metal-organic-coordination while the original crystalline-integrity is not decomposed. Further research is certainly required to disentangle the complexities in MOFs design, synthesis and modification, both experimentally and theoretically.

Mass-Rapid-Production (MRP) of MOFs

One challenging problem is the low production rate of MOFs. Currently, the conventional MOF synthesis involves multi-steps namely preparation, crystallisation, purification and activation, where both pre-heating and pre-cooling are necessary. This process leads to long fabrication times. Furthermore, the laboratory yield of MOFs is usually in milligram-scale, which is far from enough to construct the bench scale adsorption-bed or thermal compressor. The rapid synthesis of MOFs will reduce the labor costs, reaction times as well as reactor volumes. One way to overcome these problems is to increase the number of same-sized reactors in parallel, however, it is not applicable because of the limitation of laboratory equipment. Another strategy is to use the reactor with larger diameter/size. This method is also not ideal because of that the nucleation of the MOFs chemical reaction mainly takes place at the vessel surface of reactors. Hence, the size (especially the surface to volume ratio) of the reactor is a crucial parameter and MOFs with low quality may be obtained if wrong size reactor is applied. Recently, Marta et al. [205] proposed one large-scale, batch reaction system for continuous production of MOFs (Al-Fum), where high STYs (space-time-yields) of 97159 kg/m^3/day and a production rate of 5.6 kg/h are achieved. Besides that, advanced hydrothermal synthesis methods such as ultrasonic or microwave radiation are used to accelerate the rate of MOFs fabrication [206]. However, these approaches have only been tested on few MOFs (less than ten) [205]. Therefore, revised synthesis methodology should be studied.

MOFs characterisation

Currently, nitrogen adsorption is preferably chosen for the porosities study on porous materials, for it is usually readily available and easy-packing traits. However, the key problem with this technique is that due to the quadrupole nature of nitrogen molecule, the pore filling pressures could be significantly affected by its surface charges. In addition, the nitrogen adsorption temperature is kept at 77 K (boiling point of nitrogen), the low temperature and low absolute pore filling pressures will result in long equilibrium times, especially for super-micro-materials. Nowadays, argon with the boiling point of 87 K is recommended by IUPAC for adsorptive porosities determination. As compared with nitrogen, argon molecule exhibits monoatomic, spherical shape with non-polar character, hence, it is free-orientation-issue on porous materials' surface and the surface charge effect is negligible. Furthermore, the adsorption kinetics of argon at 87 K are much faster than that of nitrogen at 77 K, and less equilibrium times are required. For example, Thommes et al. [207] showed that argon performs better than nitrogen when porous materials with polar or oxidic surfaces (such as zeolites) are involved. Future research could examine whether more comprehensive results of MOFs porosities will be obtained if argon is used. Additionally, traditional characterisation-technique such as SEM could only reflect the superficial topologies and morphologies of MOFs, however, the mechanisms of the functional group additives are not fully reveled. For example, whether the functional group additives are implanted onto the organic linkers or embedded into the CUSs (coordinatively unsaturated metal sites) of MOFs. Besides these, powder properties such as density and thermal conductivity could affect the AHT system performance significantly [208], which have rarely been studied directly. In future research, more advanced techniques such as DLS/ELS (Dynamic & Electrophoretic light scattering) and TEM (Transmission electron microscopy) are needed to apply and characterise MOFs properties.

Experimental investigation of AHT

Besides the unsolved Mass-Rapid-Production (MRP) of MOFs issue, the proper assembly of MOFs onto the sorption-bed heat exchanger with efficient heat-mass transfer remains problematic. Conventionally, silica gel or activated carbon used in AHT systems are usually served in granule, pellet or bulk phases, which are easy to handle. However, MOFs are in powder forms and difficult to be packed. To date, researchers have tried methods such as metal coating to solve this problem [131]. MOFs coating will reduce the adsorptive surface area of the adsorbents, degrade the thermal conductivity and lower the limit water uptake of the system. Recently, with the development in manufacturing area, robocasting or 3D printing techniques have already been applied to synthesis porous materials for various applications. For example, Couck et al. [209] produced a honeycomb-shaped SAPO-34 zeolite monolith by DIW (direct ink writing) 3D printing method, where methyl cellulose is used for binding purpose. It is found that 3D-printed SAPO-34 delivers efficient performance on CO_2/N_2 separation with stable geometry. Tubio et al. [210] fabricated one 3D-printed Cu/Al2O3 catalyst and proposed promising catalytic efficiency. Furthermore, a hybrid 3D-printed MOF-74 (Ni) and UTSA-16 (Co) monolith is developed by Harshul et al. [211], using for CO_2 adsorption with good kinetics. However, few studies have focused on the 3D-printing MOFs used for AHT applications (adsorption chiller, heat pump, desalination or dehumidification). It is believed that MOFs-based AHT applications will be fruitfully explored by future investigations on 3D-printing MOFs.

Modelling and simulation

The universal force field (12-6 Lennard-Jones bonding + Coulomb potential) used to study the adsorbent – adsorbate interactions could only reveal 85-90% of the total binding energy [161]. Besides the interaction between molecules, the interaction contributed by bonds, angles should also be taken into account. In addition, based on the energy expansion equation [212], charge-charge plus high order effects such as dipolar moment and quadrupole moment have significant effects on total adsorbent – adsorbate interactions when polar adsorbate molecules are involved. Hence, for the future molecular dynamic simulation, more advanced and comprehensive force field should be applied. Currently, the calculation of thermodynamic property surfaces (such as the isosteric heat or the entropy of adsorption) for single-component adsorbate on MOFs is GCMC-energy-derivation based, which is not a direct calculation method. Other classic models are usually only applicable to simple parallel slit-channel or cylindrical-shape models. Therefore, more complicated thermodynamic models related to the real MOFs structures should be derived. In addition, the kinetics investigation of GCMC adsorption on MOFs has not yet been fully developed. Future research should be devoted to the development of these simulation models.

References

1. Conti, J., P. Holtberg, J. Diefenderfer, A. LaRose, J.T. Turnure, and L. Westfall, International energy outlook 2016 with projections to 2040. 2016, *USDOE Energy Information Administration (EIA), Washington, DC (United States)*
2. Chua, K., S. Chou, W. Yang, and J. Yan, Achieving better energy-efficient air conditioning–a review of technologies and strategies. *Applied Energy*, 2013. **104**: p. 87-104.
3. Chen, S., N. Li, H. Yoshino, J. Guan, and M.D. Levine, Statistical analyses on winter energy consumption characteristics of residential buildings in some cities of China. *Energy and Buildings*, 2011. **43**(5): p. 1063-1070.
4. Woolf, D., J.E. Amonette, F.A. Street-Perrott, J. Lehmann, and S. Joseph, Sustainable biochar to mitigate global climate change. *Nature Communications*, 2010. **1**: p. 56.
5. Kang, S.M., L. Polvani, J. Fyfe, and M. Sigmond, Impact of polar ozone depletion on subtropical precipitation. *Science*, 2011. **332**(6032): p. 951-954.
6. Ng, K.C., K. Thu, Y. Kim, A. Chakraborty, and G. Amy, Adsorption desalination: an emerging low-cost thermal desalination method. *Desalination*, 2013. **308**: p. 161-179.
7. Zhai, X. and R. Wang, Experimental investigation and performance analysis on a solar adsorption cooling system with/without heat storage. *Applied Energy*, 2010. **87**(3): p. 824-835.
8. Chan, K., C.Y. Chao, G. Sze-To, and K.S. Hui, Performance predictions for a new zeolite 13X/CaCl2 composite adsorbent for adsorption cooling systems. *International Journal of Heat and Mass Transfer*, 2012. **55**(11-12): p. 3214-3224.

9. Tatlıer, M. and A. Erdem-Şenatalar, Effects of metal mass on the performance of adsorption heat pumps utilizing zeolite 4A coatings synthesized on heat exchanger tubes. *International Journal of Refrigeration,* 2000. **23**(4): p. 260-268.

10. Alsaman, A.S., A.A. Askalany, K. Harby, and M.S. Ahmed, Performance evaluation of a solar-driven adsorption desalination-cooling system. *Energy,* 2017. **128**: p. 196-207.

11. Shmroukh, A.N., A.H.H. Ali, and S. Ookawara, Adsorption working pairs for adsorption cooling chillers: A review based on adsorption capacity and environmental impact. *Renewable and Sustainable Energy Reviews,* 2015. **50**: p. 445-456.

12. Aristov, Y.I., B. Dawoud, I. Glaznev, and A. Elyas, A new methodology of studying the dynamics of water sorption/desorption under real operating conditions of adsorption heat pumps: experiment. *International Journal of Heat and Mass Transfer,* 2008. **51**(19-20): p. 4966-4972.

13. Wang, R. and R. Oliveira, Adsorption refrigeration—an efficient way to make good use of waste heat and solar energy. *Progress in Energy and Combustion Science,* 2006. **32**(4): p. 424-458.

14. Jakob, U. Recent developments of solar air-conditioning in Europe. in Cryogenics and Refrigeration–*Proceedings of ICCR*. 2008.

15. Jakob, U., M. Huber, D. Dubbelfeld, and R. Aubele. Experimental investigation of a novel solar cooling system based on a small-scale water/silica gel adsorption heat pump. in *International Symposium on Innovative Materials for Processes in Energy Systems, Kyoto, Japan*. 2007.

16. Wang, D., J. Wu, Z. Xia, H. Zhai, R. Wang, and W. Dou, Study of a novel silica gel–water adsorption chiller. Part II. Experimental study. *International Journal of Refrigeration,* 2005. **28**(7): p. 1084-1091.

17. Wang, D., Z. Xia, J. Wu, R. Wang, H. Zhai, and W. Dou, Study of a novel silica gel–water adsorption chiller. Part I. Design and performance prediction. *International Journal of Refrigeration,* 2005. **28**(7): p. 1073-1083.

18. Yang, G., Z. Xia, R. Wang, D. Keletigui, D. Wang, Z. Dong, and X. Yang, Research on a compact adsorption room air conditioner. *Energy Conversion and Management,* 2006. **47**(15-16): p. 2167-2177.

19. Li, S., Z. Xia, J. Wu, J. Li, R. Wang, and L. Wang, Experimental study of a novel CaCl2/expanded graphite-NH3 adsorption refrigerator. *International Journal of refrigeration,* 2010. **33**(1): p. 61-69.

20. Han, B. and A. Chakraborty, Advanced cooling heat pump and desalination employing functional UiO-66 (Zr) metal-organic frameworks. *Energy Conversion and Management,* 2020. **213**: p. 112825.

21. Youssef, P.G., S.M. Mahmoud, and R.K. Al-Dadah, Performance analysis of four bed adsorption water desalination/refrigeration system, comparison of AQSOA-Z02 to silica-gel. *Desalination,* 2015. **375**: p. 100-107.

22. Teo, H.W.B., A. Chakraborty, and B. Han, Water adsorption on CHA and AFI types zeolites: Modelling and investigation of adsorption chiller under static and dynamic conditions. *Applied Thermal Engineering,* 2017. **127**: p. 35-45.

23. Freni, A., L. Bonaccorsi, L. Calabrese, A. Caprì, A. Frazzica, and A. Sapienza, SAPO-34 coated adsorbent heat exchanger for adsorption chillers. *Applied Thermal Engineering,* 2015. **82**: p. 1-7.

24. Pan, Q., J. Peng, H. Wang, H. Sun, and R. Wang, Experimental investigation of an adsorption air-conditioner using silica gel-water working pair. *Solar Energy,* 2019. **185**: p. 64-71.

25. Myat, A., N.K. Choon, K. Thu, and Y.-D. Kim, Experimental investigation on the optimal performance of Zeolite–water adsorption chiller. *Applied energy,* 2013. **102**: p. 582-590.

26. Rezk, A.R. and R.K. Al-Dadah, Physical and operating conditions effects on silica gel/water adsorption chiller performance. *Applied Energy*, 2012. **89**(1): p. 142-149.

27. Mahdavikhah, M. and H. Niazmand, Effects of plate finned heat exchanger parameters on the adsorption chiller performance. *Applied Thermal Engineering,* 2013. **50**(1): p. 939-949.

28. Restuccia, G., A. Freni, F. Russo, and S. Vasta, Experimental investigation of a solid adsorption chiller based on a heat exchanger coated with hydrophobic zeolite. *Applied thermal engineering,* 2005. **25**(10): p. 1419-1428.

29. Li, A., A.B. Ismail, K. Thu, K.C. Ng, and W.S. Loh, Performance evaluation of a zeolite–water adsorption chiller with entropy analysis of thermodynamic insight. *Applied energy,* 2014. **130**: p. 702-711.

30. Han, B. and A. Chakraborty, Water adsorption studies on synthesized alkali-ions doped Al-fumarate MOFs and Al-fumarate+ zeolite composites for higher water uptakes and faster kinetics. *Microporous and Mesoporous Materials,* 2019. **288**: p. 109590.

31. Canivet, J., A. Fateeva, Y. Guo, B. Coasne, and D. Farrusseng, Water adsorption in MOFs: fundamentals and applications. *Chemical Society Reviews,* 2014. **43**(16): p. 5594-5617.

32. Teo, H.W.B., A. Chakraborty, and S. Kayal, Post synthetic modification of MIL-101 (Cr) for S-shaped isotherms and fast kinetics with water adsorption. *Applied Thermal Engineering,* 2017. **120**: p. 453-462.

33. Fujie, K. and H. Kitagawa, Ionic liquid transported into metal–organic frameworks. *Coordination Chemistry Reviews,* 2016. **307**: p. 382-390.

34. An, H.J., M. Sarker, D.K. Yoo, and S.H. Jhung, Water adsorption/desorption over metal-organic frameworks with ammonium group for possible application in adsorption heat transformation. *Chemical Engineering Journal,* 2019. **373**: p. 1064-1071.

35. Butova, V.V., I.A. Pankin, O.A. Burachevskaya, K.S. Vetlitsyna-Novikova, and A.V. Soldatov, New fast synthesis of MOF-801 for water and hydrogen storage: Modulator effect and recycling options. *Inorganica Chimica Acta,* 2020. **514**: p. 120025.

36. Kim, H., S. Yang, S.R. Rao, S. Narayanan, E.A. Kapustin, H. Furukawa, A.S. Umans, O.M. Yaghi, and E.N. Wang, Water harvesting from air with metal-organic frameworks powered by natural sunlight. *Science,* 2017. **356**(6336): p. 430-434.

37. Permyakova, A., O. Skrylnyk, E. Courbon, M. Affram, S. Wang, U.H. Lee, A.H. Valekar, F. Nouar, G. Mouchaham, and T. Devic, Synthesis Optimization, Shaping, and Heat Reallocation Evaluation of the Hydrophilic Metal–Organic Framework MIL-160 (Al). *ChemSusChem,* 2017. **10**(7): p. 1419-1426.

38. Canivet, J., J. Bonnefoy, C. Daniel, A. Legrand, B. Coasne, and D. Farrusseng, Structure–property relationships of water adsorption in metal–organic frameworks. *New Journal of Chemistry,* 2014. **38**(7): p. 3102-3111.

39. Fröhlich, D., E. Pantatosaki, P.D. Kolokathis, K. Markey, H. Reinsch, M. Baumgartner, M.A. van der Veen, D.E. De Vos, N. Stock, and G.K. Papadopoulos, Water adsorption behaviour of CAU-10-H: a thorough investigation of its structure–property relationships. *Journal of Materials Chemistry A,* 2016. **4**(30): p. 11859-11869.

40. Teo, H.W.B., A. Chakraborty, Y. Kitagawa, and S. Kayal, Experimental study of isotherms and kinetics for adsorption of water on Aluminium Fumarate. *International Journal of Heat and Mass Transfer,* 2017. **114**: p. 621-627.

41. Glover, T.G., G.W. Peterson, B.J. Schindler, D. Britt, and O. Yaghi, MOF-74 building unit has a direct impact on toxic gas adsorption. *Chemical Engineering Science,* 2011. **66**(2): p. 163-170.

42. Zhao, Z., S. Wang, Y. Yang, X. Li, J. Li, and Z. Li, Competitive adsorption and selectivity of benzene and water vapor on the microporous metal organic frameworks (HKUST-1). *Chemical Engineering Journal,* 2015. **259**: p. 79-89.

43. Han, B. and A. Chakraborty, Adsorption characteristics of methyl-functional ligand MOF-801 and water systems: Adsorption chiller modelling and performances. *Applied Thermal Engineering,* 2020: p. 115393.

44. Bae, Y.-S., O.K. Farha, J.T. Hupp, and R.Q. Snurr, Enhancement of CO 2/N 2 selectivity in a metal-organic framework by cavity modification. *Journal of Materials Chemistry,* 2009. **19**(15): p. 2131-2134.

45. Wickenheisser, M., F. Jeremias, S.K. Henninger, and C. Janiak, Grafting of hydrophilic ethylene glycols or ethylenediamine on coordinatively unsaturated metal sites in MIL-100 (Cr) for improved water adsorption characteristics. *Inorganica Chimica Acta,* 2013. **407**: p. 145-152.

46. Hu, G., W. Li, and S. Li, Effects of functionalization on the performance of metal-organic frameworks for adsorption-driven heat pumps by molecular simulations. *Chemical Engineering Science,* 2019. **208**: p. 115143.

47. Kim, M., J.F. Cahill, Y. Su, K.A. Prather, and S.M. Cohen, Postsynthetic ligand exchange as a route to functionalization of 'inert'metal–organic frameworks. *Chemical Science,* 2012. **3**(1): p. 126-130.

48. Velev, O., T. Jede, R. Lobo, and A. Lenhoff, Porous silica via colloidal crystallization. *Nature,* 1997. **389**(6650): p. 447-448.

49. Yadav, M. and Q. Xu, Catalytic chromium reduction using formic acid and metal nanoparticles immobilized in a metal–organic framework. *Chemical Communications,* 2013. **49**(32): p. 3327-3329.

50. Do, D. and H. Do, Modeling of adsorption on nongraphitized carbon surface: GCMC simulation studies and comparison with experimental data. *The Journal of Physical Chemistry B,* 2006. **110**(35): p. 17531-17538.

51. Bourg, I.C. and C.I. Steefel, Molecular dynamics simulations of water structure and diffusion in silica nanopores. *The Journal of Physical Chemistry C,* 2012. **116**(21): p. 11556-11564.

52. Meng, S., E. Wang, and S. Gao, Water adsorption on metal surfaces: A general picture from density functional theory studies. *Physical Review B,* 2004. **69**(19): p. 195404.

53. Chakraborty, A., B.B. Saha, K.C. Ng, S. Koyama, and K. Srinivasan, Theoretical insight of physical adsorption for a single-component adsorbent+ adsorbate system: I. Thermodynamic property surfaces. *Langmuir,* 2009. **25**(4): p. 2204-2211.

54. Rouquerol, J., F. Rouquerol, P. Llewellyn, G. Maurin, and K.S. Sing, Adsorption by powders and porous solids: principles, methodology and applications. 2013: *Academic press*.

55. Chakraborty, A., B.B. Saha, S. Koyama, and K. Ng, On the thermodynamic modeling of the isosteric heat of adsorption and comparison with experiments. *Applied physics letters,* 2006. **89**(17): p. 171901.

56. Haber, J., Manual on catalyst characterization (Recommendations 1991). *Pure and Applied Chemistry,* 1991. **63**(9): p. 1227-1246.

57. Rouquerol, J., D. Avnir, C. Fairbridge, D. Everett, J. Haynes, N. Pernicone, J. Ramsay, K. Sing, and K. Unger, Recommendations for the characterization of porous solids (Technical Report). *Pure and Applied Chemistry,* 1994. **66**(8): p. 1739-1758.

58. Sing, K.S., Reporting physisorption data for gas/solid systems with special reference to the determination of surface area and porosity (Recommendations 1984). *Pure and Applied Chemistry,* 1985. **57**(4): p. 603-619.

59. Thommes, M., J.r. Morell, K.A. Cychosz, and M. Fröba, Combining nitrogen, argon, and water adsorption for advanced characterization of ordered mesoporous carbons (CMKs) and periodic mesoporous organosilicas (PMOs). *Langmuir,* 2013. **29**(48): p. 14893-14902.

60. Solmuş, İ., C. Yamalı, B. Kaftanoğlu, D. Baker, and A. Çağlar, Adsorption properties of a natural zeolite–water pair for use in adsorption cooling cycles. *Applied Energy,* 2010. **87**(6): p. 2062-2067.

61. Henninger, S.K., F. Jeremias, H. Kummer, and C. Janiak, MOFs for use in adsorption heat pump processes. *European Journal of Inorganic Chemistry,* 2012. **2012**(16): p. 2625-2634.

62. Seo, Y.K., J.W. Yoon, J.S. Lee, Y.K. Hwang, C.H. Jun, J.S. Chang, S. Wuttke, P. Bazin, A. Vimont, and M. Daturi, Energy-efficient dehumidification over hierachically porous metal–organic frameworks as advanced water adsorbents. *Advanced Materials,* 2012. **24**(6): p. 806-810.

63. Yu, N., R. Wang, and L. Wang, Sorption thermal storage for solar energy. *Progress in Energy and Combustion Science,* 2013. **39**(5): p. 489-514.

64. Yang, H.Y., Z.J. Han, S.F. Yu, K.L. Pey, K. Ostrikov, and R. Karnik, Carbon nanotube membranes with ultrahigh specific adsorption capacity for water desalination and purification. *Nature Communications,* 2013. **4**: p. 2220.

65. ALOthman, Z.A., A review: fundamental aspects of silicate mesoporous materials. *Materials,* 2012. **5**(12): p. 2874-2902.

66. Foo, K.Y. and B.H. Hameed, Insights into the modeling of adsorption isotherm systems. *Chemical Engineering Journal,* 2010. **156**(1): p. 2-10.

67. Everett, D.H. and J.C. Powl, Adsorption in slit-like and cylindrical micropores in the henry's law region. A model for the microporosity of carbons. *Journal of the Chemical Society, Faraday Transactions 1: Physical Chemistry in Condensed Phases,* 1976. **72**: p. 619-636.

68. Langmuir, I., The constitution and fundamental properties of solids and liquids. Part I. Solids. *Journal of the American Chemical Society,* 1916. **38**(11): p. 2221-2295.

69. Dubinin, M. The equation of the characteristic curve of activated charcoal. in Dokl. Akad. Nauk. SSSR. 1947.

70. Freundlich, H., Over the adsorption in solution. *J. Phys. Chem,* 1906. **57**(385471): p. 1100-1107.

71. Ng, C., J.N. Losso, W.E. Marshall, and R.M. Rao, Freundlich adsorption isotherms of agricultural by-product-based powdered activated carbons in a geosmin–water system. *Bioresource Technology,* 2002. **85**(2): p. 131-135.

72. Temkin, M., Kinetics of ammonia synthesis on promoted iron catalysts. *Acta physiochim. URSS*, 1940. **12**: p. 327-356.

73. Toth, J., State equation of the solid-gas interface layers. *Acta Chim. Hung.,* 1971. **69**: p. 311-328.

74. Brunauer, S., P.H. Emmett, and E. Teller, Adsorption of gases in multimolecular layers. *Journal of the American Chemical Society,* 1938. **60**(2): p. 309-319.

75. McMillan, W. and E. Teller, The assumptions of the BET theory. *The Journal of Physical Chemistry,* 1951. **55**(1): p. 17-20.

76. Sips, R., Combined form of Langmuir and Freundlich equations. *J. Chem. Phys,* 1948. **16**(429): p. 490-495.

77. Redlich, O. and D.L. Peterson, A useful adsorption isotherm. *Journal of Physical Chemistry,* 1959. **63**(6): p. 1024-1024.

78. Koble, R.A. and T.E. Corrigan, Adsorption isotherms for pure hydrocarbons. *Industrial & Engineering Chemistry,* 1952. **44**(2): p. 383-387.

79. Khan, A., R. Ataullah, and A. Al-Haddad, Equilibrium adsorption studies of some aromatic pollutants from dilute aqueous solutions on activated carbon at different temperatures. *Journal of Colloid and Interface Science,* 1997. **194**(1): p. 154-165.

80. Jnr, M.H. and A.I. Spiff, Equilibrium sorption study of Al3+, Co2+ and Ag+ in aqueous solutions by fluted pumpkin (Telfairia occidentalis HOOK f) waste biomass. *Acta Chim. Slov,* 2005. **52**: p. 174-181.

81. Hill, A.V., The possible effects of the aggregation of the molecules of haemoglobin on its dissociation curves. *J. Physiol.,* 1910. **40**: p. 4-7.

82. Chakraborty, A. and B. Sun, An adsorption isotherm equation for multi-types adsorption with thermodynamic correctness. *Applied Thermal Engineering,* 2014. **72**(2): p. 190-199.

83. Lazaridis, N. and D. Asouhidou, Kinetics of sorptive removal of chromium (VI) from aqueous solutions by calcined Mg–Al–CO3 hydrotalcite. *Water Research,* 2003. **37**(12): p. 2875-2882.

84. Qiu, H., L. Lv, B.-c. Pan, Q.-j. Zhang, W.-m. Zhang, and Q.-x. Zhang, Critical review in adsorption kinetic models. *Journal of Zhejiang University-Science A,* 2009. **10**(5): p. 716-724.

85. Saiers, J.E., G.M. Hornberger, and L. Liang, First-and second-order kinetics approaches for modeling the transport of colloidal particles in porous media. *Water Resources Research,* 1994. **30**(9): p. 2499-2506.

86. O'Shannessy, D.J. and D.J. Winzor, Interpretation of deviations from pseudo-first-order kinetic behavior in the characterization of ligand binding by biosensor technology. *Analytical Biochemistry,* 1996. **236**(2): p. 275-283.

87. Chu, K. and M. Hashim, Modeling batch equilibrium and kinetics of copper removal by crab shell. *Separation Science and Technology*, 2003. **38**(16): p. 3927-3950.

88. Lagergren, S.K., About the theory of so-called adsorption of soluble substances. *Sven. Vetenskapsakad. Handingarl*, 1898. **24**: p. 1-39.

89. Marczewski, A., Application of mixed order rate equations to adsorption of methylene blue on mesoporous carbons. *Applied Surface Science*, 2010. **256**(17): p. 5145-5152.

90. Ho, Y.-S. and G. McKay, Sorption of dye from aqueous solution by peat. *Chemical Engineering Journal*, 1998. **70**(2): p. 115-124.

91. Wang, S., H. Li, and L. Xu, Application of zeolite MCM-22 for basic dye removal from wastewater. *Journal of Colloid and Interface Science*, 2006. **295**(1): p. 71-78.

92. Ho, Y.-S., Review of second-order models for adsorption systems. *Journal of Hazardous Materials*, 2006. **136**(3): p. 681-689.

93. Sano, T., N. Yamashita, Y. Iwami, K. Takeda, and Y. Kawakami, Estimation of dealumination rate of ZSM-5 zeolite by adsorption of water vapor. *Zeolites*, 1996. **16**(4): p. 258-264.

94. Zeldowitsch, J., Über den mechanismus der katalytischen oxydation von CO an MnO2. *Acta Physicochim. URSS*, 1934. **1**: p. 364-449.

95. JO'M, B. and K. Jeng, In-situ studies of adsorption of organic compounds on platinum electrodes. *Journal of Electroanalytical Chemistry*, 1992. **330**(1-2): p. 541-581.

96. Ritchie, A., Alternative to the Elovich equation for the kinetics of adsorption of gases on solids. *Journal of the Chemical Society, Faraday Transactions 1: Physical Chemistry in Condensed Phases*, 1977. **73**: p. 1650-1653.

97. Cheung, C., J. Porter, and G. McKay, Sorption kinetic analysis for the removal of cadmium ions from effluents using bone char. *Water Research,* 2001. **35**(3): p. 605-612.

98. Sun, B. and A. Chakraborty, Thermodynamic frameworks of adsorption kinetics modeling: Dynamic water uptakes on silica gel for adsorption cooling applications. *Energy,* 2015. **84**: p. 296-302.

99. Chahine, R. and T. Bose, Low-pressure adsorption storage of hydrogen. *International Journal of Hydrogen Energy,* 1994. **19**(2): p. 161-164.

100. Fan, W. and A. Chakraborty, Isosteric heat of adsorption at zero coverage for AQSOA-Z01/Z02/Z05 zeolites and water systems. *Microporous and Mesoporous Materials,* 2018. **260**: p. 201-207.

101. Beebe, R., J. Biscoe, W. Smith, and C. Wendell, Heats of adsorption on carbon black. I. *Journal of the American Chemical Society,* 1947. **69**(1): p. 95-101.

102. Shen, D., M. Bülow, F. Siperstein, M. Engelhard, and A.L. Myers, Comparison of experimental techniques for measuring isosteric heat of adsorption. *Adsorption,* 2000. **6**(4): p. 275-286.

103. Azahar, F.H.M., S. Mitra, A. Yabushita, A. Harata, B.B. Saha, and K. Thu, Improved model for the isosteric heat of adsorption and impacts on the performance of heat pump cycles. *Applied Thermal Engineering,* 2018. **143**: p. 688-700.

104. Watabe, T. and K. Yogo, Isotherms and isosteric heats of adsorption for CO2 in amine-functionalized mesoporous silicas. *Separation and Purification Technology,* 2013. **120**: p. 20-23.

105. Michaels, A.S., Physical Adsorption of Gases. DM Young and AD Crowell. Butter-worth, Washington, DC, 1962. xii+ 426 pp. Illus. $13. 1963, *American Association for the Advancement of Science*.

106. RAHMAN, K.A., Experimental and theoretical studies on adsorbed natural gas storage system using activated carbons. 2011.

107. Rahman, K.A., A. Chakraborty, B.B. Saha, and K.C. Ng, On thermodynamics of methane+ carbonaceous materials adsorption. *International Journal of Heat and Mass Transfer*, 2012. **55**(4): p. 565-573.

108. Chakraborty, A., B.B. Saha, I.I. El-Sharkawy, S. Koyama, K. Srinivasan, and K.C. Ng, Theory and experimental validation on isosteric heat of adsorption for an adsorbent+ adsorbate system. *High Temperatures--High Pressures*, 2008. **37**(2).

109. Askalany, A.A. and B.B. Saha, Derivation of isosteric heat of adsorption for non-ideal gases. *International Journal of Heat and Mass Transfer*, 2015. **89**: p. 186-192.

110. Bae, Y.-S. and R.Q. Snurr, Optimal isosteric heat of adsorption for hydrogen storage and delivery using metal–organic frameworks. *Microporous and Mesoporous Materials*, 2010. **132**(1-2): p. 300-303.

111. Klomkliang, N., R. Kaewmanee, S. Saimoey, S. Intarayothya, D. Do, and D. Nicholson, Adsorption of water and methanol on highly graphitized thermal carbon black: The effects of functional group and temperature on the isosteric heat at low loadings. *Carbon*, 2016. **99**: p. 361-369.

112. Dulaurent, O. and D. Bianchi, Adsorption isobars for CO on a Pt/Al2O3 catalyst at high temperatures using FTIR spectroscopy: isosteric heat of adsorption and adsorption model. *Applied Catalysis A: General*, 2000. **196**(2): p. 271-280.

113. Srivastava, V.C., I.D. Mall, and I.M. Mishra, Adsorption thermodynamics and isosteric heat of adsorption of toxic metal ions onto bagasse fly ash (BFA) and rice husk ash (RHA). *Chemical Engineering Journal,* 2007. **132**(1-3): p. 267-278.

114. Cavenati, S., C.A. Grande, and A.E. Rodrigues, Adsorption equilibrium of methane, carbon dioxide, and nitrogen on zeolite 13X at high pressures. *Journal of Chemical & Engineering Data*, 2004. **49**(4): p. 1095-1101.

115. Al-Degs, Y.S., M.I. El-Barghouthi, A.H. El-Sheikh, and G.M. Walker, Effect of solution pH, ionic strength, and temperature on adsorption behavior of reactive dyes on activated carbon. *Dyes and Pigments*, 2008. **77**(1): p. 16-23.

116. Zhang, L., Design and testing of an automobile waste heat adsorption cooling system. *Applied Thermal Engineering,* 2000. **20**(1): p. 103-114.

117. Kitagawa, S., Metal–organic frameworks (MOFs). *Chemical Society Reviews,* 2014. **43**(16): p. 5415-5418.

118. Pan, Q., R. Wang, L. Wang, and D. Liu, Design and experimental study of a silica gel-water adsorption chiller with modular adsorbers. *International Journal of Refrigeration,* 2016. **67**: p. 336-344.

119. Zajaczkowski, B., Optimizing performance of a three-bed adsorption chiller using new cycle time allocation and mass recovery. *Applied Thermal Engineering,* 2016. **100**: p. 744-752.

120. Freni, A., A. Sapienza, I.S. Glaznev, Y.I. Aristov, and G. Restuccia, Experimental testing of a lab-scale adsorption chiller using a novel selective water sorbent “silica modified by calcium nitrate”. *International Journal of Refrigeration*, 2012. **35**(3): p. 518-524.

121. Lu, Z., R. Wang, and Z. Xia, Experimental analysis of an adsorption air conditioning with micro-porous silica gel–water. *Applied Thermal Engineering*, 2013. **50**(1): p. 1015-1020.

122. Qian, S., K. Gluesenkamp, Y. Hwang, R. Radermacher, and H.-H. Chun, Cyclic steady state performance of adsorption chiller with low regeneration temperature zeolite. *Energy*, 2013. **60**: p. 517-526.

123. Stock, N. and S. Biswas, Synthesis of metal-organic frameworks (MOFs): routes to various MOF topologies, morphologies, and composites. *Chemical Reviews*, 2011. **112**(2): p. 933-969.

124. Liu, S., L. Sun, F. Xu, J. Zhang, C. Jiao, F. Li, Z. Li, S. Wang, Z. Wang, and X. Jiang, Nanosized Cu-MOFs induced by graphene oxide and enhanced gas storage capacity. *Energy & Environmental Science*, 2013. **6**(3): p. 818-823.

125. Ma, J., X. Guo, Y. Ying, D. Liu, and C. Zhong, Composite ultrafiltration membrane tailored by MOF@ GO with highly improved water purification performance. *Chemical Engineering Journal*, 2017. **313**: p. 890-898.

126. Wisser, D., F.M. Wisser, S. Raschke, N. Klein, M. Leistner, J. Grothe, E. Brunner, and S. Kaskel, Biological Chitin–MOF Composites with Hierarchical Pore Systems for Air-Filtration Applications. *Angewandte Chemie International Edition*, 2015. **54**(43): p. 12588-12591.

127. García-García, P., M. Müller, and A. Corma, MOF catalysis in relation to their homogeneous counterparts and conventional solid catalysts. *Chemical Science*, 2014. **5**(8): p. 2979-3007.

128. Ehrenmann, J., S.K. Henninger, and C. Janiak, Water adsorption characteristics of MIL-101 for heat-transformation applications of MOFs. *European Journal of Inorganic Chemistry*, 2011. **2011**(4): p. 471-474.

129. Jeremias, F., D. Fröhlich, C. Janiak, and S.K. Henninger, Advancement of sorption-based heat transformation by a metal coating of highly-stable, hydrophilic aluminium fumarate MOF. *RSC Advances*, 2014. **4**(46): p. 24073-24082.

130. Cadiau, A., J.S. Lee, D. Damasceno Borges, P. Fabry, T. Devic, M.T. Wharmby, C. Martineau, D. Foucher, F. Taulelle, and C.H. Jun, Design of hydrophilic metal organic framework water adsorbents for heat reallocation. *Advanced Materials*, 2015. **27**(32): p. 4775-4780.

131. De Lange, M., T. Zeng, T. Vlugt, J. Gascon, and F. Kapteijn, Manufacture of dense CAU-10-H coatings for application in adsorption driven heat pumps: optimization and characterization. *CrystEngComm*, 2015. **17**(31): p. 5911-5920.

132. Jeremias, F., V. Lozan, S.K. Henninger, and C. Janiak, Programming MOFs for water sorption: amino-functionalized MIL-125 and UiO-66 for heat transformation and heat storage applications. *Dalton Transactions*, 2013. **42**(45): p. 15967-15973.

133. Solovyeva, M., L. Gordeeva, T. Krieger, and Y.I. Aristov, MOF-801 as a promising material for adsorption cooling: Equilibrium and dynamics of water adsorption. *Energy Conversion and Management*, 2018. **174**: p. 356-363.

134. Dechnik, J., C. Janiak, and S. De, Aluminium fumarate metal-organic framework: a super adsorbent for fluoride from water. *Journal of Hazardous Materials*, 2016. **303**: p. 10-20.

135. Youssef, P., S. Mahmoud, R. Al-Dadah, E. Elsayed, and O. El-Samni, Numerical Investigation of Aluminum Fumarate MOF adsorbent material for adsorption desalination/cooling application. *Energy Procedia*, 2017. **142**: p. 1693-1698.

136. MARTINEZ, M.R., M.R. Hill, M. Batten, K.S. Lim, A. POLYZOS, T.R. Barton, T.D. HADLEY, and A.A. MONCH, Production of metal-organic frameworks. 2018, *Google Patents*.

137. Yot, P.G., L. Vanduyfhuys, E. Alvarez, J. Rodriguez, J.-P. Itié, P. Fabry, N. Guillou, T. Devic, I. Beurroies, and P.L. Llewellyn, Mechanical energy storage performance of an aluminum fumarate metal–organic framework. *Chemical Science*, 2016. **7**(1): p. 446-450.

138. Furukawa, H., F. Gándara, Y.-B. Zhang, J. Jiang, W.L. Queen, M.R. Hudson, and O.M. Yaghi, Water adsorption in porous metal–organic frameworks and related materials. *Journal of the American Chemical Society*, 2014. **136**(11): p. 4369-4381.

139. Liu, X., N.K. Demir, Z. Wu, and K. Li, Highly water-stable zirconium metal–organic framework UiO-66 membranes supported on alumina hollow fibers for desalination. *Journal of the American Chemical Society*, 2015. **137**(22): p. 6999-7002.

140. Yang, J.-M., Q. Liu, and W.-Y. Sun, Shape and size control and gas adsorption of Ni (II)-doped MOF-5 nano/microcrystals. *Microporous and Mesoporous Materials*, 2014. **190**: p. 26-31.

141. Zhu, X.-W., X.-P. Zhou, and D. Li, Exceptionally water stable heterometallic gyroidal MOFs: tuning the porosity and hydrophobicity by doping metal ions. *Chemical Communications*, 2016. **52**(39): p. 6513-6516.

142. Ortiz, A.U., A.P. Freitas, A. Boutin, A.H. Fuchs, and F.-X. Coudert, What makes zeolitic imidazolate frameworks hydrophobic or hydrophilic? The impact of geometry and

functionalization on water adsorption. *Physical Chemistry Chemical Physics,* 2014. **16**(21): p. 9940-9949.

143. Waitschat, S., D. Fröhlich, H. Reinsch, H. Terraschke, K. Lomachenko, C. Lamberti, H. Kummer, T. Helling, M. Baumgartner, and S. Henninger, Synthesis of M-UiO-66 (M= Zr, Ce or Hf) employing 2, 5-pyridinedicarboxylic acid as a linker: defect chemistry, framework hydrophilisation and sorption properties. *Dalton Transactions,* 2018. **47**(4): p. 1062-1070.

144. Ko, N., J. Hong, S. Sung, K.E. Cordova, H.J. Park, J.K. Yang, and J. Kim, A significant enhancement of water vapour uptake at low pressure by amine-functionalization of UiO-67. *Dalton Transactions,* 2015. **44**(5): p. 2047-2051.

145. Ma, D., Y. Li, and Z. Li, Tuning the moisture stability of metal–organic frameworks by incorporating hydrophobic functional groups at different positions of ligands. *Chemical Communications*, 2011. **47**(26): p. 7377-7379.

146. Jiang, S., K.E. Gubbins, and J.A. Zollweg, Adsorption, isosteric heat and commensurate-incommensurate transition of methane on graphite. *Molecular Physics,* 1993. **80**(1): p. 103-116.

147. Peng, X., L.C. Lin, W. Sun, and B. Smit, Water adsorption in metal–organic frameworks with open-metal sites. *AIChE Journal,* 2015. **61**(2): p. 677-687.

148. Morse, P.M., Diatomic molecules according to the wave mechanics. II. Vibrational levels. *Physical Review*, 1929. **34**(1): p. 57.

149. Le Roy, R.J., N.S. Dattani, J.A. Coxon, A.J. Ross, P. Crozet, and C. Linton, Accurate analytic potentials for Li 2 (X Σ 1 g+) and Li 2 (A Σ 1 u+) from 2 to 90 Å, and the radiative lifetime of Li (2 p). *The Journal of Chemical Physics,* 2009. **131**(20): p. 204309.

150. Le Roy, R.J., C.C. Haugen, J. Tao, and H. Li, Long-range damping functions improve the short-range behaviour of 'MLR'potential energy functions. *Molecular Physics*, 2011. **109**(3): p. 435-446.

151. Coxon, J.A. and P.G. Hajigeorgiou, The ground X Σ 1 g+ electronic state of the cesium dimer: Application of a direct potential fitting procedure. *The Journal of Chemical Physics*, 2010. **132**(9): p. 094105.

152. Rappé, A.K., C.J. Casewit, K. Colwell, W.A. Goddard III, and W.M. Skiff, UFF, a full periodic table force field for molecular mechanics and molecular dynamics simulations. *Journal of the American Chemical Society*, 1992. **114**(25): p. 10024-10035.

153. Mason, E.A., Transport Properties of Gases Obeying a Modified Buckingham (Exp-Six) Potential. *The Journal of Chemical Physics*, 1954. **22**(2): p. 169-186.

154. Mourits, F.M. and F.H. Rummens, A critical evaluation of Lennard–Jones and Stockmayer potential parameters and of some correlation methods. *Canadian Journal of Chemistry*, 1977. **55**(16): p. 3007-3020.

155. Monkhorst, H.J., Calculation of properties with the coupled-cluster method. *International Journal of Quantum Chemistry*, 1977. **12**(S11): p. 421-432.

156. Bayly, C.I., P. Cieplak, W. Cornell, and P.A. Kollman, A well-behaved electrostatic potential based method using charge restraints for deriving atomic charges: the RESP model. *The Journal of Physical Chemistry*, 1993. **97**(40): p. 10269-10280.

157. Hetzer, G., P. Pulay, and H.-J. Werner, Multipole approximation of distant pair energies in local MP2 calculations. *Chemical Physics Letters*, 1998. **290**(1-3): p. 143-149.

158. Mulder, F. and C. Huiszoon, The dimer interaction and lattice energy of ethylene and pyrazine in the multipole expansion; a comparison with atom-atom potentials. *Molecular Physics,* 1977. **34**(5): p. 1215-1235.

159. Carrasco, J., A. Hodgson, and A. Michaelides, A molecular perspective of water at metal interfaces. *Nature Materials,* 2012. **11**(8): p. 667.

160. Ghosh, P., Y.J. Colón, and R.Q. Snurr, Water adsorption in UiO-66: the importance of defects. *Chemical Communications,* 2014. **50**(77): p. 11329-11331.

161. Fan, W. and A. Chakraborty, Investigation of the interaction of polar molecules on graphite surface: prediction of isosteric heat of adsorption at zero surface coverage. *The Journal of Physical Chemistry C,* 2016. **120**(41): p. 23490-23499.

162. Ali, S.M., A. Chakraborty, and K.C. Leong, CO2-assisted compression-adsorption hybrid for cooling and desalination. *Energy Conversion and Management,* 2017. **143**: p. 538-552.

163. Kayal, S., S. Baichuan, and B.B. Saha, Adsorption characteristics of AQSOA zeolites and water for adsorption chillers. *International Journal of Heat and Mass Transfer,* 2016. **92**: p. 1120-1127.

164. Ali, S.M. and A. Chakraborty, Adsorption assisted double stage cooling and desalination employing silica gel+ water and AQSOA-Z02+ water systems. *Energy conversion and management,* 2016. **117**: p. 193-205.

165. Liu, Y. and K. Leong, Numerical modeling of a zeolite/water adsorption cooling system with non-constant condensing pressure. *International Communications in Heat and Mass Transfer,* 2008. **35**(5): p. 618-622.

166. Chakraborty, A., K.C. Leong, K. Thu, B.B. Saha, and K.C. Ng, Theoretical insight of adsorption cooling. *Applied Physics Letters,* 2011. **98**(22): p. 221910.

167. Teng, W., K. Leong, and A. Chakraborty, Revisiting adsorption cooling cycle from mathematical modelling to system development. *Renewable and Sustainable Energy Reviews,* 2016. **63**: p. 315-332.

168. Zhao, W., W. Jia, M. Xu, J. Wang, Y. Li, Z. Zhang, Y. Wang, L. Zheng, Q. Li, and J. Yun, Facile synthesis of oil adsorbent carbon microtubes by pyrolysis of plant tissues. *Journal of Materials Science,* 2019. **54**(13): p. 9352-9361.

169. Mark, P. and L. Nilsson, Structure and dynamics of the TIP3P, SPC, and SPC/E water models at 298 K. *The Journal of Physical Chemistry A,* 2001. **105**(43): p. 9954-9960.

170. Abascal, J.L. and C. Vega, A general purpose model for the condensed phases of water: TIP4P/2005. *The Journal of Chemical Physics,* 2005. **123**(23): p. 234505.

171. Price, D.J. and C.L. Brooks III, A modified TIP3P water potential for simulation with Ewald summation. *The Journal of Chemical Physics,* 2004. **121**(20): p. 10096-10103.

172. Furukawa, H., F. Gandara, Y.-B. Zhang, J. Jiang, W.L. Queen, M.R. Hudson, and O.M. Yaghi, Water adsorption in porous metal–organic frameworks and related materials. *Journal of the American Chemical Society,* 2014. **136**(11): p. 4369-4381.

173. Zhang, K., Y. Chen, A. Nalaparaju, and J. Jiang, Functionalized metal–organic framework MIL-101 for CO 2 capture: multi-scale modeling from ab initio calculation and molecular simulation to breakthrough prediction. *CrystEngComm,* 2013. **15**(47): p. 10358-10366.

174. Besler, B.H., K.M. Merz Jr, and P.A. Kollman, Atomic charges derived from semiempirical methods. *Journal of Computational Chemistry,* 1990. **11**(4): p. 431-439.

175. Lan, J., D. Cao, W. Wang, and B. Smit, Doping of alkali, alkaline-earth, and transition metals in covalent-organic frameworks for enhancing CO2 capture by first-principles calculations and molecular simulations. *Acs Nano,* 2010. **4**(7): p. 4225-4237.

176. Ghoufi, A., J. Deschamps, and G. Maurin, Theoretical hydrogen cryostorage in doped MIL-101 (Cr) metal–organic frameworks. *The Journal of Physical Chemistry C,* 2012. **116**(19): p. 10504-10509.

177. Girifalco, L.A. and V.G. Weizer, Application of the Morse potential function to cubic metals. *Physical Review,* 1959. **114**(3): p. 687.

178. Delaye, J., V. Louis-Achille, and D. Ghaleb, Modeling oxide glasses with Born–Mayer–Huggins potentials: effect of composition on structural changes. *Journal of Non-Crystalline Solids*, 1997. **210**(2-3): p. 232-242.

179. Frenkel, D. and B. Smit, Understanding molecular simulation: from algorithms to applications. Vol. 1. 2001: *Elsevier*.

180. Campaná, C., B. Mussard, and T.K. Woo, Electrostatic potential derived atomic charges for periodic systems using a modified error functional. *Journal of Chemical Theory and Computation,* 2009. **5**(10): p. 2866-2878.

181. Rudenko, A., S. Bendt, and F. Keil, Multiscale modeling of water in Mg-MOF-74: From electronic structure calculations to adsorption isotherms. *The Journal of Physical Chemistry C,* 2014. **118**(29): p. 16218-16227.

182. Kiener, C., U. Muller, and M. Schubert, Organometallic aluminum fumarate backbone material. 2009, *Google Patents*.

183. Gupta, A., L.A. Clark, and R.Q. Snurr, Grand canonical Monte Carlo simulations of nonrigid molecules: siting and segregation in silicalite zeolite. *Langmuir*, 2000. **16**(8): p. 3910-3919.

184. Paranthaman, S., F.-X. Coudert, and A.H. Fuchs, Water adsorption in hydrophobic MOF channels. *Physical Chemistry Chemical Physics,* 2010. **12**(28): p. 8124-8130.

185. Hautman, J. and M.L. Klein, An Ewald summation method for planar surfaces and interfaces. *Molecular Physics,* 1992. **75**(2): p. 379-395.

186. Desbiens, N., I. Demachy, A.H. Fuchs, H. Kirsch-Rodeschini, M. Soulard, and J. Patarin, Water condensation in hydrophobic nanopores. *Angewandte Chemie International Edition,* 2005. **44**(33): p. 5310-5313.

187. Ramachandran, C.E., S. Chempath, L.J. Broadbelt, and R.Q. Snurr, Water adsorption in hydrophobic nanopores: Monte Carlo simulations of water in silicalite. *Microporous and mesoporous materials,* 2006. **90**(1-3): p. 293-298.

188. Garibay, S.J. and S.M. Cohen, Isoreticular synthesis and modification of frameworks with the UiO-66 topology. *Chemical Communications,* 2010. **46**(41): p. 7700-7702.

189. Alvarez, E., N. Guillou, C. Martineau, B. Bueken, B. Van de Voorde, C. Le Guillouzer, P. Fabry, F. Nouar, F. Taulelle, and D. De Vos, The structure of the aluminum fumarate metal–organic framework A520. *Angewandte Chemie International Edition,* 2015. **54**(12): p. 3664-3668.

190. Wißmann, G., A. Schaate, S. Lilienthal, I. Bremer, A.M. Schneider, and P. Behrens, Modulated synthesis of Zr-fumarate MOF. *Microporous and Mesoporous Materials,* 2012. **152**: p. 64-70.

191. Chakraborty, A., B. Saha, S. Koyama, and K. Ng, On the thermodynamic modeling of the isosteric heat of adsorption and comparison with experiments. *Applied Physics Letters,* 2006. **89**(17): p. 171901.

192. Anderson, R., J. Rodgers, E. Argueta, A. Biong, and D.A. Gómez-Gualdrón, Role of pore chemistry and topology in the CO2 capture capabilities of MOFs: from molecular simulation to machine learning. *Chemistry of Materials,* 2018. **30**(18): p. 6325-6337.

193. Wen, H.-M., C. Liao, L. Li, A. Alsalme, Z. Alothman, R. Krishna, H. Wu, W. Zhou, J. Hu, and B. Chen, A metal–organic framework with suitable pore size and dual functionalities for highly efficient post-combustion CO 2 capture. *Journal of Materials Chemistry A,* 2019. **7**(7): p. 3128-3134.

194. Zhang, L., A three-dimensional non-equilibrium model for an intermittent adsorption cooling system. *Solar Energy,* 2000. **69**(1): p. 27-35.

195. Prigogine, I., Introduction to thermodynamics of irreversible processes. *itti,* 1967.

196. Sun, B. and A. Chakraborty, Thermodynamic formalism of water uptakes on solid porous adsorbents for adsorption cooling applications. *Applied Physics Letters,* 2014. **104**(20): p. 201901.

197. Saha, B., S. Koyama, T. Kashiwagi, A. Akisawa, K. Ng, and H. Chua, Waste heat driven dual-mode, multi-stage, multi-bed regenerative adsorption system. *International Journal of Refrigeration,* 2003. **26**(7): p. 749-757.

198. Ng, K.C., X. Wang, Y.S. Lim, B.B. Saha, A. Chakarborty, S. Koyama, A. Akisawa, and T. Kashiwagi, Experimental study on performance improvement of a four-bed adsorption chiller by using heat and mass recovery. *International Journal of Heat and Mass Transfer,* 2006. **49**(19-20): p. 3343-3348.

199. Miyazaki, T., A. Akisawa, B.B. Saha, I. El-Sharkawy, and A. Chakraborty, A new cycle time allocation for enhancing the performance of two-bed adsorption chillers. *International Journal of Refrigeration,* 2009. **32**(5): p. 846-853.

200. Dhainaut, J., C. Avci-Camur, J. Troyano, A. Legrand, J. Canivet, I. Imaz, D. Maspoch, H. Reinsch, and D. Farrusseng, Systematic study of the impact of MOF densification into tablets on textural and mechanical properties. *CrystEngComm*, 2017. **19**(29): p. 4211-4218.

201. Khabzina, Y., J. Dhainaut, M. Ahlhelm, H.-J. Richter, H. Reinsch, N. Stock, and D. Farrusseng, Synthesis and shaping scale-up study of functionalized UiO-66 MOF for ammonia air purification filters. *Industrial & Engineering Chemistry Research,* 2018. **57**(24): p. 8200-8208.

202. Du, S., X. Li, Z. Yuan, C. Du, W. Wang, and Z. Liu, Performance of solar adsorption refrigeration in system of SAPO-34 and ZSM-5 zeolite. *Solar Energy,* 2016. **138**: p. 98-104.

203. Chen, C., R. Wang, Z. Xia, J. Kiplagat, and Z. Lu, Study on a compact silica gel–water adsorption chiller without vacuum valves: design and experimental study. *Applied Energy,* 2010. **87**(8): p. 2673-2681.

204. Tso, C., C.Y. Chao, and S. Fu, Performance analysis of a waste heat driven activated carbon based composite adsorbent–water adsorption chiller using simulation model. *International Journal of Heat and Mass Transfer*, 2012. **55**(25-26): p. 7596-7610.

205. Rubio-Martinez, M., T.D. Hadley, M.P. Batten, K. Constanti-Carey, T. Barton, D. Marley, A. Mönch, K.S. Lim, and M.R. Hill, Scalability of Continuous Flow Production of Metal–Organic Frameworks. *ChemSusChem,* 2016. **9**(9): p. 938-941.

206. Khan, N.A. and S.H. Jhung, Synthesis of metal-organic frameworks (MOFs) with microwave or ultrasound: Rapid reaction, phase-selectivity, and size reduction. *Coordination Chemistry Reviews,* 2015. **285**: p. 11-23.

207. Thommes, M., Textural characterization of zeolites and ordered mesoporous materials by physical adsorption, in *Studies in Surface Science and Catalysis*. 2007, Elsevier. p. 495-XIII.

208. Wang, L., Z. Tamainot-Telto, R. Thorpe, R.E. Critoph, S.J. Metcalf, and R. Wang, Study of thermal conductivity, permeability, and adsorption performance of consolidated composite activated carbon adsorbent for refrigeration. *Renewable Energy*, 2011. **36**(8): p. 2062-2066.

209. Couck, S., J. Cousin-Saint-Remi, S. Van der Perre, G.V. Baron, C. Minas, P. Ruch, and J.F. Denayer, 3D-printed SAPO-34 monoliths for gas separation. *Microporous and Mesoporous Materials,* 2018. **255**: p. 185-191.

210. Tubío, C.R., J. Azuaje, L. Escalante, A. Coelho, F. Guitián, E. Sotelo, and A. Gil, 3D printing of a heterogeneous copper-based catalyst. *Journal of Catalysis,* 2016. **334**: p. 110-115.

211. Thakkar, H., S. Eastman, Q. Al-Naddaf, A.A. Rownaghi, and F. Rezaei, 3D-printed metal–organic framework monoliths for gas adsorption processes. *ACS Applied Materials & Interfaces*, 2017. **9**(41): p. 35908-35916.

212. Hirschfelder, J.O., Advances in Chemical Physics, Volume 12: Intermolecular Forces. Vol. 24. 2009: *John Wiley & Sons.*

Appendices

A1. Porous Characteristics

UiO-66 (Zr) based MOFs

The N_2 adsorption isotherms for all UiO-66 based MOFs are shown in Figure A1. The results show type I isotherms. The N_2-MOF interaction is very strong in the Henry's law region.

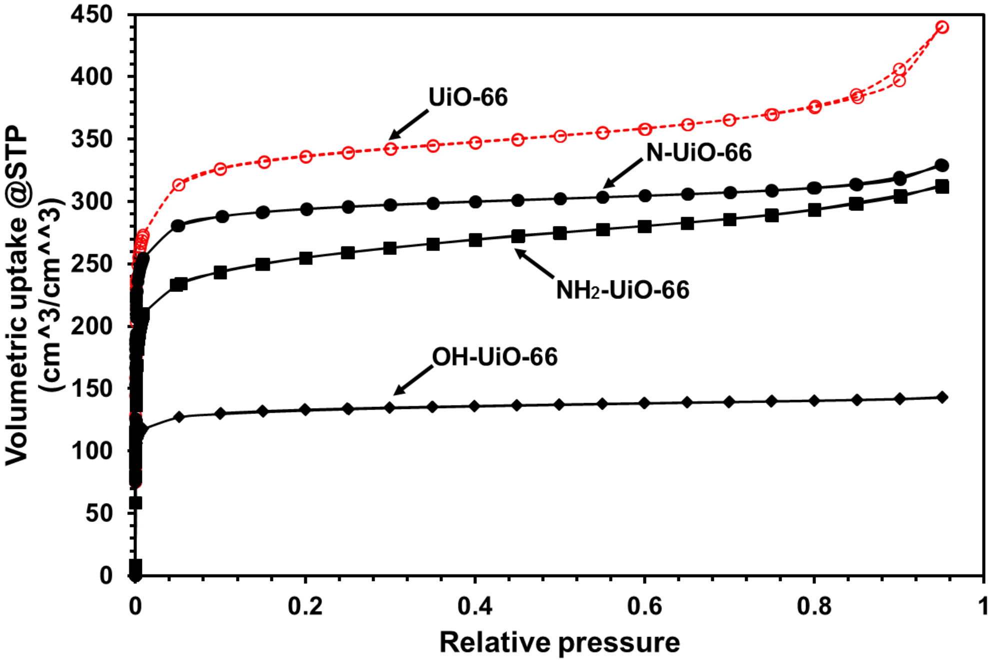

Figure A1: N_2 adsorption isotherms for original and functionalised UiO-66 MOFs adsorbents.

The pore size distribution (PSD) curves calculated by density functional theory (DFT) and the results are shown in Figure A2. It is found that the parent and the functionalised UiO-66 (Zr) MOFs are highly microporous. However, the number of micro-pores is decreased for–NH_2 functional groups assisted UiO-66 (Zr) MOFs.

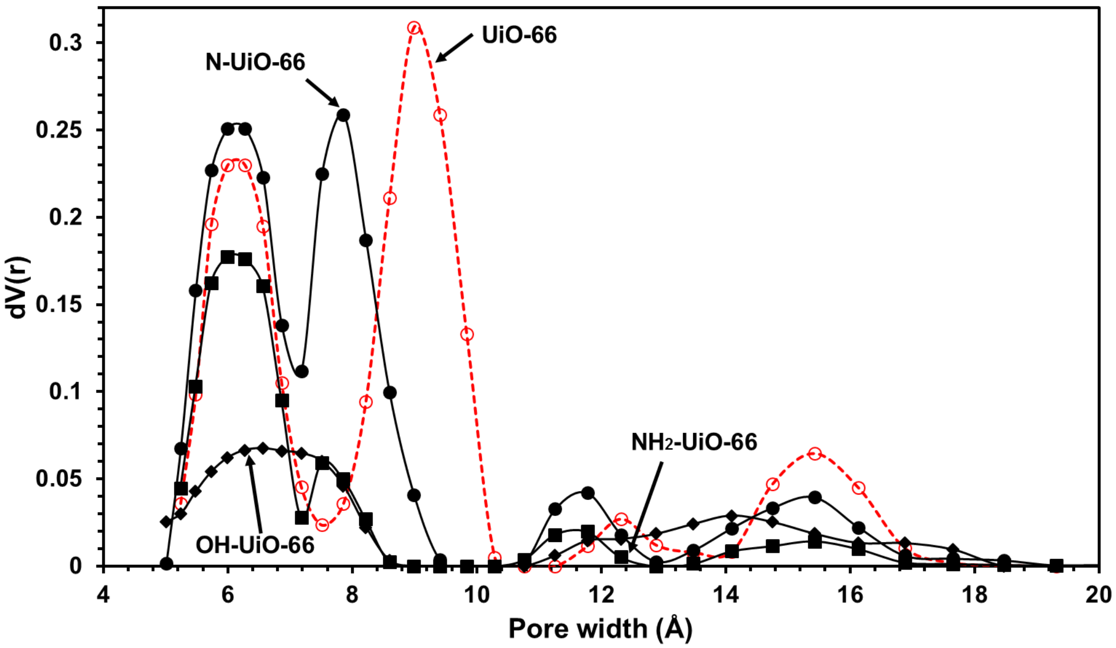

Figure A2: Pore size distribution of functionalised UiO-66 MOFs adsorbents employing DFT analysis.

MOF-801 (Zr) based MOFs

Figure A3 shows the N_2 adsorption isotherm results. All the functionalised adsorbents show the similar N_2 adsorption performance without major differences. It is found that the original MOF-801 has the higher N_2 uptake as compared with functionalised MOF-801 (Zr) adsorbent, which indicates that the additional methyl functional groups may obstruct the N_2 molecules from being adsorbed into the pores of the MOFs framework.

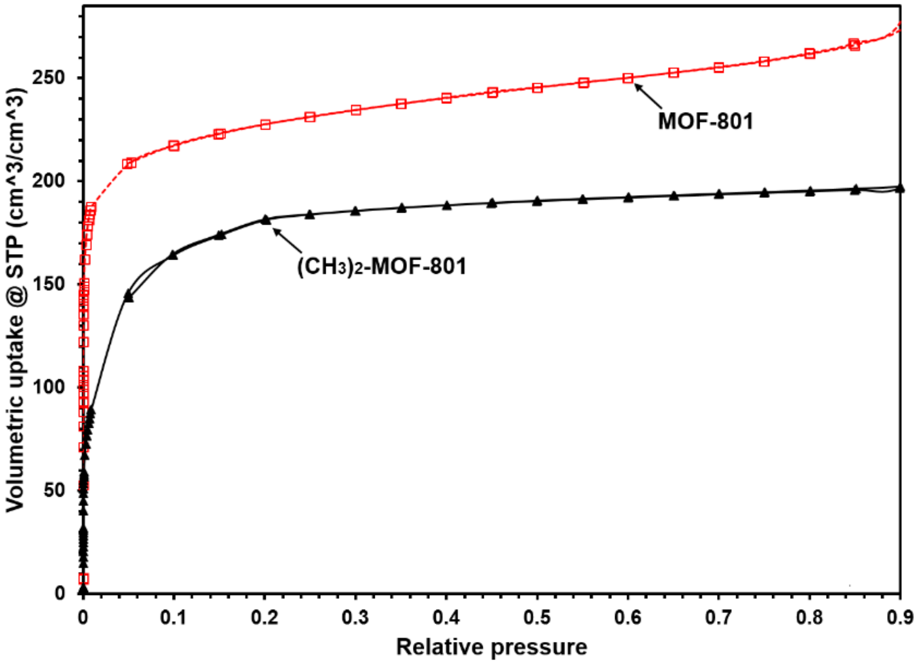

Figure A3: N_2 adsorption isotherms for original and functionalised fumarate-based MOFs adsorbents. Here, (□) is MOF-801 (Zr) and (▲) indicates $(CH_3)_2$-MOF-801 (Zr).

Figure A4 shows the pore size distribution (PSD) curves of functionalised adsorbents, and the parent MOF is presented for comparison purpose. It is observed that the pore width mainly varies from 5.0 Å to 15 Å, which indicates that fumarate-based MOFs consists majority of micropores through their surface. With the addition of dual-methyl functional groups, $(CH_3)_2$-MOF-801 (Zr) results an increment of pore distributions with the pore size ranging from 12.0 Å to 20 Å.

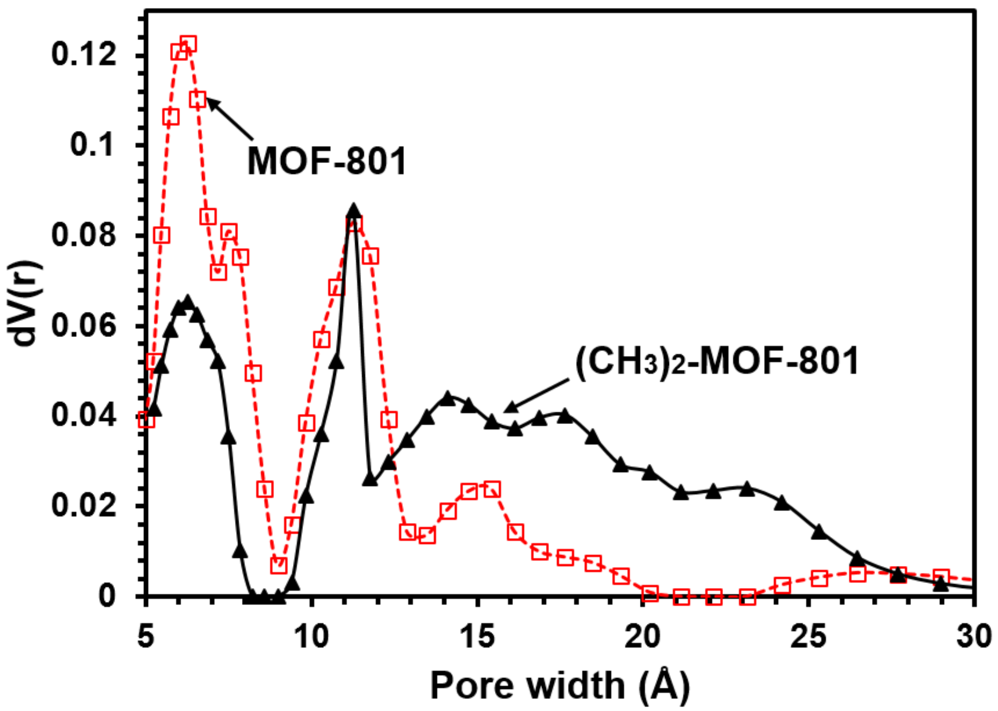

Figure A4: Pore size distribution of functionalised fumarate-based MOFs adsorbents employing DFT analysis. Here, (□) is MOF-801 (Zr) and (▲) indicates $(CH_3)_2$-MOF-801 (Zr).

Al-Fum based MOFs

Figure A5 shows N_2 adsorption isotherms of 5% doped Li^+, Na^+, K^+ Al-Fum, 10%, 30%, 50% mixed AFI/CHA-Al-Fum and parent Al-Fum. It is found that original Al-Fum has the highest N_2 uptake as compared to post-synthesised adsorbent samples. This is due to the fact that some of the doped alkali metal cations may obstruct the N_2 molecules from being adsorbed into the pores of the adsorbents, and the poor affinity between the AFI/CHA zeolite and nitrogen also results a lower N_2 uptake. Furthermore, all the post-synthesised Al-Fum adsorbents (10%, 30%, 50% mixed AFI/CHA-Al-Fum and 5% doped Li^+, Na^+, K^+ Al-Fum) shares the similar N_2 adsorption performance without any major difference.

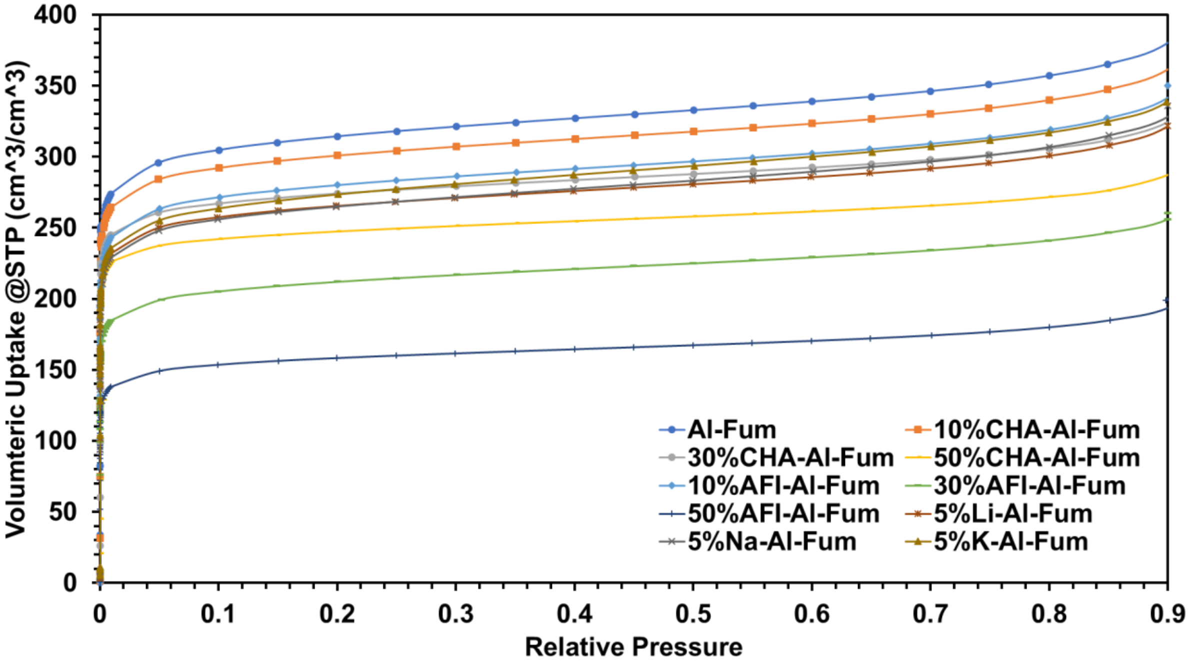

Figure A5: N_2 adsorption isotherm for the original and post-synthesis Al-Fum adsorbents.

Figure A6 (a-c) shows pore size distribution (PSD) curves of both the parent and the post-synthesised adsorbents. It is found that the pore widths of alkali metal cations doped and zeolite-based adsorbent mixed Al-Fum adsorbents vary from 6 Å to 15 Å with similar amount of increment in pore volume, which implies the majority of micropores throughout the material surface. The existence of alkali dopants or zeolite results the decrement of adsorbent's mesopores distribution, which indicates that the post-synthesis process would be a reliable method to achieve the "S-shaped" isotherm.

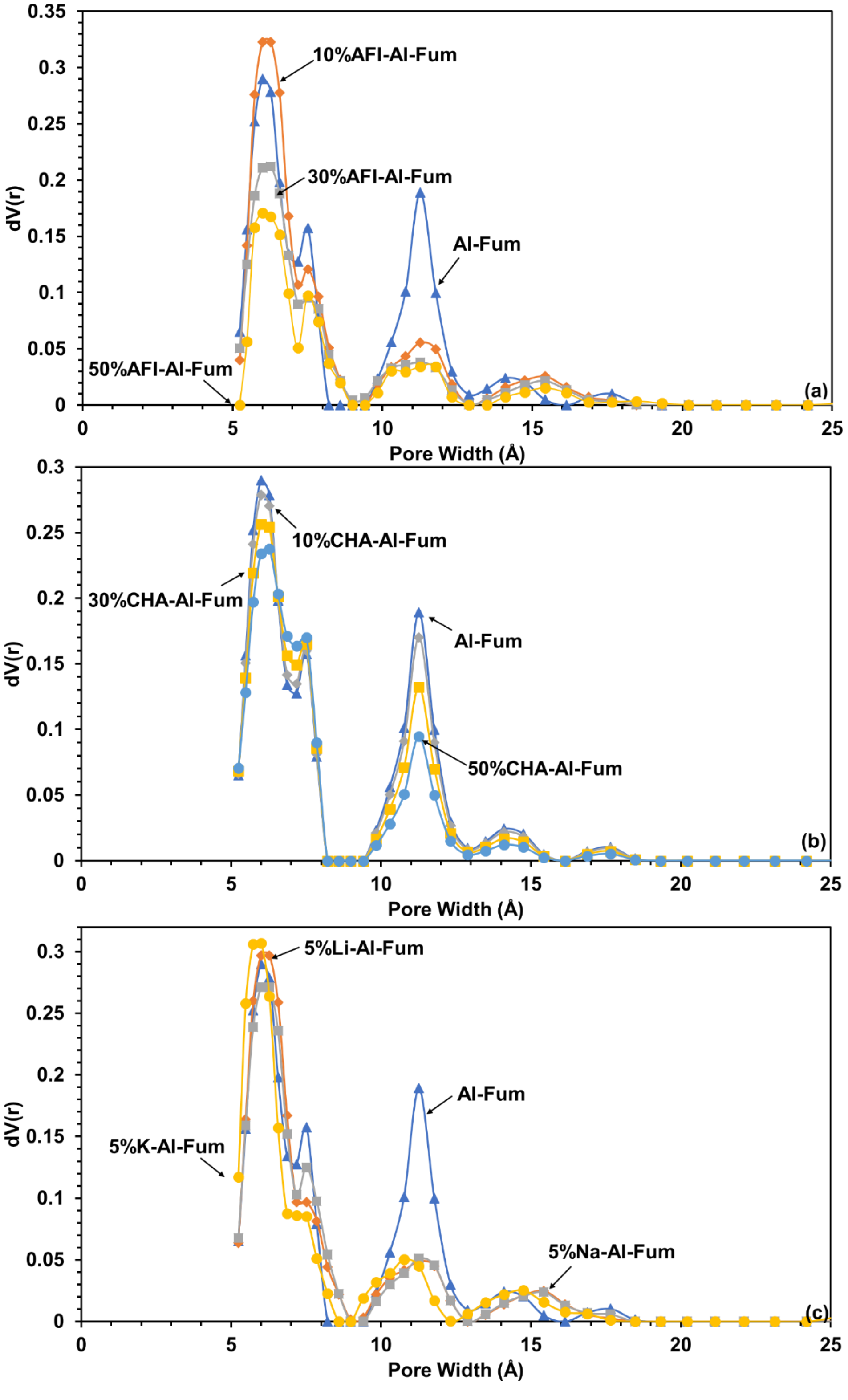

Figure A6: Pore size distribution of the original and post-synthesis Al-Fum adsorbents employing DFT analysis.

A2. Entropy Generation ($\dot{S}_{gen}$) Sutdy

Al-Fum based MOFs

For Al-Fum + water AHT system, the cyclic-steady-state entropy generation ($\dot{S}_{gen}$) profiles of each component (evaporator, condenser, adsorption-bed and desorption-bed) are shown in Figure A7, where the switching time, half-cycle time, chilled water inlet, cooling water inlet and regeneration temperature is 25 s, 500 s, 14.8 °C, 30 °C and 80 °C, respectively. Furthermore, the detailed entropy analysis for modified Al-Fum based AHT systems are furnished in Table A.1-A.3, from where one can easily analyse the entropy generation performances of AHT operation cycle.

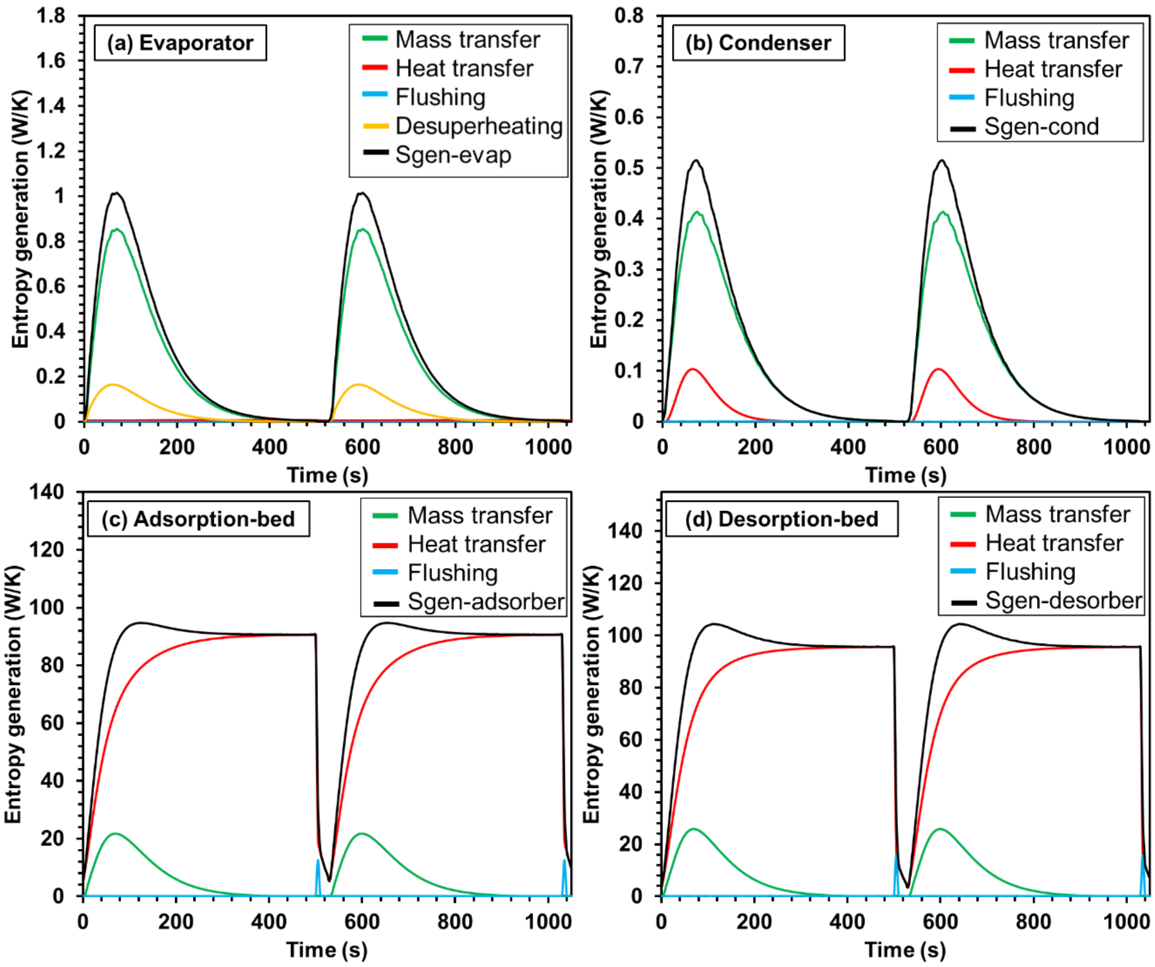

Figure A7: The entropy generation ($\dot{S}_{gen}$) for each major component of Al-Fum + water AHT system: (a) evaporator; (b) condenser; (c) adsorption-bed and (d) desorption-bed.

Table A.1: Entropy generation ($\dot{S}_{gen}$) study on the major components of the 5% Li-Al-Fum MOFs based AHT systems with the highlighting of the contributions by processes.

	$\dot{S}_{gen-MT}$ (W/K)	$\dot{S}_{gen-HT}$ (W/K)	$\dot{S}_{gen-flushing}$ (W/K)	$\dot{S}_{gen-desuperheating}$ (W/K)	$\dot{S}_{gen-overall}$ (W/K)
Evaporator	2.03	0.005	0.004	0.61	2.65
Condenser	0.83	0.74	0.035	-	1.605
Adsorber	5.95	89.64	12.20	-	107.79
Desorber	6.03	93.36	15.60	-	114.99

Table A.2: Entropy generation ($\dot{S}_{gen}$) study on the major components of the 30% AFI-Al-Fum MOFs based AHT systems with the highlighting of the contributions by processes.

	$\dot{S}_{gen-MT}$ (W/K)	$\dot{S}_{gen-HT}$ (W/K)	$\dot{S}_{gen-flushing}$ (W/K)	$\dot{S}_{gen-desuperheating}$ (W/K)	$\dot{S}_{gen-overall}$ (W/K)
Evaporator	1.84	0.006	0.004	0.64	2.49
Condenser	0.65	1.30	0.01	-	1.96
Adsorber	4.79	89.53	12.17	-	106.49
Desorber	4.75	93.09	15.56	-	113.40

Table A.3: Entropy generation ($\dot{S}_{gen}$) study on the major components of the 30% CHA-Al-Fum MOFs based AHT systems with the highlighting of the contributions by processes.

	$\dot{S}_{gen-MT}$ (W/K)	$\dot{S}_{gen-HT}$ (W/K)	$\dot{S}_{gen-flushing}$ (W/K)	$\dot{S}_{gen-desuperheating}$ (W/K)	$\dot{S}_{gen-overall}$ (W/K)
Evaporator	1.82	0.005	0.005	0.51	2.34
Condenser	0.76	0.74	0.03	-	1.53
Adsorber	5.57	89.56	12.19	-	107.32
Desorber	5.63	93.21	15.60	-	114.44

UiO-66 (Zr) based MOFs

Figure A8 shows the $\dot{S}_{gen}$ analysis of each component of the UiO-66 (Zr) based AHT systems where the operation conditions are : switching time/half-cycle time/chilled water inlet/cooling water inlet/regeneration temperature = 25 s/500 s/14.8 °C/30 °C/80 °C, respectively. It is found that the $\dot{S}_{gen}$ trends of the UiO-66 (Zr) based AHT system is similar as compared with those of the Al-Fum + water AHT system. However, it is found that for the adsorber/desorber, the $\dot{S}_{gen}$ by the heat transfer contributes the most percentage (> 95%) of the overall $\dot{S}_{gen}$. It is because of that due to the extremely long hydrophobic length of the UiO-66 (Zr), rarely no water transfer is recorded in the AHT loop ($\Delta q \approx 0$). Hence, the effect of the $\dot{S}_{gen}$ caused by the mass transfer is negligible. The $\dot{S}_{gen}$ analysis of the functionalised UiO-66 (Zr) is furnished in Table A4 – A6. It is observed that by implanting the hydrophilic functional groups into the structure of the parent UiO-66 (Zr), the hydrophilicity of the adsorbents at the low pressure region is enhanced, more water transfer per adsorption/desorption cycle (Δq) is obtained, and the effect of the $\dot{S}_{gen}$ caused by the mass transfer becomes more significant. Furthermore, the overall $\dot{S}_{gen}$ is ranked as: NH_2-UiO-66 (Zr) > OH-UiO-66 (Zr) > N-UiO-66 (Zr) > UiO-66 (Zr).

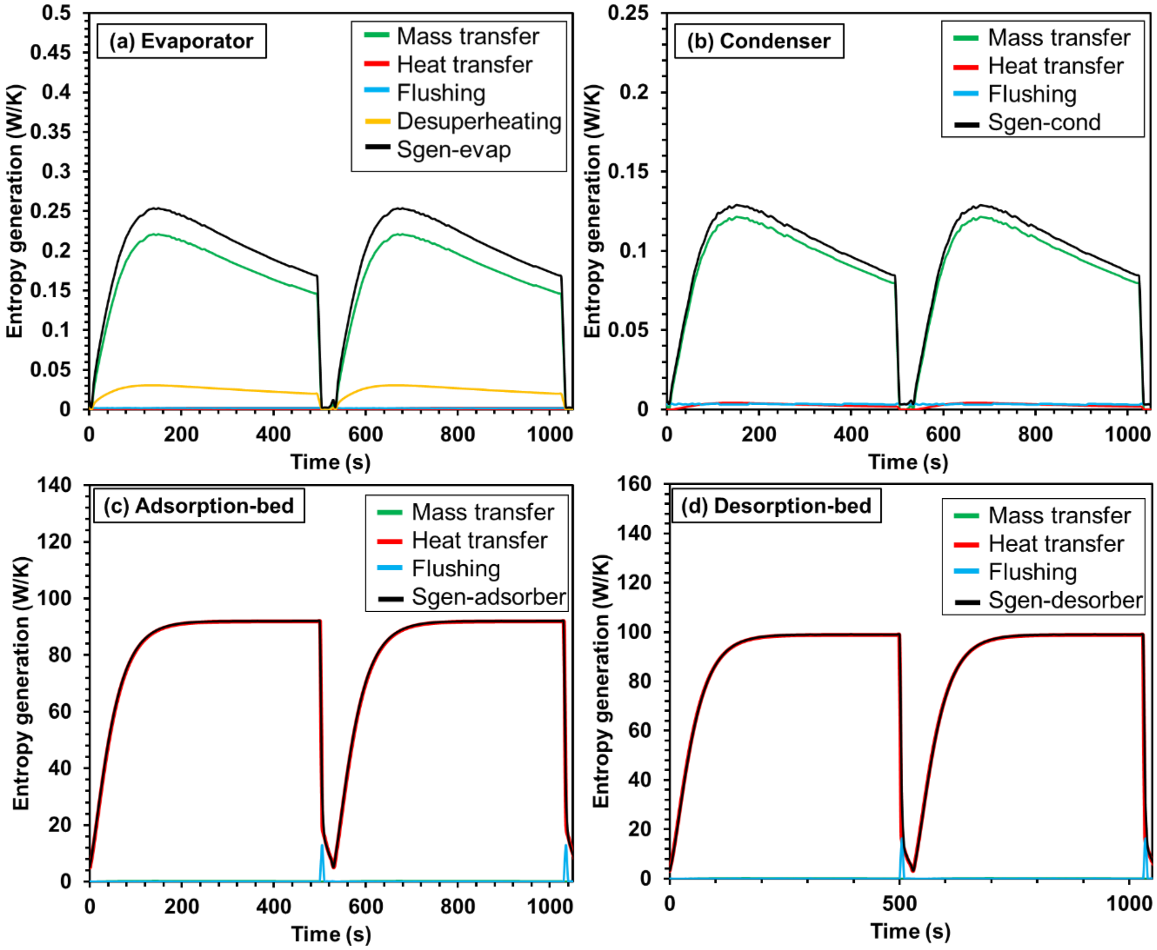

Figure A8: The entropy generation ($\dot{S}_{gen}$) for each major component of UiO-66 (Zr) + water AHT system: (a) evaporator; (b) condenser; (c) adsorption-bed and (d) desorption-bed.

Table A.4: Entropy generation ($\dot{S}_{gen}$) study on the major components of the OH-UiO-66 (Zr) MOFs based AHT systems with the highlighting of the contributions by processes.

	$\dot{S}_{gen-MT}$ (W/K)	$\dot{S}_{gen-HT}$ (W/K)	$\dot{S}_{gen-flushing}$ (W/K)	$\dot{S}_{gen-desuperheating}$ (W/K)	$\dot{S}_{gen-overall}$ (W/K)
Evaporator	0.17	0.012	0.002	0.043	0.227
Condenser	0.078	0.33	0.001	-	0.409
Adsorber	2.16	86.67	11.71	-	100.54
Desorber	7.99	89.59	14.97	-	112.55

Table A.5: Entropy generation ($\dot{S}_{gen}$) study on the major components of the N-UiO-66 (Zr) MOFs based AHT systems with the highlighting of the contributions by processes.

	$\dot{S}_{gen-MT}$ (W/K)	$\dot{S}_{gen-HT}$ (W/K)	$\dot{S}_{gen-flushing}$ (W/K)	$\dot{S}_{gen-desuperheating}$ (W/K)	$\dot{S}_{gen-overall}$ (W/K)
Evaporator	0.081	0.006	0.003	0.022	0.112
Condenser	0.038	0.157	0.001	-	0.196
Adsorber	2.56	86.66	12.08	-	101.3
Desorber	1.72	92.19	15.35	-	109.26

MOF-801 (Zr) based MOFs

The $\dot{S}_{gen}$ analysis of the major component of the MOF-801 (Zr) based AHT systems is shown in Figure A9, from where one can analyse the $\dot{S}_{gen}$ contribution of each process. Hence, the switching time, half-cycle time, chilled water inlet, cooling water inlet and regeneration temperature is 25 s, 500 s, 14.8 °C, 30 °C and 80 °C, respectively. It is observed that the $\dot{S}_{gen}$ raised in the evaporator and condenser is mainly caused by the mass transfer and the $\dot{S}_{gen}$ generated in the sorption-bed is mainly due to the heat transfer. It is because of that the parent MOF-801 (Zr) is a super hydrophilic adsorbent and rarely no water vapour is released during the desorption process ($\Delta q \approx 0$). By introducing the hydrophobic methyl functional groups, the hydrophilicity of the parent MOF-801 (Zr) is weaken and more water is desorbed at the current regeneration temperature (80 °C). Therefore, more water vapour is transferred through the sorption-bed and the effect of the mass transfer become evident.

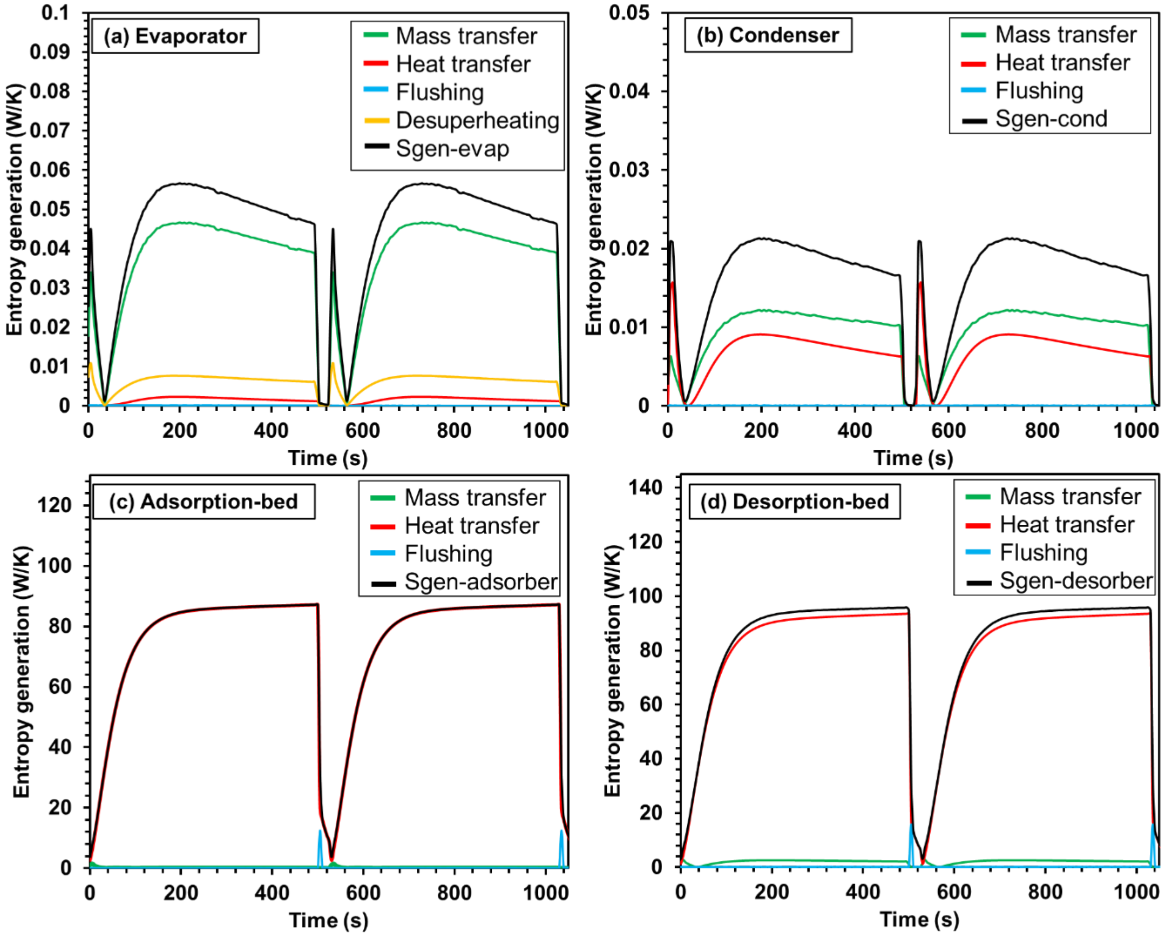

Figure A9: The entropy generation ($\dot{S}_{gen}$) for each major component of MOF-801 (Zr) + water AHT system: (a) evaporator; (b) condenser; (c) adsorption-bed and (d) desorption-bed.

A3. Comparison Study on GCMC Simulation and Experiment

Al-Fum based MOFs

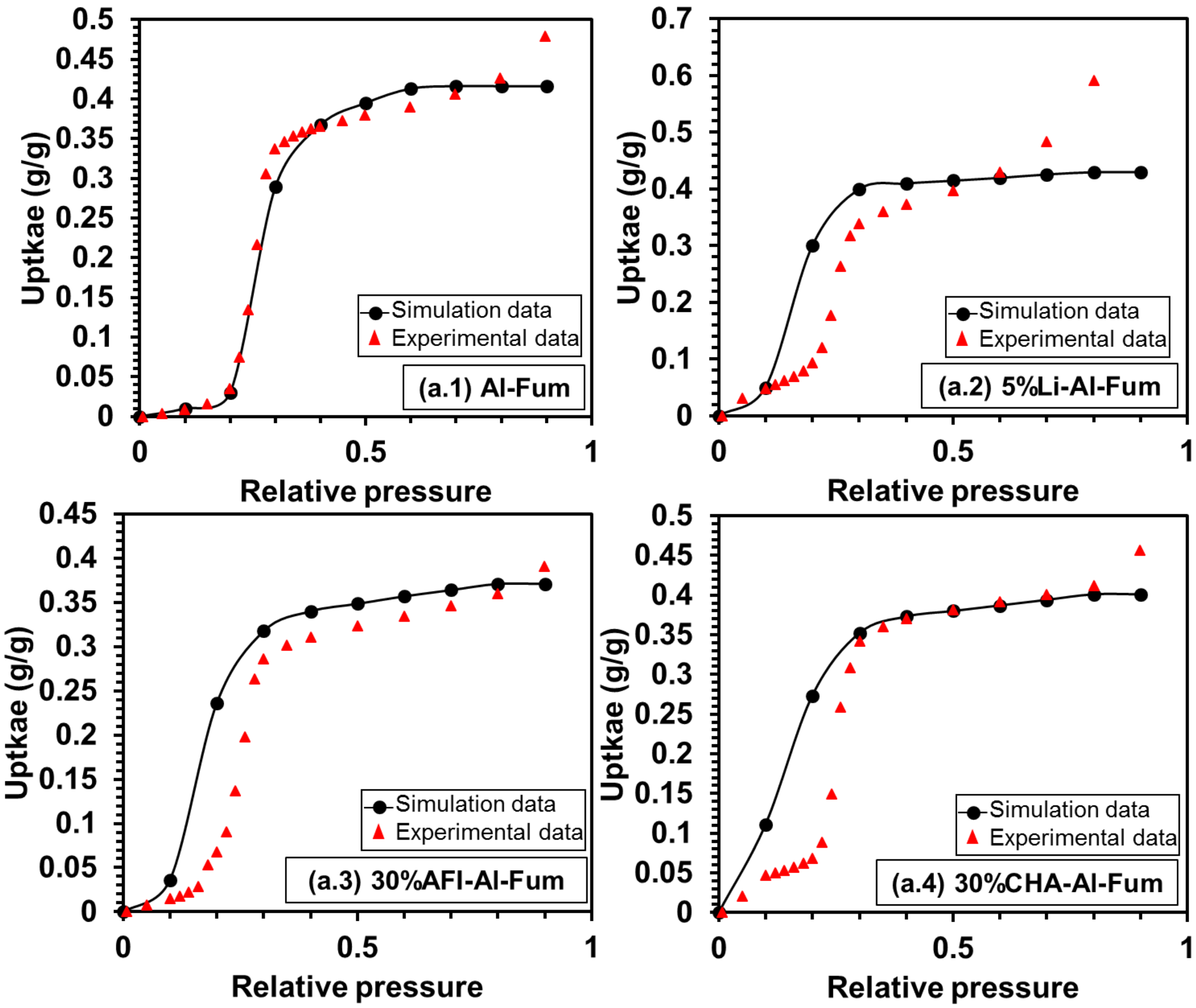

Figure A10: The GCMC simulated water adsorption isotherms on various original modified Al-Fum based adsorbents. Here, experimental data is shown for comparison purpose. (black-solid line: GCMC simulation results; red-dotted marker: experimental data)

Figure A10 shows the comparison study between the GCMC results and experimental data for Al-Fum based MOFs + water adsorption system. Good agreements are found between the GCMC predicted water adsorption isotherm and experimentally obtained data for all the original and modified MOF systems within a reasonable error range (5% – 10 %). In addition, the differences between the GCMC simulation and experimental data may be caused by the limitation of the simulation. For example, the simulation framework of Al-Fum is assumed as perfect crystal without any defects, which could not be achieved in the experiment conditions.

Furthermore, the quality of the MOFs is not the only reason caused the differences between the experimental and GCMC results. Many other factors as well as the simulation limitations could also affect the results in predicting the hydrophobic length of water adsorption. For example, as mentioned in the manuscript, research works have pointed out that smaller hydrophobic length will be obtained if SPC/E water molecule model is used instead of the TIP4P water molecule model, even under the same GCMC algorithm. Hence, in our research, all the simulations are carried under the same conditions using the same water molecule model. The only variable is the framework of the materials (adsorbents).

UiO-66 (Zr) based MOFs

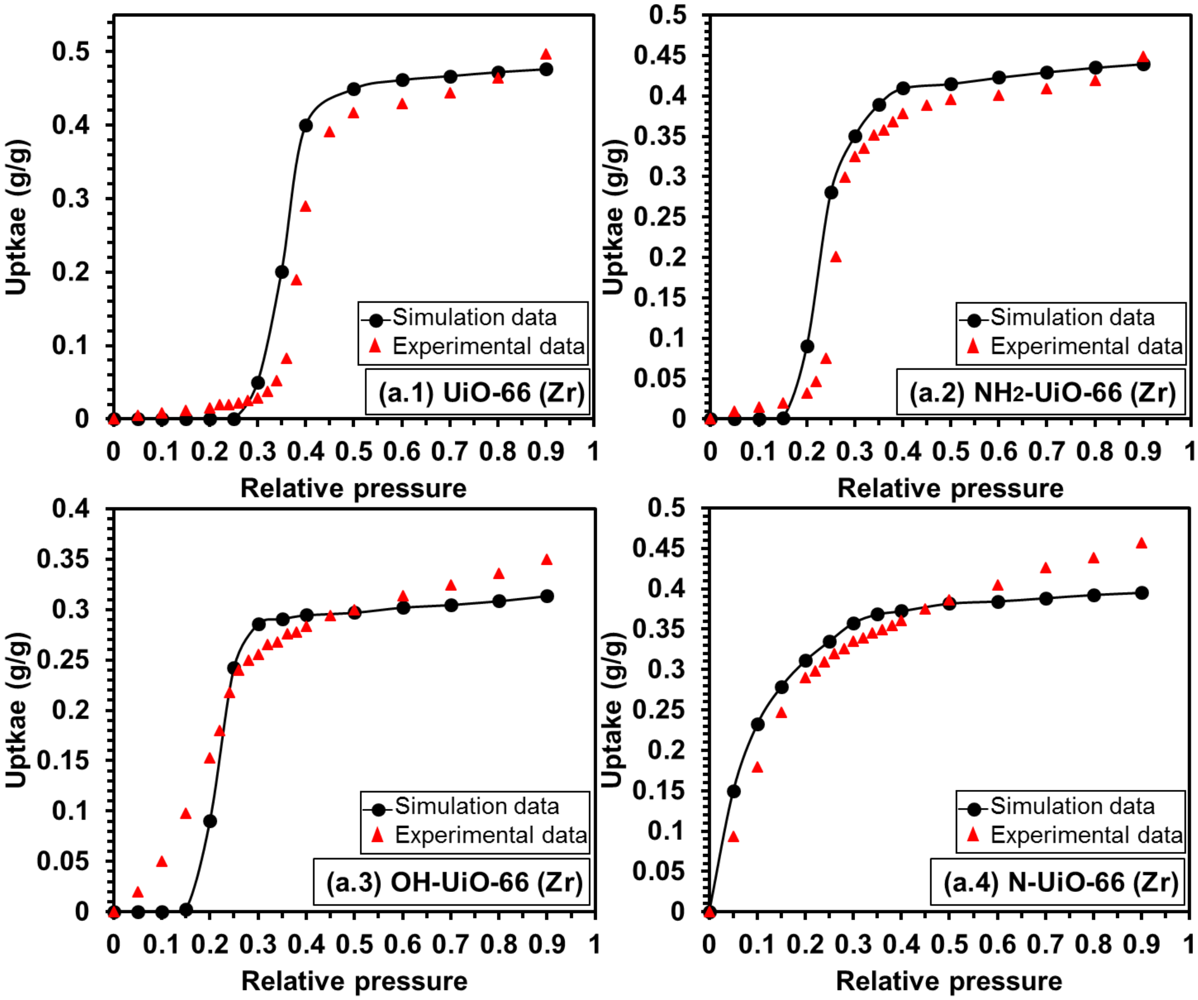

Figure A11: The GCMC simulated water adsorption isotherms on various original and functionalised UiO-66 (Zr) adsorbents. Here, experimental data is shown for comparison purpose. (black-solid line: GCMC simulation results; red-dotted marker: experimental data)

MOF-801 (Zr) based MOFs

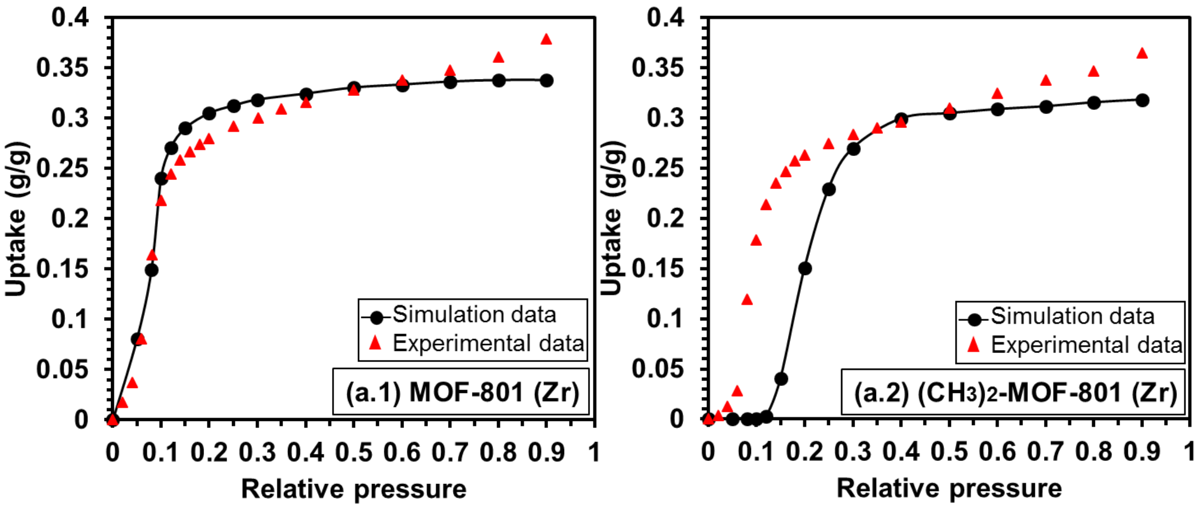

Figure A12: The GCMC simulated water adsorption isotherms on various original and functionalised MOF-801 (Zr) adsorbents. Here, experimental data is shown for comparison purpose. (black-solid line: GCMC simulation results; red-dotted marker: experimental data)

A4. Comparison Study on Adsorption Isotherm and Kinetics Fitting

Al-Fum based MOFs

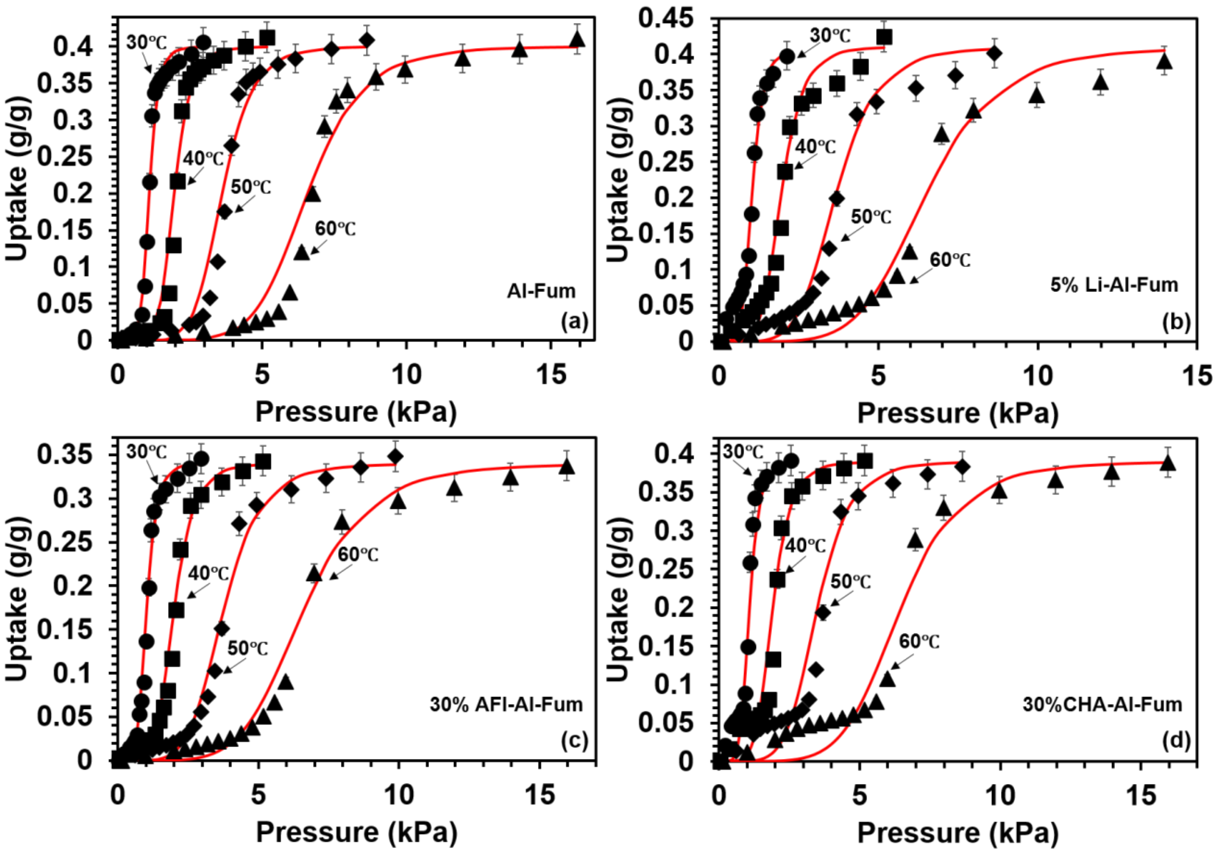

Figure A13: Adsorption isotherms of water vapour on (a) Al-Fum, (b) 5% Li-doped Al-Fum, (c) 30% AFI-mixed Al-Fum and (d) 30% CHA-mixed Al-Fum MOFs for the pressures up to saturated condition with temperatures ranging from 30 ℃ to 60 ℃. Hence, the black markers represent the experimental data and the red lines stand for the fitting curves.

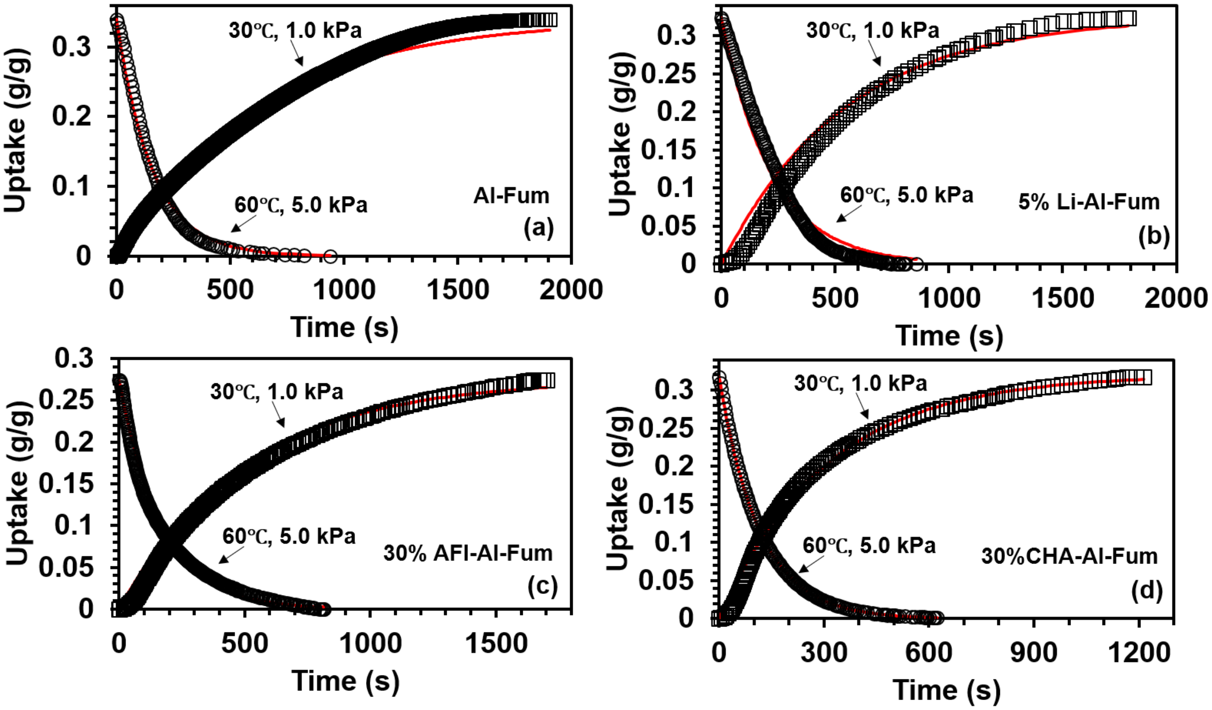

Figure A14: The amount of water uptake/offtake under dynamic conditions for (a) Al-Fum, (b) 5% Li-doped Al-Fum, (c) 30% AFI-mixed Al-Fum and (d) 30% CHA-mixed Al-Fum MOFs (adsorption: 30 ℃ and 1.0 kPa; desorption: 60 ℃ and 5.0 kPa). Hence, the black markers denote the experimental data and the red lines represent the fitting results.

A5. Pressure-Temperature-Uptake diagram analysis

Al-Fum based MOFs

The variation of the Al-Fum based adsorbents' temperature and water vapours' pressure under the AAHT cyclic steady operations is shown on the Dühring diagram (Figure A15). Here, the regeneration temperature, cold water inlet temperature and chilled water inlet temperature, switching time and half cycle time is kept at 80 ℃, 30 ℃, 14.8 ℃, 25 s and 500 s, respectively. Dühring diagrams under other regeneration temperature (60, 70 and 90 ℃) conditions are also displayed in the Figure A16-A18 for comprehensive understanding. Four AAHT operation stages are shown as: adsorption stage, pre-heating stage, desorption stage and pre-cooling stage, from where one could observe the momentary water vapour uptake/offtake under various pressure and temperature conditions. It is found that the maximum water vapour uptake-offtake difference (Δq) of all the Al-Fum based MOFs could be ranged as: 5% Li-Al-Fum > 30% CHA-Al-Fum > 30% AFI Al-Fum > parent Al-Fum. First, hot-to-cold swing occurs and the pressure drops down to and maintain as evaporator pressure during the adsorption process. The entire bed follows the isosteric path during the switching period. It is noted here that a rise of pressure may be found during the adsorption process as there is more water vapour in the adsorber with the addition of isosteric heats. Additionally, both the pressure and temperature increase at the end of the following cold-to-hot thermal swing section. Hence, desorption process occurs within the bed. Finally, both the bed temperature and pressure decrease as cooling water is flowed to the heat exchange and the AAHT operation cycle continues.

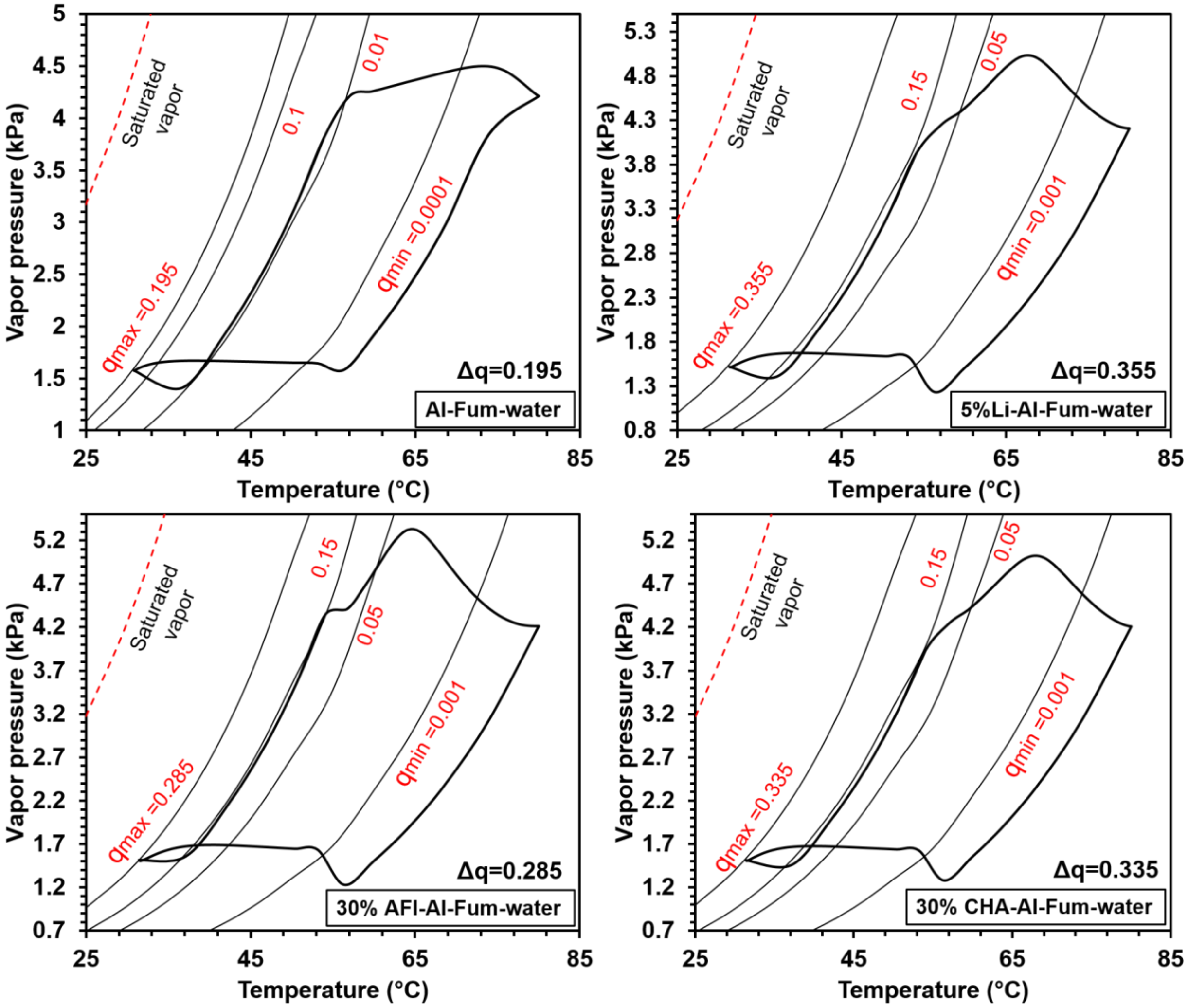

Figure A15: The Dühring (pressure-temperature, P-T) diagram of water - AAHT system under cyclic-steady-state adopting parent and modified Al-Fum based MOFs as adsorbents.

Figure A16 shows the Dühring diagram of Al-Fum MOFs based AAHT systems with the regeneration temperature of 60 ℃. Here, four AAHT operation phases are labelled as: adsorption stage (G-B), pre-heating stage (B-D), desorption stage (D-F) and pre-cooling stage (F-G),

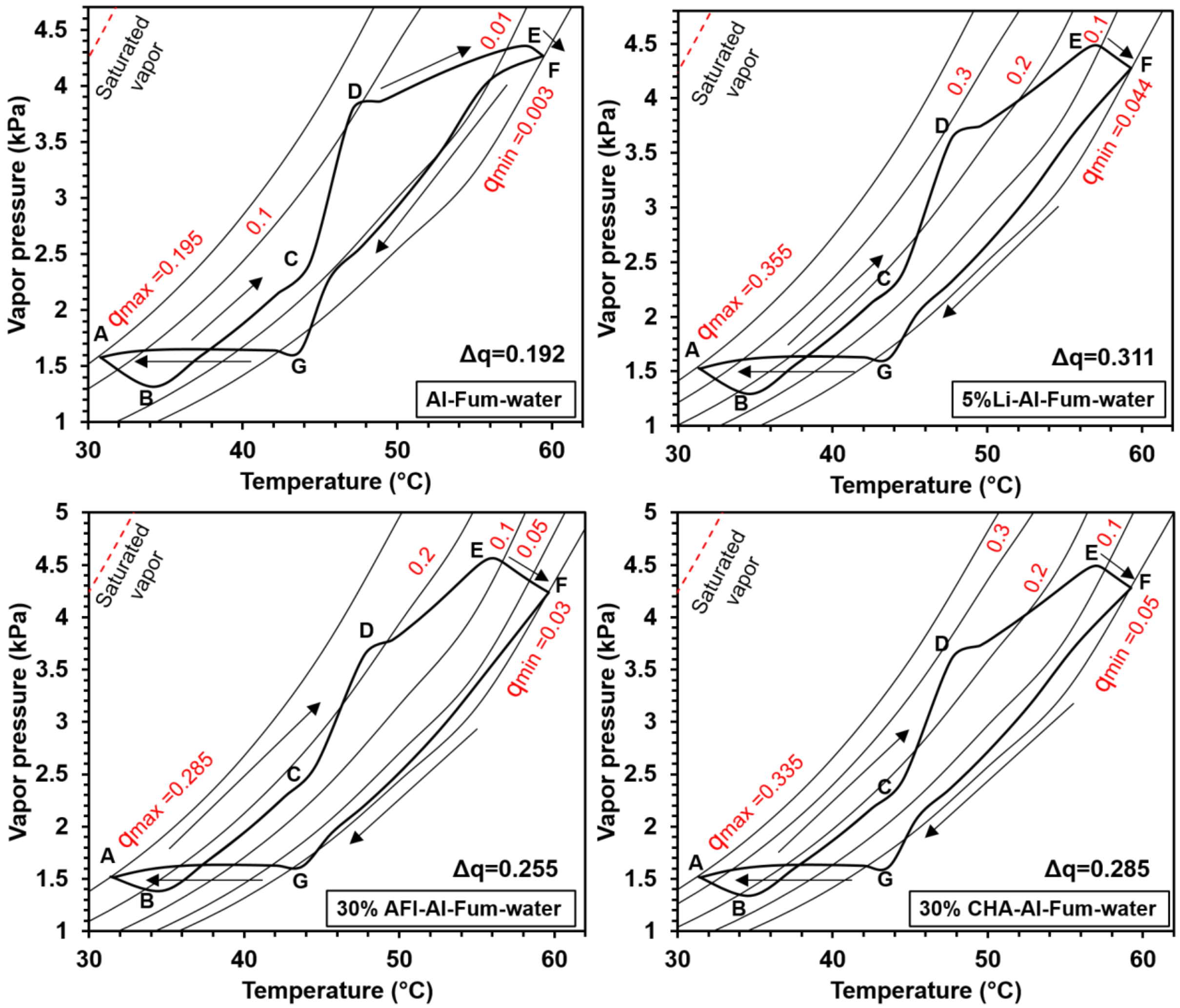

Figure A16: The *Dühring* (pressure-temperature, P-T) diagram of Al-Fum MOFs and zeolite composites based AAHT system at the inlet conditions of 60 ℃/30 ℃/14.8 ℃/25 s/500 s (regeneration temperature/cold water inlet temperature/chilled water inlet temperature/switching time/half cycle time).

Figure A17 shows the Dühring diagram of Al-Fum MOFs based AAHT systems with the regeneration temperature of 70 ℃, where significant improvements of water vapour uptake-offtake difference (Δq) are found for all the adsorbents (especially for modified Al-Fum MOFs).

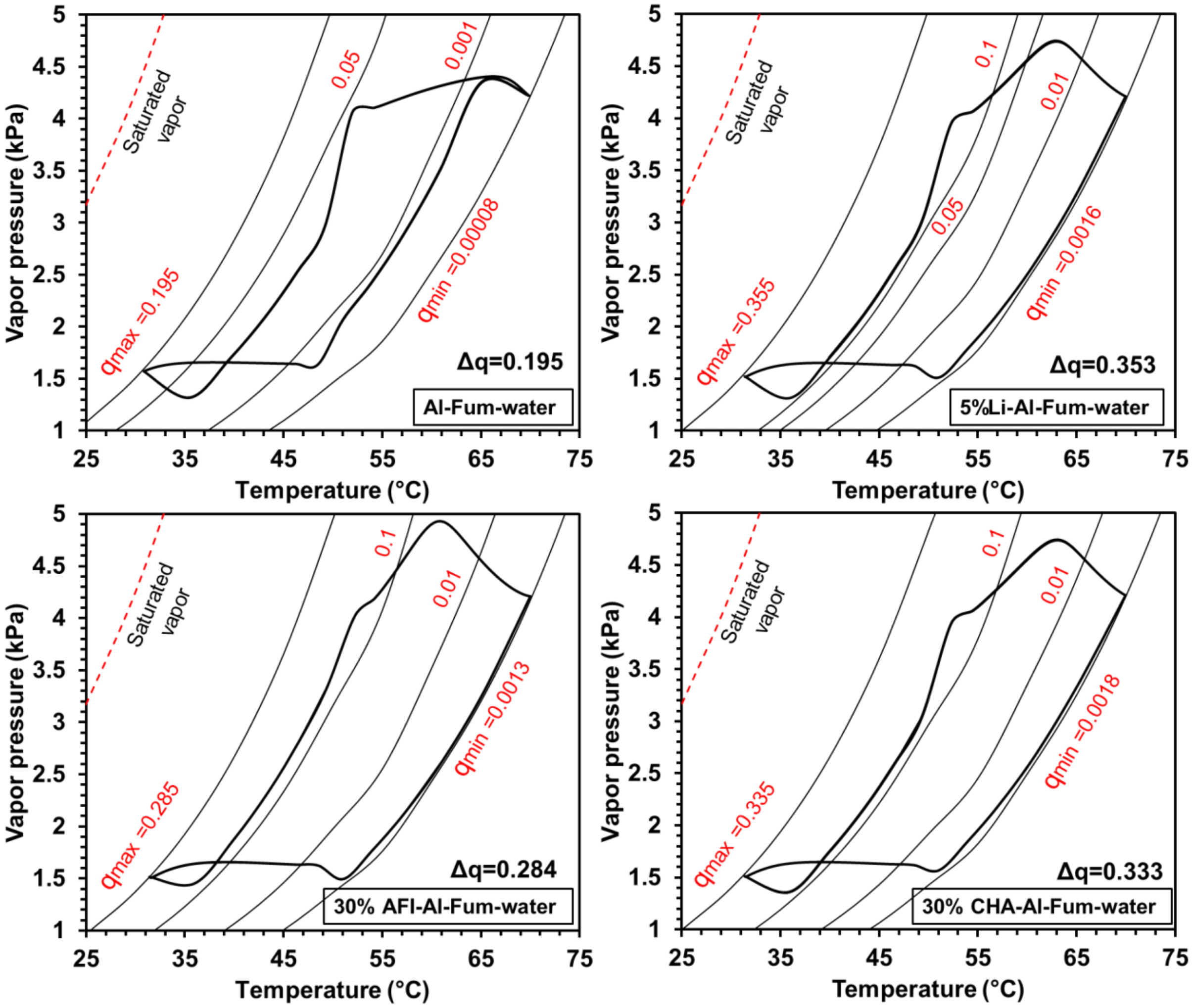

Figure A17: The $Dühring$ (pressure-temperature, P-T) diagram of Al-Fum MOFs and zeolite composites based AAHT system at the inlet conditions of 70 ℃/30 ℃/14.8 ℃/25 s/500 s (regeneration temperature/cold water inlet temperature/chilled water inlet temperature/switching time/half cycle time).

Figure A18 displays the Dühring diagram of Al-Fum MOFs based AAHT systems under higher regeneration conditions (90 ℃), where complete desorption of water vapour is observed for all the systems and cooling capacity of all the materials is maximized.

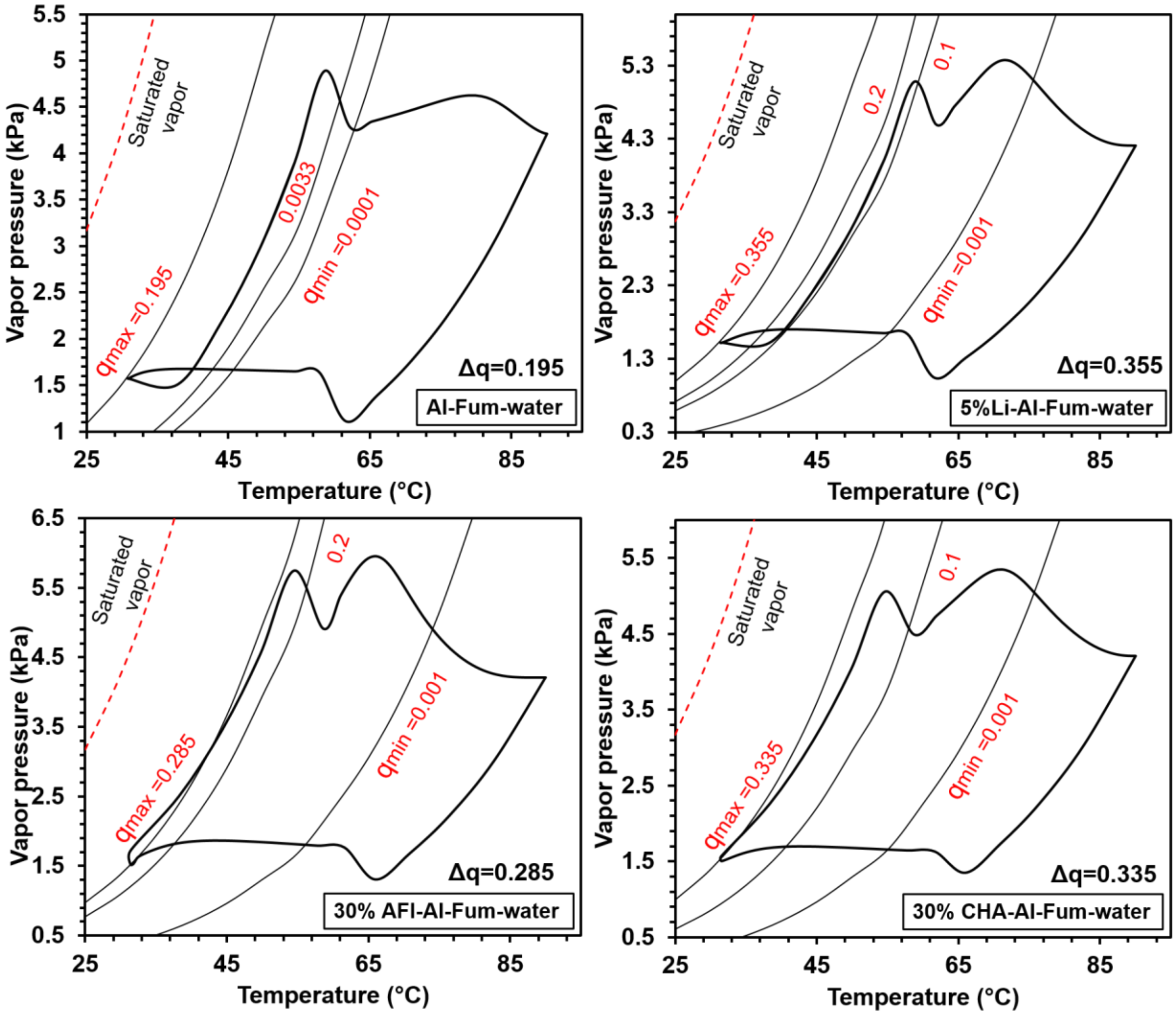

Figure A18: The *Dühring* (pressure-temperature, P-T) diagram of Al-Fum MOFs and zeolite composites based AAHT system at the inlet conditions of 90 ℃/30 ℃/14.8 ℃/25 s/500 s (regeneration temperature/cold water inlet temperature/chilled water inlet temperature/switching time/half cycle time).

The water uptake-offtake difference (Δq) for Al-Fum based AAHT system at various regeneration temperatures (60 to 90 °C) is summarized in Table A.6. It is observed that due to the hydrophobic trait of the parent Al-Fum, it works well at the regeneration temperature of 60 °C (Δq = 0.192 g/g). The maximum cooling capacity of the parent Al-Fum is achieved at the regeneration temperature of 70 °C (Δq = 0.195 g/g) and no improvement of Δq is found as the regeneration temperature increases up to 90 °C. On the other hand, higher Δq under higher regeneration temperatures are found for all the modified Al-Fum based MOFs for their enhanced hydrophilicity. For example, at the regeneration temperature of 60 °C, the Δq for 5% Li-Al-Fum, 30% AFI-Al-Fum and 30% CHA-Al-Fum is 0.311 g/g, 0.255 g/g and 0.285 g/g, respectively. As the regeneration temperature increases to 70 °C, the Δq for 5% Li-Al-Fum, 30% AFI-Al-Fum and 30% CHA-Al-Fum is 0.353 g/g (+13.5%), 0.284 g/g (+11.4) and 0.333 g/g (+16.8), respectively. As the regeneration temperature increases to 80 °C, small improvement of Δq (0.001 to 0.002 g/g) is found for all the modified Al-Fum and the maximum cooling capacity is reached.

Table A.6: Water uptake-offtake difference (Δq) at various regeneration temperatures (60 to 90 °C) for original and modified Al-Fum based AAHT systems (cold water inlet temperature/chilled water inlet temperature/switching time/half cycle time = 30 ℃/14.8 ℃/25 s/500 s).

	Δq (T_{regen}= 60 °C)	Δq (T_{regen}= 70 °C)	Δq (T_{regen}= 80 °C)	Δq (T_{regen}= 90 °C)
Al-Fum	0.192	0.195	0.195	0.195
5% Li-Al-Fum	0.311	0.353	0.355	0.355
30%AFI-Al-Fum	0.255	0.284	0.285	0.285
30%CHA-Al-Fum	0.285	0.333	0.335	0.335

A6. MATLAB Code for Adsorption Assisted Heat Transformation Modelling

```
function main = AlFumAHT()

clc; clear all; close all; clf;

global Flag1
global Tcw_in Thw_in T_chw_in T_chw_out T_w_bedA_out T_w_bedD_out T_w_cond_out
global P_bedA P_bedD w_bedA w_bedD
global Mads Qst Rw A wm n D_so Rp Ea R Cpads hfg_C
global m_dot_cw_bed m_dot_cw_cond m_dot_hw_bed m_dot_chw
global Mhx_bedCphx_bed Mhx_condCphx_cond Mhx_evpCphx_evp M_ref_L_cond
M_ref_L_evp;
global UA_bedA UA_bedD U_cond A_cond U_evp A_evp As

t_normal = 500;                                    %Time for normal operation
```

```
t_sw = 25;                                        %Time for switching

t_cycle = (t_normal+t_sw);                        %Total cycle time

step = 5;                                              %Evaluate every 5 seconds
N_cyc = 20;                                            %No. of cycles evaluated

Tcw_in = 30+273;                                       %Kelvin
Thw_in = 80+273;                                       %Kelvin
T_chw_in = 14.8+273;

As = 1056.26;                                           %m^2/g
Rw = 0.4619;                                            %kj/kg-k
A = 8.5E-4;                                             %(1/Pa)
wm = 0.4;
n = 6.8;
Qst = 2.74E3;                                           %kJ/kg
hfg_C = 2442;

D_so = 2.54E-4;                                         % m2/s
Rp = 1E-4;                                              %m
Ea = 41.20;                                             %kJ/mol
R = 8.3144621E-3;                                       %kJ/mol.K
Cpads = 0.805;                                          %Cp of MOF (kJ/kg.K)

Mads = 18;                                               %kg

 %=====================================================================
                        Heat Exchanger Parameters
%=====================================================================
Mhx_bedCphx_bed = 100;                                      % Kg*Kj/Kg-k
UA_bedA = 1.5;                                              % kW/K
UA_bedD = 2.8;                                              % kW/K
m_dot_cw_bed =  1.52;                                       %kg/s
m_dot_hw_bed =  1.28;                             %Hot water mass flow rate (kg/s)

Mhx_condCphx_cond = 24*0.386;                               % Kg*Kj/Kg-k
U_cond = 4.115;
A_cond =  3.73;
M_ref_L_cond = 5;
m_dot_cw_cond = 1.37;


Mhx_evpCphx_evp = 8.9*0.386;                                % Kg*Kj/Kg-k
U_evp = 2.557;
A_evp = 1.91;
```

```
M_ref_L_evp = 12;
m_dot_chw = 0.71;

%=========================================================================
                                        %Initial Values
Time_i   = 0;

T_evp_i = 30+273;
T_cond_i = 30+273;

T_bedA_i = 30+273;                                                                    %Kelvin

Ps_bedA_i = 10^3*(-5.007261711E-15*T_bedA_i^6 + 1.249032418E-11*T_bedA_i^5 -
1.135454979E-08*T_bedA_i^4 + 5.164337223E-06*T_bedA_i^3 - 1.275119405E-
03*T_bedA_i^2 + 1.643475641E-01*T_bedA_i - 8.706432224E+00);
P_bedA_i = 10^3*(-5.007261711E-15*T_evp_i^6 + 1.249032418E-11*T_evp_i^5 -
1.135454979E-08*T_evp_i^4 + 5.164337223E-06*T_evp_i^3 - 1.275119405E-03*T_evp_i^2 +
1.643475641E-01*T_evp_i - 8.706432224E+00);                                  %kPa

%hf_bedA_i = refpropm('H',  'T', T_bedA_i, 'Q', 0, 'water')*1E-3;
%hg_bedA_i = refpropm('H',  'T', T_bedA_i, 'Q', 1, 'water')*1E-3;
hfg_bedA_i = (10^3*(6.40224E-12*T_evp_i^5 - 3.93212E-08*T_evp_i^4 + 3.63907E-
05*T_evp_i^3 - 1.39601E-02*T_evp_i^2 + 4.34707E+00*T_evp_i + 1.82254E+03)-
10^3*(1.95664E-10*T_evp_i^5 - 3.36772E-07*T_evp_i^4 + 2.34408E-04*T_evp_i^3 -
8.21171E-02*T_evp_i^2 + 1.86089E+01*T_evp_i - 2.15617E+03))*1E-3;

if(Ps_bedA_i <= P_bedA_i)

    w_bedA_i = wm;

else
    w_bedA_i = wm*((A*exp(n*(Qst-
hfg_C)/(Rw*T_bedA_i))*(P_bedA_i/Ps_bedA_i)^n)/(1+(A*exp(n*(Qst-
hfg_C)/(Rw*T_bedA_i))-1)*(P_bedA_i/Ps_bedA_i)^n));

end

T_bedD_i = 30+273;

Ps_bedD_i = 10^3*(-5.007261711E-15*T_bedD_i^6 + 1.249032418E-11*T_bedD_i^5 -
1.135454979E-08*T_bedD_i^4 + 5.164337223E-06*T_bedD_i^3 - 1.275119405E-
03*T_bedD_i^2 + 1.643475641E-01*T_bedD_i - 8.706432224E+00);
P_bedD_i = 10^3*(-5.007261711E-15*T_cond_i^6 + 1.249032418E-11*T_cond_i^5 -
1.135454979E-08*T_cond_i^4 + 5.164337223E-06*T_cond_i^3 - 1.275119405E-
03*T_cond_i^2 + 1.643475641E-01*T_cond_i - 8.706432224E+00);          %kPa
```

```
%hf_bedD_i = refpropm('H',  'T', T_bedD_i, 'Q', 0, 'water')*1E-3;
%hg_bedD_i = refpropm('H',  'T', T_bedD_i, 'Q', 1, 'water')*1E-3;
hfg_bedD_i = (10^3*(6.40224E-12*T_cond_i^5 - 3.93212E-08*T_cond_i^4 + 3.63907E-
05*T_cond_i^3 - 1.39601E-02*T_cond_i^2 + 4.34707E+00*T_cond_i + 1.82254E+03)-
10^3*(1.95664E-10*T_cond_i^5 - 3.36772E-07*T_cond_i^4 + 2.34408E-04*T_cond_i^3 -
8.21171E-02*T_cond_i^2 + 1.86089E+01*T_cond_i - 2.15617E+03))*1E-3;

if(Ps_bedD_i <= P_bedD_i)

       w_bedD_i = wm;

else
       w_bedD_i = wm*((A*exp(n*(Qst-
hfg_C)/(Rw*T_bedD_i))*(P_bedD_i/Ps_bedD_i)^n)/(1+(A*exp(n*(Qst-
hfg_C)/(Rw*T_bedD_i))-1)*(P_bedD_i/Ps_bedD_i)^n));

end

%=====================================================================
t = Time_i;
s = 0;
cycle = 0;

g = 0;
h = 0;

for M =1:N_cyc              %Main loop for evaluating cycles

    t_round = 0;
    Q_D = 0;
    Q_E = 0;
    Q_C = 0;
    Q_A = 0;



    for L = 1:step:t_cycle

        s = s+1;                  %s is a counter. add counter

        t = t+step;              %count elapsed time


        Time(s) = t;              %Time is an array containing t where the process is evaluated at

        t_round = t_round + step; %count elapsed time in one for-next loop
```

```
    if(t_round <= t_normal)     %check whether the elapsed time has passed the normal
operation time
      Flag1 = 1 ;             %adsorption/desorption
    elseif((t_round > t_normal)&&(t_round <= t_cycle))
      Flag1 = 0 ;            %switching mode
    end;

    Timerange1 = [Time_i t];        %set time range to be used to solve differential eqns.
    Initialvalues = [w_bedA_i T_bedA_i w_bedD_i T_bedD_i T_cond_i T_evp_i];    %Initial
values being used to solve diff. eqns. Being stored first to Y before it is being used.

    option1 = odeset('RelTol', 1E-4, 'AbsTol', 1E-4);       %setting error tolerance

    Y = ode45(@ddydwdt, Timerange1, Initialvalues, option1);    %solving all the diff eqns. in
ddydwdt.m file --> the step is being decided by matlab

    Y_t = deval(Y,t);        %Y_t's values are only Y's value at t; not all the values of Y
evaluated

    %Storing the newly calculated value into array of variables

    w_bedA(s) = Y_t(1);
    T_bedA(s) = Y_t(2);
    w_bedD(s) = Y_t(3);
    T_bedD(s) = Y_t(4);
    T_cond(s) = Y_t(5);
    T_evp(s)  = Y_t(6);


    if(Flag1 == 1)

      Tcw_bed_in  = Tcw_in;
      Tcw_bed_out = T_w_bedA_out;
      Thw_bed_in  = Thw_in;
      Thw_bed_out = T_w_bedD_out;

    elseif(Flag1 == 0)

      Tcw_bed_in  = Tcw_in;
      Tcw_bed_out = T_w_bedD_out;
      Thw_bed_in  = Thw_in;
      Thw_bed_out = T_w_bedA_out;

    end
```

```
T_cw_cond_in = Tcw_in;
T_cw_cond_out = T_w_cond_out;


%============================================================
                        Adsorption/Desorption Switching
%============================================================


if ((mod(M,2)==1)||(M == 1))

T_bed2(s) = T_bedD(s);
W_bed2(s) = w_bedD(s);
T_bed1(s) = T_bedA(s);
W_bed1(s) = w_bedA(s);
P_bed1(s) = P_bedA;
P_bed2(s) = P_bedD;

else

T_bed1(s) = T_bedD(s);
W_bed1(s) = w_bedD(s);
T_bed2(s) = T_bedA(s);
W_bed2(s) = w_bedA(s);
P_bed2(s) = P_bedA;
P_bed1(s) = P_bedD;

end;

Tcond_in(s)  = T_cw_cond_in;
Tcond_out(s) = T_cw_cond_out;
T_cw_in(s) = Tcw_bed_in;
T_cw_out(s) = Tcw_bed_out;
T_hw_in(s) = Thw_bed_in;
T_hw_out(s) = Thw_bed_out;
T_chill_in(s) = T_chw_in;
T_chill_out(s) = T_chw_out;

Hcw_bed_out = 1E-3*10^3*(1.95664E-10*Tcw_bed_out^5 - 3.36772E-07*Tcw_bed_out^4 + 2.34408E-04*Tcw_bed_out^3 - 8.21171E-02*Tcw_bed_out^2 + 1.86089E+01*Tcw_bed_out - 2.15617E+03);
Hcw_bed_in = 1E-3*10^3*(1.95664E-10*Tcw_bed_in^5 - 3.36772E-07*Tcw_bed_in^4 + 2.34408E-04*Tcw_bed_in^3 - 8.21171E-02*Tcw_bed_in^2 + 1.86089E+01*Tcw_bed_in - 2.15617E+03);
```

```
    Hhw_bed_in = 1E-3*10^3*(1.95664E-10*Thw_bed_in^5 - 3.36772E-07*Thw_bed_in^4 + 2.34408E-04*Thw_bed_in^3 - 8.21171E-02*Thw_bed_in^2 + 1.86089E+01*Thw_bed_in - 2.15617E+03);
    Hhw_bed_out = 1E-3*10^3*(1.95664E-10*Thw_bed_out^5 - 3.36772E-07*Thw_bed_out^4 + 2.34408E-04*Thw_bed_out^3 - 8.21171E-02*Thw_bed_out^2 + 1.86089E+01*Thw_bed_out - 2.15617E+03);

    H_cw_cond_out = 1E-3*10^3*(1.95664E-10*T_cw_cond_out^5 - 3.36772E-07*T_cw_cond_out^4 + 2.34408E-04*T_cw_cond_out^3 - 8.21171E-02*T_cw_cond_out^2 + 1.86089E+01*T_cw_cond_out - 2.15617E+03);
    H_cw_cond_in = 1E-3*10^3*(1.95664E-10*T_cw_cond_in^5 - 3.36772E-07*T_cw_cond_in^4 + 2.34408E-04*T_cw_cond_in^3 - 8.21171E-02*T_cw_cond_in^2 + 1.86089E+01*T_cw_cond_in - 2.15617E+03);

    Hfg_cond =(10^3*(6.40224E-12*Y_t(5)^5 - 3.93212E-08*Y_t(5)^4 + 3.63907E-05*Y_t(5)^3 - 1.39601E-02*Y_t(5)^2 + 4.34707E+00*Y_t(5) + 1.82254E+03)-10^3*(1.95664E-10*Y_t(5)^5 - 3.36772E-07*Y_t(5)^4 + 2.34408E-04*Y_t(5)^3 - 8.21171E-02*Y_t(5)^2 + 1.86089E+01*Y_t(5) - 2.15617E+03))*1E-3;

    H_chw_in = 1E-3*10^3*(1.95664E-10*T_chw_in^5 - 3.36772E-07*T_chw_in^4 + 2.34408E-04*T_chw_in^3 - 8.21171E-02*T_chw_in^2 + 1.86089E+01*T_chw_in - 2.15617E+03);
    H_chw_out = 1E-3*10^3*(1.95664E-10*T_chw_out^5 - 3.36772E-07*T_chw_out^4 + 2.34408E-04*T_chw_out^3 - 8.21171E-02*T_chw_out^2 + 1.86089E+01*T_chw_out - 2.15617E+03);


    dq_D = (m_dot_hw_bed*step)*(Hhw_bed_in - Hhw_bed_out)/t_cycle;
    Q_D = Q_D + dq_D;


    dq_A = (m_dot_cw_bed*step)*(Hcw_bed_out - Hcw_bed_in)/t_cycle;
    Q_A = Q_A + dq_A;

    dq_E = (m_dot_chw*step)*(H_chw_in - H_chw_out)/t_cycle;

    Q_E = Q_E + dq_E;

    dq_C = (m_dot_cw_cond*step)*(H_cw_cond_out - H_cw_cond_in)/t_cycle;

    Q_C = Q_C + dq_C;

    %Storing the newly calculated value as the initial values for the next round of calculation
    Time_i = t;
    w_bedA_i = Y_t(1);
    T_bedA_i = Y_t(2);
```

```
        w_bedD_i = Y_t(3);
        T_bedD_i = Y_t(4);
        T_cond_i = Y_t(5);
        T_evp_i = Y_t(6);

        T_chw_in = T_chw_in;

         if ((t >= (N_cyc*t_cycle - 2*t_cycle))&&(t <= (N_cyc*t_cycle - t_sw)))

          g = g+step;

          h = h+1;

          Time_plot(h) = g;

          T_bed1_plot(h) = T_bed1(s) -273;
          T_bed2_plot(h) = T_bed2(s) - 273;
          T_cond_plot(h) = T_cond(s)-273;
          T_evp_plot(h)  =  T_evp(s)-273;


          W_bed1_plot(h) = W_bed1(s);
          W_bed2_plot(h) = W_bed2(s);

          P_bed1_plot(h) = P_bed1(s);
          P_bed2_plot(h) = P_bed2(s);

        else

          a = 0 ;

        end


    end

    Q_evp(M) = Q_E
    Q_des(M) = Q_D
    Q_ads(M) = Q_A;
    Q_cond(M)= Q_C;

    Q_add(M) = (Q_evp(M) + Q_des(M));
    Q_rej(M) = (Q_ads(M) + Q_cond(M));

    Error(M)    = ((Q_evp(M) + Q_des(M)) - (Q_ads(M) + Q_cond(M)))*100/(Q_ads(M) +
Q_cond(M))
```

```
    COP(M) = Q_evp(M)/Q_des(M);                            %COP for adsorption cooling application
    SCP(M) = Q_evp(M)/(2*Mads);                            %SCP for adsorption cooling application
    COPh(M) = (Q_cond(M)+ Q_ads(M))/Q_des(M);   %COPh for adsorption heating application
    SHP(M) = (Q_cond(M)+ Q_ads(M))/(2*Mads);      %SHP for adsorption heating application
    PR(M) = (w_bedA(s)*hfg_C)/Q_des(M);               %PR (performance ratio)for desalination
    SDWP(M) = t_cycle*(24*3600/t_cycle)*(Q_cond(M)/(hfg_C*Mads)); % for desalination
    cycle(M) = M;

    w_bedA_i = Y_t(3);
    T_bedA_i = Y_t(4);
    w_bedD_i = Y_t(1);
    T_bedD_i = Y_t(2);


end

figure (1)
plot(Time, (T_bed1), Time, (T_bed2), Time, (T_cond), Time, (T_evp));
hold all;

figure (2)
plot(Time, (P_bed1), Time, (P_bed2));
hold all;

figure(3)
plot(Time, W_bed1, Time, W_bed2);
hold all;

figure(4)
plot(cycle,COP);

hold all;

figure(5)
plot(cycle,SCP);

hold all;

figure(6)
plot(cycle,COPh);

hold all;

figure(7)
plot(cycle,SHP);
```

```
hold all;

figure(8)
plot(cycle,PR);

hold all;

figure(9)
plot(cycle,SDWP);

hold all;

figure (10)
plot(Time, (T_cw_out), Time, (T_hw_out), Time, (T_chill_out), Time, (Tcond_out));

hold all;

end


function dy = ddydwdt(t, Y)

global Flag1;
global Tcw_in Thw_in T_chw_in T_chw_out T_w_bedA_out T_w_bedD_out T_w_cond_out
global P_bedA P_bedD w_bedA w_bedD
global m_dot_cw_bed m_dot_hw_bed m_dot_cw_cond m_dot_chw
global Mads Qst Rw A wm n D_so Rp Ea R Cpads hfg_C
global Mhx_bedCphx_bed Mhx_condCphx_cond Mhx_evpCphx_evp M_ref_L_cond
M_ref_L_evp As

dy = zeros(6,1);        %dy is a 5x1 matrix; syntax = zeros(row, column)

%Storing initial values from Main function to local variables

 w_bedA = Y(1); T_bedA = Y(2);

 T_evp = Y(6);

 w_bedD = Y(3);  T_bedD = Y(4);

 T_cond = Y(5);

 %if T_cond <= 275

  %   T_cond = 278;
```

```
 %elseif T_cond >= 370

  %       T_cond = 368;
%end

 % if T_evp <= 275

  %   T_evp = 278;

 %elseif T_evp >= 370

  %      T_evp = 365;
 %end

   %if T_bedA <= 280

    %  T_bedA = 298;

  %elseif T_bedA >= 370

   %      T_bedA = 368;
   %end

% if T_bedD <= 290

 %    T_bedD = 298;

 %elseif T_bedD >= 370

  %       T_bedD = 368;
 %end
 %=============================Bed1=================================%
 %checking the current mode; normal mode or switching mode

 if(Flag1 == 1)                        %Bed1 is under adsorption mode
    T_w_bedA_in  = Tcw_in;
    m_dot_w_bedA = m_dot_cw_bed;
 elseif(Flag1 == 0)                    %Bed1 is under switching mode
    T_w_bedA_in  = Thw_in;             %Pre-heating for the adsorption process
    m_dot_w_bedA = m_dot_hw_bed;
 end


if(Flag1 == 1)
```

```
    P_bedA = 10^3*(-5.007261711E-15*T_evp^6 + 1.249032418E-11*T_evp^5 - 1.135454979E-
08*T_evp^4 + 5.164337223E-06*T_evp^3 - 1.275119405E-03*T_evp^2 + 1.643475641E-
01*T_evp - 8.706432224E+00);
    Ps_bedA = 10^3*(-5.007261711E-15*T_bedA^6 + 1.249032418E-11*T_bedA^5 -
1.135454979E-08*T_bedA^4 + 5.164337223E-06*T_bedA^3 - 1.275119405E-03*T_bedA^2 +
1.643475641E-01*T_bedA - 8.706432224E+00);
    %hf_bedA = refpropm('H',  'T', T_bedA, 'Q', 0, 'water')*1E-3;
    %hg_bedA = refpropm('H',  'T', T_bedA, 'Q', 1, 'water')*1E-3;
    %hfg_bedA = (10^3*(6.40224E-12*T_evp^5 - 3.93212E-08*T_evp^4 + 3.63907E-
05*T_evp^3 - 1.39601E-02*T_evp^2 + 4.34707E+00*T_evp + 1.82254E+03)-
10^3*(1.95664E-10*T_evp^5 - 3.36772E-07*T_evp^4 + 2.34408E-04*T_evp^3 - 8.21171E-
02*T_evp^2 + 1.86089E+01*T_evp - 2.15617E+03))*1E-3;
    hfg_bedA = (10^3*(6.40224E-12*T_bedA^5 - 3.93212E-08*T_bedA^4 + 3.63907E-
05*T_bedA^3 - 1.39601E-02*T_bedA^2 + 4.34707E+00*T_bedA + 1.82254E+03)-
10^3*(1.95664E-10*T_bedA^5 - 3.36772E-07*T_bedA^4 + 2.34408E-04*T_bedA^3 -
8.21171E-02*T_bedA^2 + 1.86089E+01*T_bedA - 2.15617E+03))*1E-3;
    if(Ps_bedA <= P_bedA)

       w_star_bedA = wm;

    else
       w_star_bedA = wm*((A*exp(n*(Qst-
hfg_C)/(Rw*T_bedA))*(P_bedA/Ps_bedA)^n)/(1+(A*exp(n*(Qst-hfg_C)/(Rw*T_bedA))-
1)*(P_bedA/Ps_bedA)^n));

    end;



    %w_bedA_const= 15*D_so/Rp^2;



elseif(Flag1 == 0)

    w_star_bedA = w_bedA;
    theta_bedA = w_star_bedA/wm;
    %hf_bedA = refpropm('H',  'T', T_bedA, 'Q', 0, 'water')*1E-3;
    %hg_bedA = refpropm('H',  'T', T_bedA, 'Q', 1, 'water')*1E-3;
    hfg_bedA = (10^3*(6.40224E-12*T_bedA^5 - 3.93212E-08*T_bedA^4 + 3.63907E-
05*T_bedA^3 - 1.39601E-02*T_bedA^2 + 4.34707E+00*T_bedA + 1.82254E+03)-
10^3*(1.95664E-10*T_bedA^5 - 3.36772E-07*T_bedA^4 + 2.34408E-04*T_bedA^3 -
8.21171E-02*T_bedA^2 + 1.86089E+01*T_bedA - 2.15617E+03))*1E-3;
    %hfg_bedA = (10^3*(6.40224E-12*T_evp^5 - 3.93212E-08*T_evp^4 + 3.63907E-
05*T_evp^3 - 1.39601E-02*T_evp^2 + 4.34707E+00*T_evp + 1.82254E+03)-
10^3*(1.95664E-10*T_evp^5 - 3.36772E-07*T_evp^4 + 2.34408E-04*T_evp^3 - 8.21171E-
02*T_evp^2 + 1.86089E+01*T_evp - 2.15617E+03))*1E-3;
    K_bedA = A*exp(n*(Qst-hfg_C)/(Rw*T_bedA));
```

```
   Ps_bedA = 10^3*(-5.007261711E-15*T_bedA^6 + 1.249032418E-11*T_bedA^5 -
1.135454979E-08*T_bedA^4 + 5.164337223E-06*T_bedA^3 - 1.275119405E-03*T_bedA^2 +
1.643475641E-01*T_bedA - 8.706432224E+00);
   P_bedA = Ps_bedA*(theta_bedA/(K_bedA-theta_bedA*(K_bedA-1)))^(1/n);
   %kads_A = 18*P_bedA/(2*pi*18*R*T_bedA)^0.5 * exp(-(Ea/(R*T_bedA)))*189.6;
   %w_bedA_const= 0; %kads_A*(P_bedA/Ps_bedA)^n + (kads_A/K_bedA)*(1-
(P_bedA/Ps_bedA)^n);
end

T_w_bedA_out = BedHex(T_bedA, T_w_bedA_in, m_dot_w_bedA);

h_w_bedA_in = 1E-3*10^3*(1.95664E-10*T_w_bedA_in^5 - 3.36772E-07*T_w_bedA_in^4 +
2.34408E-04*T_w_bedA_in^3 - 8.21171E-02*T_w_bedA_in^2 + 1.86089E+01*T_w_bedA_in
- 2.15617E+03);
h_w_bedA_out = 1E-3*10^3*(1.95664E-10*T_w_bedA_out^5 - 3.36772E-
07*T_w_bedA_out^4 + 2.34408E-04*T_w_bedA_out^3 - 8.21171E-02*T_w_bedA_out^2 +
1.86089E+01*T_w_bedA_out - 2.15617E+03);
CpabeA = 10^3*(-1.35090E-11*T_bedA^5 + 2.40993E-08*T_bedA^4 - 1.71323E-
05*T_bedA^3 + 6.07609E-03*T_bedA^2 - 1.07591*T_bedA + 8.02982E01)*1E-3;

%==============================Bed2==================================%
%checking the current mode; normal mode or switching mode


 if(Flag1 == 1)                    %Bed2 is under desorption mode
   T_w_bedD_in  = Thw_in;
   m_dot_w_bedD = m_dot_hw_bed;

 elseif(Flag1 == 0)                 %Bed2 is under switching mode
   T_w_bedD_in  = Tcw_in;            %Pre-cooling for the desorption process
   m_dot_w_bedD = m_dot_cw_bed;

end

if(Flag1 == 1)

   P_bedD = 10^3*(-5.007261711E-15*T_cond^6 + 1.249032418E-11*T_cond^5 -
1.135454979E-08*T_cond^4 + 5.164337223E-06*T_cond^3 - 1.275119405E-03*T_cond^2 +
1.643475641E-01*T_cond - 8.706432224E+00);
   Ps_bedD = 10^3*(-5.007261711E-15*T_bedD^6 + 1.249032418E-11*T_bedD^5 -
1.135454979E-08*T_bedD^4 + 5.164337223E-06*T_bedD^3 - 1.275119405E-03*T_bedD^2 +
1.643475641E-01*T_bedD - 8.706432224E+00);
   %hf_bedD = refpropm('H', 'T', T_bedD, 'Q', 0, 'water')*1E-3;
   %hg_bedD = refpropm('H', 'T', T_bedD, 'Q', 1, 'water')*1E-3;
   %hfg_bedD = (10^3*(6.40224E-12*T_cond^5 - 3.93212E-08*T_cond^4 + 3.63907E-
05*T_cond^3 - 1.39601E-02*T_cond^2 + 4.34707E+00*T_cond + 1.82254E+03)-
```

```
10^3*(1.95664E-10*T_cond^5 - 3.36772E-07*T_cond^4 + 2.34408E-04*T_cond^3 - 8.21171E-02*T_cond^2 + 1.86089E+01*T_cond - 2.15617E+03))*1E-3;
    hfg_bedD = (10^3*(6.40224E-12*T_bedD^5 - 3.93212E-08*T_bedD^4 + 3.63907E-05*T_bedD^3 - 1.39601E-02*T_bedD^2 + 4.34707E+00*T_bedD + 1.82254E+03)-10^3*(1.95664E-10*T_bedD^5 - 3.36772E-07*T_bedD^4 + 2.34408E-04*T_bedD^3 - 8.21171E-02*T_bedD^2 + 1.86089E+01*T_bedD - 2.15617E+03))*1E-3;

    if(Ps_bedD <= P_bedD)

        w_star_bedD = wm;

    else
        w_star_bedD = wm*((A*exp(n*(Qst-hfg_C)/(Rw*T_bedD))*(P_bedD/Ps_bedD)^n)/(1+(A*exp(n*(Qst-hfg_C)/(Rw*T_bedD))-1)*(P_bedD/Ps_bedD)^n));

    end;


    %w_bedD_const= 15*D_so/Rp^2;

elseif(Flag1 == 0)

    w_star_bedD = w_bedD;
    theta_bedD = w_star_bedD/wm;
    %hf_bedD = refpropm('H', 'T', T_bedD, 'Q', 0, 'water')*1E-3;
    %hg_bedD = refpropm('H', 'T', T_bedD, 'Q', 1, 'water')*1E-3;
    hfg_bedD = (10^3*(6.40224E-12*T_bedD^5 - 3.93212E-08*T_bedD^4 + 3.63907E-05*T_bedD^3 - 1.39601E-02*T_bedD^2 + 4.34707E+00*T_bedD + 1.82254E+03)-10^3*(1.95664E-10*T_bedD^5 - 3.36772E-07*T_bedD^4 + 2.34408E-04*T_bedD^3 - 8.21171E-02*T_bedD^2 + 1.86089E+01*T_bedD - 2.15617E+03))*1E-3;
    %hfg_bedD = (10^3*(6.40224E-12*T_cond^5 - 3.93212E-08*T_cond^4 + 3.63907E-05*T_cond^3 - 1.39601E-02*T_cond^2 + 4.34707E+00*T_cond + 1.82254E+03)-10^3*(1.95664E-10*T_cond^5 - 3.36772E-07*T_cond^4 + 2.34408E-04*T_cond^3 - 8.21171E-02*T_cond^2 + 1.86089E+01*T_cond - 2.15617E+03))*1E-3;
    K_bedD = A*exp(n*(Qst-hfg_C)/(Rw*T_bedD));
    Ps_bedD = 10^3*(-5.007261711E-15*T_bedD^6 + 1.249032418E-11*T_bedD^5 - 1.135454979E-08*T_bedD^4 + 5.164337223E-06*T_bedD^3 - 1.275119405E-03*T_bedD^2 + 1.643475641E-01*T_bedD - 8.706432224E+00);
    P_bedD =  Ps_bedD*(theta_bedD/(K_bedD-theta_bedD*(K_bedD-1)))^(1/n);
    %kads_D = 18*P_bedD/(2*pi*18*R*T_bedD)^0.5 * exp(-(Ea/(R*T_bedD)))*189.6;
    %w_bedD_const= 0; %kads_D*(P_bedD/Ps_bedD)^n + (kads_D/K_bedD)*(1-(P_bedD/Ps_bedD)^n);

end
```

```
T_w_bedD_out = BedHex(T_bedD, T_w_bedD_in, m_dot_w_bedD);

h_w_bedD_in = 1E-3*10^3*(1.95664E-10*T_w_bedD_in^5 - 3.36772E-07*T_w_bedD_in^4 +
2.34408E-04*T_w_bedD_in^3 - 8.21171E-02*T_w_bedD_in^2 + 1.86089E+01*T_w_bedD_in
- 2.15617E+03);
h_w_bedD_out = 1E-3*10^3*(1.95664E-10*T_w_bedD_out^5 - 3.36772E-
07*T_w_bedD_out^4 + 2.34408E-04*T_w_bedD_out^3 - 8.21171E-02*T_w_bedD_out^2 +
1.86089E+01*T_w_bedD_out - 2.15617E+03);
CpabeD = 10^3*(-1.35090E-11*T_bedD^5 + 2.40993E-08*T_bedD^4 - 1.71323E-
05*T_bedD^3 + 6.07609E-03*T_bedD^2 - 1.07591*T_bedD + 8.02982E01)*1E-3;

%==============================Condenser===============================
T_w_cond_in  = Tcw_in;
m_dot_w_cond = m_dot_cw_cond;

T_w_cond_out  = CondHex(T_cond, T_w_cond_in, m_dot_w_cond);

h_fg_cond =(10^3*(6.40224E-12*T_cond^5 - 3.93212E-08*T_cond^4 + 3.63907E-
05*T_cond^3 - 1.39601E-02*T_cond^2 + 4.34707E+00*T_cond + 1.82254E+03)-
10^3*(1.95664E-10*T_cond^5 - 3.36772E-07*T_cond^4 + 2.34408E-04*T_cond^3 - 8.21171E-
02*T_cond^2 + 1.86089E+01*T_cond - 2.15617E+03))*1E-3;

h_f_cond = 1E-3*10^3*(1.95664E-10*T_cond^5 - 3.36772E-07*T_cond^4 + 2.34408E-
04*T_cond^3 - 8.21171E-02*T_cond^2 + 1.86089E+01*T_cond - 2.15617E+03);
h_f_w_cond_in = 1E-3*10^3*(1.95664E-10*T_w_cond_in^5 - 3.36772E-07*T_w_cond_in^4 +
2.34408E-04*T_w_cond_in^3 - 8.21171E-02*T_w_cond_in^2 + 1.86089E+01*T_w_cond_in-
2.15617E+03);
h_f_w_cond_out = 1E-3*10^3*(1.95664E-10*T_w_cond_out^5 - 3.36772E-
07*T_w_cond_out^4 + 2.34408E-04*T_w_cond_out^3 - 8.21171E-02*T_w_cond_out^2 +
1.86089E+01*T_w_cond_out- 2.15617E+03);

Cp_ref_L_cond = 10^3*(-1.35090E-11*T_cond^5 + 2.40993E-08*T_cond^4 - 1.71323E-
05*T_cond^3 + 6.07609E-03*T_cond^2 - 1.07591*T_cond + 8.02982E01)*1E-3;

%==============================Evaporator==============================

T_chw_out  = EvpHex(T_evp, T_chw_in, m_dot_chw);

h_fg_evp =(10^3*(6.40224E-12*T_evp^5 - 3.93212E-08*T_evp^4 + 3.63907E-05*T_evp^3 -
1.39601E-02*T_evp^2 + 4.34707E+00*T_evp + 1.82254E+03)- 10^3*(1.95664E-10*T_evp^5 -
3.36772E-07*T_evp^4 + 2.34408E-04*T_evp^3 - 8.21171E-02*T_evp^2 +
1.86089E+01*T_evp - 2.15617E+03))*1E-3;

h_f_chw_in = 1E-3*10^3*(1.95664E-10*T_chw_in^5 - 3.36772E-07*T_chw_in^4 + 2.34408E-
04*T_chw_in^3 - 8.21171E-02*T_chw_in^2 + 1.86089E+01*T_chw_in - 2.15617E+03);
```

```
h_f_chw_out = 1E-3*10^3*(1.95664E-10*T_chw_out^5 - 3.36772E-07*T_chw_out^4 +
2.34408E-04*T_chw_out^3 - 8.21171E-02*T_chw_out^2 + 1.86089E+01*T_chw_out-
2.15617E+03);

Cp_ref_L_evp = 10^3*(-1.35090E-11*T_evp^5 + 2.40993E-08*T_evp^4 - 1.71323E-
05*T_evp^3 + 6.07609E-03*T_evp^2 - 1.07591*T_evp + 8.02982E01)*1E-3;

%===============================================================

%Linear Driving Force
 %dy(1) = (w_bedA_const*exp(-Ea/(R*Y(2)))*(w_star_bedA - Y(1)));
 %dy(1) = (1-exp(-(t*w_bedA_const)))*(w_star_bedA - Y(1));
 if (Flag1 == 1)
 P_A = 10^3*(-5.007261711E-15*Y(6)^6 + 1.249032418E-11*Y(6)^5 - 1.135454979E-
08*Y(6)^4 + 5.164337223E-06*Y(6)^3 - 1.275119405E-03*Y(6)^2 + 1.643475641E-01*Y(6) -
8.706432224E+00);
 Ps_A = 10^3*(-5.007261711E-15*Y(2)^6 + 1.249032418E-11*Y(2)^5 - 1.135454979E-
08*Y(2)^4 + 5.164337223E-06*Y(2)^3 - 1.275119405E-03*Y(2)^2 + 1.643475641E-01*Y(2) -
8.706432224E+00);
 hfg_A =(10^3*(6.40224E-12*Y(2)^5 - 3.93212E-08*Y(2)^4 + 3.63907E-05*Y(2)^3 -
1.39601E-02*Y(2)^2 + 4.34707E+00*Y(2) + 1.82254E+03)- 10^3*(1.95664E-10*Y(2)^5 -
3.36772E-07*Y(2)^4 + 2.34408E-04*Y(2)^3 - 8.21171E-02*Y(2)^2 + 1.86089E+01*Y(2) -
2.15617E+03))*1E-3;
 kads_A = 18*(P_A*10^3)/(2*pi*18*R*Y(2))^0.5 * exp(-(Ea/(R*Y(2))))*As;
 K_bedA = A*exp(n*(Qst-hfg_C)/(Rw*Y(2)));
 w_bedA_const = kads_A*(P_A/Ps_A)^n + (kads_A/K_bedA)*(1-(P_A/Ps_A)^n);
 dy(1) = (kads_A*(P_A/Ps_A)^n - w_bedA_const*Y(1)/wm)*wm;
 elseif (Flag1 == 0)
  dy(1) = 0;
 end
 %dy(1) = (kads_A*(P_A/Ps_A)^n - w_bedA_const*Y(1)/wm)*wm;

%dT/dt from Energy Balance equation for BedA
 dy(2) = ((Qst* Mads * dy(1))-(m_dot_w_bedA*(h_w_bedA_out-h_w_bedA_in)))/(Mads*Cpads
+ Mhx_bedCphx_bed + Mads*Y(1)*CpabeA);

%Linear Driving Force
 %dy(3) = (w_bedD_const*exp(-Ea/(R*Y(4)))*(w_star_bedD - Y(3)));
 %dy(3) = (1-exp(-(t*w_bedD_const)))*(w_star_bedD - Y(3));
 if (Flag1 == 1)
 P_D = 10^3*(-5.007261711E-15*Y(5)^6 + 1.249032418E-11*Y(5)^5 - 1.135454979E-
08*Y(5)^4 + 5.164337223E-06*Y(5)^3 - 1.275119405E-03*Y(5)^2 + 1.643475641E-01*Y(5) -
8.706432224E+00);
 Ps_D = 10^3*(-5.007261711E-15*Y(4)^6 + 1.249032418E-11*Y(4)^5 - 1.135454979E-
08*Y(4)^4 + 5.164337223E-06*Y(4)^3 - 1.275119405E-03*Y(4)^2 + 1.643475641E-01*Y(4) -
8.706432224E+00);
```

```
 hfg_D =(10^3*(6.40224E-12*Y(4)^5 - 3.93212E-08*Y(4)^4 + 3.63907E-05*Y(4)^3 -
1.39601E-02*Y(4)^2 + 4.34707E+00*Y(4) + 1.82254E+03)- 10^3*(1.95664E-10*Y(4)^5 -
3.36772E-07*Y(4)^4 + 2.34408E-04*Y(4)^3 - 8.21171E-02*Y(4)^2 + 1.86089E+01*Y(4) -
2.15617E+03))*1E-3;
 kads_D = 18*(P_D*10^3)/(2*pi*18*R*Y(4))^0.5 * exp(-(Ea/(R*Y(4))))*As;
 K_bedD = A*exp(n*(Qst-hfg_C)/(Rw*Y(4)));
 w_bedD_const = kads_D*(P_D/Ps_D)^n + (kads_D/K_bedD)*(1-(P_D/Ps_D)^n);
 dy(3) = (kads_D*(P_D/Ps_D)^n - w_bedD_const*Y(3)/wm)*wm;
 elseif (Flag1 == 0)
 dy(3) = 0;
 end
 %dy(3) = (kads_D*(P_D/Ps_D)^n - w_bedD_const*Y(3)/wm)*wm;

%dT/dt from Energy Balance equation for Bed1
 dy(4) = (((m_dot_w_bedD*(h_w_bedD_in - h_w_bedD_out) + Qst* Mads *
dy(3))))/(Mads*Cpads + Mhx_bedCphx_bed + Mads*Y(3)*CpabeD);

%Energy balance for condenser
 dy(5) = (-Mads*dy(3)*h_fg_cond - m_dot_w_cond*(h_f_w_cond_out - h_f_w_cond_in) +
Mads*dy(3)*h_f_cond)/(Mhx_condCphx_cond + M_ref_L_cond*Cp_ref_L_cond);

%Energy balance for evaporator
 dy(6) = (m_dot_chw*(h_f_chw_in - h_f_chw_out) - h_f_cond*Mads*dy(3) -
h_fg_evp*Mads*dy(1))/(Mhx_evpCphx_evp + M_ref_L_evp*Cp_ref_L_evp);


end



function [ T_w_bed_out] = BedHex(T_bed, T_w_bed_in, m_dot_w_bed)

global  UA_bedA UA_bedD Thw_in Tcw_in

if (T_w_bed_in == Tcw_in)
    Cp_w_bed = 10^3*(-1.35090E-11*T_bed^5 + 2.40993E-08*T_bed^4 - 1.71323E-
05*T_bed^3 + 6.07609E-03*T_bed^2 - 1.07591*T_bed + 8.02982E01)*1E-3;
    T_w_bed_out = T_bed + (T_w_bed_in - T_bed)*exp((-
UA_bedA)/(m_dot_w_bed*Cp_w_bed));
elseif (T_w_bed_in == Thw_in)
    Cp_w_bed = 10^3*(-1.35090E-11*T_bed^5 + 2.40993E-08*T_bed^4 - 1.71323E-
05*T_bed^3 + 6.07609E-03*T_bed^2 - 1.07591*T_bed + 8.02982E01)*1E-3;
    T_w_bed_out = T_bed + (T_w_bed_in - T_bed)*exp((-
UA_bedD)/(m_dot_w_bed*Cp_w_bed));
end
end
```

```
function T_w_cond_out  = CondHex(T_cond, T_w_cond_in, m_dot_w_cond)

global U_cond A_cond

Cp_w_cond =  10^3*(-1.35090E-11*T_cond^5 + 2.40993E-08*T_cond^4 - 1.71323E-05*T_cond^3 + 6.07609E-03*T_cond^2 - 1.07591*T_cond + 8.02982E01)*1E-3;

T_w_cond_out = T_cond + (T_w_cond_in - T_cond)*exp((-U_cond*A_cond)/(m_dot_w_cond*Cp_w_cond));

end

function T_chw_out  = EvpHex(T_evp, T_chw_in, m_dot_chw)

global U_evp A_evp

Cp_w_evp = 10^3*(-1.35090E-11*T_evp^5 + 2.40993E-08*T_evp^4 - 1.71323E-05*T_evp^3 + 6.07609E-03*T_evp^2 - 1.07591*T_evp + 8.02982E01)*1E-3;

T_chw_out = T_evp + (T_chw_in - T_evp)*exp((-U_evp*A_evp)/(m_dot_chw*Cp_w_evp));

end
```